POLISH
ACADEMY
OF SCIENCES

COMMITTEE OF
THERMODYNAMICS
AND COMBUSTION

INSTITUTE OF
FLUID FLOW
MACHINERY

archives of thermodynamics

QUARTERLY

ISSN 1231-0956

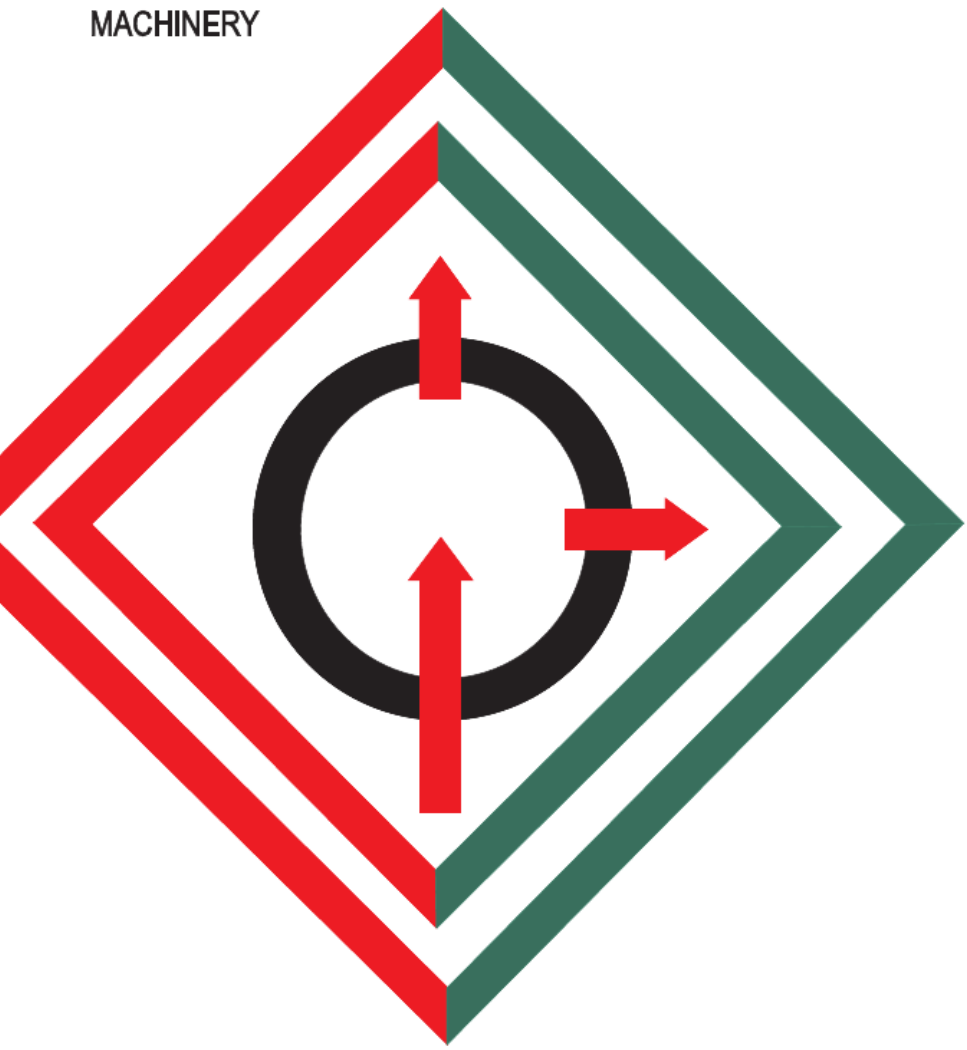

Vol. 44
2023
No. 2

archives of thermodynamics *Appears since 1980*

Aims and Scope

The aim of the quarterly journal Archives of Thermodynamics (AoT) is to disseminate knowledge between scientists and engineers worldwide and to provide a forum for original research conducted in the field of thermodynamics, heat transfer, fluid flow, combustion and energy conversion in various aspects of thermal sciences, mechanical and power engineering. Besides original research papers, review articles are also welcome.

The journal scope of interest encompasses in particular, but is not limited to:

Classical and extended non-equilibrium thermodynamics,
Thermodynamic analysis including exergy,
Thermodynamics of heating and cooling,
Thermodynamics of nuclear power generation,
Thermodynamics in defense engineering,
Advances in thermodynamics,
Experimental, theoretical and numerical heat transfer,
Thermal and energy system analysis,
Renewable energy sources including solar energy,
Secondary fuels and fuel conversion,
Heat and momentum transfer in multiphase flows and nanofluids,
Energy transition,
Advanced energy carriers,
Energy storage and efficiency,
Energy in buildings,
Hydrogen energy,
Combustion and emissions,
Turbomachinery,
Thermal energy conversion,
Integrated energy systems,
Distributed energy generation,
Thermal incineration of wastes and waste heat recovery.

POLISH ACADEMY OF SCIENCES
COMMITTEE OF THERMODYNAMICS AND COMBUSTION
INSTITUTE OF FLUID FLOW MACHINERY

archives of thermodynamics

QUARTERLY
Vol. 44
2023
No. 2

Editorial Office

IMP PAN Publishers
The Szewalski Institute of Fluid Flow Machinery, Fiszera 14, 80-231 Gdańsk, Poland,
Phone: (+48) 58-341-12-71 int. 141, E-mail: redakcja@imp.gda.pl
https://www.imp.gda.pl/archives-of-thermodynamics/

Publication funding of this journal is provided by resources of the Polish Academy of Sciences and the Szewalski Institute of Fluid Flow Machinery

Terms of subscription outside Poland
Annual subscription rate outside Poland (2023) is 152 EUR. Price of single issue is 38 EUR. Previously published volumes are available on request. Subscription orders should be sent directly to **IMP PAN Publishers, The Szewalski Institute of Fluid Flow Machinery PASci, ul. Fiszera 14, 80-231 Gdansk, Poland**; dr Jarosław Frączak, phone: (+48) 58-52-25-230; e-mail: jfrk@imp.gda.pl. Payments should be transferred to the bank account of IMP PAN: IBAN 28 1130 1121 0006 5498 9520 0011 at Bank Gospodarstwa Krajowego; Code SWIFT: GOSKPLPW

Warunki prenumeraty w Polsce
Roczna prenumerata (2023 r.) wynosi 260.00 PLN. Cena pojedynczego numeru wynosi 65.00 PLN. Osiągalne są również wydania archiwalne. Zamówienia z określeniem okresu prenumeraty, nazwiskiem i adresem odbiorcy należy kierować bezpośrednio do Wydawcy (Instytut Maszyn Przepływowych im. R. Szewalskiego PAN, ul. Fiszera 14, 80-231 Gdańsk, dr Jarosław Frączak, e-mail: jfrk@imp.gda.pl). Wpłaty prosimy kierować na konto Instytutu Maszyn Przepływowych PAN nr 28 1130 1121 0006 5498 9520 0011 w Banku Gospodarstwa Krajowego

Articles in *Archives of Thermodynamics* are abstracted and indexed within:

Applied Mechanics Reviews • Arianta • Baidu Scholar • BazTech • Cabell's Directory • Celdes • Chemical Abstracts Service (CAS) – CAplus • CNKI Scholar (China National Knowledge Infrastucture) • CNPIEC • EBSCO (relevant databases) • EBSCO Discovery Service • Elsevier – SCOPUS • ESCI (Emerging Sources Citation Index) • Genamics JournalSeek • Google Scholar • Inspec • Index Copernicus • J-Gate • Journal TOCs • Naviga (Softweco) • Paperbase • Pirabase • POL-index • Polymer Library • Primo Central (ExLibris) • ProQuest (relevant databases) • ReadCube • Referativnyi Zhurnal (VINITI) • SCImago (SJR) • Summon (Serials Solutions/ProQuest) • TDOne (TDNet) • TEMA Technik und Management • Ulrich's Periodicals Directory/ulrichsweb • WorldCat (OCLC)

ISSN 1231-0956
ISSN 2083-6023 (Online)
Journals PAS – Electronic Library Polish Academy of Sciences
https://journals.pan.pl/ather

Typeset in LaTeX by
Drukarnia Braci Grodzickich Sp.j. 05-500 Piaseczno, ul. Geodetów 47a

Printed and bound by
Gimpo, 02-858 Warszawa, ul. Transportowców 11

archives
of thermodynamics
Vol. **44**(2023), No. 2

Contents

archives
of thermodynamics
Vol. **44**(2023), No. 2, 3–20
DOI: 10.24425/ather.2023.146556

Effect of D-shaped, reverse D-shaped and U-shaped turbulators in solar air heater on thermo-hydraulic performance

ABHISHEK GHILDYAL[a]
VIJAY SINGH BISHT[a]
PRABHAKAR BHANDARI[b*]
KAMAL SINGH RAWAT[c]

[a] Veer Madho Singh Bhandari Uttarakhand Technical University, Faculty of Technology, Dehradun 248007, India

[b] K.R. Mangalam University, School of Engineering and Technology, Department of Mechanical Engineering, Gurugram, Haryana 122103, India

[c] Meerut Institute of Engineering and Technology, Mechanical Engineering Department, Meerut 250005, India

Abstract As the cost of fuel rises, designing efficient solar air heaters (SAH) becomes increasingly important. By artificially roughening the absorber plate, solar air heaters' performance can be augmented. Turbulators in different forms like ribs, delta winglets, vortex generators, etc. have been introduced to create local wall turbulence or for vortex generation. In the present work, a numerical investigation on a solar air heater has been conducted to examine the effect of three distinct turbulators (namely D-shaped, reverse D- and U-shaped) on the SAH thermo-hydraulic performance. The simulation has been carried out using the computational fluid dynamics, an advanced and modern simulation technique for Reynolds numbers ranging from 4000 to 18000 (turbulent airflow). For the purpose of comparison, constant ratios of turbulator height/hydraulic diameter and pitch/turbulator height, of 0.021 and 14.28, respectively, were adopted for all SAH configurations. Furthermore, the fluid flow has also been analyzed using turbulence kinetic energy and velocity contours. It was observed that the U-shaped turbulator has the highest value of Nusselt number followed by D-shaped

*Corresponding Author. Email: prabhakar.bhandari40@gmail.com

and reverse D-shaped turbulators. However, in terms of friction factor, the D-shaped configuration has the highest value followed by reverse D-shaped and U-shaped geometries. It can be concluded that among all SAH configurations considered, the U-shaped has outperformed in terms of thermo-hydraulic performance factor.

Keywords: CFD; Renewable energy; Solar air heater; Turbulence kinetic energy; Thermo-hydraulic performance

Nomenclature

A_P	–	heat transfer area, mm^2
C_p	–	specific heat capacity, J/(kgK)
D_h	–	hydraulic diameter, mm
e	–	rib height, mm
fr	–	friction factor
h	–	heat transfer coefficient, W/m^2K
H	–	duct height, mm
I	–	heat flux, W/m^2
k	–	thermal conductivity, W/(m K)
l	–	duct length, mm
$\dot{m}$	–	mass flow rate, kg/s
Nu	–	Nusselt number
Pi	–	pitch, mm
p	–	pressure, Pa
Δp	–	pressure drop, Pa
Re	–	Reynolds number
$\dot{Q}_u$	–	useful heat gain, W
T	–	temperature, K
U	–	mean airflow velocity in the duct, m/s
u_i	–	air flow velocity component in i direction ($i = 1, 2$)
W	–	duct width, mm

Greek symbols

ρ	–	density, kg/m^3
μ	–	dynamic viscosity, Ns/m^2
λ	–	thermal diffusivity, m^2/s
v	–	kinematic viscosity, m^2/s

Subscripts

in	–	inlet
F	–	fluid
out	–	outlet
P	–	absorber plate
t	–	solar air heater with turbulator
s	–	smooth solar air heater

Abbreviations

SAH	–	solar air heater
SST	–	shear stress transport
CFD	–	computational fluid dynamics
ASHRAE	–	American Society of Heating, Refrigerating and Air-Conditioning Engineers
THPF	–	thermo-hydraulic performance factor
RNG	–	renormalization group

1 Introduction

The majority of energy is mainly produced using traditional energy sources such as coal, oil, and natural gas. As a result, traditional energy sources are decreasing at an alarming rate. Furthermore, these energy sources also pollute the environment significantly. So, in order to meet the energy needs of such a vast population, some non-traditional energy sources are needed that do not affect the environment and are easily available. As a result, the usage of alternative energy sources such as solar, wind, biomass, and hydropower has been explored very much in recent decades. Major sources are primarily derived from solar energy either directly or indirectly. Solar energy has been used for a variety of applications, including water heating and cooling, space heating, water purification, cooking, and power generation [1–3]. One of the most common uses of solar energy is room heating via a device known as a solar air heater (SAH). SAH is a better device in terms of handiness, maintenance, and environmental damage. However, one of the major drawbacks of SAH is its poor thermal performance, which is caused by a low heat transfer rate from the absorber plate to the fluid flow, i.e. air. Generally, the flow in SAH is in a turbulent regime as more flow has to take place. So, when air molecules collide with a stationary surface, a thin viscous sublayer forms near the wall in turbulent boundary layers, where the damping impact of molecular viscosity on turbulent velocity fluctuation is dominant, as indicated by Bopche *et al.* [4]. Because of the comparatively low velocity of the air and reduced thermal conductivity, the heat transfer rate between the absorber plate and the air in this viscous sublayer is adversely affected. However, artificial roughness, such as baffles and ribs, twisted tapes, dimples, etc. can be used to overcome this problem [5–8]. This roughness causes turbulence inside the air duct,

which causes the laminar sublayer to break down, increasing the heat transfer coefficient. Artificial roughness, on the other hand, causes friction loss. As a result, turbulence must only be induced in the laminar sublayer, i.e. near the duct surface. Turbulators' applications are not limited to solar air heater but has also been used in other cooling devices such as photovoltaic/thermal collector [9], gas turbine blades [10], and car radiator [11].

Chaube *et al.* [12] studied numerically a solar air heater with ribs having square, rectangle, chamfered, circular, semi-circular, and triangular shapes. They observed that rectangular ribs have yielded the best thermo-hydraulic performance. They also pointed out that the shear stress transport (SST) turbulence model, i.e. SST k-ω model, accurately predicts the experimental value. Karmare *et al.* [13] employed rib grits in a circular, triangular, and square shape with five distinct angles of attack of 54°, 56°, 58°, 60°, and 62°. Their study involved Reynolds numbers ranging from 3600 to 17 000. In the commercial solver (Ansys Fluent), they used the k-epsilon model. They found that a 58° angle of attack has yielded optimum performance. Rajput *et al.* [14] used square, triangular, rectangular, and chamfered turbulators to evaluate flow properties in a SAH. For the analysis, they employed the SST k-ω turbulent model. They observed that triangular and chamfered turbulators provided better thermal characteristics while rectangular turbulators have the best overall performance index among all the configurations. Chaube *et al.* [15] analyzed nine different forms of ribs in a rectangular duct using the SST k-ω model in the CFD program. They found that rectangular ribs with a surface area of 3 mm × 5 mm had the best performance index. Furthermore, they also pointed out that two-dimensional analysis predicts the experimental results more accurately. Yadav and Bhagoria performed a parametric computational study on a solar air heater having equilateral triangular sectioned rib roughness on the absorber plate [16]. They reported that the thermo-hydraulic performance parameter varies between 1.36 and 2.11 for different geometrical parameters of ribs. Semalty *et al.* [17] employed a novel approach of multiple broken arc and circular protrusions as roughness in a solar air heater and found that such configuration improves the thermal performance of the solar air heater with a minimum penalty of frictional pressure drop. Bohra *et al.* [18] roughened their absorber plate with 45° Z-shaped baffles in their numerical study and found that a blockage ratio of 0.3 yielded optimum performance.

Following the above discussion, we have found that the turbulator shapes can significantly affect the thermo-hydraulic performance of a solar air

heater. So, in the present work, three different shaped turbulators i.e. D-shaped, reverse D-shaped, and U-shaped were studied. They are named according to their constructional feature. As per the best knowledge of the authors, these turbulator configurations have not been reported for solar air heaters and the same is the novelty of the present work. These turbulators were attached to the absorber plate to disturb the viscous sublayer. Furthermore, the investigation was carried out to visualize the impact of variation in Reynolds number on the fluid flow characteristics, heat transfer, and friction. The prime objective of the present work is to explore the possibility of enhancement in the thermo-hydraulic performance of solar air heaters using differently shaped turbulators.

2 Numerical modelling

2.1 Computational domain

Using three various types of turbulators, a two-dimensional numerical analysis was carried out to see how the performance of the solar air heater would change. The schematic diagram of the solar air heater in its operation is shown in Fig. 1a. The geometries of turbulators employed in this study were U-shaped, D-shaped, and reverse D-shaped as depicted in Fig. 1b. In this study, we built the two-dimensional rectangular SAH duct domain in the same way as Chaube *et al.* [15] did. The 2D flow domain was designed using the principles of ASHRAE standard 93-2003 [19]. The use of a numerical approach, i.e. computational fluid dynamics solver, is more common in similar types of problems [20, 22, 23] and predicts the flow physics accurately. The present simulations has been carried out in the CFD commercial code Ansys Fluent V 16.0. The duct is divided into three sections. The input and output sections are 245 and 115 mm, respectively. The length of the test segment is 280 mm. The area where the absorber plate is installed is known as the test section. The absorber plate is where the various turbulators are mounted. On this absorber plate, a continuous heat flux of $I = 1000$ W/m^2 is applied to model the solar radiation. The rib height is kept constant at 0.7 mm and the pitch is kept at 10 mm. The temperature of the working fluid and ambient air at the inlet is 300 K. The hydraulic diameter is estimated to be 33.33 mm. Table 1 summarises the parameters applied in the simulations.

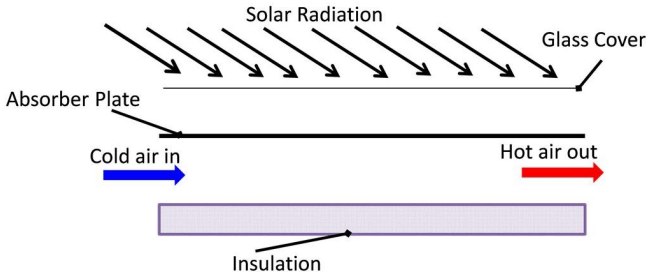

(a)

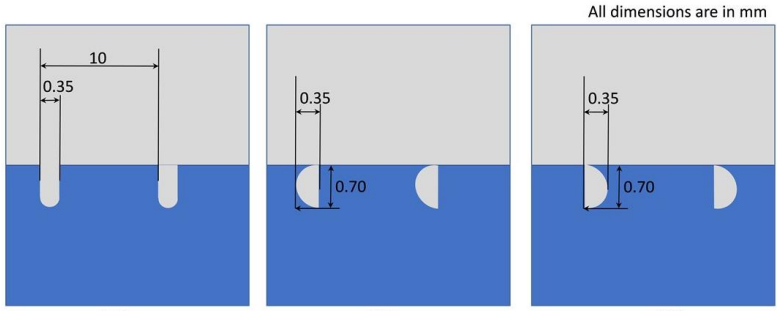

(b)

Figure 1: A diagram of the solar air heater (a) and differently shaped turbulators: U-shaped (b1), reverse D-shaped (b2), and D-shaped (b3).

Table 1: Parameters employed in the analysis.

Parameters	Symbols	Values
Total length of the duct, mm	L	640
Duct width, mm	W	100
Duct height, mm	H	20
Roughness ribs height, mm	E	0.7
Pitch, mm	Pi	10
Hydraulic diameter, mm	D_h	33.33
Relative roughness pitch	Pi/e	14.285
Relative roughness height	e/D_h	0.021
Uniform heat flux, W/m^2	I	1000
Reynolds number	Re	4000, 8000, 12000, 16000, 18000
Inlet temperature of the air, K	T_{in}	300

2.2 Grid generation

The computational domain of SAH has been discretized in quadrilateral structural meshing. Furthermore, to get uniform meshing throughout SAH, face meshing and body sizing of 0.2 mm was used. The meshed image of SAH having D-shaped turbulators is shown in Fig. 2 with a zoomed view. The grid independence test has also been carried out to predict results more accurately in lesser computational time. The grid convergence index (GCI) has been used to measure the relative change in the corresponding magnitude with the grid refinement [24, 25]. However, in the present work, the average Nusselt number for different mesh sizes has been compared. Table 2 highlights the change in the Nusselt number with variation in the number of elements in the computational domain. As the number of elements for the D-shaped configuration increases, the percentage variation of the Nusselt number decreases. Furthermore, it was observed that the mesh size between the last two cases has very low variation, so the number of 319 907 cells was considered in further studies.

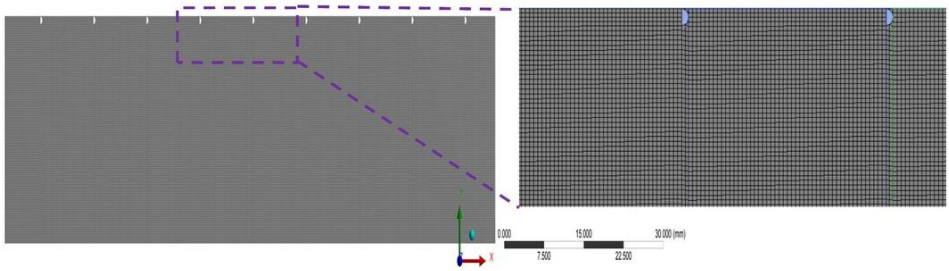

Figure 2: Meshing of SAH having D-shaped turbulators.

Table 2: Grid independence test in SAH with the D-shaped turbulators.

Number of nodes	Number of cells	Nusselt number	Variation, %
280781	100242	66.32	–
564231	201264	92.68	39.74
898165	300127	110.89	19.65
966392	319907	114.59	3.34
1001879	340213	114.74	0.13

2.3 Governing equations

The fluid phenomenon in artificially roughened rectangular solar air heater ducts is solved by using steady-state two-dimensional continuity equation, time-independent incompressible Navier–Stokes equations and the energy equation [5, 17]. These equations can be written in the Cartesian tensor system as follows:

Equations of continuity:

$$\frac{\partial u_i}{\partial x_i} = 0, \quad i = 1,\, 2\,, \tag{1}$$

where x_i are the Cartesian coordinates and u_i are the components of fluid velocity in x_i-direction.

Equations of momentum:

$$\frac{\partial\left(u_i u_j\right)}{\partial x_j} = \frac{1}{\rho}\frac{-\partial p}{\partial x_i} + \frac{\partial\left[\nu\left(\dfrac{\partial u_i}{\partial x_j} + \dfrac{\partial u_j}{\partial x_i}\right)\right]}{\partial x_j} - \frac{\partial\left(\overline{u_i' u_j'}\right)}{\partial x_j}, \quad i, j = 1, 2\,, \tag{2}$$

where p is the pressure, ρ and μ are the density and dynamic viscosity of air, respectively, over-bar denotes a time averaged quantity and prime denotes the deviation from average. The last term on the right-hand side of Eq. (2) is the Reynolds stress tensor and represents the effect of the turbulent fluctuations on the decomposed velocity and pressure fields.

Equation of energy:

$$\frac{\partial}{\partial x_j}\left(u_j T\right) = \frac{\partial}{\partial x_j}\left[\left(\lambda + \lambda_t\right)\frac{\partial T}{\partial x_j}\right], \tag{3}$$

where T is the thermodynamic temperature at different location. The symbols λ and λ_t are molecular thermal diffusivity and turbulent thermal diffusivity, respectively.

Adding turbulators in the fluid flow duct enhances heat transfer, as predicted by calculating Nusselt numbers [26, 27]. In addition to this enhancement, the friction factor also increases. In artificially roughened solar air heaters, the Nusselt number is calculated as follows:

$$\mathrm{Nu} = \frac{hD_h}{k} = \frac{\dot{Q}_u D_h}{A_P\left(T_P - T_F\right)k}, \tag{4}$$

where A_P is the heat transfer area, D_h, k, and h denote the hydraulic diameter of the duct, the thermal conductivity of air, and the heat transfer

coefficient between the air and SAH absorber plate, respectively. Parameters T_P and T_F are the average temperatures of the absorber plate and fluid, respectively. The quantity $\dot{Q}_u$ is the heat gained by air during its flow in the SAH duct and is calculated using the equation

$$\dot{Q}_{\boldsymbol{u}} = \dot{m} C_p \left(T_{\text{out}} - T_{\text{in}}\right), \tag{5}$$

where $\dot{m}$ is the mass flow rate of air in the duct, C_p is the specific heat capacity, T_{out} and T_{in} are temperatures of air at the outlet and inlet cross-sections, respectively.

The friction factor is calculated as

$$fr = \frac{\dfrac{\Delta p}{l} D_h}{\dfrac{1}{2}\rho U^2}, \tag{6}$$

where Δp is the pressure drop across the test section length (l) of an artificially roughened solar air heater and U is the mean velocity of the air i.e. resultant of u_i and u_j. The Reynolds number is calculated as

$$\text{Re} = \frac{\rho U D_h}{\mu}, \tag{7}$$

where μ is the dynamic viscosity of air.

Thermo-hydraulic performance factor (THPF) has been proposed by Webb and Eckert [28] and the expression used in the present work is

$$\text{THPF} = \frac{\dfrac{\text{Nu}_t}{\text{Nu}_s}}{\left(\dfrac{fr_t}{fr_s}\right)^{\frac{1}{3}}}, \tag{8}$$

where subscripts t and s stand for solar air heater duct with and without turbulators, respectively.

2.4 Validation of results

The results of the present numerical model have been validated with the research outcomes of Yadav and Bhagoria [16]. They opted equilateral triangular sectioned rib on the absorber plate of the solar air heater. The geometry, similar to Yadav and Bhagoria [16] has been created and simulated in commercial code Ansys under the constant value of heat flux

(1000 W/m^2) and using RNG k-ε turbulence model. The variation of two different parameters, i.e. Nusselt number (Nu) and friction factor (fr) with respect to Reynolds number (Re) has been compared as illustrated in Fig. 3. It is observed that our numerical model results are similar to those reported by Yadav and Bhagoria [16]. The deviation in Nu value and fr value can be due to assumptions considered in the present simulation like constant thermophysical property of the working fluid, incompressible flow, etc.

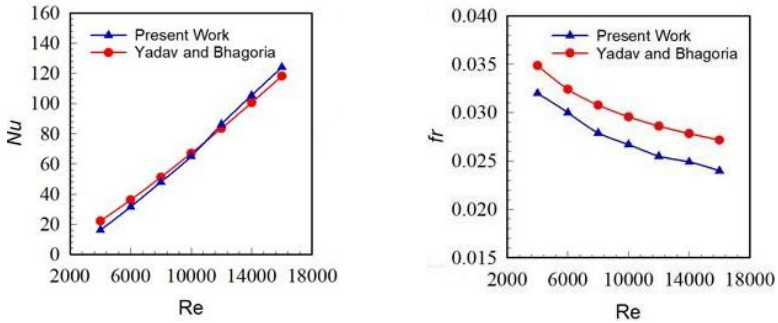

(a) (b)

Figure 3: Comparison of the Nusselt number (a) and friction factor (b) values obtained in the present work with those of Yadav and Bhagoria [16].

3 Results and discussion

The results of the CFD analysis of a roughened solar air heater were thoroughly reviewed. With the help of Ansys Fluent findings, we explored aspects such as heat transfer characteristics, pressure drop, friction factor, turbulent kinetic energy, temperature change, and energy conversion. With the inclusion of different turbulators, the SAH performance varies. Finally, the thermo-hydraulic performance factor is used to compare all three configurations. All simulations were studied under the constant value of relative roughness pitch ($Pi/e = 14.285$) and relative roughness height ($e/D_h = 0.021$).

3.1 Velocity contour

The variation in the velocity of the flowing fluid, i.e. air inside the duct, is depicted in Fig. 4. Furthermore, the figure also shows the zoomed view of the computational domain near the turbulators. The contours have been

plotted for Reynolds number of 18000. The fluctuation in velocity will be reduced if a smooth surface is chosen. However, if some roughness is applied inside the duct, the velocity variation will be greater because the space available for air circulation around the ribs is limited, and the velocity of air should rise below the ribs to maintain a consistent mass flow rate. The turbulence inside the duct will rise as the air velocity increases. This

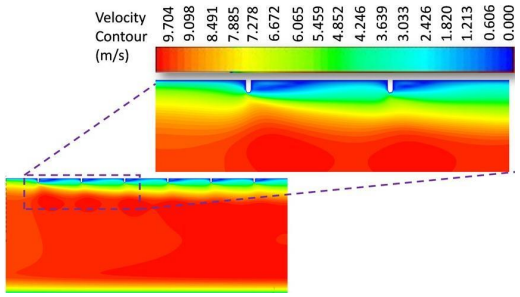

(a)

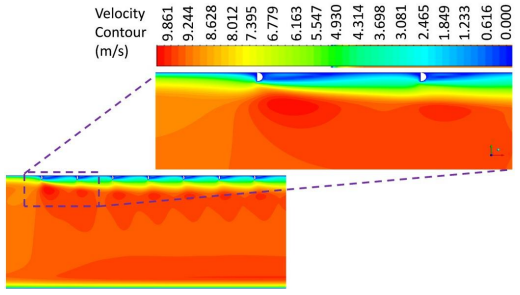

(b)

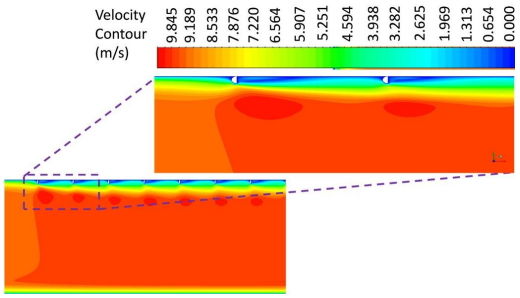

(c)

Figure 4: Velocity contour in the SAH duct employing (a) U-shaped roughness, (b) D-shaped roughness, and (c) reverse D-shaped roughness.

will increase heat transfer between the absorber plate and the air, which is the primary goal of adopting varied roughness. However, there is a penalty, i.e. increase in pressure drop along the flow direction. Due to that more pumping power is required to flow fluid through the duct of SAH.

3.2 Turbulent kinetic energy contour

The mean kinetic energy per unit mass associated with eddies in turbulent flow is known as turbulent kinetic energy. With the help of turbulence kinetic energy, we can directly describe the strength of turbulence in the flow field. The thermal phenomenon in an artificially roughened SAH can be explained using turbulent kinetic energy contours. The contours show that the largest value of turbulent kinetic energy is found near the absorber plate and between the first and second rib and that it decreases along the absorber plate length. The variations of turbulent kinetic energy in SAH for differently shaped turbulators (i.e. U-, D-, and reverse D-shaped) are depicted in Fig. 5.

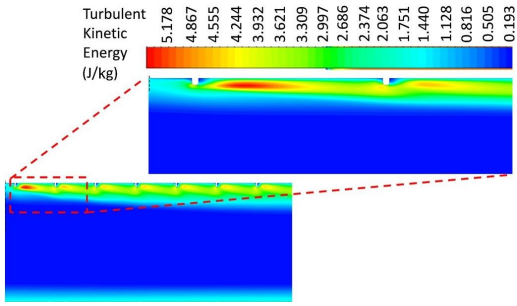

(a)

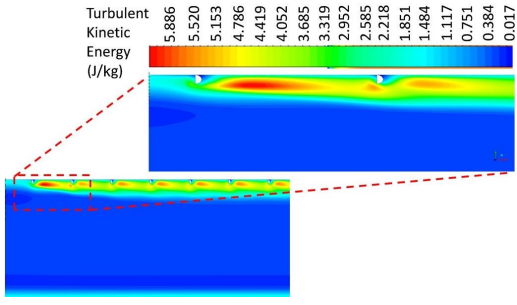

(b)

Figure 5: For caption see next page.

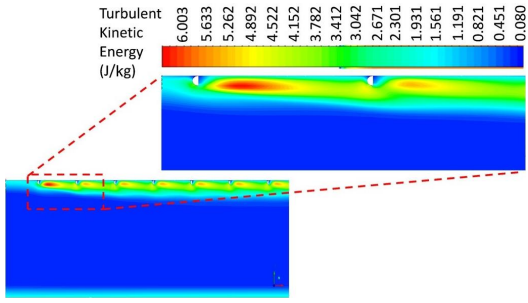

(c)

Figure 5: Turbulent kinetic energy contour in the SAH duct employing (a) U-shaped roughness, (b) D-shaped roughness, and (c) reverse D-shaped roughness.

3.3 Heat transfer and Fluid flow characteristics

A numerical analysis of the solar air heater was carried out in order to determine the heat transfer enhancement. To improve heat transfer, we used three different types of ribs in our investigation. The U-shaped, D-shaped, and reverse D-shaped ribs were considered. All other parameters were maintained constant, hence the properties of the solar heater are mostly determined by the Reynolds number. In this study, the Reynolds numbers ranged from 4000 to 18000. At a Reynolds number of 18000, the maximum heat transfer is obtained. Variation of the Nusselt number with respect to the Reynolds number for all SAH configurations is depicted in Fig. 6. As can

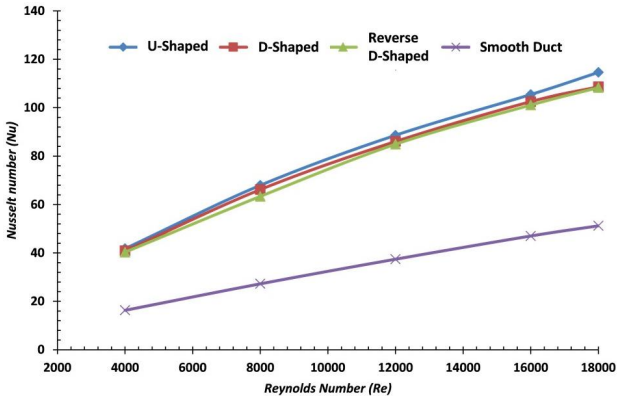

Figure 6: Variation of Nusselt number with Reynolds number for different turbulator geometries.

be seen from the figure, among all configurations U-shaped roughness has shown the best performance.

The change in friction factor with Reynolds number from 4000 to 18000 for all configurations is demonstrated in Fig. 7. As artificial roughness was introduced in the smooth absorber plate, the friction factor increased for all roughened geometries. While among all configurations, U-shaped geometry has shown a minimal friction factor.

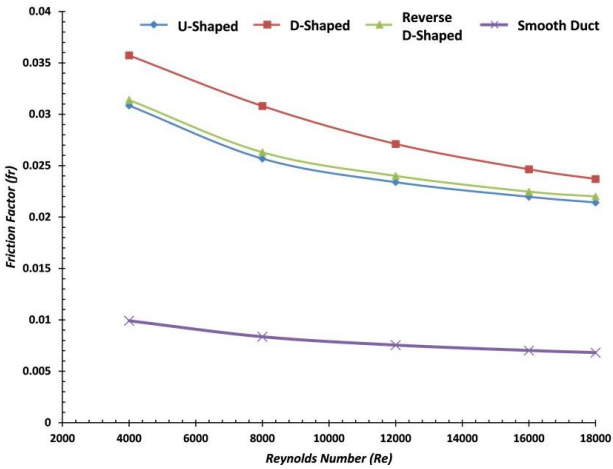

Figure 7: Variation of friction factor with Reynolds number for different turbulator geometries.

3.4 Thermo-hydraulic performance factor

Using different surface roughness in the solar air heater results in enhanced thermal performance but at the expense of pressure drop penalty. Different terms such as the figure of merit, coefficient of performance, thermal performance factor, etc. have been used in the literature to evaluate the design efficacy [29,30]. The term thermo-hydraulic performance factor has been outlined by Webb and Eckert [28] in the design of the solar air heater and the same has been incorporated here. Obtained results are presented in Fig. 8. They illustrate that among the considered configurations, SAH with U-shaped roughness has the highest value of THPF followed by reverse D-shaped and D-shaped geometries. Furthermore, the THPF value decreases continuously with the Reynolds number due to an exponential increase in pressure drop. The highest THPF of 1.762 was reported for

U-shaped roughness at Re = 4000. There are various optimization techniques like Taguchi [31], Taguchi-Topsis [32], the preference selection index method [33], the hybrid entropy-VIKOR (VIšekriterijumsko KOmpromisno Rangiranje) method [34], the hybrid analytical hierarchy process and preference ranking organization method for enrichment evaluations technique [35], analysis of variance [36], etc., which can be opted in SAH for effective performance.

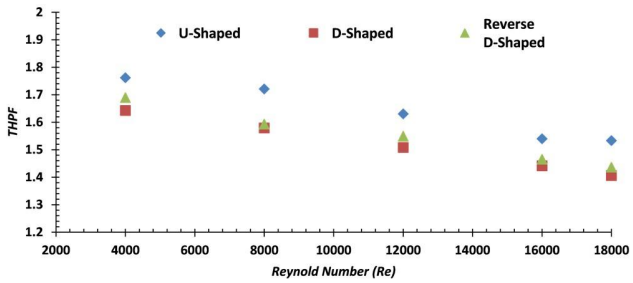

Figure 8: Variation in thermo-hydraulic performance factor as a function of Reynolds number for various geometries.

4 Conclusion

In the present work, a two-dimensional CFD model of a solar air heater having an artificially roughened absorber plate has been analyzed. For comparison purposes, three different roughness shapes, namely D-shaped, reverse D-shaped, and U-shaped were studied for constant turbulator height to hydraulic diameter and pitch to turbulator height ratios of 0.021 and 14.28, respectively. The heat transfer and flow friction characteristics of different roughness shape configurations were compared. The following are the outcomes of the above investigation:

- For the investigation of a two-dimensional rectangular duct, the RNG k-ε model provides satisfactory accuracy.
- For all types of geometry, the Nusselt number increases with an increase in the Reynolds number while the friction factor decreases.
- The presence of turbulators in a solar air heater significantly increases the heat transfer rate but at the expense of an increased friction factor. The maximum enhancement in the Nusselt number was 2.56 times

while the highest friction factor increment was 3.60 times relative to the smooth solar air heater.

- Among different turbulator configurations, the U-shaped configuration has shown the highest value of Nusselt number followed by the D-shaped and reverse D-shaped. In terms of friction factor, the D-shaped configuration had the highest value followed by reverse D-shaped and U-shaped configurations irrespective of Reynolds number.

- Among the examined configurations, SAH with U-shaped turbulators has shown the best thermo-hydraulic performance factor, with the highest value of 1.76 at the Reynolds number of 4000.

Received 2 November 2022

References

[1] Saxena A., Goel V.: *Solar air heaters with thermal heat storages*. Chin. J. Eng. (2013), 4, 90279.

[2] Saxena A., Varun, El-Sebaii A.A.: *A thermodynamic review of solar air heaters*. Renew. Sust. Energ. Rev. **43**(2015), 863–890.

[3] Saxena A., Srivastava G., Tirth V.: *Design and thermal performance evaluation of a novel solar air heater*. Renew. Energ. **77**(2015), 501–511.

[4] Bopche S.B., Tandale M.S.: *Experimental investigations on heat transfer and frictional characteristics of a turbulent or roughened solar air heater duct*. Int. J. Heat Mass Transf. **52**(2009), 2834–2848.

[5] Singh B.P., Bisht V.S., Bhandari P., Rawat K.S.: *Thermo-fluidic modelling of a heat exchanger tube with conical shaped insert having protrusion and dimple roughness*. Aptisi Trans. Technopreneurship (ATT) **3**(2021), 2, 13–29.

[6] Singh B.P., Bisht V.S., Bhandari P.: *Numerical study of heat exchanger having protrusion and dimple roughened conical ring inserts*. In: Advances in Fluid and Thermal Engineering (B.S. Sikarwar, B. Sundén, Q. Wang, Eds.), Lect. Notes Mech. Eng. Springer, 2021, 151–162.

[7] Kharhwal H., Singh S.: *Effect of serrated circular rings on heat transfer augmentation of circular tube heat exchanger*. Arch. Thermodyn. **43**(2022), 2, 129–155.

[8] Kumar V.: *Effect of serrated circular rings on heat transfer augmentation of circular tube heat exchanger*. Arch. Thermodyn. **41**(2020), 3, 57–89.

[9] Kaewchoothong N., Sukato T., Narato P., Nuntadusit C.: *Flow and heat transfer characteristics on thermal performance inside the parallel flow channel with alternative ribs based on photovoltaic/thermal (PV/T) system*. Appl. Therm. Eng. **185**(2021), 116237.

[10] Kaewchoothong N., Maliwan K., Takeishi K., Nuntadusit C.: *Effect of inclined ribs on heat transfer coefficient in stationary square channel*. Theor. Appl. Mech. Lett. **7**(2017), 6, 344–350.

[11] Thapa R.K., Bisht V.S., Bhandari P., Rawat K.S.: *Numerical study of car radiator using dimple roughness and nanofluid*. Arch. Thermodyn. **43**(2022), 3, 125–140.

[12] Chaube A., Sahoo P.K., Solanki S.C.: *Effect of roughness shape on heat transfer and flow friction characteristics of solar air heater with roughened absorber plate*. WIT Trans. Eng. Sci. **53**(2006), 43–51.

[13] Karmare S.V., Tikekar A.N.: *Analysis of fluid flow and heat transfer in a rib grit roughened surface solar air heater using CFD*. Sol. Energy **84**(2010), 3, 409–417.

[14] Rajput R.S., Bhagoria J.L., Giri A.K., Kumar A.: *Study of heat transfer and friction characteristic of various artificial roughness in solar air heater duct by using computational fluid dynamics (CFD) software*. In: Proc. Int. Conf. on Advances in Renewable Energy (ICARE 2010), MANIT Bhopal, June 26-29, 2010, 048.

[15] Chaube A., Sahoo P.K., Solanki, S.C.: *Analysis of heat transfer augmentation and flow characteristics due to rib roughness over absorber plate of a solar air heater*. Renew. Energ. **31**(2006), 317–331.

[16] Yadav A.S., Bhagoria J.L.: *A CFD based thermo-hydraulic performance analysis of an artificially roughened solar air heater having equilateral triangular sectioned rib roughness on the absorber plate*. Int. J. Heat Mass Transf. **70**(2014), 1016–1039.

[17] Semalty A., Bisht V.S., Bhandari P., Rawat K., Singh J., Kumar K., Dixit A.K.: *Thermodynamic investigation on solar air heater having roughness as multiple broken arc and circular protrusion*. Mater. Today: Proc. **69**(2022), 2, 181–186.

[18] Bohra J., Bisht V.S., Bhandari P., Rawat K.S., Singh J., Kumar K., Rawat B.: *Effect of variable blockage height ratio on performance for solar air heater roughened with 45° Z-shaped baffles*. Mater. Today: Proc. **69**(2022), 2, 153–157.

[19] ANSI/ASHRAE Standard 93-2003. Method of Testing to Determine the Thermal Performance of Solar Collectors. American Society of Heating, Refrigeration and Air Conditioning Engineers, Atlanta 2003.

[20] Güler H.Ö., Sözen A., Tuncer A.D., Afshari F., Khanlari A., Şirin C., Gungor A.: *Experimental and CFD survey of indirect solar dryer modified with low-cost iron mesh*. Sol. Energy **197**(2020), 371–384.

[21] Afshari F., Muratçobanoğlu B.: *Thermal analysis of Fe_3O_4/water nanofluid in spiral and serpentine mini channels by using experimental and theoretical models*. Int. J. Environ. Sci. Technol. **20**(2023), 2037–2052.

[22] Afshari F., Ceviz M.A., Mandev E., Yıldız F.: *Effect of heat exchanger base thickness and cooling fan on cooling performance of Air-To-Air thermoelectric refrigerator; experimental and numerical study*. Sustain. Energy Tech. Assess. **52**(2022), 102178.

[23] Bhandari P., Prajapati Y.K.: *Influences of tip clearance on flow and heat transfer characteristics of open type micro pin fin heat sink*. Int. J. Therm. Sci. **179**(2022), 107714.

[24] Kaewchoothong N., Nuntadusit C.: *Flow and heat transfer behaviors in a two-pass rotating channel with rib turbulators using computational fluid dynamics*. Heat Transf. Eng. **44**(2023), 2, 175–195.

[25] Puzu N.O., Prasertsan S., Nuntadusit C.: *Heat transfer enhancement and flow characteristics of vortex generating jet on flat plate with turbulent boundary layer.* Appl. Therm. Eng. **148**(2019), 196–207.

[26] Piya I., Narato P., Wae-hayee M., Nuntadusit C.: *Flow and heat transfer characteristic of inclined oval trench dimples with numerical simulation.* CFD Lett. **12**(2020), 11, 61–71.

[27] Eiamsa-ard S., Nuntadusit C., Promvonge P.: *Effect of twin delta-winged twisted-tape on thermal performance of heat exchanger tube.* Heat Transf. Eng. **34**(2013), 15, 1278–1288.

[28] Webb R.L., Eckert E.R.G.: *Application of rough surface to heat exchanger design.* Int. J. Heat Mass Transf. **15**(1972), 9, 1647–165.

[29] Bhandari P., Prajapati Y.K.: *Fluid flow and heat transfer behavior in distinct array of stepped micro-pin fin heat sink.* J. Enhanc. Heat Transf. **28**(2021), 4, 31–61.

[30] Bhandari P.: *Numerical investigations on the effect of multi-dimensional stepness in open micro pin fin heat sink using single phase liquid fluid flow.* Int. Commun. Heat Mass Transf. **138**(2022), 106392.

[31] Chauhan R., Singh T., Kumar N., Patnaik A., Thakur N.S.: *Experimental investigation and optimization of impinging jet solar thermal collector by Taguchi method.* Appl. Therm. Eng. **116**(2017), 100–109.

[32] Sharma A., Awasthi A., Singh T., Kumar R., Chauhan R.: *Experimental investigation and optimization of potential parameters of discrete V down baffled solar thermal collector using hybrid Taguchi-TOPSIS method.* Appl. Therm. Eng. **209**(2022), 118250.

[33] Chauhan R., Singh T., Thakur N.S., Patnaik A.: *Optimization of parameters in solar thermal collector provided with impinging air jets based upon preference selection index method.* Renew. Energ. **99**(2016), 118–126.

[34] Chauhan R., Kim S.C.: *Thermo-hydraulic characterization and design optimization of dimpled/protruded absorbers in solar heat collectors.* Appl. Therm. Eng. **154**(2019), 217–227.

[35] Chauhan R., Singh T., Patnaik A., Thakur N.S., Kim S.C., Fekete G.: *Experimental investigation and multi objective optimization of thermal-hydraulic performance in a solar heat collector.* Int. J. Therm. Sci. **147**(2020), 106130.

[36] Kumar R., Goel V., Singh P., Saxena A., Kashyap A.S., Rai A.: *Performance evaluation and optimization of solar assisted air heater with discrete multiple arc shaped ribs.* J. Energy Stor. **26**(2019), 100978

archives
of thermodynamics
Vol. **44**(2023), No. 2, 49–68
DOI: 10.24425/ather.2023.146558

The performance analysis of dusty photovoltaic panel

MINAKSHI KATOCH
VINEET DAHIYA
SURENDRA KUMAR YADAV*

K.R. Mangalam University, Gurugram – 122103, India

Abstract Solar photovoltaic power is widely utilized in the energy industry. The performance of solar panels is influenced by different variables, including solar radiation, temperature, wind speed, relative humidity and the presence of haze or dirt. Outdoor solar panels are particularly susceptible to a decrease in energy efficiency due to the accumulation of dust particles in the air, which occurs as a result of natural weather conditions. The extent of dust deposition is primarily determined by factors such as the tilt angle of the panel, wind direction, cleaning frequency as well as local meteorological and geographical conditions. The dust on the solar cell glazing reduces the optical transmittance of the light beam, causing shadowing and diminishing the energy conversion productivity of the panels. Sand storms, pollution levels and snow accumulations all significantly impact the photovoltaic panel performance. These circumstances reduce the efficiency of solar panels. The experiment was carried out on two identical dust-accumulated and dust-free panels. The evaluation was carried out in two different situations on the off-grid stand-alone system: in a simulated atmosphere and in an open space during the day. The current-voltage curves have been developed for both panels at various tilt degrees. The features provide sufficient information to analyse the performance of the panels under consideration. The measurements demonstrate that as dust collects on the panel's surface, the average output power and short circuit current decrease dramatically. The installation tilt angle affected the ratio of efficiency and average power outputs of dusty and clean panels.

Keywords: Dust accumulation; Tilt angle; Photovoltaics; Solar panel; Transmittance

*Corresponding Author. Email: s.k.yadav86@gmail.com

Nomenclature

G	–	irradiance, W/m^2
G_{ref}	–	irradiance at STC = 1000 W/m^2
I	–	output current, A
I_d	–	diode current, A
I_o	–	diode reverse saturation current, A
I_p	–	current in parallel resistance branch, A
I_s	–	source current, A
k	–	Boltzman constant, $= 1.38 \times 10^{-23}$ J/K
m	–	diode ideality factor
N_s	–	number of PV cells connected in series
P	–	power, W
q	–	electron charge, $= 1.6 \times 10^{-15}$ C
R_p	–	parallel resistance, Ω
R_s	–	series resistance, Ω
T	–	cell temperature, K
T_c	–	p-n junction cell temperature, K
V	–	terminal voltage, V

Greek symbols

ε	–	band gap, = 1.12 eV for silicon
μ_{sc}	–	temperature coefficient of short circuit current, A/K
η	–	efficiency

Subscripts

oc	–	open circuit
sc	–	short circuit
av	–	average

Acronyms

PV	–	photovoltaics
STC	–	standard test conditions

1 Introduction

Over the recent decades, the steady growth in the installed capacity of power generation by solar photovoltaics (PV) has been observed all over the globe. Photovoltaic generators produce clean energy by extensively using solar energy and converting it into electrical energy. Technological advancements, ecological and prise aspects have attracted a lot of special attention from governments, investors, and researchers. Several studies and research works have been done in associated areas.

The desert regions are the most popular locations for solar plant installations because of land availability and great solar potential. Different parameters influence the performance of PV generators in deserted areas, including the capability of the glass cover to transmit solar radiation, the intensity of solar radiation, the installation angle of the PV cell, the properties of the solar cell materials, the location of installation, temperature, etc.

For the panels installed in the open air, the factor responsible for the gradual degradation of transmittance is an accumulation of dust. Dust deposited on the glass top of the PV system reduces the transmission coefficient, which significantly results in a drop of energy conversion efficiency. The PV literature is concerned with the problems that occur due to dust and sand. The experimental study by Hassan *et al.* [1] provided information that the degradation is fast in the period of the first month and found a reduction of 33.5% in PV panel efficiency. It was analyzed by Rehman and El-Amin [2], Cabanillas and Munguía [3] that the dust deposited on the module cover may cause a significant reduction in the performance of PV. A reduction by 5% in one month was recorded in Saudi Arabia, by 1% in one month in Abu Dhabi, UAE and by 5.8% in 20 days in Hermosillo, Mexico. The operation of PV systems largely depends on the site location and weather conditions. The dust accumulation rate of 1–50 mg/m^2/day was reported in Colorado by Boyle *et al.* [4] and 150–300 mg/m^2/day in Egypt, undergoing visible variation, which is specifically due to the variable weather conditions. Furthermore, the impact of cooling on the PV electrical output was studied with the advanced cooling system in Pakistan by Bashir *et al.* [5] to have an insight into performance analysis. The deposition of dust is a challenge in the looming deployment of PV systems as shown by Javed *et al.* [6], Adinoyi and Said [7]. During the dust storm, the output of PV modules can even drop down to 20%.

The studies of the impact of dust accumulation on PV output performance play an important role in sustainable progress. The study by Mehmood *et al.* [8] showed that coarser dust particles have a more significant impact on PV panels' performance than fine particles. The dust particle size, chemical properties and thickness have been studied to better understand the physicochemical properties of dust depositions. For the study of the impact of dust sedimentation on PV performance, some work has been done to unearth the influencing parameters. The results showed that dust accumulation is highly dependent on the wind direction, pressure, tilt angle, azimuth angle, surface friction, humidity and the time duration for which the panels are placed in the environment. It elucidates the fact

that the deposition rate significantly affects the decreasing efficiency, which is majorly dependent on the weather conditions.

Most recent broad and accurate experimental studies have been conducted and reported by Darwish *et al.* [9] on the impact of variable temperature dust particles in dust accumulation on solar PV panels. The comprehensive and satisfactory studies were conducted in controlled laboratory conditions under unnatural weather. But the natural weather environment has an enormous impact on dust accumulation; it is tedious to simulate and consider all the variables. So, to better simulate the natural environmental conditions of Tehran, researchers performed the study under external natural conditions. Middle east countries like Iran have a massive solar generation perspective, but dust deposition is an unavoidable circumstance. The performance and energy conversion in PV depend on different environmental factors, solar irradiance, installation tilt angle and wind direction as reported by Cabrera-Tobar *et al.* [10]. The studies powerfully depict that the dust clouds on the modules cause a significant reduction in efficiency, particularly during sand storms and in polluted areas. Therefore, cleaning PV surfaces is essential for maintaining the operating efficiency at a high level in the desert region.

There are several studies done on dust accumulation in PV. It was observed that the tilt angle strongly impacts the dust density. Also, the wavelength loss due to the accumulated dust has been studied. The effects of dust size and composition have been carefully investigated by Sanusi [11]. The necessity of cleaning the dusty or polluted module glass covers is observed in various studies, but cleaning issues remain a concern in desert regions where the water supply is limited and requires minimum cleaning frequencies for maintaining the system performance at a high level. Though, research on the frequency of cleaning dust from the PV module glass covers has been minimal. Kaldellis [12] conducted a study in Greece on panels tilted at 30° with red soil particles with a diameter of less than 150 μm, ash particles with a diameter of less than 10 μm and limestone particles with a diameter of less than 60 μm. The experimental study was conducted under the ambient temperature within the range of accumulated dust density from 0.12 g/m^2 to 3.75 g/m^2. The reduction in performance was observed from 2.3% to 7.5%. In Germany, Schill *et al.* [13] conducted tests at the optimal tilt angle for five months under visible light and found a reduction of 20% in efficiency. Klugmann-Radziemska [14] in Poland conducted a study for two years on the panels at a tilt angle of 37°. The particles settled over the panel were 50 μm in diameter, and few particles above 50 μm. The data

collected indicated a reduction in efficiency by 0.8% per day. In Morocco, Azouzoute *et al.* [15] investigated the performance of the solar panels at an angle of 32°, for three months. The dust deposited on the unclean glass top panels was of density 1.6 g/m^2 and the resulting reduction in efficiency was equal to 35%. The dust particles of different sizes and different densities were investigated under laboratory conditions by Lu *et al.* [16]. The results of the eight week simulated environment experimentation in China have shown that under visible light of wavelength 350 nm to 800 nm, the reduction in the efficiency was from 28.8% to 43.41%. In India, Bergin *et al.* [17] conducted a performance evaluation for which the data was collected during continuous 30 days in the Gujrat state. After the analyses, a reduction in efficiency by 50% was observed. Al-addous [18] conducted an experimental study in Jordan for 16 weeks and observed a reduction from 1.37% to 5.02% per year. In China, Chen [19] collected the data for one week to check the performance of solar panels. The panels were under environmental conditions at an angle of 20°, the deposited dust density was found equal to 0.644 g/m^2, which reduced the efficiency by 7.8% per week. In the Bangladesh, Rehman *et al.* [20] conducted their study with the uncleaned panels under the natural conditions for one month to check the reduction in efficiency. The results showed a drastic reduction by up to 35%.

The latest new technologies are evolved with recent development in the field of neural network. Abdulghafor *et al.* [21] studied the modern seven artificial neutral network approaches, which are used to precisely estimate the thermal performance of a solar air heater based on input data such as mass flow rate, ambient temperature, plate temperature, wind speed and direction, relative humidity, and so on. Statistical error analysis with the mean square error and correlation coefficient was used to evaluate the neural network models. However, Mzad *et al.* [22] addressed the modelling of PV cooling employing a single nozzle with low temperature, minimal mass flow, and low pressure, with droplet velocity ranging from 0.1 to 1.7 m/s. The droplet size of the nozzle spray is a critical component that influences contact efficiency and panel cooling. The solar energy is a popular way of green energy generation but still there are some limitations. Węcel *et al.* [23] studied that the megawatt capacity photovoltaic power stations have a substantial negative indication in the energy generation capability of producing energy exclusively during the day. This needs the use of massive energy storage systems. The storage can be made more effective by combining optimised PV cells with an electrolyzer. The solar energy production can be more efficient if the solar radiation received at the earth surface

can be predicted. Daghsen *et al.* [24] studied the two optimised regression models that are utilised to generate the Petela model and the ASHRAE method for energy conservation and solar energy forecasting, respectively. These models were used to create the universal patterns for solar radiation exergy accounting.

Various researchers from different countries studied the behaviour of the panels and analysed the reduction in efficiency. In India, there are many regions which are prone to sand and dust particles, but this is not the only factor which leads the dirt to be deposited. The urbanization has given birth to rapid development in the infrastructure and construction, and the building of concrete jungles gives rise to the deposition of nanoparticles. The burning of residual grass in the fields, the deposition of soot particles and festivals like Diwali are big contributors to polluting the panels.

In the paper, Section 1 gives a brief introduction with a literature review. The works of various researchers from different countries were studied. Section 2 gives the mathematical modelling of the solar panels, where the voltage and current equations are solved with the Matlab Simulink. Graphs of dependence between the voltage and current are also drawn at various radiation levels. The dust particles tend to reduce the radiation effect by providing the shadowing effect. Section 3 gives the experimental setup of the solar panels. Section 4 discusses the observations and results. It also gives a deep analysis of the obtained results. The conclusions of the paper are given in Section 5.

2 Mathematical Model

The photovoltaic panel can be shown as an electric circuit, as shown in Fig. 1, where the radiation (G) is incident on the panel, and the current generated is supplied to the resistances and the diode.

The current flow is given by the formula

$$I = I_s - I_d - I_p\,. \tag{1}$$

The diode current (I_d) is directly proportional to the reverse saturation current (I_0) and is given by

$$I_d = I_0 \left[\exp\left(\frac{qV}{mkT}\right) - 1\right], \tag{2}$$

where m is the diode ideality factor, which is constant and depends on the PV cell technology, k is the Boltzman constant, q is the electron charge,

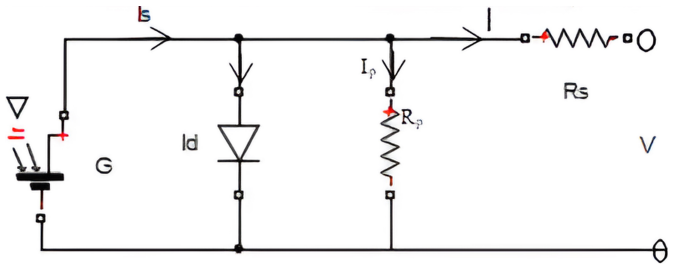

Figure 1: Single diode model with R_s and R_p.

T is the cell temperature and V is the terminal voltage). If we neglect the shunt resistance in the circuit, then the current can be written as

$$I = I_s - I_s \left[\exp\left(\frac{qV}{mkT} \right) - 1 \right], \tag{3}$$

by putting the diode current equation. Under the short circuit conditions when $V = 0$ and open circuit conditions when $I = 0$, the short circuit current can be found from the given equation

$$I_{sc} = I = I_s - I_o \left[\exp\left(\frac{qV}{mkT} \right) - 1 \right] \quad \text{at} \quad V = 0, \tag{4}$$

and the voltage equation can be written as

$$V = V_{oc} \frac{mkT}{q} \ln\left(1 + \frac{I_{sc}}{I_o} \right) \quad \text{at} \quad I = 0, \tag{5}$$

where V_{oc} is the open circuit voltage and I_{sc} is the short circuit current.

The diode current and current through the series resistance can be expressed in terms of voltage and current as

$$I_d = I_0 \left[\exp\left(\frac{V + IR_s}{a} \right) - 1 \right], \tag{6}$$

$$I = I_s - I_0 \left[\exp\left(\frac{V + IR_s}{a} \right) - 1 \right], \tag{7}$$

where

$$a = \frac{N_s mkT_c}{q}. \tag{8}$$

These equations are for the case when the shunt resistance is not present. If the shunt resistance is present, then the equation given below is considered:

$$I = I_s - I_0 \left[\exp\left(\frac{V + IR_s}{a} \right) - 1 \right] - \frac{V + IR_s}{R_p}. \tag{9}$$

Various parameters are used in these equations and directly affect these values. The output current at the standard test conditions (STC) is given as

$$I = I_{s,\mathrm{ref}} - I_{o,\mathrm{ref}} \left[\exp\left(\frac{V}{a_{\mathrm{ref}}} \right) - 1 \right], \tag{10}$$

where a_{ref} is the value of a at temperature 25°C .

If the PV cell is short-circuited the value of $I_{s,\mathrm{ref}}$ can be written as

$$I = I_{s,\mathrm{ref}} - I_{o,\mathrm{ref}} \left[\exp\left(\frac{0}{a_{\mathrm{ref}}} \right) - 1 \right] = I_{s,\mathrm{ref}}\,, \tag{11}$$

which is valid during the ideal cases:

The source current depends on both the irradiance and temperature:

$$I_s = \frac{G}{G_{\mathrm{ref}}} \left(I_{s,\mathrm{ref}} + \mu_{\mathrm{ref}} \Delta T \right), \tag{12}$$

where $\Delta T = T_c - T_{c,\mathrm{ref}}$ and $T_{c,\mathrm{ref}} = 298$ K and μ_{ref} is the temperature coefficient of short circuit current in A/K.

The simulation was done based on the above equations using multi-paradigm programming language and numerical computing environment MATLAB Simulink – version 2020b [25]. The simulation was run to draw characteristics of the PV panel under various conditions. The irradiance (G) is the factor that is most affected by the dust particles. The panel under the dust does not receive its best radiation. Figure 2 shows the simulation

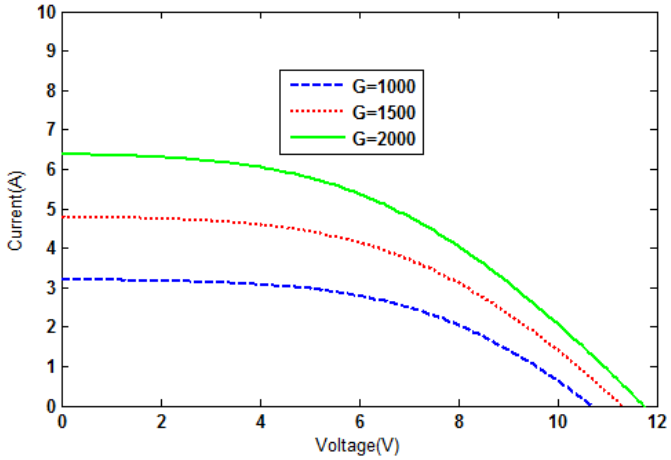

Figure 2: Simulink results under different radiation levels.

result under different radiation levels. The simulation models show that as the radiation level decreases, the short circuit tends to decrease too, decreasing with the voltage.

3 Experimental setup

The measuring techniques were utilized to get current-voltage curves from two similar PV panels, one panel is perfectly clean, and the other is polluted with dust as shown in Fig. 3. In the primary consideration, both panels are set under controlled indoor unnatural conditions in the laboratory. The tilt angle varied, and I–V qualities were recorded. In the second consideration, panels are put in the natural habitat outdoors under natural daylight. The study aims at analyzing the PV performance with the changing tilt angle and dust deposition. The identical panels are subjected to different ambient conditions and dust depositions in indoor and outdoor conditions. The dirt deposited on the PV surface depends on various parameters, which include the installation tilt angle, physical characteristics of the dust and local atmosphere. In general, the optimal angle for installation of the PV surface, which receives the maximum direct radiation, is highly dependent on the PV site. The best installation angle varies with the season and sun position, however, the regular angle adjustment is uneconomical. Therefore, the best tilt angle for engineering applications is approximately equal to the local latitude. In this study, in order to examine the impact of dust deposition, five various tilt angles (0°, 10°, 20°, 30°, 40°) have been considered. The indoor test setup has two comparable panels, one next to the other,

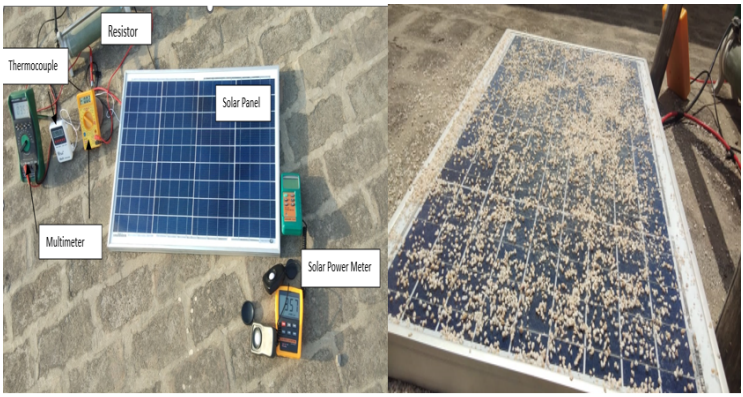

Figure 3: Experimental setup.

mounted parallel to the ground. The arrangements are made to change the light intensity of the sun-simulating lamps set over each panel.

The characteristics I–V were plotted using a data logger interfaced with the panels. A Tenmars portable solar power radiation measuring tester [26] is used to measure the intensity of light over the panel. In the indoor experimental setup, the bulb light intensity is kept at 500 W/m^2. The temperature of the solar module was measured from the back of the module with the platinum resistance thermocouple PT100. The cell operating temperature was maintained during the experiment between 35°C to 42°C. The fans controlled the panel temperature by cooling the back of the solar modules. The reading of voltage and current was recorded for various tilt angles. The I–V curves were obtained for both panels. During the dust simulation, sand was taken as the dust particle. The dust was spread over the panel non-uniformly, which covered 80% of the surface area. As the tilt angles assumed values above 20°, at 30° and 40°, 5.1% and 15.75% of sand dropped on the floor from the panel.

Outdoor experimental test arrangements were installed at a Gurugram roof-top location (latitude 28.45°N, longitude 77.02°E). The test had a roof-mounted polycrystalline PV panel with no shading effect, which was installed with an adjustable tilt angle parallel to the ground surface facing south. The two panels under consideration received the same insolation levels, kept in the same atmospheric natural conditions. The PV cell operating temperatures measured were recorded between 45°C and 65°C. The dust with non-niform distribution of covering density was set up in the experimentation. During the investigation, the insolation level was 950 W/m^2, the atmospheric temperature was 43°C, and the wind speed was 9.3 km/h.

4 Results and discussions

In the unnatural environmental conditions, the temperature, bulb light intensity and tilt angle of the installation were controlled for the comprehensive investigation. One panel with dust accumulated and the other with the clean surface were examined. The recording of readings started from 0° tilt angle at the light intensity of 500 W/m^2 and temperature 35°C. First I–V curves were plotted for the initial tilt angle. Then, the tilt angle was increased in steps of 10° starting from 0° up to 40°. The readings were recorded when the module temperature was 35°C to 42°C. The I–V curves for the two panels under study at different tilt angles are drawn in Figs. 4–8.

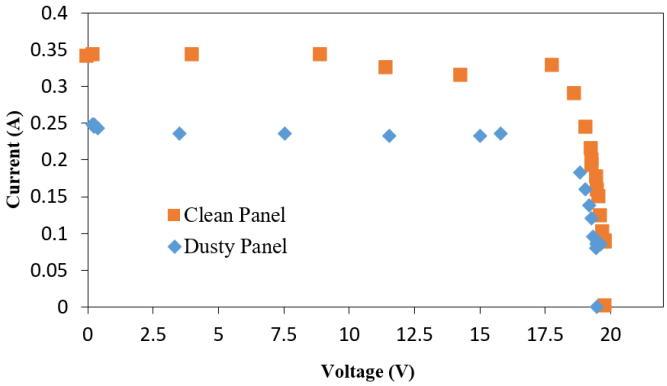

Figure 4: I–V characteristics at 500 W/m^2 and 0° tilt angle in laboratory conditions.

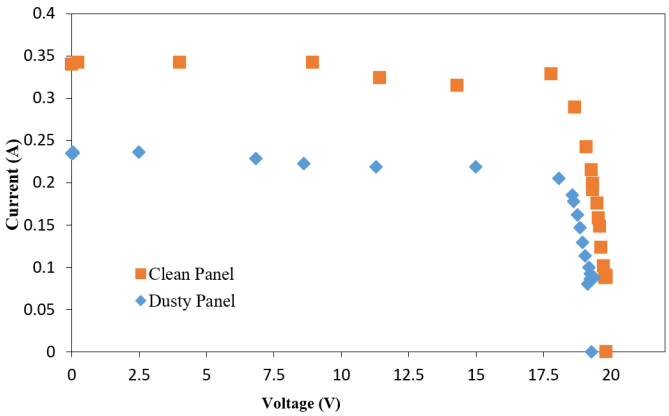

Figure 5: I–V characteristics at 500 W/m^2 and 10° tilt angle in laboratory conditions.

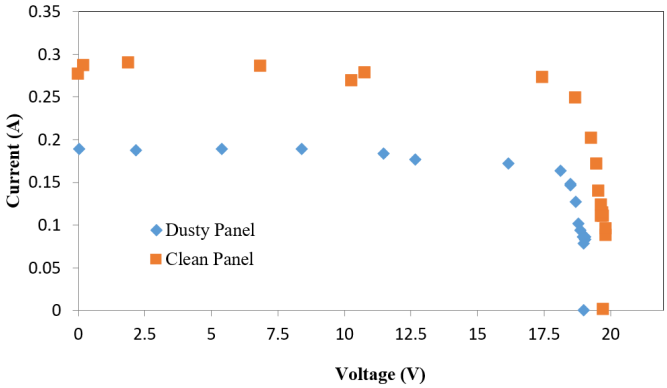

Figure 6: I–V characteristics at 500 W/m^2 and 20° tilt angle in laboratory conditions.

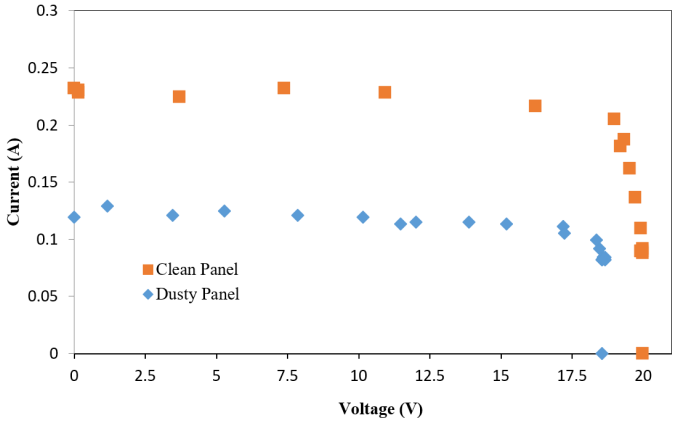

Figure 7: I–V characteristics at 500 W/m^2 and 30° tilt angle in laboratory conditions.

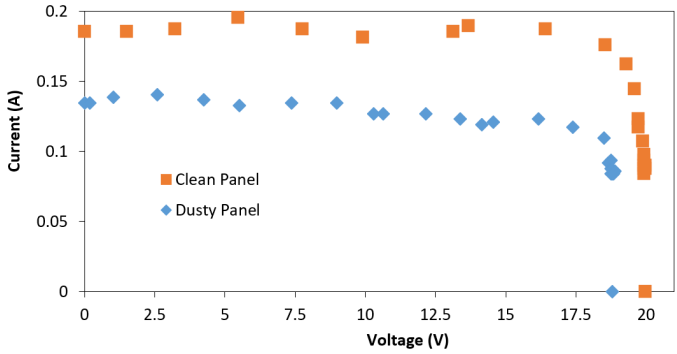

Figure 8: I–V characteristics at 500 W/m^2 and 40° tilt angle in laboratory conditions.

Tables 1 and 2 give the various parameters of dusted panels with respect to those of clean panels, including the voltages and currents. The power of the solar panels is determined from the product of open circuit voltage and short circuit current given as

$$P = V_{oc} I_{sc}\,. \tag{13}$$

The efficiency of the solar panel can be calculated from the given equation:

$$\eta = \frac{P}{G\,A} 100\,, \tag{14}$$

where G is the irradiance and A is the total surface area of the solar panel.

Table 1: Ratio of open circuit voltage and short circuit current under controlled indoor conditions.

Tilt angle (°)	Solar module temperature (°C)		Ratio of short circuit currents (%)	Ratio of open circuit voltages (%)
	Clean	Dusty	$I_{sc\,\mathrm{dusty}}/I_{sc\,\mathrm{clean}}$	$V_{oc\,\mathrm{dusty}}/V_{oc\,\mathrm{clean}}$
0	35	35	72.57	99.52
10	37	35	69.14	97.78
20	35	39	66.89	95.58
30	37	42	54.06	93.39
40	37	40	72.00	94.62

Table 2: Ratio of efficiency and average power under controlled indoor conditions.

Tilt angle (°)	Ratio of efficiencies (%)	Ratio of average powers (%)
	$\eta_{\mathrm{dusty}}/\eta_{\mathrm{clean}}$	$P_{av\,\mathrm{dusty}}/P_{av\,\mathrm{clean}}$
0	64.14	62.87
10	63.56	69.85
20	62.63	76.62
30	49.12	66.17
40	62.67	71.05

The readings from the panels under investigation were obtained for different tilt angles. The following conclusions can be drawn:

- Sand-deposited panels were observed to have the operating temperatures higher by 2°C to 7°C than those of the sand-free panels under the same insolation level.

- The sand spread over the panel was non-uniformly distributed with a density of 12.5 g/m^2 at a zero degree tilt angle. As the tilt angle increased, the sand density decreased reaching 10.5 g/m^2 at 40°. The average power loss for the given sand densities is from 38% to 24%.

- It may be observed from the presented tables that accumulation of dust does not have a high impact on the open circuit voltage. The ratio of the open circuit voltages between dusty and clean panels varied from 93.39% to 99.52%. The values of the open circuit voltage

of the clean and sand-accumulated panels were nearly identical. The voltage difference is visible at angles above 10°; the impact may be because of the module temperature increase.

- The short circuit current ratios varied from 54.06% to 72.57%. The dust deposited on the panels gives larger differences in short-circuit current ratios than in the open-circuit voltage ratios. The graphs show that sand has a sizable impact on the short-circuit current. The percentage ratio tends to decrease with the increase in the tilt angle, but for the largest angle, it suddenly increased. It was most likely due to the temperature increase and reduction of dust density over the panel by 15.75% due to the gravity and more radiation responsible for the power generation available on the panel.

- The ratio of efficiencies of dusty and clean panels is minimum at 30°, but no such correlation was found for this.

The experiment under natural conditions was conducted on the rooftop of a building in Gurugram in the month April. The sand spread over the panel was non-uniform. The sand density was nearly equal. The two panels were kept parallel to the ground, one with non-uniformly distributed sand and the other with a clean surface. During the outdoor investigation, the temperature of the sand varied from 40–45°C. The solar cells had experienced a temperature difference of approximately 10°C. I–V curves for clean and dusty panels at different tilt angles and at an increased radiation rate are shown in Figs. 9–13.

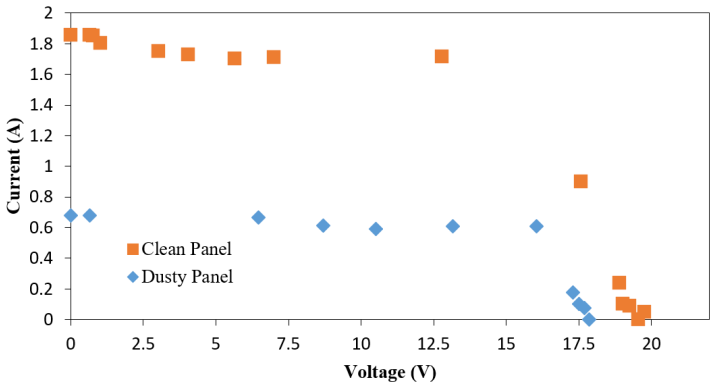

Figure 9: I–V characteristics at 950 W/m^2, 0° tilt angle in natural conditions.

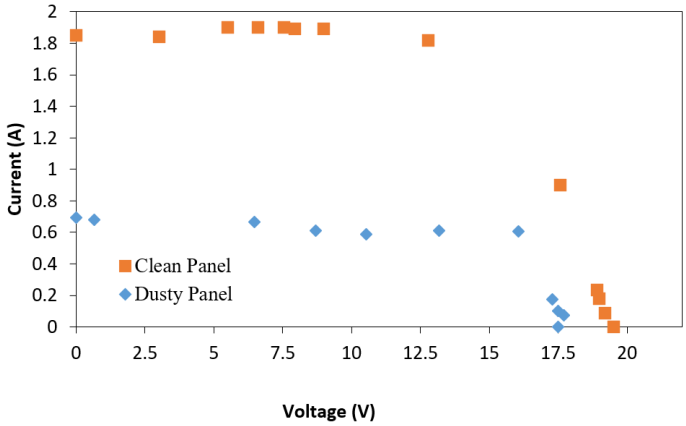

Figure 10: I–V characteristics at 950 W/m^2, 10° tilt angle in natural conditions.

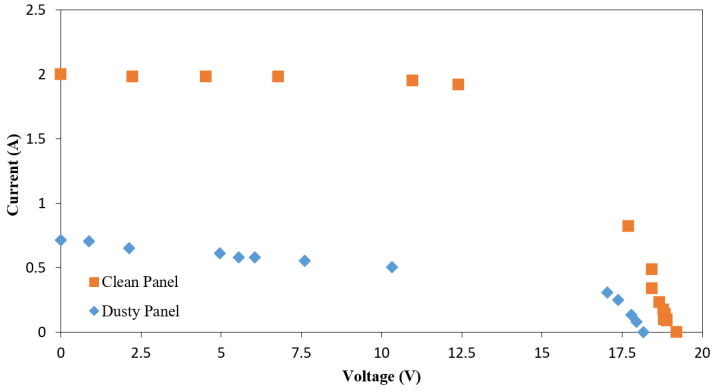

Figure 11: I–V characteristics at 950 W/m^2, 20° tilt angle in natural conditions.

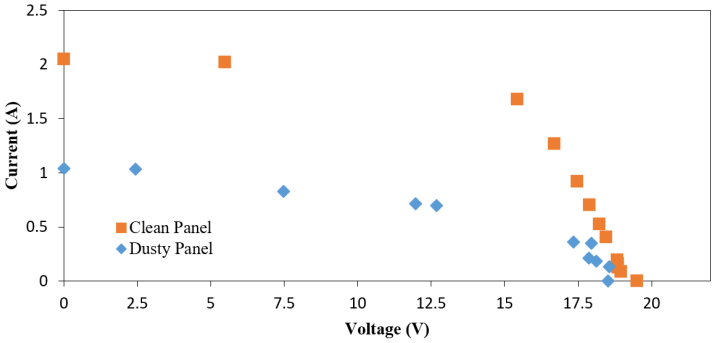

Figure 12: I–V characteristics at 950 W/m^2, 30° tilt angle in natural conditions.

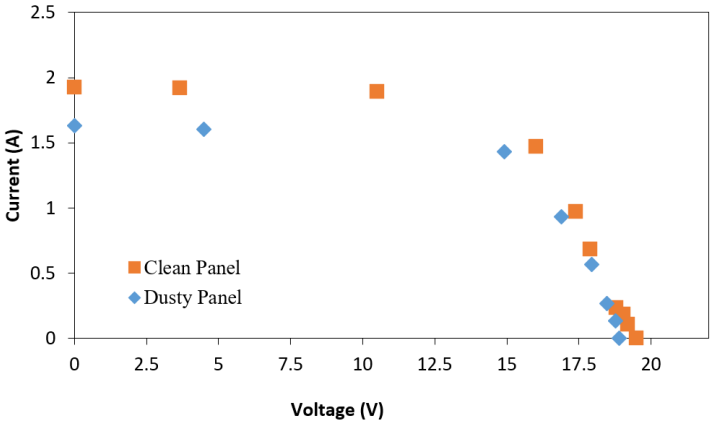

Figure 13: I–V characteristics at 950 W/m^2, 40° tilt angle in natural conditions.

The calculated ratios of short circuit currents, open circuit voltages, efficiencies, and average powers between the two studied panels are gathered in Tables 3 and 4. The outdoor experimentation was conducted at different insolation levels. The following observations were made:

- The non-uniform distribution of sand did not strongly impact the open circuit voltage ratio.
- A sizeable impact of sand accumulation was seen in the short circuit currents of the panels. In natural conditions, solar radiations have an adverse effect on the short circuit currents. In the clean panels, the short circuit currents were below 2 A for 0° and 10°, at 20°, 30° and 40°, approximately invariant. In the sand-deposited panel short

Table 3: Ratio of open circuit voltage and short circuit current of dusty and clean panels under natural conditions.

Tilt angle of the panel (°)	Ratio of short circuit currents (%)	Ratio of open circuit voltages (%)
	$I_{sc\,\mathrm{dusty}}/I_{sc\,\mathrm{clean}}$	$V_{oc\,\mathrm{dusty}}/V_{oc\,\mathrm{clean}}$
0	36.60	91.30
10	37.39	89.70
20	35.60	94.58
30	50.63	94.93
40	84.74	96.97

circuit currents were below 1 A for angles 0°, 10°, 20°, 30°, and the current rose above 1.5 A at 40°. This is due to the reduction in dust density over the panel.

- The average power ratio was between 45.19–52.63% for 0°to 30° tilt angles. For 40°, the ratio of average powers for the clean and dusty panels was quite different.
- The ratio of dusty to clean panel efficiencies is minimum at the tilt angle 20°, and no correlation was observed for this.

Table 4: Ratio of average powers and efficiencies of dusty and clean panels under natural conditions.

Tilt angle (°)	Ratio of efficiencies (%)	Ratio of average powers (%)
	$\eta_{dusty}/\eta_{clean}$	$P_{av\ \mathrm{dusty}}/P_{av\ \mathrm{clean}}$
0	41.99	52.57
10	42.79	52.63
20	29.80	45.19
30	34.15	46.03
40	90.59	86.47

5 Conclusions

The study was done to provide early insight into the effects of collected dust on the photovoltaic (PV) panel performance. The study describes the indoor controlled and outdoor natural conditioned experimental setups. The experiment yields the current-voltage characteristics curves for various tilt angles, temperatures and insolation levels, i.e., 500 W/m^2 indoors and 950 W/m^2 outdoors. The investigation was carried out on two similar panels, and a thorough analysis was conducted to determine the impact of dust accumulation on the panel performance. The monitored panel temperature was found to increase in dust accumulated PV panels, more in the natural open-air conditions than in the indoor conditions. The contaminated panel's short circuit currents were greatly decreased, whereas the open-circuit voltages had only slightly reduced values. The efficiencies and average powers of dusty PV panels were found to significantly decrease

with respect to clean panels. The collection of airborne dust particles significantly lowers the optical transmittance of solar cell glazing.

The density of dust sitting over the panel with the particle dimensions and colour can be considered for future work. The dimension of the polydisperse particles with scanning electron microscopy and transmission electron microscopy can be useful in analysing the behaviour of the dust particles, which can be further used in designing the cleaning methodologies for specific locations. The horizontal panels amass dust with a high particle density. Panels with dust deposition suffer from substantial power loss, causing massive solar power-producing houses to suffer from electrical and economic power loss. The generation must be kept running by cleaning the panels regularly. Cleaning at regular intervals with self-cleaning technology may be implemented with solar panels to achieve optimal transmission through solar cell glazing. Because urban regions are more prone to pollution, it is recommended to employ auto-cleaning technologies to obtain optimal energy conversion efficiency from solar panels. The location of the site determines the frequency of cleaning.

Acknowledgements

The indoor experimental research work was conducted at the National Physics Laboratory, Delhi in the simulated environmental parameters – temperature, light intensity and tilt angles.

Received 7 February 2023

References

[1] Hassan A.H., Rahoma U.A., Elminir H.K., Fathy A.M.: *Effect of airborne dust concentration on the performance of PV modules.* J. Astron. Soc. Egypt **13**(2005), 1, 24–38.

[2] Rehman S., El-Amin I.: *Performance evaluation of an off-grid photovoltaic system in Saudi Arabia.* Energy **46**(2012), 451–458.

[3] Cabanillas R.E., Munguía H.: *Dust accumulation effect on efficiency of Si photovoltaic modules.* J. Renew. Sustain. Ener. **3**(2011), 043114.

[4] Boyle L., Flinchpaugh H., Hannigan M.P.: *Natural soiling of photovoltaic cover plates and the impact on transmission.* Renew. Energ. **77**(2015), 166–173.

[5] Bashir M.A., Ali H.M., Amber K.P., Bashir M.W., Hassan A.L.I., Imran S., Sajid M.: *Performance investigation of photovoltaic modules by back surface water cooling.* Therm. Sci. 1–11(2016).

[6] Javed W., Wubulikasimu Y., Figgis B., Guo B.: *Characterization of dust accumulated on photovoltaic panels in Doha.* Qatar. Sol. Energy **142**(2017), 123–135.

[7] Adinoyi Muhammed J., Said Syed A.M.: *Effect of dust accumulation on the power outputs of solar photovoltaic modules.* Renew. Energ. **60**(2013), 633–636.

[8] Mehmood U., Al-Sulaiman F.A., Yilbas B.S.: *Characterization of dust collected from PV modules in the area of Dhahran, Kingdom of Saudi Arabia, and its impact on protective covers for photovoltaic applications.* Sol. Energy **141**(2017), 203–209.

[9] Darwish Z.A., Kazem H.A., Sopian K., Al-Goul M.A., Alawadhi H.: *Effect of dust pollutant type on photovoltaic performance.* Renew. Sust. Energ. Rev. **4**1(2015), 735–744.

[10] Cabrera-Tobar A., Bullich-Massagué E., Aragüés-Peñalba M., Gomis-Bellmunt O.: *Topologies for large scale photovoltaic power plants.* Renew. Sust. Energ. Rev. **59**(2016), 309–319.

[11] Sanusi Y.: *The performance of amorphous silicon PV system under Harmattan dust conditions in a tropical area.* Pacific J. Sci. Technol. **13**(2012), 168–175.

[12] Kaldellis J.K., Kapsali M.: *Simulating the dust effect on the energy performance of photovoltaic generators based on experimental measurements.* Energy **36**(2011), 8, 5154–5161

[13] Schill C., Brachmann S., Koehl M.: *Impact of soiling on IV-curves and efficiency of PV-modules.* Sol. Energy **112**(2015), 259–262.

[14] Klugmann-Radziemska E.: *Degradation of electrical performance of a crystalline photovoltaic module due to dust deposition in northern Poland.* Renew. Energ. **78**(2015), 418–426.

[15] Azouzoute A., Merrouni A.A., Garoum M.: *Soiling loss of solar glass and mirror samples in the region with arid climate.* Energ. Rep. **6**(2020), 693–698.

[16] Lu H., Lu L., Wang Y.: *Numerical investigation of dust pollution on a solar photovoltaic (PV) system mounted on an isolated building.* Appl. Energ. **180**(2016), 27–36.

[17] Bergin M.H., Ghoroi C., Dixit D., Schauer J.J., Shindell D.T.: *Large reductions in solar energy production due to dust and particulate air pollution.* Environ. Sci. Tech. Let. **4**(2017), 8, 339–344.

[18] Al-Addous M., Dalala Z., Alawneh F., Class C.B.: *Modeling and quantifying dust accumulation impact on PV module performance.* Sol. Energy **194**(2019), 86–102.

[19] Chen J., Pan G., Ouyang J., Ma J., Fu L., Zhang L.: *Study on impacts of dust accumulation and rainfall on PV power reduction in East China.* Energy **194**(2020), 116915.

[20] Rahman M.M., Islam M.A., Karim A.H.M.Z., Ronee A.H.: *Effects of natural dust on the performance of PV panels in Bangladesh.* Int. J. Mod. Edu. Comp. Sci. **4**(2012), 10, 26–32.

[21] Abdulghafor I.A., Mohannad J.M.: *Design of thermoelectric radiant cooling – photovoltaic panels system in the building.* Arch. Thermodyn. **43**(2022), 4, 85–108.

[22] Mzad H, Otmani A.: *Simulation of photovoltaic panel cooling beneath a single nozzle based on a configurations framework.* Arch. Thermodyn. **42**(2021), 1, 115–128.

[23] Węcel D, Ogulewicz W.: *Study on the possibility of use of photovoltaic cells for the supply of electrolysers*. Arch. Thermodyn. **32**(2011), 4, 33–53.

[24] Daghsen K, Lounissi D, Bouaziz N.: *A universal model for solar radiation exergy accounting: Case study of Tunisia*. Arch. Thermodyn. **2**(2022), 2, 97–118.

[25] Mathworks: *Matlab, Simlink, and Stateflow User Guide* (Version 5.0). Mathworks, 2020. https://www.mathworks.com/content/dam/mathworks/mathworks-dot-com/solutions/mab/mab-control-algorithm-modeling-guidelines-using-matlab-simulink-and-stateflow-v5.pdf (accessed 31 May 2022).

[26] Tenmars TM-207: *Solar Power Meter User Guide* (Version 1.0). 2022. https://5.imimg.com/data5/KK/GD/MY-2169304/solar-meter-tm-207.pdf (accessed 10 Feb. 2022).

archives
of thermodynamics
Vol. **44**(2023), No. 2, 21–48
DOI: 10.24425/ather.2023.146557

The influence of thermophysical properties of frozen soil on the temperature of the cast-in-place concrete pile in a negative temperature environment

ZIYING LIU[a*]
TIANLAI YU[b]
NING YAN[b]
LIPENG GU[b]

[a] Northeast Forestry University, College of Home and Art Design, Harbin, 150040, China

[b] Northeast Forestry University, College of Civil Engineering, Harbin, 150040, China

Abstract Thermophysical properties of frozen soil have a great influence on the quality of cast-in-place concrete piles. In this paper, the embedded concrete temperature monitoring system is used to test the variation law of the concrete temperature during the construction of the bored pile. Thermophysical properties of permafrost around piles are tested. Based on the theory of three-phase unsteady heat conduction of soil, the influence of specific heat capacity, thermal conductivity, thermal diffusivity, and latent heat of phase transformation on the temperature change of a concrete pile is systematically studied. The thermal parameter is obtained which exerts the most significant influence on the temperature field. According to the influence degree of frozen soil on pile temperature, the order from high to low is thermal conductivity, thermal diffusivity, latent heat of phase change, and specific heat capacity. The changes in pile wall temperature caused by the change of these properties range between 2.60–10.97°C, 1.49–9.39°C, 2.16–2.36°C, and 0.24–3.45°C, respectively. The change percentages of parameters vary between 35.77–47.12%, 12.22–40.20%, 12.46–32.25%, and 3.83–20.31%, respectively. Therefore, when designing and constructing concrete foundation piles, the influence of the thermal conductivity of frozen

*Corresponding Author. Email: tianlaiyu@yandex.com

soil on concrete pile temperature should be considered first. The differences between the simulated and measured temperature along the concrete pile in the frozen soil varying with the respective thermal properties are: –2.99–7.98°C, –1.89–4.99°C, –1.20–1.99°C, and –1.76–1.27°C. Polyurethane foam and other materials with small thermal conductivity can be added around the pile to achieve pile insulation.

Keywords: Thermal properties of frozen soil; Temperature of the cast-in-place concrete pile; Negative temperature environment; Ice-rich permafrost; Heat conductivity coefficient

Nomenclature

C	–	volumetric heat capacity, J/(m^{3}K)
c	–	specific heat capacity, J/(kg·K)
d	–	test time, day
h	–	position of measuring point in the pile, m
L	–	volumetric latent heat of phase change, kJ/m^3
L'	–	latent heat of phase change, kJ/kg
Q	–	heat of hydration, kJ/kg
$s(t)$	–	freezing and thawing boundary position of soil over time
T	–	temperature, K
T_g	–	boundary temperature, K
W	–	single-side concrete cement content, kg/m^3

Greek symbols

a	–	thermal diffusivity, m^2/s
ρ	–	density of concrete, kg/m^3
ρ_d	–	dry density of soil, kg/m^3
λ	–	thermal conductivity, W/(m·K)
ω	–	water content, %

Subscripts

f	–	freezing state
u	–	unfreezing (thawing)

1 Introduction

Daxinganling and Xiaoxinganling in the northeast of China belong to the degraded island permafrost region with an area of about 216 600 km^2 [1]. In the construction of highway projects, the basic bridge cast-in-place pile is widely used. After the cast-in-place pile is poured, the concrete dissipates heat and exchanges heat with the surrounding soil. The negative temperature environment of the surrounding soil affects the formation of concrete

strength [2–4], which influences the quality of the concealed project and causes potential safety hazards. The thermal and physical properties of frozen soil are the main subject of frozen soil research. Frozen soil in negative temperature affects the quality of pile formation by acting on the temperature field of concrete piles. Therefore, it is necessary to find the thermophysical parameter that has a great impact on the concrete pile. It is beneficial to improve the pile foundation design and construction scheme and improve the project quality.

Some progress has been achieved in the study of the thermophysical properties of frozen soil and the temperature field of pile foundations. Yu *et al.* [5] analyzed the influence of the temperature of casting concrete on structural temperature stress. The temperature field change and thermal stress change were obtained at different ages of hardening under different temperatures of casting concrete. And the control measures of the temperature of casting concrete were proposed during mass concrete pouring. Li and Sun studied the influence of concrete hydration heat on the temperature field of a pile foundation in a high-temperature permafrost area [6]. The results of the study indicated that the refreezing time could be reduced and the construction period could be shortened by adding fly ash, slag, and other admixtures into the concrete because this method could lower the temperature of casting concrete [7–9]. Other researchers analyzed the distribution law of the temperature field of the asphalt pavement structure of the old cement pavement. Along the depth of the pavement, the temperature, daily range, temperature gradient, and rate of temperature change were nonlinear distributions. And there is a phenomenon that the amplitude of change decreases and the stage of the change lags [10,11]. According to the basic principles of thermology and the needs of structural design, by taking a bridge in Shanghai as the object, Liu and Geng examined the influence of basic thermal parameters on the temperature field and temperature effect of concrete structures [12]. They focused on the effect of the radiation absorption coefficient and the surface heat exchange coefficient. By taking a concrete box beam as an example, some researchers used meteorological parameters to calculate and analyze the sunshine temperature field. And the vertical temperature difference distribution was obtained according to the calculation of temperature field fitting [13–15]. Cai conducted computational research on indoor fire environment and temperature field of concrete structures [16]. Daghsen *et al.* designed a universal model for solar radiation (exergy) accounting based on a case study in Tunisia [17]. Based on the thermophysical properties of cement mud and the temperature value of

micropiles, Alekseev and Zorin established 02erical models. They studied the interaction between bored micropile and permafrost, then analyzed the strength of micropile [18]. Fajobi *et al.* [19] and Zhang *et al.* [20] studied the section internal temperature distribution of a newly proposed regenerative energy storage pile foundation system. The thermal conductivity of concrete, the specific heat capacity of concrete, the size of the pile foundation, and other parameters were considered. Xiao *et al.* [21] analyzed the response of the temperature cycle to temperature change, cycle, and different water content of the soil-concrete interface.

Former researchers studied the influence of certain factors on the temperature field, and the research on the temperature of casting concrete and meteorological conditions is relatively mature. As for the study of thermal and physical properties, most of them are limited to the use of thermophysical parameters as the modeling conditions. And the final goal is to investigate the temperature field or strength and mechanical properties of the pile foundation. However, there is little research on the influence of thermophysical parameters of frozen soil on the temperature field of pile foundations. This paper refers to the influence of the thermophysical parameters of the concrete box girder and suspension bridge main cable superstructure on the temperature field [22–24]. And it focuses on the research of the specific heat capacity, thermal conductivity, thermal diffusivity, phase change latent heat, and other thermophysical parameters of the frozen soil under the negative temperature environment. At the same time, the temperature influence degree of the cast-in-place concrete pile after pouring will be discussed. So, it can provide a reference for improving the design and construction of the pile foundation.

2 Experimental study on the temperature field of foundation pile in the construction stage

2.1 The main contents of the field study and the choice of the test site

The test site is located in Mohe County, Heilongjiang province, at the south-eastern edge of the permafrost region of Eurasia and the northernmost part of China. The east longitude is 121°07′–124°20′, the northern latitude is 52°10′–53°33′, and the average elevation is 550 m [25]. The site has a developed water system, and rich wetland resources, with a total

area of 3935 ha. There is continuous permafrost, with a thickness of 50–100 m [26,27]. The average annual temperature is about –5.5°C. The lowest temperature is –52.3°C, and the highest temperature is 38.9°C. The average annual precipitation is 460.8 mm, and the annual average icing period is 7 months [28]. In the past 50 years, the temperature in the Mohe area has increased by 0.357°C every 10 years, and the warming trend is obvious [29].

The test site is located between pile no. 10 and pile no. 11 of the K424+380 newly-built permafrost bridge in the Zhangling-xilingji section of the national highway from Beijing to Mohe. The geological soil layer and the type of frozen soil were determined by field sample drilling and indoor geotechnical tests [20–22], as shown in Fig. 1.

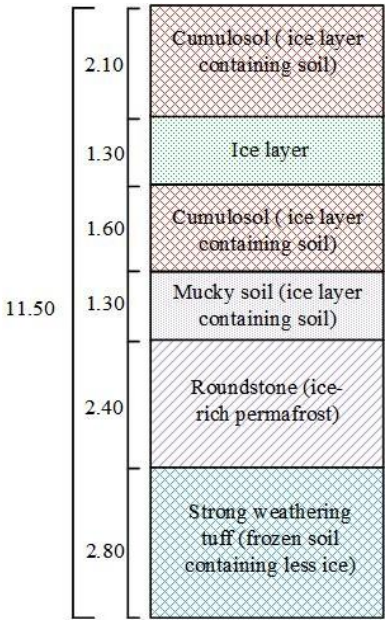

Figure 1: Map of the geological soil layer of the test site (unit in m).

This study demonstrates the influence of thermophysical properties of frozen soil on the temperature of the concrete cast-in-place pile body in a negative temperature environment. A test pile with a diameter of 1.4 m and a length of 11.5 m was poured at the test site on October 31, 2017. The ordinary C30 concrete commonly used in this area was used, and the mixing ratio of cement/fly ash/sand/gravel/water was 1/0.290/2.762/3.373/0.545. When heat transfer occurred between the hydration heat release of the pile and the

permafrost around the pile after pouring concrete, a temperature detection system was set up at the test pile to dynamically monitor the temperature changes. And the influence of permafrost on the pile foundation is analyzed.

2.2 Experimental research program and implementation

With the help of a parallel temperature measuring line, the temperature of the concrete pile wall is observed. The temperature measuring line is the same length as the pile, both of which are 11.5 m. In order to place temperature sensors in each layer of soil as far as possible, 13 temperature sensors are placed at unequal intervals. This is based on the geological survey drawings of the design institute and the distance between adjacent sensors ranging from 0.55–1.30 m. The first temperature is at a depth of 0.2 m below the surface. The temperature measuring line is located at the pile wall 0.1 m from the pile-soil interface. The vertical profile of the sensor temperature observation system is shown in Fig. 2. The temperature monitoring system began to collect temperature data from the piling day, and the observation period was from October 31, 2017 to November 29, 2017,

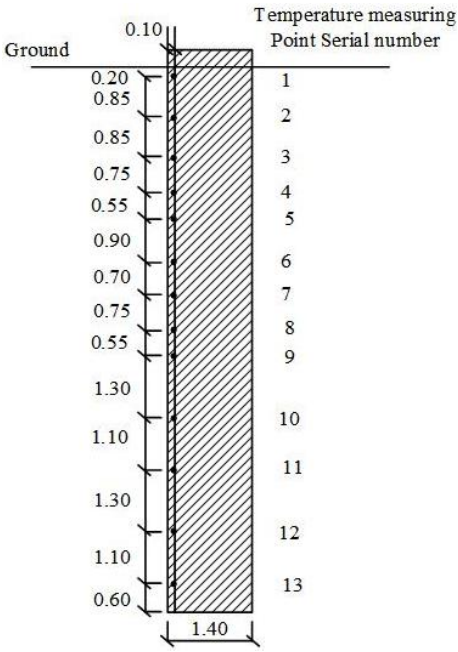

Figure 2: The vertical profile of pile wall temperature measuring points (unit in m).

lasting for 30 days. According to the instructions of the National Meteorological Science Data Center on the statistical method of the daily value of ground temperature [31], the data collected 4 times a day (at 02:00, 08:00, 14:00, 20:00) were used to calculate the daily average.

The temperature monitoring system is composed of the lower and the upper computers. The system structure is shown in Fig. 3. The lower computer includes a temperature sensor, a temperature acquisition module, a power supply control module, a wireless transceiver module, and a fully sealed box. According to the pre-set time of the temperature acquisition module, the lower computer is used to collect the ground temperature data. And the data is transferred to the upper computer through the GPRS (general packet radio service) point-to-point wireless transmission system. The upper computer includes the computer and data-receiving platform. Its function is to receive data and process the data to generate a text file. By setting the data acquisition time of the temperature acquisition module, the temperature can be monitored dynamically. This is the biggest advantage of this intelligent monitoring system. In the continuous low-temperature environment in winter, this monitoring system can use an independent solar energy power supply system to ensure the continuity and stability of the temperature acquisition module.

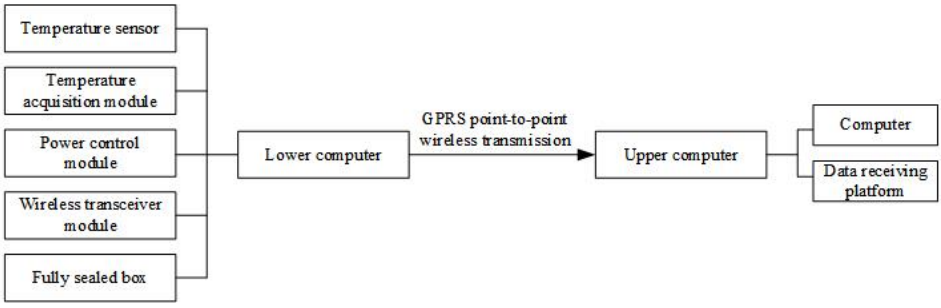

Figure 3: Schematic diagram of temperature monitoring system structure.

As shown in Fig. 4, the temperature sensor uses a JMT-36C resistive temperature sensing element. A three-layer sealing protection waterproof process is adopted. And the outermost layer uses stainless steel shell for protection and sealing. The temperature measurement range is –40°C to +150°C, the sensitivity is 0.1°C, and the accuracy is ±1°C. According to the sensor layout scheme, each temperature measuring wire with a single-head thermistor is bound one by one to the main bar of the reinforcing cage with

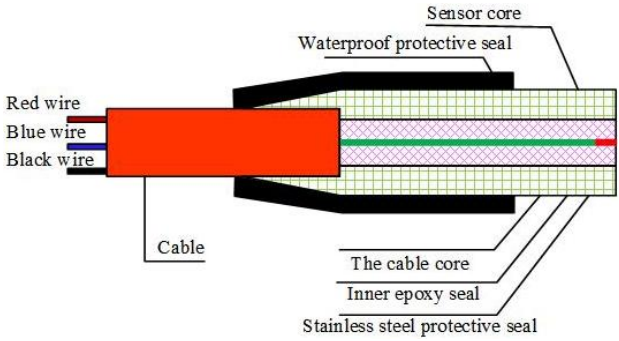

Figure 4: Internal structure of temperature sensor.

insulation and waterproof adhesive tape. And it is poured into the concrete pile together with a reinforcing cage. The elements of measuring system are shown in Fig. 5. The shape of the circle standing on the ground is the reinforcement cage, and the red binding line on the ground is the temperature measurement line.

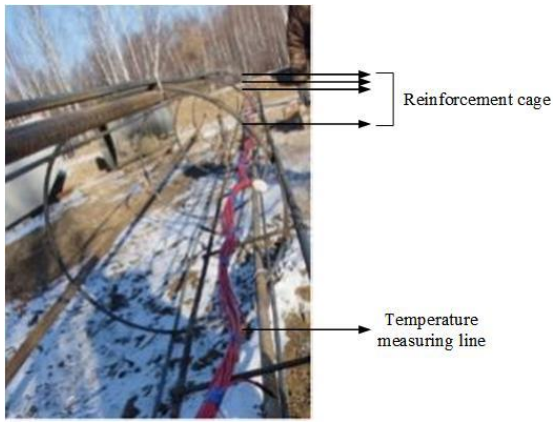

Figure 5: Arrangement of the measuring system elements.

The temperature acquisition module is the core of the intelligent temperature observation system. It integrates the main control chip, clock, large-capacity data storage, wireless transmission module, power interface, data interface, rechargeable battery, etc. The temperature acquisition module can work independently. According to the set measurement start time and interval time to ensure the continuity and non-loss of data, it can automatically complete the measurement and store it in the memory. The power

control module consists of two parts, a solar panel and an external accumulator. When the capacity of the external accumulator is insufficient, the rechargeable battery built into the temperature acquisition module can continue to measure regularly. A mobile phone card is installed in the wireless transmission module to realize the function of remote data transmission.

2.3 Experimental study on temperature field of concrete

Figure 6 shows the curves of temperature changing with time in the refreezing process in each measuring point at the pile wall after pouring the pile. It can be seen from the figure that the temperature change of the concrete pile has gone through two main stages: the temperature rising period of the hydration heat release pile body and the refreezing stage of the pile body when the permafrost around absorbs heat. In the first stage, with the massive heating of concrete hydration, the pile wall temperature rises in a negative temperature environment. The rate of rise varies at different depths, and the peak temperature is different. The temperature rise rate of the No. 10 measuring point at the depth of 7.4 m is the highest, with an average daily temperature increase of 4.7°C in 2 days, and 4.0°C in 3 days. This is because the moisture content of the gravel layer located at the measuring point is as low as 0.7%, which is less than that of other soil layers. On the one hand, when the concrete starts to hydrate and release heat, and the permafrost is melting around the pile, the free water in the pores of the boulder soil is permeated by gravity into the strongly weathered tuff

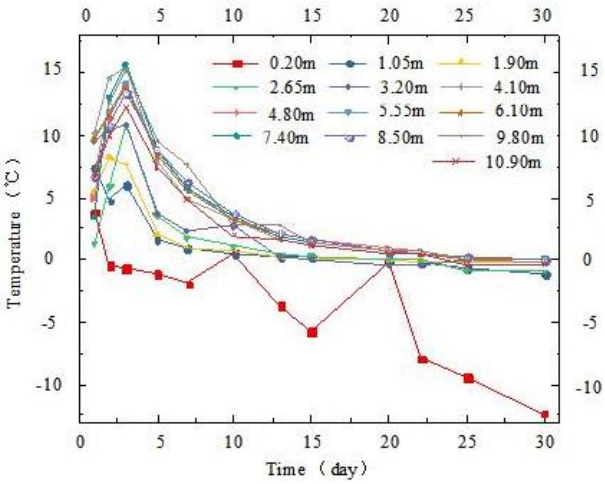

Figure 6: The temperature curve of the pile wall.

with larger pores. On the other hand, the capillary water in the boulder soil moves up into the silty soil along the fine pores under the action of surface tension. At the same time, since the silty soil layer is a soil-containing ice layer, the frozen water is far greater than the underlying cryo-rich soil layer. Thus, under the action of the gravity of soil particles and molecules, the bound water in the unfrozen water in the gravel soil (cryo-rich soil layer) constantly migrates to the frozen area (soil-containing ice layer). That is, the bound water migrates to the silty soil. The movement of these water molecules eventually results in the moisture content of the boulder layer being lower than that of the overlying and underlying soil layers, and even lower than that of other non-adjacent cohesive soil layers. The temperature rise of the No. 1 and No. 2 measuring points near the surface is negative due to the influence of the external atmospheric environment. And the temperature drop of the No. 1 measuring point is the fastest. The other measuring points are in the state of temperature rise. The peak temperature reached by each temperature measuring point is 15.7°C at the highest, which is generated on the third day in the No. 10 measuring point. The peak temperature in 2 days is 14.5°C and it is produced in the No. 6 measuring point at the depth of 4.10 m. In the second stage, the heat release of concrete hydration is less than the heat absorption of the frozen soil around the pile, and the temperature of the pile body gradually decreases. The cooling rate of the No. 6 measuring point at a depth of 4.10 m is the largest, followed by the No. 4 measuring point at a depth of 2.65 m. The daily cooling amounts of the two are 3.8°C and 3.6°C, respectively. By 20 days, the negative temperature begins to appear at the No. 5 measuring point at a depth of 3.2 m. By 30 days, the temperature of each measuring point is below 0.1°C.

The law of temperature changing with the depth at different measuring points is divided into two types. The first one involves the No. 1 measuring point at a depth of 0.20 m, which is most disturbed by external meteorological conditions, and the temperature change there is basically the same as the temperature change trend of the day. The other category covers the measuring points located below 2.65 m that are almost no longer affected by the atmospheric environment. At those points the temperature first rises and then falls, reaching the peak temperature on the 3rd day. And the nature of temperature change is very similar.

The temperature in the measuring points near the interfaces of different types of soil layers generally fluctuates slightly. For example, the No. 9 measuring point at a depth of 6.10 m is located near the interface between the

silty soil layer and the gravel soil layer. The temperature at this measuring point on the 3rd day is 13.9°C, while the temperatures measured on the same day at the No. 8 and No. 10 points adjacent to it are 14.2°C. The No. 11 measuring point at a depth of 8.5 m is located near the interface between the round stone and the strongly weathered tuff. The temperature at this measuring point on the 3rd day is 13.4°C, while for the No. 10 and No. 12 measuring points adjacent to it, the temperatures on the same day are 15.7°C and 15.3°C, respectively. In the negative temperature environment, the temperature value at the interface of the soil layer is generally slightly lower than that of the center measuring point of the adjacent soil layer, which is easy to produce errors. In order to reduce the measurement error caused by the location of the temperature measuring point, this paper selects the temperature value of the measuring point located at the center of each soil layer for research. Therefore, measuring points 2, 4, 6, 8, and 10 are selected as the following research object.

3 Thermophysical parameter analysis model

This paper establishes a two-dimensional model (Fig. 7), which is 14.0 m deep and 11.4 m wide. It is divided into 6 layers: the cumulosol layers between 0 and 2.1 m, and between 3.4 and 5.0 m, the ice layer between 2.1

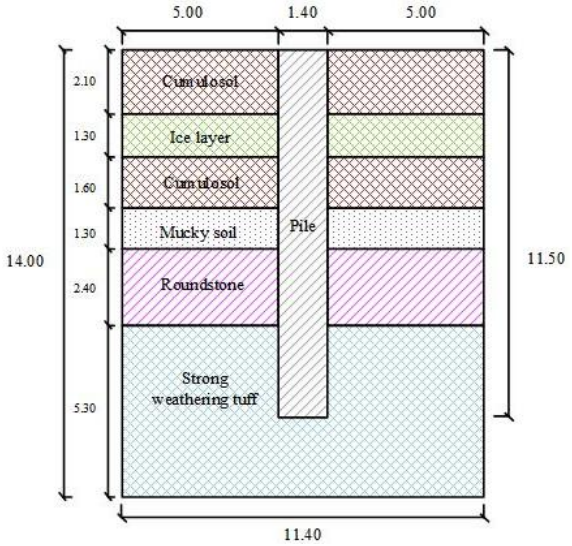

Figure 7: Pile foundation and geological model (unit in m).

and 3.4 m, the muddy layer between 5.0 and 6.3 m, the round stone layer between 6.3 and 8.7 m, and a strong weathering tuff layer between 8.7 and 14.0 m. The pile length is 11.5 m and the pile diameter is 1.4 m. The model has 127 202 units and 258 596 nodes.

3.1 Thermal property test of soil

The dry density and water content shall be determined by the combined method of frozen soil density. Specific heat capacity, thermal conductivity, and thermal diffusivity are measured by the ISOMET-2104 heat transfer analyzer [33]. The latent heat of phase change can be calculated after the actual measurement of unfrozen water content. In the model, the change of the latent heat of phase change is characterized by the change in the initial ground temperature. The ice-related data can be obtained from the relevant literature [6]. The geotechnical parameter data of frozen soil such as dry density, water content, specific heat capacity, thermal conductivity, and thermal diffusivity are shown in Table 1.

Table 1: Geotechnical parameters

Soil layer	Dry density of frozen soil (kg/m^3)	Water content (%)	Specific heat capacity (J/kg·K)		Thermal conductivity (W/m·K)		Thermal diffusivity $\times 10^{-6}$ (m^2/s)	
			freeze	thaw	freeze	thaw	freeze	thaw
Cumulosol	300	282.5	1339.0	1259.8	3.41	1.45	2.21	1.00
Ice layer	470	124.5	2090.0	4217.7	2.21	0.56	1.17	0.13
Cumulosol	1170	69.1	1121.8	1046.6	3.41	1.45	1.54	0.70
Mucky soil	1040	58.1	1024.2	715.0	2.02	1.48	1.20	1.25
Roundstone	1830	19.8	680.4	485.6	2.07	1.55	1.39	1.46
Strong weathering tuff	2220	10.7	642.3	639.3	3.66	1.57	2.32	1.00

3.2 Establishment of the thermophysical analysis model

3.2.1 Soil control equation

When the permafrost is in a frozen state, the moisture in the soil condenses into ice and there is very little flowing water. Thus, the convection heat transfer between the surface of the soil particles and the flowing water can be ignored. When the frozen soil is in a thawing or semi-thawing

state, the water in the soil changes from solid to liquid phase, and the latent heat of the ice-water phase transition releases (or absorbs) a large amount of heat. The convective heat transfer between the soil and water is insignificant [25].

In soil, heat conduction is more effective than convective heat transfer. Thus, convection heat transfer can be ignored, and only heat conduction and ice-water phase transition are considered. The heat transfer process can be divided into two states: the freezing state and the thawing state, which may be described by the equations, respectively:

$$C_f \frac{\partial T_f}{\partial t} = \frac{\partial}{\partial x}\left(\lambda_f \frac{\partial T_f}{\partial x}\right) + \frac{\partial}{\partial y}\left(\lambda_f \frac{\partial T_f}{\partial y}\right), \tag{1}$$

$$C_u \frac{\partial T_u}{\partial t} = \frac{\partial}{\partial x}\left(\lambda_u \frac{\partial T_u}{\partial x}\right) + \frac{\partial}{\partial y}\left(\lambda_u \frac{\partial T_u}{\partial y}\right), \tag{2}$$

where the subscripts f and u represent the freezing state and thawing states, respectively. Parameter T stands for the temperature, C is the volumetric heat capacity of the soil, and λ stands for its thermal conductivity.

The ice-water phase change process $s(t)$ can be expressed as:

$$T_f\left[s(t), t\right] = T_u\left[s(t), t\right] = T_m\,, \tag{3}$$

$$\lambda_f \frac{\partial T_f}{\partial n} - \lambda_u \frac{\partial T_u}{\partial n} = L \frac{ds(t)}{dt}\,, \tag{4}$$

where T_m represents the temperature of the freeze-thaw interface, t denotes time, and $\partial/\partial n$ is the derivative in a direction that is outwardly normal (perpendicular). Quantity L stands for the latent heat per unit volume, and it can be calculated as follows [6]:

$$L = \rho_d L'\left(\omega - \omega_u\right), \tag{5}$$

where L' is the latent heat of water, which usually takes 333.7 kJ/kg, ρ_d is the dry density of soil, ω is the water content, and ω_u is the unfrozen-water content.

3.2.2 Pile foundation control equation

In concrete hydration, adiabatic temperature rise in pile foundation at t after concrete pouring can be expressed as follows:

$$T(t) = \frac{WQ}{c\rho}\left(1 - e^{-kt}\right), \tag{6}$$

where W is single-side concrete cement content, Q is the heat of hydration per kilogram of cement, ρ is the concrete density assumed at 2400 kg/m^3, and c is the specific heat of concrete ranging between 0.92 and 1.00 kJ/(kg·K) [25]. Here, it takes 0.96 kJ/(kg·K). Parameter k is the adjustment coefficient of hydration heat of admixture with different dosage, whose value is available in the range of 0.2–0.4. Time (t) in Eq. (6) is expressed in days.

3.2.3 Boundary condition

According to meteorological data of the Mohe region [11], the boundary temperature of the natural surface can be described by

$$T_g = 5.35 - 40.015 \cos \frac{2\pi(t - 105)}{365}. \tag{7}$$

The initial temperature of frozen soil at the bottom and lateral boundary of the model is –3°C. The initial temperature of concrete is 10°C. The unit of time (t) is expressed in days, and the unit of temperature (T_g) is °C.

3.3 Validity of thermal analysis model

The temperature profile is used to verify the model (Figs. 8 and 9). In Fig. 8, the red area on the left is a higher-temperature area, the right (dark blue) is a lower-temperature area, and between them is a temperature gradient area. It can be seen from Fig. 9 that on November 3, 2017 and November 7, 2017, the maximum temperature difference between the two dates is 0.84°C

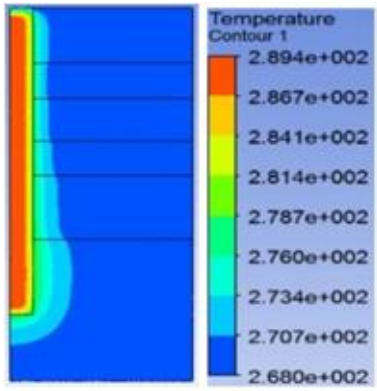

Figure 8: The pile-soil temperature field after pouring concrete for 3 days (unit in K).

and 0.62°C, respectively. The simulation results are in agreement with the measured results, and the model calculation results are reliable.

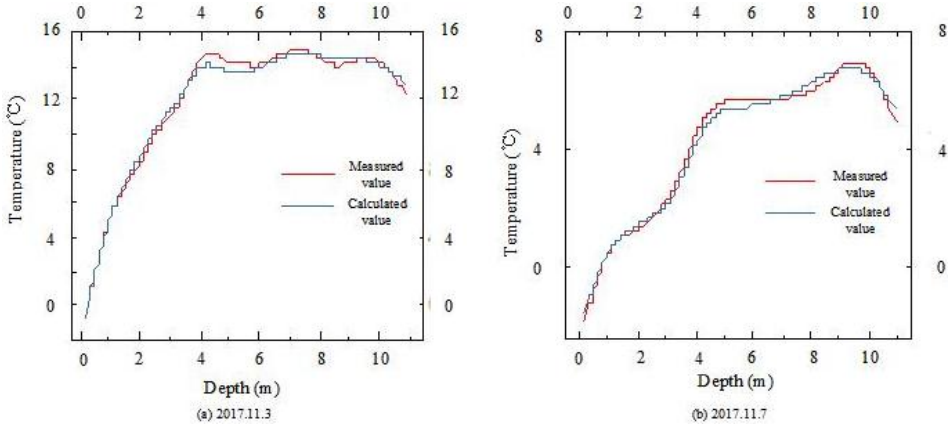

Figure 9: Experimental verification of pile wall simulation temperature: a) November 3, 2017, b) November 7, 2017.

4 The influence of frozen soil thermophysical properties on the temperature field of pile foundation

As can be seen from Fig. 6, the temperature reaches the maximum when concrete is poured for 3 days. In the present work, the pile-soil three-phase heat conduction model has been utilized. It considers the factors of frozen soil including specific heat capacity, thermal conductivity, thermal diffusivity and latent heat of phase change. Based on this, the impact of thermophysical properties of frozen soil on the temperature field of the foundation pile is analyzed.

4.1 Specific heat capacity

According to the references, the specific heat capacity of frozen soil ranges from 0.71–4.22 kJ/(kg·K) [31, 32]. Therefore, the values of specific heat capacity applied in the model are 0.7, 1.0, 2.09, 3, and 4.22 kJ/(kg·K). As can be seen from Fig. 10, when the specific heat capacity increases from 0.7 to 4.22 kJ/(kg·K), the temperature of the concrete pile wall in different soil layers decreases. From the top cumulosol layer ($h = 1.05$ m) to the

shallow depth in the strongly weathering tuff layer ($h = 9.80$ m), the pile wall temperature corresponding to each soil layer decreases from 6.20°C, 11.04°C, 15.98°C, 14.67°C, 16.90°C, 17.00°C to 5.96°C, 10.46°C, 14.85°C, 13.58°C, 14.33°C, 13.55°C. The temperature reductions are 0.24°C, 0.58°C, 1.13°C, 1.09°C, 2.57°C, 3.45°C, respectively, accounting for the changes of about 3.83%, 5.26%, 7.05%, 7.42%, 15.22%, 20.31%. It can be seen that the greater the depth of the pile body, the greater the proportion of the decrease in the pile wall temperature.

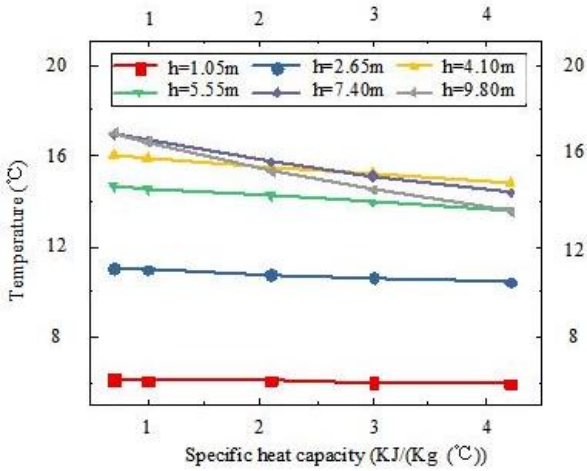

Figure 10: The variation of pile wall temperature with the change in specific heat capacity.

As the specific heat capacity increases, the temperature difference between the simulated temperature and the measured temperature of the pile wall at different depths decreases. It can be seen from Fig. 11 that when specific heat capacity is at the lower limit of 0.7 kJ/(kg·K), the temperature difference of the pile wall at different measuring points shows an increasing trend as the depth increases. The temperature difference values are 0.47°C, 1.21°C, and 1.70°C, respectively, of which those obtained for adjacent cumulosol layer and mucky layer (Fig. 11, $h = 4.10$ m and $h = 5.55$ m) are very close. The difference between the maximum and minimum value of temperature difference is 1.6°C. For the specific heat capacity increased to 4.22 kJ/(kg·K), the temperature difference is just opposite to the initial value of temperature difference, i.e. it becomes a negative value. That is, the maximum value appears in the top cumulosol layer, whereas the minimum value appears in the strongly weathering tuff layer at the largest

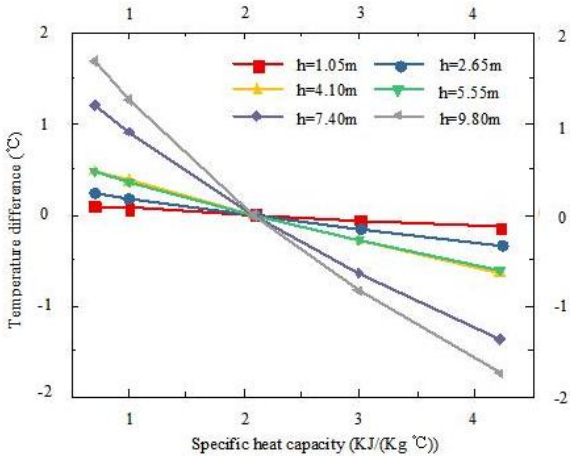

Figure 11: The variation of the temperature difference between the simulated and measured temperature of the pile wall with the change in specific heat capacity.

burial depth. The difference between the maximum and minimum value of temperature difference is 1.62°C. With increasing depth the temperature difference decreases to –0.14°C, –0.34°C, –0.65°C, –0.62°C, –1.37°C, –1.76°C, respectively.

4.2 Thermal conductivity

The value of thermal conductivity of frozen soil ranges from 0.18–3.79 W/(m·K) [5, 29], while that of ice ranges from 0.08–2.21 W/(m·K) [27]. Therefore, the values of thermal conductivity considered in the model are 0.08, 1.0, 2.21, 3.0, and 4.0 W/(m·K), respectively. As can be seen in Fig. 12 that when thermal conductivity increases from 0.08 W/(m·K) to 4.0 W/(m·K), wall temperature of the concrete pile in different soil layers decreases. From the upper cumulosol layer (h = 1.05 m) to the shallow depth in the strongly weathering tuff layer (h = 9.80 m), the pile wall temperature corresponding to each soil layer decreases from 7.49°C, 13.66°C, 20.09°C, 18.52°C, 22.79°C, 23.28°C to 4.89°C, 8.90°C, 13.10°C, 11.89°C, 12.87°C, 12.31°C, respectively, and the temperature drops are 2.60°C, 4.76°C, 6.99°C, 6.62°C, 9.92°C, and 10.97°C, respectively, accounting for the changes of about 34.68%, 34.83%, 34.80%, 35.77%, 43.53%, 47.12%. It can be seen that the greater the depth of the pile body, the greater the proportion of the decrease in the pile wall temperature.

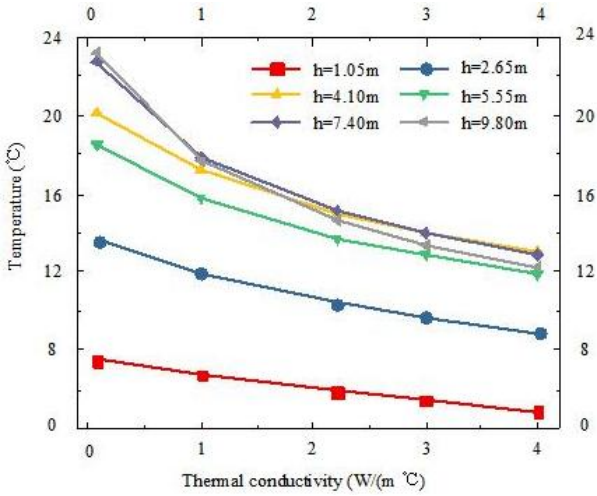

Figure 12: The variation of pile wall temperature with the change in thermal conductivity.

As the thermal conductivity increases, the temperature difference between the simulated temperature and the measured temperature of the pile wall at different depths decreases. As is demonstrated in Fig. 13 when the thermal

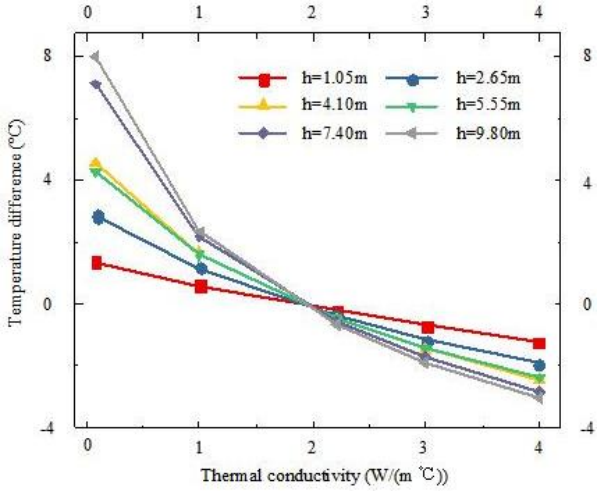

Figure 13: The variation of the temperature difference between the simulated and measured temperature of the pile wall with the change of thermal conductivity.

conductivity is at the lower limit of 0.08 W/(m·K), the temperature difference at different measuring points shows an increasing trend as the depth increases. The temperature difference values are 1.39°C, 2.86°C, 4.59°C, 4.32°C, 7.09°C, and 7.98°C, respectively, of which the temperature differences obtained for the adjacent cumulosol layer and mucky layer (Fig. 13, $h = 4.10$ m and $h = 5.55$ m) are very close. The difference between the maximum and minimum value of temperature difference is 6.59°C. With an increase in thermal conductivity, the temperature difference of the pile wall decreases. When thermal conductivity increases to 4.0 W/(m·K), the temperature difference value is just opposite to the initial temperature difference value. That is, the maximum value appears in the upper cumulosol layer, and the minimum value appears in the strongly weathering tuff layer at the largest burial depth. The difference between the maximum and minimum temperature difference is 1.78°C. Compared with the initial temperature difference (6.59°C), the difference is reduced by 4.81°C. It can be seen that with increasing thermal conductivity, the difference in the temperature difference of the pile wall measured at each depth is narrowing. The temperature difference decreases with the depth to –1.21°C, –1.90°C, –2.40°C, –2.31°C, –2.83°C, –2.99°C, which means the decreases by 2.60°C, 4.76°C, 6.99°C, 6.62°C, 9.92°C, and 10.97°C, respectively.

4.3 Thermal diffusivity

Thermal diffusivity is the ratio of thermal conductivity to volumetric heat capacity. For frozen soil in a frozen state, it ranges from 0.139×10^{-6} m^2/s to 0.783×10^{-6} m^2/s. In the thawing state, it varies between 0.172×10^{-6} and 1.531×10^{-6} m^2/s [5, 29]. In the model, the values of 0.1×10^{-6}, 0.4×10^{-6}, 0.8×10^{-6}, 1.2×10^{-6}, and 1.6×10^{-6} m^2/s were applied. The results in Fig. 14 show that with the increase of thermal diffusivity from 0.1×10^{-6} m^2/s to 1.6×10^{-6} m^2/s, the temperature of the concrete pile wall in different soil layers decreases. From the upper cumulosol layer to the shallow surface of the strongly weathering tuff layer, the pile wall temperature corresponding to each soil layer decreases from 7.93°C, 12.18°C, 17.71°C, 17.69°C, 20.69°C, 23.35°C to 4.96°C, 10.69°C, 14.75°C, 12.87°C, 13.81°C, 13.96°C, respectively. The temperature reductions are 2.97°C, 1.49°C, 2.96°C, 4.82°C, 6.88°C, 9.39°C, respectively, which amount to about 37.46%, 12.22%, 16.71%, 27.23%, 33.24%, 40.20%, respectively. It can be seen that from the ice layer ($h = 2.65$ m) to the highly weathering tuff layer ($h = 9.80$ m), the greater the depth of the pile body, the

greater the proportion of the decrease in the pile wall temperature. Near the surface, the temperature drop of the pile wall is greater than that in the ice layer and beneath it. Thus, the proportion of temperature decrease is greater. It is larger than that of the ice layer, cumulosol layer, and mucky layer beneath it. And it is only slightly smaller than that of the strongly weathering tuff layer.

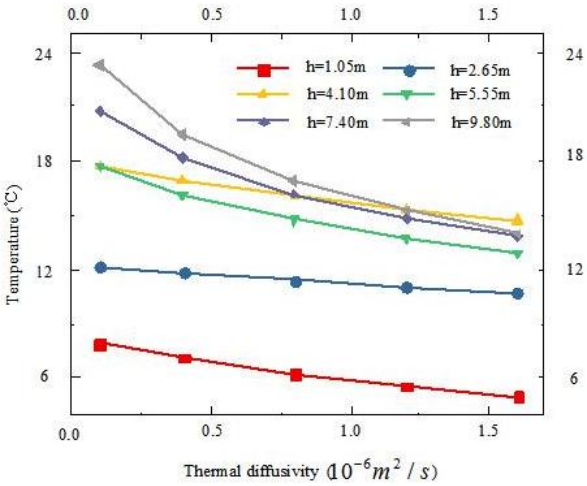

Figure 14: The variation of pile wall temperature with the change of thermal diffusivity.

As the thermal diffusivity increases, the temperature difference between the simulated temperature and the measured temperature of the pile wall at different depths decreases (Fig. 15). When the thermal diffusivity is at the lower limit of 0.1×10^{-6} m^2/s, except for cumulosol at the surface, the temperature difference of the pile wall increases with the depth. The maximum temperature difference of 8.05°C is predicted in the strongly weathering tuff layer ($h = 9.80$ m), and the minimum of 1.38°C in the ice layer ($h = 2.65$ m). With an increase in thermal diffusivity, the temperature difference of the pile wall decreases at each measuring point. For the largest considered thermal diffusivity, of 1.6×10^{-6} m^2/s, the maximum temperature difference appears in the ice layer, which is –0.24°C. The minimum temperature difference appears in the muddy layer, i.e. at a measuring point depth of 7.40 m, and it is –1.89°C. The drop in temperature difference increases with the depth, and for successive measuring points it amounts to 2.97°C, 1.49°C, 2.96°C, 4.82°C, 6.88°C, and 9.39°C, respectively.

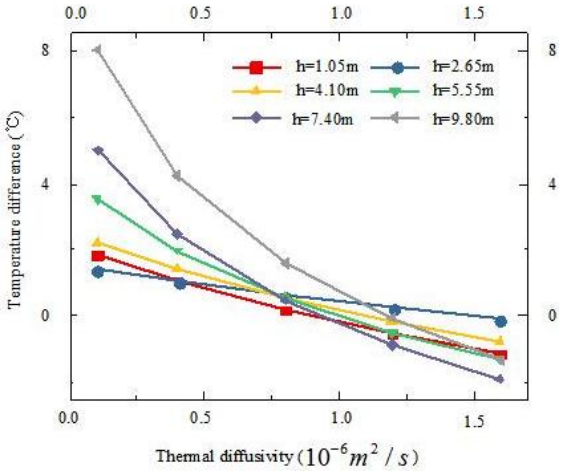

Figure 15: The variation of the temperature difference between the simulated and measured temperature of the pile wall with the change in thermal diffusivity.

4.4 Latent heat of phase change

The change of unfrozen-water content in each layer with temperature is shown in Fig. 16. The fitting formulas of unfrozen water content (ω_u) for T given in °C corresponding to the particular soil layers are as follows:

$$\omega_u = 7.470 + 7.466T + 2.324T^2 + 0.226T^3, \qquad (R^2 = 0.988), \tag{8}$$

$$\omega_u = 82.225 + 47.783T + 12.907T^2 + 1.180T^3, \qquad (R^2 = 0.997), \tag{9}$$

$$\omega_u = 79.009 + 51.481T + 14.215T^2 + 1.311T^3, \qquad (R^2 = 0.997), \tag{10}$$

$$\omega_u = 17.163 + 17.057T + 5.299T^2 + 0.515T^3, \qquad (R^2 = 0.988), \tag{11}$$

$$\omega_u = 0.093 - \frac{5.377}{T}, \qquad (R^2 = 0.995), \tag{12}$$

$$\omega_u = -0.114 - \frac{4.107}{T}, \qquad (R^2 = 0.995). \tag{13}$$

In formulas (8)–(13), ω represents water content, T represents temperature, and R^2 represents a variable.

Substituting the unfrozen water content (Eqs. (8)–(13)) into formula (5), the latent heat of phase change can be calculated. According to the monitoring data of the original ground temperature, the ground temperature of each soil layer in this area from June to November remains almost unchanged. Therefore, the ground temperature at this time is selected as

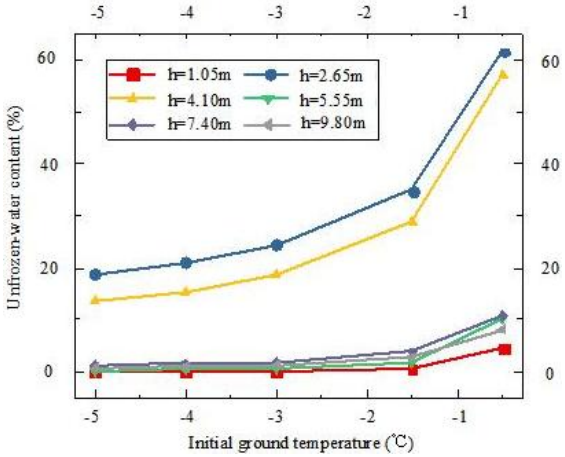

Figure 16: The change of unfrozen water content in the soil layers with initial ground temperature.

the initial ground temperature, ranging from –4.7°C to 0.67°C. The initial ground temperature values in the model are –5.0°C, –4.0°C, –3.0°C, –1.5°C, and –0.5°C, respectively. The relationship between the latent heat of phase change of each frozen soil layer and temperature is shown in Fig. 17.

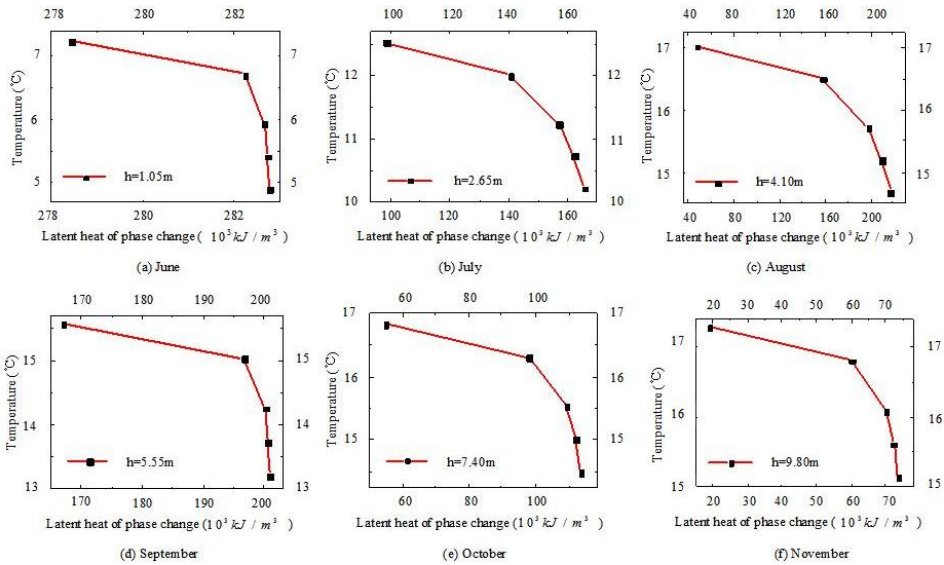

Figure 17: Variation of pile wall temperature with the latent heat of phase change at different depths.

As can be seen from the figure, when the initial ground temperature increases from -5°C to -0.5°C, the latent heat of phase change of each soil layer varies greatly. It is the largest in the cumulosol layer closest to the surface, as shown in Fig. 17a. Its value changes from 278.46×10^3 kJ/m^3 to 282.75×10^3 kJ/m^3, and the difference is only 4.29×10^3 kJ/m^3. The cumulosol layer under the ice layer at a depth of 4.10 m has the largest value of latent heat of phase change (Fig. 17c). The minimum value is 47.55×10^3 kJ/m^3 and the maximum value is 217.43×10^3 kJ/m^3. The variable quantity is 169.88×10^3 kJ/m^3. The latent heat of different soil layers has different effects on the corresponding pile wall temperature. In the cumulosol layer at a depth of 1.05 m, the latent heat of the frozen soil is the largest and the temperature of the pile wall is the lowest, ranging between 4.90°C and 7.24°C. In November, the test site is covered with snow, and the temperature change of the pile wall is mainly affected by the hydration heat release of the concrete and thermophysical properties of the soil around the pile. But it is less disturbed by surface meteorological conditions. Therefore, the low temperature of the pile wall of the soil layer is mainly caused by the latent heat of the phase transition of the soil. The soil absorbs the hydration heat of the concrete and stores the internal energy in the soil particles and the middle of ice and water. Although the ice-water phase change and soil-water structure change occur, the temperature change caused by the pile wall is very small. On the contrary, at the depth of 9.80 m, due to the low water content of the strongly weathering tuff layer, the latent heat of phase transition is small, varying only from 19.18×10^3 kJ/m^3 to 73.84×10^3 kJ/m^3. Thus, the pile wall temperature here is as high as 15.13–17.29°C, and it is the maximum temperature of each soil layer. The latent heat of the phase change of the ice layer (Fig. 17b) is between that of the surface soil layer and the shallow surface soil layer. Its value changes from 98.58×10^3 to 165.90×10^3 kJ/m^3, and the variation is only 67.32×10^3 kJ/m^3. The corresponding pile wall temperature is different from that of other soil layers. The temperature of the soil layer is obviously higher than the one of the pile wall corresponding to the surface soil layer. And it is also significantly lower than the pile wall temperature corresponding to other soil layers. The temperature ranges from 10.21°C to 12.51°C, but the temperature difference is similar to those predicted for other soil layers, and it is 2.3°C. Although the unfrozen-water content changes little with the initial moisture content and dry bulk density in the frozen soil [28], the latent heat of phase change is greatly affected by the change in unfrozen water content. From the irregular change of the soil

layer in Figs. 17a–f, the latent heat of phase change is not only affected by temperature but is also related to multiple factors. These factors are the water content of the soil body and the structure between the soil and water, which is more complicated.

4.5 The comparative analysis of the influence of permafrost thermophysical properties on the temperature field in foundation piles

The thermophysical properties have different effects on the temperature of concrete piles, as shown in Table 2. In the table, the influence of the thermophysical parameters on the temperature of the concrete pile body shows a consistent rule. It is analyzed from three aspects. The first is the change in pile wall temperature caused by the change of a thermophysical property. The second is the percentage change in temperature based on the parameter values for the respective soil layer. The third is the difference between the simulated and measured temperature at each considered point that changes with the thermophysical parameter value. The comparison illustrates that thermal conductivity has the greatest impact on the temperature of the pile body. The thermal diffusivity and latent heat of phase change have less impact, and the specific heat capacity has the least influence on it.

Table 2: The comparison of the influence of permafrost thermophysical properties on the concrete pile temperature

Property	Symbol	Temperature range* (°C)	Percentage change (%)	Range of temperature difference** (°C)
Specific heat capacity	c	0.24–3.45	3.83–20.31	–1.76–1.27
Thermal conductivity	λ	2.60–10.97	35.77–47.12	–2.99–7.98
Thermal diffusivity	α	1.49–9.39	12.22–40.20	–1.89–4.99
Latent heat of phase change	L	2.16–2.36	12.46-32.25	–1.20–1.99

*Refers to the pile wall temperature change in the soil layer with the change of respective property.
**Refers to the difference between the simulated and measured temperature.

Therefore, in the construction of a bridge pile foundation, it is needed to ensure the quality of the concrete pile and reduce the rate of temperature reduction of the pile body. Considering that the thermal conductivity of

frozen soil has the greatest influence on the temperature field of the foundation pile, this problem can be solved by adding materials with low thermal conductivity around the pile. For example, polyurethane foam (the thermal conductivity is only 0.017–0.023 W/(m·K)) and asbestos can be used. On the other hand, the thermal conductivity of the soil increases with an increase in the dry bulk density as well as the soil water content. And it decreases with the increase of the dispersion of the solid particles in the soil [27]. Therefore, in order to effectively reduce the thermal conductivity of the frozen soil around the pile, the heat preservation of the pile body can be achieved by replacing the soil with a small dry bulk density, moderately increasing the dispersion of solid particles, and reducing the water content.

5 Conclusions

Aiming at the problem that the thermo-physical properties of frozen soil have a great impact on the quality of cast-in-place concrete piles, the variation law of concrete temperature during the construction of bored piles is studied, and some results are obtained.

- Under the negative temperature environment, the temperature change of the concrete pile body is a dynamic process, including two stages of temperature rise and refreezing of hydration. In the temperature rising stage, the temperature rises fastest at a depth of 7.40 m, and the peak temperature is the highest. The average daily temperature rise in 2 days is 4.75°C and the average daily temperature rise in 3 days is 4.07°C; the peak temperature is generated on the third day and the temperature is 15.7°C.

- In the refreezing period, the descending speed of temperature is the highest at a depth of 4.10 m, and the daily cooling rate is 3.85°C. After 30 days, the temperature at each measuring point is below 0.1°C. Each measuring point at a depth below 2.65 m is almost no longer affected by the atmospheric environment. The temperature first rises and then falls, and reaches the peak value on the third day. The change law is very similar.

- Thermophysical properties of frozen soil have different effects on concrete piles. According to the influence of frozen soil on the temperature of the pile body, the order from high to low is the thermal

conductivity, thermal diffusivity, latent heat of phase change, and specific heat capacity. The changes in the pile wall temperature caused by the change of thermophysical property values of the soil are: 2.60–10.97°C by thermal conductivity, 1.49–9.39°C by thermal diffusivity, 2.16–2.36°C by the latent heat of phase change, and 0.24–3.45°C by specific heat capacity. The percentage changes are within 35.77–47.12%, 12.22–40.20%, 12.46–32.25%, and 3.83–20.31%, respectively. The corresponding differences between the simulated and measured temperature along the pile due to the changes in the thermophysical soil parameters are –2.99–7.98°C, –1.89-4.99°C, –1.20–1.99°C, –1.76–1.27°C.

Acknowledgements

The research reported in this paper was supported by founding from the National Natural Science Foundation of China (NSFC) (No. 51408258) and the Basic Scientific Research Operating Expenses of Central Universities (No. 2572015BB03). The support is gratefully acknowledged.

Received 21 November 2022

References

[1] Zhou Y.W., Guo D.X., Qiu G.Q.: *Quaternary permafrost in China.* Quaternary Science Reviews **6**(1991), 10, 5114–517.

[2] Liu N.F., Li N., He M., Xu S.: *Analyzing the factors controlling the bearing capacity of cast-in-place piles based on a thermo-hydro-mechanical coupling model.* J. Glaciol. Geocryol. **6**(2014), 36, 1471–1478.

[3] Lu X.Y., Liu Y.Y., Bian H.B., Sun Z.H., Wang C. Y., Qiu X. M.: *The application of extruded polystyrene boards in frost heaving prevention of concrete lining channel.* J. Shandong Univ. (Nat. Sci. Ed.) **3**(2019), 50, 460–467.

[4] Wyczółkowski R., Strychalska D., Bagdasaryan V.: *Correlations for the thermal conductivity of selected steel grades as a function of temperature in the range of 0–800° C.* Arch. Thermodyn. **43**(2022), 29–45.

[5] Yu D., Tang H.Y., Ma W.Y., Wang Y., Lv W.B.: *The effect of moldling temperature on thermal stresses of massive concrete roadbed structure.* J. Rail. Sci. Eng. **9**(2019), 2150–2155 (in Chinese).

[6] Li J.N., Sun X.X.: *Influence of hydration heat on temperature distribution field along piles in warm permafrost regions.* J. Rail. Sci. Eng. **12**(2019), 2984–2990 (in Chinese).

[7] Huang J.W.: *Study on temperature field of pavement structure of old cement concrete pavement with asphalt layer*. South China Univ. Technol., Guangzhou 2017 (in Chinese).

[8] Song C.N.: *Research on pavement temperature field and pavement working environment temperature index in desert area*. Chang'an Univ., Xi'an 2006 (in Chinese).

[9] Ge Y.J., Zhai D., Zhang G.Q.: *Experimental study on temperature field of concrete cable-stayed bridge*. China J. Highw. Transp. (1996), 2, 76–83 (in Chinese).

[10] Huang Z.G.: *Field monitoring and 02erical analysis of temperature field of long-span suspension bridges*. South China Univ. Technol., Guangzhou 2016 (in Chinese).

[11] Hu C.B., Zeng H.G.: *A study on monitor measurement of temperature field of cement concrete pavements structure in Fujian province*. Highway (2007), 8, 69–77 (in Chinese).

[12] Liu W.Y., Geng Y.M.: *The influence of thermal parameters on the temperature field of concrete structures*. China Concrete Cement Prod. (2005), 1, 11–15 (in Chinese).

[13] Xiao J.Z., Song Z.W., Zhao Y., Qian Y.H.: *Analysis of solar temperature action for concrete structure based on meteorological parameters*. China J. Civ. Eng. **43**(2010), 4, 30–36 (in Chinese).

[14] Zeng S.Z.: *Experimental study on temperature field of concrete structure in freeze-thaw environment*. Harbin Inst. Technol. 2016 (in Chinese).

[15] Li Y.: *Simulation calculation of temperature field of mass concrete based on independent covering numerical manifold method*. CSTA, 2015 (in Chinese).

[16] Cai X.Y.: *Theoretical study on indoor fire environment and temperature field calculation of concrete structure*. Sichuan Archit. (2007), 5, 56–58 (in Chinese).

[17] Daghsen K., Lounissi D., Bouaziz N.: *A universal model for solar radiation exergy accounting: Case study of Tunisia*. Archiv. Thermodyn. **43**(2022), 2, 97–118.

[18] Alekseev A.Z., Zorin D.: *Interaction of the augercast micropiles with permafrost*. IOP Conf. Ser.: Mater. Sci. Eng. **365**(2018), 042056.

[19] Fajobi M.A., Loto R.T., Oluwole O.O.: *Corrosion behavior of steel in acidic medium for petroleum systems*. MACEM **1**(2020), 1, 25–26.

[20] Zhang D., Mamesh Z., Sailauova D., Shon C.S., Lee D., Kim J.: *Temperature distributions inside concrete sections of renewable energy storage pile foundations*. Appl. Sci. **9**(2019), 22, 4776.

[21] Xiao S., Suleiman M.T., Al-Khawaja M.: *Investigation of effects of temperature cycles on soil-concrete interface behavior using direct shear tests*. Soils Found. **59**(2019), 5, 1213–1227.

[22] Wang Y., Zhu D.Y., Ye J.S.: *Parametric analysis of concrete box-girder thermal action*. Mod. Transport. Technol. **12**(2008), 5, 95–99 (in Chinese).

[23] Zhang W., Zhang L.L., Zhong N.: *Temperature field research based on main cable thermal parameters of suspension bridge*. J. Chongqing Jiaotong Univ. (Nat. Sci.) **1**(2016), 35, 1–4 (in Chinese).

[24] Ahmad S.N., Prakash O.: *Thermal performance evaluation of an earth-to-air heat exchanger for the heating mode applications using an experimental test rig*. Archiv. Thermodyn. **43**(2022), 1, 185–207.

[25] Lu Y., Yu W.B., Guo M., Liu W.: *Spatiotemporal variation characteristics of land cover and land surface temperature in Mohe County, Heilongjiang Province.* J. Glaciol Geocryol. **39**(2017), 5, 1137–1147 (in Chinese).

[26] Jin H.J., Wang S.L., Lu L.Z., Yu S.P.: *Features of permafrost degradation in Hinggan Mountains, Northeastern China.* Sci. Geogr. Sinica **29**(2009), 2, 223–228 (in Chinese).

[27] Jehhef K.A., Abas Siba M.A.A.: *Effect of surfactant addition on the nanofluids properties: A review.* Acta Mech. Malay. **2**(2019), 2, 1–19.

[28] Chen L., Yu W.B., Yi X., Wu Y., Ma Y.: *Application of ground penetration radar to permafrost survey in Mohe County, Heilongjiang Province.* J. Glaciol. Geocryol. **37**(2015), 3, 723-730 (in Chinese).

[29] Yu W., Guo M., Chen L., Lai Y.M., Yi X., Xu L.L.: *Influence of urbanization on permafrost: A case study from Mohe County, Northernmost China.* Cryosphere Discuss. **8**(2014), 4, 4327–4348.

[30] China meteorological data network. https://data.cma.cn/data/cdcindex/cid/6d1b5efbdcbf9a58.html (accessed 17 May 2022).

[31] Andersland O.B., Ladanyi B.: *Frozen Ground Engineering* (2nd Edn.). Wiley, 2004., (China Architecture&Building Press, Beijing 2003), (accessed 10 April 2022).

[32] Zheng X.Q., Fan G.S., Xing S.Y.: *Movement of Water in Seasonal Unsaturated Freeze-Thaw Soil.* Geological Publishing House, Beijing 2002, 22–27 (in Chinese).

[33] https://www.researchgate.net/figure/Measurement-of-thermal-properties-using-the-ISOMET-2104_fig2_311089537 (accessed 7 May 2022).

archives
of thermodynamics
Vol. **44**(2023), No. 2, 69–85
DOI: 10.24425/ather.2023.146559

Study of the effect of geometric shape on the quality of mixing: Examining the effect of length of the baffles

MALIKA SEDDIK BOUCHOUICHA[a]
HOUSSEM LAIDOUDI[a*]
SOUAD HASSOUNI[a]
OLUWOLE DANIEL MAKINDE[b]

[a] University of Science and Technology of Oran Mohamed-Boudiaf,
Faculty of Mechanical Engineering,
BP 1505, El-Menaouer, Oran, 31000, Algeria

[b] Stellenbosch University, Faculty of Military Science,
Private Bag X2, Saldanha 7395, South Africa

Abstract This work is an attempt to study the behaviour of fluid in the mixing vessel with a two-bladed or four-bladed impeller. The working fluid is complex, of a shear-thinning type and the Oswald model is used to describe the fluid viscosity. The study was accomplishedby numerically solving the governing equations of momentum and continuity. These equations were solved for the following range of conditions: 50–1000 for the Reynolds number, 0–0.15 for the baffle length ratio, and the number of impeller blades 2 and 4. The simulations were done for the steady state and laminar regime. The results show that the increase in baffle length (by increasing the ratio baffle length ratio) decreases the fluid velocity in the vessel. Increasing the speed of rotation of the impeller and/or increasing the number of blades improves the mixing process. Also, the length of the baffles does not affect the consumed power.

Keywords: Baffles; Stirred vessel; Non-Newtonian fluid, Steady simulation, CFD

[*]Corresponding Author. Email: houssem.laidoudi@univ-usto.dz

Nomenclature

D	–	diameter of the vessel, m
H	–	height of the vessel, m
h	–	diameter of the impeller, m
k_s	–	weak function factor
l	–	length of the baffle, m
m	–	fluid consistency, Pa s^n
N	–	rotational velocity, rad/s
n	–	power-law index
N_p	–	power number
P	–	mechanical power, W
p	–	pressure, Pa
p^*	–	dimensionless pressure
Q_v	–	viscous dissipation, m/s^2
R^*	–	dimensionless diameter
r, θ, z	–	cylindrical coordinates
Re	–	Reynolds number
V_r	–	radial velocity, m/s
V_z	–	axial velocity, m/s
V_θ	–	tangential velocity, m/s

Greek symbols

$\dot{\gamma}$	–	shear rate, 1/s
μ	–	dynamic viscosity, Pa s
ρ	–	density, kg/m^3
τ	–	shear stress, Pa

1 Introduction

The study of mechanical agitation is considered one of the most important studies that witnessed the interest of many researchers recently. This is mainly due to its sensitive presence in many areas of industry including the pharmaceutical industry, food manufacturing, cosmetics manufacturing, medical analyses and so on.

The mixing process using a mechanical mixer is evaluated by two main factors, namely: the quality of the mixture obtained and the duration of mixing with the mechanical energy consumed. Therefore, the research in this field aims at designing of a mixer capable of mixing the fluid effectively with the effects of saving energy and mixing time.

There are quite a few researchers who have investigated in this direction. Hadjeb *et al.* [1] researched the shape of the agitator by combining two

previous simple shapes of an agitator, namely: a helical screw and a two-blade impeller. The fluid studied in this paper was that of a highly viscous fluid, while the vessel had a simple cylindrical type without any baffle. The results of the research showed that this new form has the ability to raise the quality of mixing. Laidoudi [2] accomplished a numerical work on the effect of shape of the mixer on the quality of mixing. The form studied in this paper consists in holes in the blades of the two-bladed agitator. The form of the vessel was cylindrical without baffles. The working fluid was Newtonian and the flow regime was perfectly laminar. The results showed that this new form has a tendency to improve the mixing quality. Ameur [3] studied the effect of the form of the vessel on the mixing quality, while the form of the impeller was kept fixed (Scaba 6SRGT- six-curved bladed impeller impeller). The forms studied here are: a dished bottomed cylindrical vessel, a flat bottomed cylindrical vessel and a closed spherical vessel. The results of the research confirm that the shape of the vessel affects the quality of mixing.

There is also a group of researchers who studied mixing of complex fluids using a mechanical agitator where the impeller has curved blades [4–12]. Some investigators [13–19] also studied the effect of baffles inside the vessel on the quality of mixing. The behaviour of the fluid in the vessel has been understood with the determination of energy consumed.

Ameur [20] conducted the numerical simulation of shear-thinning fluid in a cylindrical vessel stirred by a turbine. The study examined the effect of impeller shape on the characteristics of mixing. The mechanical power consumed by the impeller has been evaluated according to the power number. The model of Oswald has been used to define the viscosity.

There are also other works [21–32] that have studied different groups of fluids inside vessels with mechanical agitators of different shapes and sizes. Furthermore, recent studies show that the fluid motion inside the vessels is mainly related to the geometry of the vessel and rotating objects [33–44]. Generally, it can be concluded that the performance of the mixer and the mixing process can actually be improved if the process is analyzed and the effects of the engineering parts are known.

From the aforementioned previous investigations, the following becomes clear: the mixing process for complex fluids is one of the most important factors in industrial applications such as the manufacture of medicines, organic compounds and foodstuffs. Also, the mixing process is related to the geometric shape of the mixer and the quality of the fluid. In addition to this, each fluid must be studied in order to know its exact behaviour.

Accordingly, this work presents a study of a type of complex fluid inside a mixer. The general shape of the mixer undergoes geometric changes in order to determine the shape that helps in accelerating the process of mixing the fluid and reducing the mechanical energy consumed. Accordingly, the elements studied here are: the speed of rotation of the impeller, the number of blades and the length of baffles placed in the vessel.

This research can be used to enhance results related to industrial applications such as the process of mixing pharmaceuticals, cosmetics and alimentary. This research can also be a reference for pedagogical works related to the mixing process.

2 The studied system

The mixing system studied in this paper is presented in Fig. 1. The system mainly consists of a flat bottom vessel ofa circular cross-section (Fig. 1a). The height (H) and diameter (D) of the vessel are equal ($H = D = 400$ mm). The vessel has four baffles evenly distributed by 90°. The length of the baffle is (l) which is given by the ratio $l/D = 0.05$, 0.1, 0.15 and 0.25. The vessel is assumed to be completely filled with a complex shear-thinning fluid. The cylindrical vessel is equipped with a two-bladed impeller (Fig. 1b) or a four-bladed impeller (Fig. 1c). The diameter of the impeller

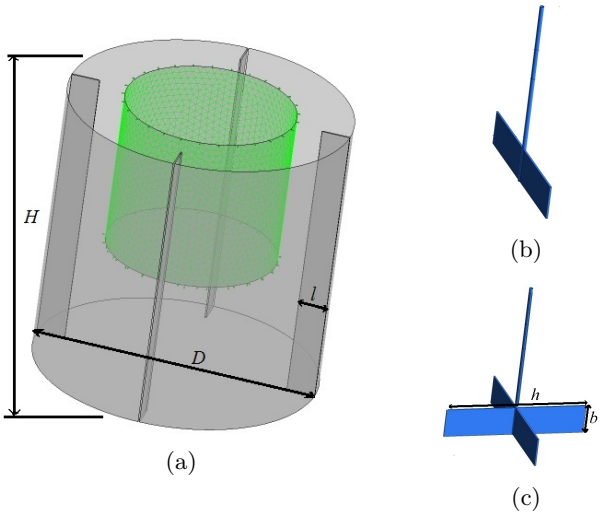

(a) (b) (c)

Figure 1: General view on the mixing system.

is equal to $h = D/2$, while the height of the impeller blade (b) is given by the ratio $b/D = 0.1$. The agitator is placed in the vessel at the clearance $D/2$. The thickness of the blade is 2 mm. The impeller rotates at a uniform speed expressed in terms of Reynolds number.

3 Mathematical formulation

The fluid used in this research is of polymer type, which has the behaviour of a shear-thinning fluid. For the shear-thinning fluids, the dynamic viscosity (μ) becomes apparent and it is expressed according to the Oswald model as:

$$\mu = m\dot{\gamma}^{n-1}, \tag{1}$$

where $\dot{\gamma}$ is the shear rateThis type of apparent dynamic viscosity is specific to shear-thinning fluids, meaning that as the shear rate between fluid layers increases, this dynamic viscosity decreases. This type of fluid has two rheological characteristics, namely, the flow consistency (m), and the power-law index (n), which are evaluated as 13.2×10^{-3} Pa s^n and 0.85×10^{-3} Pa s^n, respectively. The density of this fluid is 998 kg/m^3. These values were taken from the results of experimental work done by Venneker *et al.* [31].

In order to control the flow regime, the rotation of the impeller is expressed by the Reynolds number:

$$\mathrm{Re} = \frac{\rho N^{2-n} D^2}{m k_s^{n-1}}, \tag{2}$$

where ρ and N refer to the fluid density and rotational speed of the impeller. k_s is the weak function, it is a dimensionless value which is equal to 11.5. This value is taken from [20].

The power consumption is characterized by a dimensionless quantity which is called the power number as:

$$N_p = \frac{P}{\rho N^3 D^5}, \tag{3}$$

where P is the power consumption and it is calculated as:

$$P = \mu \int\limits_{\text{vessel volume}} Q_v \, dv, \tag{4}$$

where dv is written in cylindrical coordinates as:

$$dv = r \, dr \, d\theta \, dz, \tag{5}$$

Q_v indicates the viscous dissipation:

$$Q_v = \frac{1}{\mu^2}\left(2\tau_{rr}^2 + 2\tau_{\theta\theta}^2 + 2\tau_{zz}^2 + 2\tau_{rz}^2 + 2\tau_{r\theta}^2 + 2\tau_{z\theta}^2\right), \tag{6}$$

where

$$\tau_{rr} = -2\mu\left(\frac{\partial v_r}{\partial r}\right), \tag{7}$$

$$\tau_{r\theta} = -\mu\left[r\frac{\partial\left(\frac{v_\theta}{r}\right)}{\partial r} + \frac{1}{r}\frac{\partial v_r}{\partial \theta}\right], \tag{8}$$

$$\tau_{rz} = -\mu\left(\frac{\partial v_r}{\partial z} + \frac{\partial v_z}{\partial r}\right). \tag{9}$$

Equations (1)–(9) can be used to solve differential equations that model the fluid behaviour. These equations can be written as follows [45–47]:

$$\frac{1}{r}\frac{\partial\left(\rho r V_r\right)}{\partial r} + \frac{1}{r}\frac{\partial\left(\rho V_\theta\right)}{\partial \theta} + \frac{\partial\left(\rho r V_z\right)}{\partial z} = 0, \tag{10}$$

$$\rho\left(V_r\frac{\partial V_r}{\partial r} + \frac{V_\theta}{r}\frac{\partial V_r}{\partial \theta} + V_z\frac{\partial V_r}{\partial z} - \frac{V_\theta^2}{r}\right) = -\frac{\partial p}{\partial r} + \mu\left[\frac{\partial}{\partial r}\left(\frac{1}{r}\frac{\partial}{\partial r}\left(rV_r\right)\right) + \frac{1}{r^2}\frac{\partial^2 V_r}{\partial \theta^2} + \frac{\partial^2 V_r}{\partial z^2} - \frac{2}{r^2}\frac{\partial V_\theta}{\partial \theta}\right], \tag{11}$$

$$\rho\left(V_r\frac{\partial V_\theta}{\partial r} + \frac{V_\theta}{r}\frac{\partial V_\theta}{\partial \theta} + V_z\frac{\partial V_\theta}{\partial z} + \frac{V_r V_\theta}{r}\right) = -\frac{1}{r}\frac{\partial p}{\partial \theta} + \mu\left[\frac{\partial}{\partial r}\left(\frac{1}{r}\frac{\partial}{\partial r}\left(rV_\theta\right)\right) + \frac{1}{r^2}\frac{\partial^2 V_\theta}{\partial \theta^2} + \frac{\partial^2 V_\theta}{\partial z^2} + \frac{2}{r^2}\frac{\partial V_r}{\partial \theta}\right], \tag{12}$$

$$\rho\left(V_r\frac{\partial V_z}{\partial r} + \frac{V_\theta}{r}\frac{\partial V_z}{\partial \theta} + V_z\frac{\partial V_z}{\partial z}\right) = -\frac{\partial p}{\partial z} + \mu\left[\frac{1}{r}\frac{\partial}{\partial r}\left(r\frac{\partial V_z}{\partial r}\right) + \frac{1}{r^2}\frac{\partial^2 V_z}{\partial \theta^2} + \frac{\partial^2 V_z}{\partial z^2}\right]. \tag{13}$$

These equations are written in dimensional form, some non-dimensional variables are given as:

$$(r^*, Z^*) = \frac{(r, z)}{D}, \qquad (V_r^*, V_\theta^*, V_z^*) = \frac{(V_r, V_\theta, V_z)}{ND}, \qquad p^* = \frac{p}{\rho(ND)^2}, \qquad R^* = \frac{2r}{D}. \tag{14}$$

4 Simulation steps

Since the vessel includes baffles, multiple reference frame (MRF) technique was employed. This technique mainly depends on dividing the domain of computation into two main parts. The first part is fixed and includes the walls of the vessel with the baffles, while the second is in rotation and includes the impeller. This technique was used in many previous works, including [2, 18, 19]. In the absence of baffles inside the vessel, a rotating reference frame (RRF) can be used as in works [1, 3, 8].

In order to achieve this simulation, both static and movable parts were created by using Gambit. A tetrahedral mesh with concentration of elements around the impeller was generated as it is shown in Fig. 2. The grid elements are constructed in this way because the flow layers are very sensitive in the vicinity of the impeller, which is the main cause of the fluid motion. The number of grid elements was selected based on the results of grid independency tests.

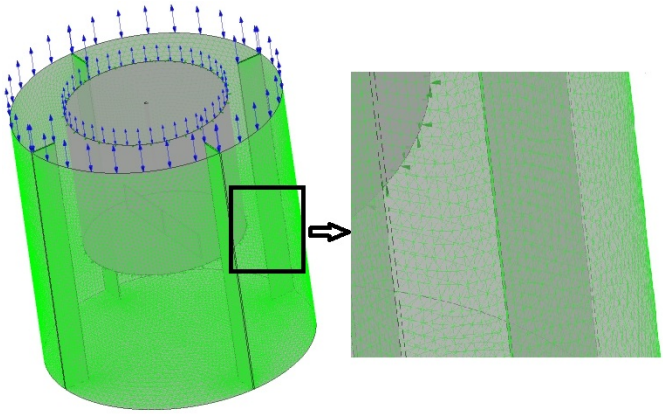

Figure 2: Computational mesh of the mixing domain.

The commercial computational fluid dynamics package Ansys-CFX was used to perform the calculations, solving the differential equations of conservation of mass and momentum (continuity and Navier-Stokes equations). The SIMPLE (semi-implicit method for pressure linked equations) algorithm was used for pressure-velocity coupling. The calculation results terminate when the residua in equations become less than 10^{-7}. No-slip boundary condition was employed around the walls of the impeller and the vessel. This condition provides the velocity gradient due to the effect of viscosity.

5 Results and discussion

Before presenting the new results we must verify the effectiveness of the method used in solving the considered problems. Therefore, we repeated the same experiment that was done by Youcefi *et al.* [32] and Ameur and Bouzit [8]. The first work is experimental, while the second work is numerical. Both works concentrate on a two-bladed impeller that rotates at a certain speed in a cylindrical vessel. The comparison of results between previous works and our results is shown in Fig. 3. The first graph shows the change of tangential velocity along the radius of the vessel. The graph shows a good agreement between the results. The second graph is for the variation of power number as a function of Reynolds number. Also, this graph shows a good agreement between the results.

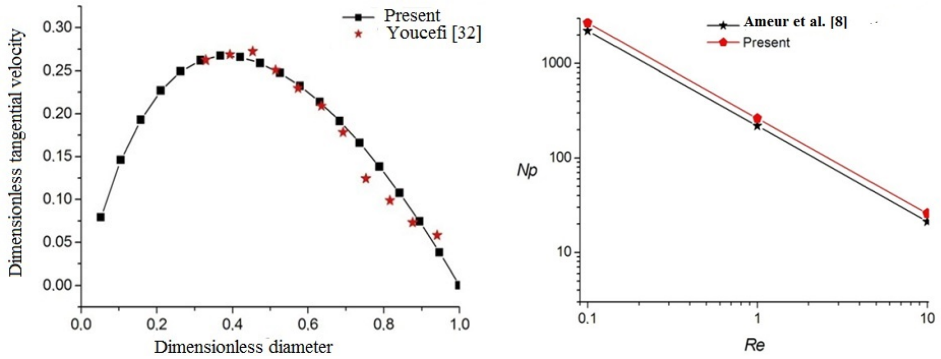

Figure 3: Validation test.

Figure 4 shows the effect of rotational speed and the number of blades on the fluid motion in the middle section of the vessel with respect to the direction z ($Z^* = z/D = 0.5$), for the vessel without baffles. Note that there are steady vortices near the walls of the container in the first case (two-bladed impeller), for Re = 50. But as the fluid speed increases, either by increasing the rotational speed or increasing the number of blades, this gradually dampens these vortices. This observation is similar to the one that was made in the previous work [2]. In other words, when the movement of the impeller is weak, vortices form near the impeller, while they disappear when the mixing speed increases. Furthermore, it is deduced from Fig. 4 that increasing the number of blades accelerates the movement of the fluid inside the vessel.

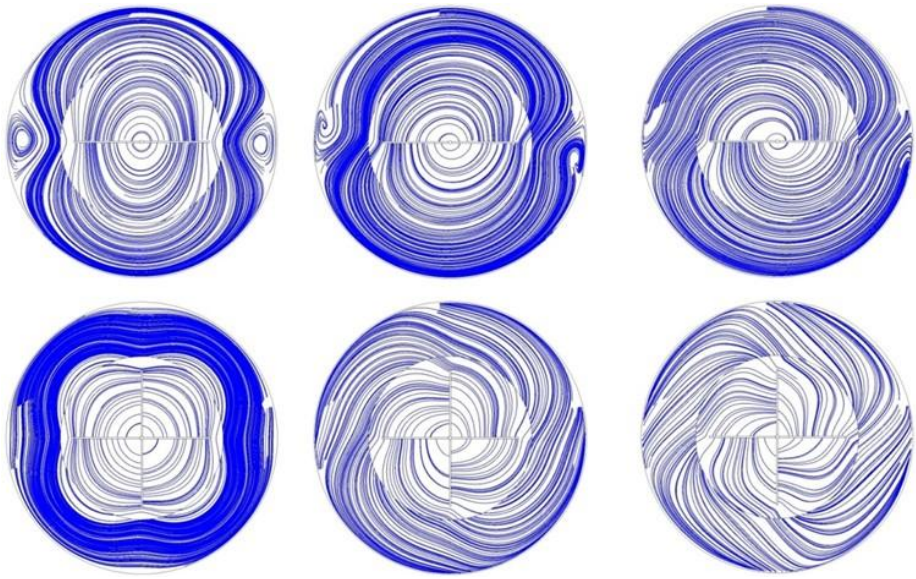

Re = 50 Re = 100 Re = 1000

Figure 4: Streamlines at $Z^* = 0.5$ and $l/D = 0$ for three values of Re; two-bladed impeller (top), four-bladed impeller (bottom).

Figure 5 presents the tangential velocity contours as a function of Reynolds number and the number of blades. Note that the greater the Reynolds num-

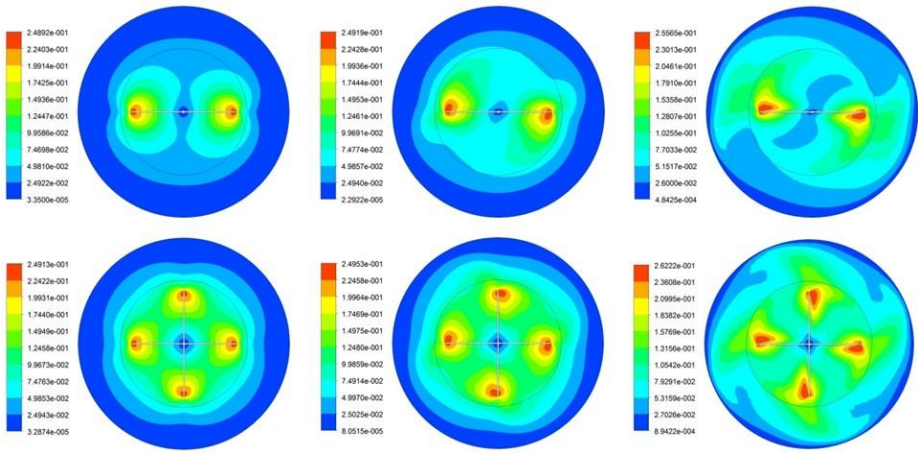

Re = 50 Re = 100 Re = 1000

Figure 5: Contours of tangential velocity at $Z^* = 0.5$ and $l/D = 0$ four three values of Re; two-bladed impeller (top), four-bladed impeller (bottom).

ber and/or the number of blades, the greater the fluid velocity expansion within the space, which gives the mixing efficiency.In addition to this, the uniform distribution of velocity indicates that the studied physical phenomenon has no evolution in terms of time. It is also noted that the fluid velocity is at its maximum value near the blades of the impeller and then gradually decreases towards the wall of the vessel. Figure 6 illustrates the linear distribution of the tangential velocity along the container radius. Values of the velocity and the location are written non-dimensionally. These values are taken at three locations in the direction Z^*, 0.25, 0.5 and 0.75, at a fixed value of Re = 50. It is noticed that the fluid speed increases closer to the impeller location. Also, the greater the number of blades, the higher the fluid velocity.

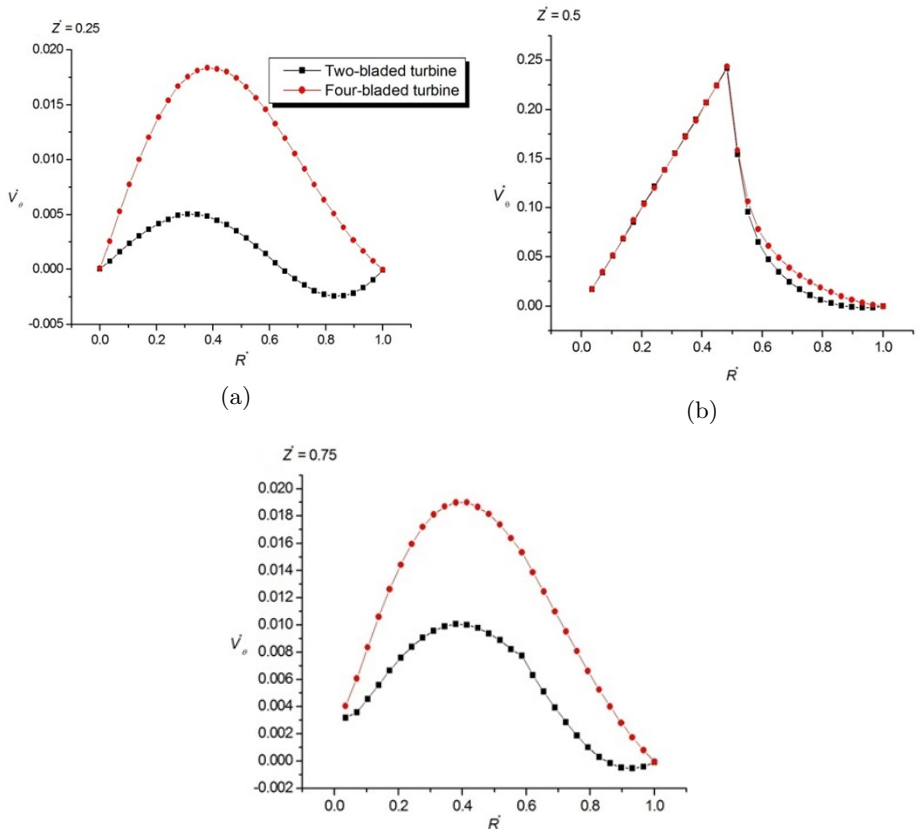

Figure 6: Dimesnionless tangential velocity (V_θ^*) along the diemensionless radius (R^*) of the vessel for Re = 50: (a) $Z^* = 0.25$, (b) $Z^* = 0.5$, (c) $Z^* = 0.75$.

Figure 7 shows the streamlines at the height $Z^* = 0.5$ of the vessel for three values of baffle length ratio (l/D) and for the rotational speed corresponding to Re = 100. The first row is for the case of a two-bladed impeller and the second row is for the case of a four-bladed impeller. It is clear that there is a formation of recirculation zones around the baffles. The size of these zones increases gradually with the increasing length of the baffles.

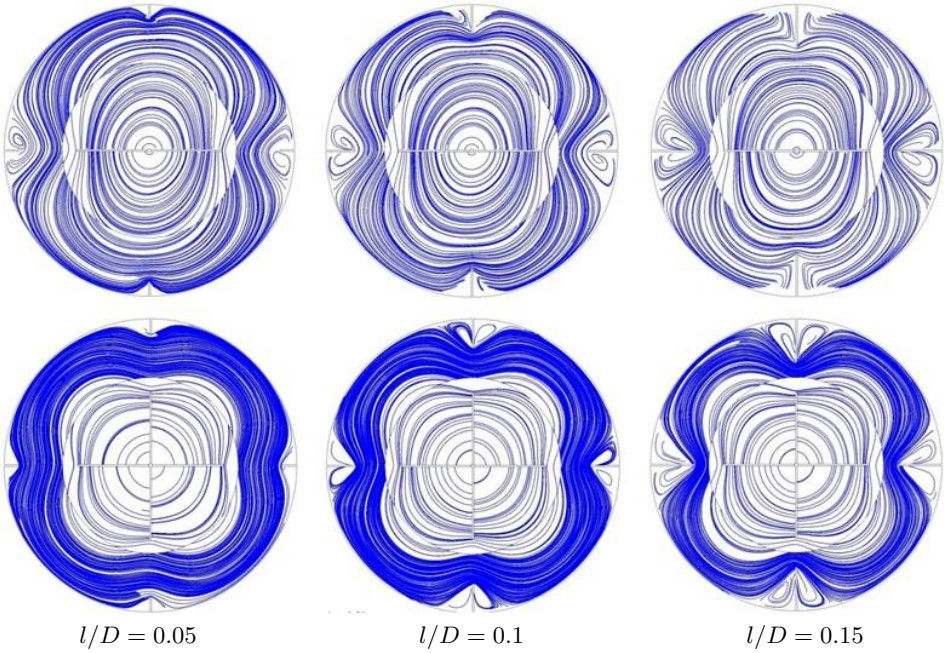

Figure 7: Streamlines at $Z^* = 0.5$ and Re = 100 for three values of the ratio l/D; two-bladed impeller (top), four-bladed impeller (bottom).

Figure 8 shows the tangential velocity contours at the same height ($Z^* = 0.5$) and under the same previous conditions. It is noted that the increase in the length of baffles reduces the flow velocity.

Figure 9 shows the distribution of tangential velocity along the radius of the vessel at the height of $Z^* = 0.25$ of the vessel for three baffle length ratios for the case of a two-bladed impeller and the case of a four-bladed impeller. The rotational speed of the impeller is constant in all cases and corresponds to the value of Reynolds number equal to 500. It is noticed that as the length of the baffles increases, the value of the flow velocity

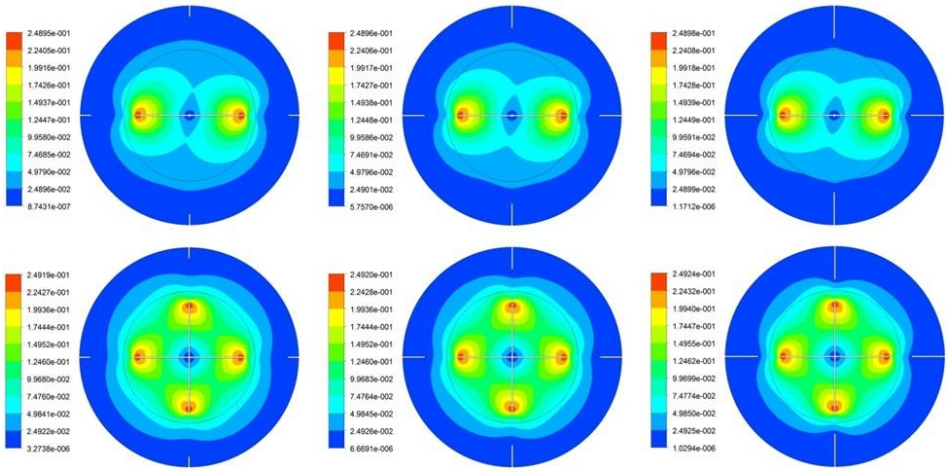

$l/D = 0.05$ $l/D = 0.1$ $l/D = 0.15$

Figure 8: Contours of tangential velocity at $Z^* = 0.5$ and $l/D = 0$ four three values of Re; two-bladed impeller (top), four-bladed impeller (bottom).

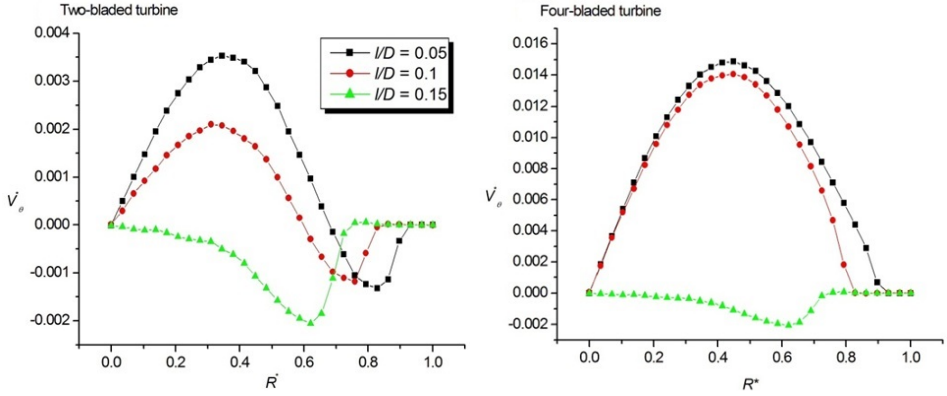

(a) (b)

Figure 9: Dimensionless tangential velocity (V_θ^*) along the dimensionless radius (R^*) of the vessel for $Z^* = 0.25$ and different ratios of l/D at Re = 500: (a) two-bladed impeller, (b) four-bladed impeller.

decreases. The baffle makes the value of the velocity zero next to it and this is very evident at the end of the graphs of the first and second case. It is also noticed that the presence of the baffle has the ability to change the pattern of fluid motion inside the container.

Figure 10 shows the variation of the power number versus Reynolds number and the baffle length ratio. The first graph (Fig. 10a) is for the case of a two-bladed agitator and the graph (Fig. 10b) is for the case of a four-bladed agitator. Before proceeding with analyses of the figure, we remember that the shear-thinning fluid in the one that the increased flow velocity decreases the viscosity of the fluid. Then, it is clear that the increase inthe number of blades increases the power number due to the increase of fluid friction. On the other hand, for the two cases considered, an increase in the value of Re decreases the value of power number due to the decrease of the fluid viscosity with the increasing flowvelocity. However, the effect of length of the baffles is clearly absent for both casesof two-bladed and four-bladed impellers. The power number decreases with Re, because with the increase of Re, the frictional force is reduced, and this is what reduces the total energy of the impeller.

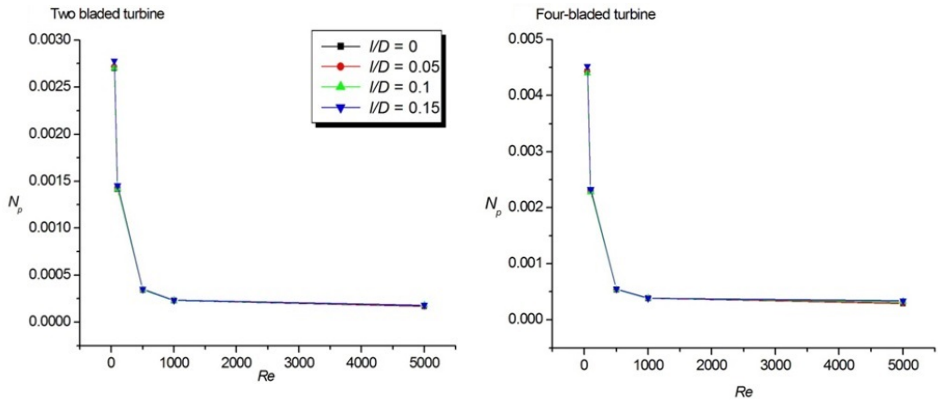

(a) (b)

Figure 10: Variation of power number versus Re and ratio l/D: (a) two-bladed impeller, (b) four-bladed impeller.

6 Conclusions

This work describes the results of numerical simulation of a complex fluid in a mechanical mixer. The work was carried out in order to understand the mixing process of this fluid. Some geometrical modifications were performed in order to know their effect on the mixing process. The points dealt with are: the rotational speed of the impeller, the number of blades and the length of the baffles added on the vessel wall. The effect of these parameters

on the flow velocity in the vessel and the consumed mechanical energy was investigated. After analyzing the results, the following facts were noted:

- Increasing the number of blades and/or the rotational speed of the impeller increases the flow velocity inside the vessel.
- The presence of the baffles on the vessel walls obstructs the flow motion, and this is what makes the speed of the flow decrease as the length of the baffles increases.
- The power number decreases as the rotational speed increases, while the length of the baffles has no effect on this number.
- The power number increases with the increasing number of blades.
- As for the fluid motion, it is more consistent with the higher rotational speed of the impeller.

Received 13 February 2023

References

[1] Hadjeb A., Bouzit M., KamlaY., Ameur H.: *A new geometrical model for mixing of highly viscous fluids by combiningtwo-blade and helical screw agitators*. Pol. J. Chem. Technol. **19**(2017), 3, 83–9l.

[2] Laidoudi H.: *Hydrodynamic analyses of the flow patterns in stirred vessel of two-bladed impeller*. J. Serb. Soc. Comput. Mech. **14**(2020), 2, 117–132.

[3] Ameur H.: *Agitation of yield stress fluids in different vessel shapes*. Eng. Sci. Technol. Int. J. **19**(2016), 1, 189–196.

[4] Galindo E., Nienow A.W.: *Mixing of highly viscoussimulated xanthan fermentation broths with the Lightnin A-315 impeller*. Biotechnol. Prog. **8**(1992), 3, 233–239.

[5] Galindo E., Nienow A.W.: *Performance of the Scaba 6SRGT agitator in mixing of simulated xanthan gumbroths*. Chem. Eng. Technol. **16**(1993), 2, 102–108.

[6] Amanullah A., Hjorth S.A., Nienow A.W.: *Cavern sizes generated in highly shear thinning viscous fluids by Scaba 3SHP1 impellers*. Food Bioprod. Process. **75**(1997), 4, 232–238.

[7] Pakzad L., Ein-Mozaffari F., Chan P.: *Using computational fluid dynamics modeling to study the mixing of pseudoplastic fluids with a Scaba 6SRGT impeller*. Chem. Eng. Process. **47**(2008), 12, 2218–2227.

[8] Ameur H., Bouzit M.: *Power consumption for stirring shear thinning fluids by two-blade impeller*. Energy **50**(2013), 326–332.

[9] Ameur H., Bouzit M., Ghenaim A.: *Numerical studyof the performance of multistage Scaba 6SRGT impellersfor the agitation of yield stress fluids in cylindrical tanks.* J. Hydrodyn. **27**(2015), 3, 436–442.

[10] Patel D., Ein-Mozaffari F., Mehrvar M.: *Improvingthe dynamic performance of continuous-flow mixing ofpseudoplastic fluids possessing yield stress using Maxblend impeller.* Chem. Eng. Res. Des. **90**(2012), 4, 514–523.

[11] Kazemzadeh A., Ein-Mozaffari F., Lohi A.: *Investigation of hydrodynamic performances of coaxial mixersin agitation of yield-pseudoplasitc fluids: single and double-central impellers in combination with the anchor.* Chem. Eng. J. **294**(2016), 417–430.

[12] Kazemzadeh A., Ein-Mozaffari F., Lohi A.: *Effect of the rheological properties on the mixing of Herschel-Bulkley fluids with coaxial mixers: applications of tomography, CFD, and response surface methodology.* Can. J. Chem. Eng. **94**(2016), 12, 2394–2406.

[13] Ammar M., Abid M.S.: *Numerical investigation of turbulent flow generated in baffled stirred vessels equipped with three different turbines in one and two-stage system.* Energy **36**(2011), 8, 5081–5093.

[14] Vilard G., Verdone N.: *Production of metallic iron nanoparticles in a baffled stirred tank reactor: Optimization via computational fluid dynamics simulation.* Particuology **52**(2020), 83–96.

[15] Laidoudi H., Ameur H.: *Complex fluid flow in annular space under the effects of mixed convection and rotating wall of the outer enclosure.* Heat Transfer **51**(2022), 5, 3741–3767.

[16] Tacay C.D., Payunescu M.: *Suspension of solid particles in spherical stirred vessels.* Chem. Eng. Sci. **55**(2000), 15, 2989–2993.

[17] Vakili M.H., Esfahany M.N.: *CFD analysis of turbulence in a baffled stirred tank, a three-compartment model.* Che. Eng. Sci. **64**(2009), 2, 351–362.

[18] Foukrach M., Bouzit M., Ameur M., Kamla Y.: *Influence of the vessel shape on the performance of a mechanically agitated system.* Chem. Pap. **73**(2019), 469–480.

[19] Laidoudi H., Ameur H.: *Investigation of the mixed convection of power-law fluids between two horizontal concentric cylinders: Effect of various operating conditions.* Therm. Sci. Eng. Prog. **20**(2020), 100731.

[20] Ameur H.: *Mixing of shear thinning fluids in cylindrical tanks: Effect of the impeller blade designand operating conditions.* Int. J. Chem. React. Eng. **14**(2016), 1025–1033.

[21] Ghotli R.A., Abdul Aziz A.R., Ibrahim S., Baroutian S., Niya A.A.: *Study of various curved-blade impeller geometrieson power consumption in stirred vessel using response surface methodology.* J. Taiwan Inst. Chem. Eng. **44**(2013), 2, 192–201.

[22] Khapre A., Munshi B.: *Numerical investigation of hydrodynamic behavior of shear thinning fluids in stirred tank.* J. Taiwan Inst. Chem. Eng. **56** (2015), 16–27.

[23] Luan D., Chen Q., Zhou S.: *Numerical simulation and analysis of power consumption and Metzner-Otto constant for impeller of 6PBT.* Chin. J. Mech. Eng. **27**(2014) 635–640.

[24] Sossa-Echeverria J., Taghipour F.: *Computational simulation of mixing flow of shear thinning non-Newtonianfluids with various impellers in a stirred tank*. Chem. Eng. Proc. **93**(2015), 66–78.

[25] Woziwodzki S., Broniarz-Press L., Ochowiak M.: *Transitional mixing of shear-thinning fluids in vessels with multiple impellers*. Chem. Eng. Techn. **33**(2010), 7, 1099–1106.

[26] Zhao J., Gao Z., Bao Y.: *Effects of the blade shape on the trailing vortices in liquid flow*. Chin. J. Chem. Eng. **19**(2011), 2, 232–242.

[27] Khopkar A.R., Mavros P., Ranade V.V., Bertrand J.: *Simulation of flow generated by an axial-flow impeller: batch and continuousoperation*. Chem. Eng. Res. Des. **82**(2004), 6, 737–751.

[28] Konfršt B., Konfršt J., Fořt I., Kotek M., Chára Z. *Study of the turbulent flow structure around astandard Rushton impeller*. Chem. Process. Eng. **35**(2014), 1, 137–147.

[29] Hartmann H., Derksen J.J., Montavon C., Pearson J., Hamill I.S.: *Assessment of large eddy and RANS stirredsimulations by means of LDA*. Chem. Eng. Sci. **59**(2004), 2419–2432.

[30] Devarajulu C., Loganathan M.: *Effect of impeller clearance and liquid level on critical impeller speed in an agitated vesselusing different axial and radial impellers*. J. Appl. Mech. **9**(2016), 6, 2753–2761.

[31] Venneker B., Derksen J., Vanden Akker H.E.A.: *Turbulent flow of shear-thinning liquids in stirred tanks – The effects of Reynolds number and flow index*. Chem. Eng. Res. Des. **88**(2010), 7, 827–43.

[32] Youcefi A.: *Etude expérimentale de l'écoulement de fluide viscoélastique autour d'un agitateur bipale dans une cuve agitée*. (*Experimental study of viscoelastic fluid flow around two-blade impeller in a stirred vessel*). PhD thesis, Ecole Nationale Polytechnique, Toulouse 1993 (in French).

[33] Ahmed S., Mansour M., Hussein A.K., Sivasankaran S.: *Mixed convection from a discrete heat source in enclosures with two adjacent moving walls and filled with micropolar nanofluids*. Eng. Sci. Tech. Int. J. **19**(2016), 1, 364–376.

[34] Laidoudi H., Helmaoui M.: *Enhancement of natural convection heat transfer in concentric annular space using inclined elliptical cylinder*. J. Naval Archit. Mar. Eng. **17**(2020), 2, 89–99.

[35] Al-Rashed A., Aich W., Kolsi L., Mahian O., Hussein A.K., Borjini M.: *Effects of movable-baffle on heat transfer and entropy generation in a cavity saturated by CNT suspensions: Three-dimensional modeling*. Entropy **19**(2017), 5, 200–216.

[36] Laidoudi H., Bouzit M.: *The effect of asymmetrically confined circular cylinder and opposing buoyancy on fluid flow and heat transfer*. Defect Diffus. Forum **374**(2017), 18–28.

[37] Hussein A.K., Rout S., Fathinia F., Chand R., Mohammed H.: *Natural convection in a triangular top wall enclosure with a solid strip*. J. Eng. Sci. Tech. **10**(2015), 10, 1326–1341.

[38] Acharya N.: *Buoyancy driven magnetohydrodynamic hybrid nanofluid flow within a circular enclosure fitted with fins.* Int. Commun. Heat Mass Transf. **133**(2022), 105980.

[39] Li Z., Hussein A.K., Younis O., Afrand M., Feng S.: *Natural convection and entropy generation of a nanofluid around a circular baffle inside an inclined square cavity under thermal radiation and magnetic field effects.* Int. Commun. Heat Mass Transf. **116**(2020), 104650.

[40] Acharya N., Maity S., Kundu P.K.: *Differential transformed approach of unsteady chemically reactive nanofluid flow over a bidirectional stretched surface in presence of magnetic field.* Heat Transf. **49**(2020), 6, 3917–3942.

[41] Hassouni S., Laidoudi H., Makined O.D., Bouzit M., Haddou B.: *A qualitative study of mixing a fluid inside a mechanical mixer with the effect of thermal buoyancy.* Arch. Thermodyn. **44**(2023), 1, 105–119.

[42] Bulat P.V., Volkov K. N.: *Fluid/solid coupled heat transfer analysis of a free rotating disc.* Arch. Thermodyn. **39**(2018), 3, 169–192.

[43] Bouakkaz R., Ouali A.E., Khelili Y., Faouzi S., Tiauiria I.: *Unconfined laminar nanofluid flow and heat transfer around a rotating circular cylinder dissipating uniform heat flux in the steady regime.* Arch. Thermodyn. **40**(2019), 4, 3–20.

[44] Bouakkaz R., Salhi F., Khelili Y., Quazzazi M., Talbi K.: *Unconfined laminar nanofluid flow and heat transfer around a rotating circular cylinder in the steady regime.* Arch. Thermodyn. **38**(2017), 2, 3–20.

[45] Ramla M., Laidoudi H., Bouzit M.: *Behaviour of a non-newtonian fluid in a helical tube under the influence of thermal buoyancy.* Acta Mech. Autom. **16**(2022), 2, 111–118.

[46] Mokeddem M., Laidoudi H., Makinde O.D., Bouzit M.: *3D simulation of incompressible poiseuille flow through 180 curved duct of square cross-section under effect of thermal buoyancy.* Period. Polytech. Mech. Eng. **63**(2019), 4, 257–269

[47] Mokeddem M., Laidoudi H., Bouzit M.: *3D simulation of Dean vortices at 30 position of 180 curved duct of square cross-section under opposing buoyancy.* Defect Diffus. Forum **389**(2018), 153–163.

archives
of thermodynamics
Vol. **44**(2023), No. 2, 87–114
DOI: 10.24425/ather.2023.146560

Mixed convection heat transfer of a nanofluid in a square ventilated cavity separated horizontally by a porous layer and discrete heat source

HAMDI MESSAOUD[a]*
SAHI ADEL[a]
OURRAD OUERDIA[b]

[a] Université de Bejaia, Laboratoire de Physique Théorique, Faculté de Technologie, Algeria

[b] Université de Bejaia, Laboratoire de Physique Théorique, Faculté des Sciences Exactes, Algeria

Abstract Laminar mixed convection heat transfer in a vented square cavity separated by a porous layer filled with different nanofluids (Fe_3O_4, Cu, Ag and Al_2O_3) has been investigated numerically. The governing equations of mixed convection flow for a Newtonian nanofluid are assumed to be two-dimensional, steady and laminar. These equations are solved numerically by using the finite volume technique. The effects of significant parameters such as the Reynolds number ($10 \leq \mathrm{Re} \leq 1000$), Grashof number ($10^3 \leq \mathrm{Gr} \leq 10^6$), nanoparticle volume fraction ($0.1 \leq \phi \leq 0.6$), porous layer thickness ($0 \leq \gamma \leq 1$) and porous layer position ($0.1 \leq \delta \leq 0.9$) are studied. Numerical simulation details are visualized in terms of streamline, isotherm contours, and average Nusselt number along the heated source. It has been shown that variations in Reynolds and Darcy numbers have an impact on the flow pattern and heat transfer within a cavity. For higher Reynolds ($\mathrm{Re} > 100$), Grashof ($\mathrm{Gr} > 10^5$) numbers and nanoparticles volume fractions the heat transfer rate is enhanced and it is optimal at lower values of Darcy number ($\mathrm{Da} = 10^{-5}$). In addition, it is noticed that the porous layer thickness and location have a significant effect on the control of the heat transfer rate inside the cavity. Furthermore, it is worth noticing that Ag nanoparticles presented the largest heated transfer rate compared to other nanoparticles.

Keywords: Mixed convection; Vented cavity; Porous layer; Finite volume method

*Corresponding Author. Email: messaoud.hamdi@univ-bejaia.dz

Nomenclature

a	–	thickness of porous layer, m
b	–	position of porous layer, m
C_p	–	heat capacity, J/kg K
Da	–	Darcy number
F	–	the inertia coefficient
h	–	length of heated source, m
g	–	gravitational acceleration, m/s^2
Gr	–	Grashof number
K	–	permeability of porous layer
L	–	cavity length and height, m
Nu	–	Nusselt number
P	–	dimensionless pressure
Pr	–	Prandtl number
Ra	–	Rayleigh number
Re	–	Reynolds number
T	–	temperature, K
U, V	–	dimensionless velocity components
u, v	–	velocity components in x, y directions, m/s
w	–	size of inlet and outlet port
X, Y	–	dimensionless coordinates
x, y	–	Cartesians coordinates, m

Greek symbols

α	–	thermal diffusivity, m^2/s
β	–	thermal expansion coefficient at constant pressure, 1/K
δ	–	dimensionless position of porous layer
γ	–	dimensionless thickness of porous layer
ε	–	porosity of porous layer
λ	–	thermal conductivity, W/m K
μ	–	dynamic viscosity, Pa s
ρ	–	density of fluid, kg/m^3
ϕ	–	nanoparticles volume fraction
θ	–	dimensionless temperature

Subscripts and superscripts

eff	–	effective
f	–	fluid
h, c	–	hot and cold temperature
i, j	–	x–y components
nf	–	nanofluid
p	–	porous medium
s	–	solid

1 Introduction

The study of mixed convection in an open or vented cavity induced by combined effects of mechanical inflow and buoyancy force has so far been a fundamental research area and requires comprehensive analysis to understand the physics of resulting flow and heat transfer. This is frequently encountered in engineering applications such as cooling of electronic and microelectronic equipment, heating and air conditioning, solar energy collection, nuclear reactors and heat exchangers [1–7].

The vented cavity is one of the most studied geometries in heat transfer, due to its application in electronic equipment cooling. Different configurations have been studied. Mehrizi *et al.* [8] used the lattice Boltzmann method (LBM) to investigate the effect of nanoparticles suspension on the mixed convection in a square cavity with inlet and outlet ports and a hot obstacle in the vented cavity. It was found that the heat transfer rate enhanced with the increasing nanoparticles volume concentration. Ismael and Jasim [9] investigated fluid-structure interaction in mixed convection inside a vented cavity having two inlet and outlet openings. They reported that a flexible fin enhances the Nusselt number better than a rigid fin. Benzema *et al.* [10] used the thermodynamic second law to study magnetohydrodynamic (MHD) mixed convection heat transfer in a vented irregular cavity filled with a hybrid nanofluid. Their results showed that adding nanoparticles to water improves heat transfer but increases total entropy generation. Selimefendigil and Oztop [11] examined magnetohydrodynamics forced convection in a layered U-shaped vented cavity with a porous layer under the wall corrugation impact. It was found that the flow field and heat transfer are impacted by the Reynolds number, Hartmann number and Darcy number. Ataei-Dadavi *et al.* [12] conducted an experimental study of mixed convection in a vented, differentially side-heated cubical cavity filled with a porous medium. The results showed that there are three different flow and heat transfer regimes depending on the Richardson number. Dhahad *et al.* [13] studied numerically mixed convection in a vertically vented cavity using the spectral element method. Moayedi [14] investigated the heat transfer of Cu-water nanofluid in laminar convection around double rotating cylinders in a vented cavity with different inlet and outlet ports. They reported that the mean Nusselt number increases with the nanofluid volume fraction and rotational Reynolds number. Velkennedy *et al.* [15] have studied convective flow in a ventilated cavity having two outlets and one inlet with cold partitions using the finite difference method. They showed that

the presence of cold partitions modifies the flow structure inside a ventilated cavity. Recently, Jamshed *et al.* [16] conducted a numerical analysis of MHD mixed convection in a ventilated porous cavity with a heated elliptic inner cylinder filled with nanofluid. They demonstrated that the average Nusselt number increases when the Richardson number and porosity ratio increase.

Currently, mixed convection in nanofluids has been the subject of several theoretical, experimental and especially numerical studies. Among them; Benos and Sarris [17] presented an analytical study of MHD natural convection of nanofluid in a shallow cavity. Arani *et al.* [18] have used the finite volume method to solve numerically the natural convection in a square cavity with a heated horizontal plate containing a nanofluid. Results showed that the mean Nusselt number increases with the increasing nanoparticles volume fraction and decreases as the heated plate location varies from the top to bottom of the cavity. Selimefendigil and Öztop [19] studied mixed convection in a lid-driven cavity filled with ferrofluid in the presence of two rotating cylinders. They observed that flow patterns and thermal transport are affected by the Reynolds number and magnetic dipole strength variations. Rabbi *et al.* [20] studied MHD mixed convection in a ferrofluid filled lid-driven cavity for different heater configurations. They observed that the higher Richardson number enhances the heat transfer rate, although the higher Hartmann number decreases the heat transfer rate. Elshehabey *et al.* [21] investigated numerically natural convection with a nonlinear Boussinesq approximation in an inclined and partially open cavity. Jakeer *et al.* [22] studied magneto-hybrid nanofluid flow in a lid-driven porous cavity with an inside heated square obstacle. Recently, Wang and Xu [23] investigated mixed convection in an inclined lid-driven cavity filled with a hybrid nanofluid. They indicated that hybrid nanofluid is superior to traditional heat transfer fluids for heat transfer enhancement. Jayaprakash *et al.* [24] suggested a mathematical model to illustrate the flow and radiative heat transfer of a hybrid nanofluid over a curved stretching sheet. Their results showed that the heat transfer enhanced with the increasing radiation parameter and Biot number. Dutta *et al.* [25] performed a study of mixed convection in a ventilated cavity filled with viscoplastic hybrid nanofluid and with a mounted heated solid obstacle. It is observed from their analysis that the heat transfer rate enhanced with the inclusion of Cu nanoparticles in Al_2O_3-viscoplastic fluid.

Convection heat transfer within an enclosure filled with a porous medium has become important owing to its benefits in diversified applications in various areas. Numerous studies have explored the phenomenon. Neild and

Bejan [26] presented a board literature review about convection in porous media. Balla *et al.* [27] investigated the flow and heat transfer of the MHD boundary layer in a nanofluid-filled inclined porous square cavity. Their results are obtained for different values of the Rayleigh number, inclination angle, magnetic field and nanofluid volume fraction. The effect of MHD convection of nanofluid in a porous enclosure with sinusoidal heating was investigated by Malik and Nayak [28]. They found that the heat transfer rate and entropy generation depend on the Grashof, Hartmann and Darcy numbers. Sheremet *et al.* [29] studied mixed convection in a square porous cavity filled with a water-based nanofluid under suction/injection zones effects. It has been found that an increase in Rayleigh and Darcy numbers leads to flow acceleration near the heated wall. Abu-Hamdeh *et al.* [30] investigated the impact of various parameters in a lid-driven cavity filled with porous media having a one-side opening in the presence of heat generation. They found that the heat transfer rate rises and decreases as the heater length and Grashof number increase, respectively. Maboud *et al.* [31] considered the unsteady MHD incompressible Casson fluid flow in porous media. Kumar *et al.* [32] examined the non-Newtonian hybrid nanofluid flow through a porous moving rotating disk. Kashyap and Dass [33] investigated numerically the influence of inclination of the cavity on mixed convection in a double-sided lid-driven cavity with a hot porous square blockage. The results reveal that the inclination significantly impacts the heat transfer rate and entropy production. Alsedais *et al.* [34] examined the influence of radiation and heat generation on MHD mixed convection of a nanofluid in an inclined undulating porous cavity containing an obstacle. Choudhary and Ray [35] worked on a porous-corrugated enclosure containing a discrete heat source. They found that different parameters (Rayleigh, Darcy and Hartmann numbers) have a significant effect on flow behaviour. Nammi *et al.* [36] have explored numerically unsteady natural convection heat transfer within a square-shaped porous cavity with four heated cylinders. Recently, Kumar *et al.* [37] used original mathematical models to evaluate convective flow dynamics of viscous dissipative heat and mass transfer in a doubly stratified fluid saturated porous enclosure.

Convection heat transfer with a superposed fluid and porous layers confined in an enclosure (partly layered enclosure) have been studied early because of their great mathematical and practical interest, such as in fuel cells, solidification, and many other systems [38–41]. Aly *et al.* [42] studied the effects of wavy nanofluid/porous interface on mixed convection and entropy generations of Cu-water nanofluid. Under the influence of a uniform

inclined magnetic field, Astanina *et al.* [43] explored natural convection in an open trapezoidal cavity including a porous layer and a ferrofluid layer. Their result showed that growth of the porous layer height leads to a reduction of the heat transfer rate. Selimefendigil and Öztop [44] studied the curved porous layer impact on forced convection heat transfer and entropy generation in a vented cavity filled with hybrid nanofluid under inclined magnetic field effects by using the finite volume method. Gibanov *et al.* [45] examined MHD mixed convection in a lid-driven cavity partially filled with a porous medium saturated with a ferrofluid. It is found that the magnetic field inclination angle and porous layer height influence greatly the heat transfer enhancement and fluid flow intensification. Al-Srayyih *et al.* [46] investigated natural convection inside a superposed enclosure filled with composite porous-hybrid nanofluid layers. They observed that the heat transfer rate in a hybrid nanofluid is higher than within pure fluid. Al-Zamily [47] carried out a numerical analysis of natural convection and entropy generation in a cavity filled with multi-layers of porous medium and nanofluid with heat generation. They showed that the Nusselt number depends on the heat source position. Moria [48] studied improvements of porous layers in natural convection of an L-shape enclosure, with different parameters considered. Recently, Alsabery *et al.* [49] provided a numerical investigation of two-phase flow and heat transfer for hybrid nanofluid in a wavy enclosure partially filled with a porous medium. They indicated that hybrid nanofluid is better for heat transfer enhancement compared to simple nanofluid. It's worthy of note that there are other interesting papers on this subject with various other applications [50–53].

Motivated by the above-mentioned research, the present study focuses on numerical simulations of mixed convection in a ventilated square cavity filled with different nanofluids containing a horizontal porous layer with a heated source. It should be noted that this investigation is driven by the need to understand the heat transfer mechanisms in heat exchangers by analyzing the performance of the insertion of a porous layer associated with the addition of nanoparticles to the base fluid.

2 Mathematical formulation

We consider steady laminar, two-dimensional, mixed convection inside a vented square cavity filled with nanofluid having a horizontal porous layer with thickness a ($\gamma = a/L$) and position b ($\delta = b/L$). A schematic of

the problem under investigation and the coordinate system are shown in Fig. 1.

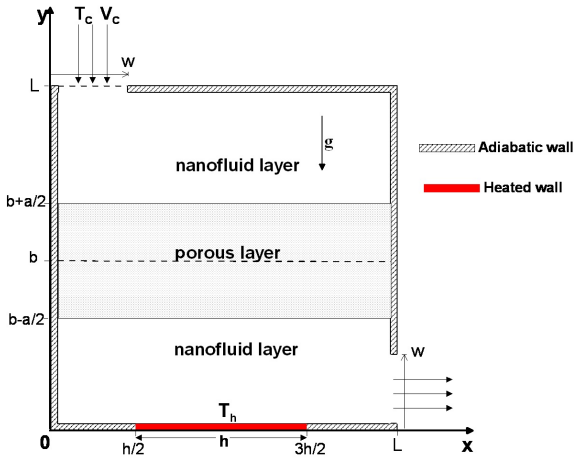

Figure 1: Schematic description of the physical system.

The cavity side length and height are denoted by L. The inflow opening is located on the left of the upper wall and the outflow opening of the cavity is fixed at the right wall bottom. The inlet port size is the same as that of the outlet port, which is equal to $w = 0.2L$. It is assumed that incoming flow is at a constant velocity (V_c) and low temperature (T_c). A heat source is located at the middle of the bottom wall with a higher temperature T_h and at a length denoted by $h = 0.5L$, and all other walls are thermally insulated. Basic fluid (water) and different spherical nanoparticles are in thermal equilibrium and their properties are presented in Table 1.

Table 1: Physical properties of the based fluid and nanoparticles [45, 49]

Physical property	Units	Base fluid (water)	Fe_3O_4	Cu	Ag	Al_2O_3
C_p	J/kg K	4179	670	385	235	765
ρ	kg/m^3	997.1	5200	8933	10500	3970
λ	W/m K	0.613	6	401	429	40
$\beta \times 10^{-5}$	K^{-1}	21.0	1.3	1.67	1.89	0.85
μ	Pa s	0.001003	–	–	–	–

The Forchheimer–Brinkman-extended Darcy model and Boussinesq approximation are applicable. The domain boundaries are impermeable, while

the interface between clear fluid and porous medium is permeable. The porous medium is saturated with a nanofluid that is in local thermodynamic equilibrium with the solid matrix and is assumed to be homogeneous and isotropic. Nanofluid thermophysical properties are constant, except for the density variation, which is determined based on the Boussinesq approximation. Governing conservation equations for laminar and steady Newtonian fluid flow with consideration of the above-mentioned assumptions can be written in the following form:

For the nanofluid layer:

Continuity

$$\frac{\partial u}{\partial x}+\frac{\partial v}{\partial y}=0\,. \tag{1}$$

Momentum

$$v\frac{\partial u}{\partial y}=-\frac{1}{\rho_{nf}}\frac{\partial p}{\partial x}+\frac{\mu_{nf}}{\rho_{nf}}\left(\frac{\partial^2 u}{\partial x^2}+\frac{\partial^2 u}{\partial y^2}\right), \tag{2}$$

$$v\frac{\partial u}{\partial y}=-\frac{1}{\rho_{nf}}\frac{\partial p}{\partial x}+\frac{\mu_{nf}}{\rho_{nf}}\left(\frac{\partial^2 u}{\partial x^2}+\frac{\partial^2 u}{\partial y^2}\right). \tag{3}$$

Energy

$$u\frac{\partial T}{\partial x}+v\frac{\partial T}{\partial y}=\alpha_{nf}\left(\frac{\partial^2 T}{\partial x^2}+\frac{\partial^2 T}{\partial y^2}\right). \tag{4}$$

For the porous layer:

Continuity

$$\frac{\partial u}{\partial x}+\frac{\partial v}{\partial y}=0\,. \tag{5}$$

Momentum

$$\begin{aligned} u\frac{\partial u}{\partial x}+v\frac{\partial u}{\partial y}=&-\frac{\varepsilon^2}{\rho_{nf}}\frac{\partial p}{\partial x}+\frac{\varepsilon\mu_{nf}}{\rho_{nf}}\left(\frac{\partial^2 u}{\partial x^2}+\frac{\partial^2 u}{\partial y^2}\right)\\ &-\frac{\mu_{nf}\varepsilon^2}{\rho_{nf}K}u+\frac{F\varepsilon^2}{\sqrt{K}}u\sqrt{u^2+v^2}\,, \end{aligned} \tag{6}$$

$$\begin{aligned} u\frac{\partial v}{\partial x}+v\frac{\partial v}{\partial y}=&-\frac{\varepsilon^2}{\rho_{nf}}\frac{\partial p}{\partial y}+\frac{\varepsilon\mu_{nf}}{\rho_{nf}}\left(\frac{\partial^2 v}{\partial x^2}+\frac{\partial^2 v}{\partial y^2}\right)\\ &-\frac{\mu_{nf}\varepsilon^2}{\rho_{nf}K}v+\frac{F\varepsilon^2}{\sqrt{K}}v\sqrt{u^2+v^2}+\frac{\varepsilon^2(\rho\beta)_{nf}}{\rho_{nf}}g\,(T-T_C)\,. \end{aligned} \tag{7}$$

Energy

$$u\frac{\partial T}{\partial x}+v\frac{\partial T}{\partial y}=\alpha_{\text{eff}}\left(\frac{\partial^2 T}{\partial x^2}+\frac{\partial^2 T}{\partial y^2}\right), \tag{8}$$

where ε is the porosity and K is the porous medium permeability, F is the inertia coefficient, α_{eff} is the effective thermal diffusivity of the porous medium. The inertia coefficient can be expressed mathematically by

$$F=\frac{1.75}{\sqrt{150\varepsilon^3}}, \tag{9}$$

while the effective thermal diffusivity of the porous layer is given by

$$\alpha_{\text{eff}}=\frac{\lambda_{\text{eff}}}{\rho C_P}. \tag{10}$$

The effective thermal conductivity of the porous layer is given by

$$\lambda_{\text{eff}}=\varepsilon\lambda_{nf}+(1-\varepsilon)\lambda_s, \tag{11}$$

where λ_s represents the porous medium thermal conductivity and λ_{nf} indicates the nanofluid thermal conductivity.

Effective physical properties of the nanofluid were applied in the form [39,45]:

- nanofluid density

$$\rho_{nf}=(1-\phi)\rho_f+\phi\rho_p, \tag{12}$$

- nanofluid buoyancy coefficient

$$(\rho\beta)_{nf}=(1-\phi)(\rho\beta)_f+\phi(\rho\beta)_p, \tag{13}$$

- nanofluid heat capacitance

$$(\rho C_p)_{nf}=(1-\phi)(\rho C_P)_f+\phi(\rho C_P)_S, \tag{14}$$

- nanofluid thermal conductivity

$$\frac{\lambda_{nf}}{\lambda_f}=\frac{\lambda_p+2\lambda_f-2\phi\,(\lambda_f-\lambda_p)}{\lambda_p+2\lambda_f+\phi\,(\lambda_f-\lambda_p)}, \tag{15}$$

- thermal diffusivity

$$\alpha_{nf}=\frac{\lambda_{nf}}{(\rho C_P)_{nf}}, \tag{16}$$

- nanofluid viscosity (Brinkman [54])

$$\mu_{nf} = \frac{\mu_f}{(1-\phi)^{2.5}}\,. \tag{17}$$

The above equations were written in a non-dimensional form using the following variables:

$$\begin{aligned} X &= \frac{x}{L}\,, \quad Y = \frac{y}{L}\,, & U &= \frac{u}{V_c}\,, \\ V &= \frac{v}{V_c}\,, \quad \theta = \frac{T-T_c}{T_h-T_c}\,, & P &= \frac{p}{\rho V_c^2}\,. \end{aligned} \tag{18}$$

For the nanofluid layer:

$$\frac{\partial U}{\partial X} + \frac{\partial V}{\partial Y} = 0, \tag{19}$$

$$U\frac{\partial U}{\partial X} + V\frac{\partial U}{\partial Y} = -\frac{\partial P}{\partial X} + \frac{1}{\mathrm{Re}}\frac{\mu_{nf}\rho_f}{\mu_f\rho_{nf}}\left(\frac{\partial^2 U}{\partial X^2} + \frac{\partial^2 U}{\partial Y^2}\right), \tag{20}$$

$$\begin{aligned} U\frac{\partial V}{\partial X} + V\frac{\partial V}{\partial Y} = &-\frac{\partial P}{\partial Y} \\ &+ \frac{1}{\mathrm{Re}}\frac{\mu_{nf}\rho_f}{\mu_f\rho_{nf}}\left(\frac{\partial^2 V}{\partial X^2} + \frac{\partial^2 V}{\partial Y^2}\right)\frac{\rho_{nf}\beta_{nf}}{\rho_{nf}\beta_f}\frac{\mathrm{Gr}}{\mathrm{Re}^2}\theta, \end{aligned} \tag{21}$$

$$U\frac{\partial \theta}{\partial X} + V\frac{\partial \theta}{\partial Y} = \frac{\alpha_{nf}}{\alpha_f}\frac{1}{\mathrm{Re}\,\mathrm{Pr}}\left(\frac{\partial^2 \theta}{\partial X^2} + \frac{\partial^2 \theta}{\partial Y^2}\right). \tag{22}$$

For the porous layer:

$$\frac{\partial U}{\partial X} + \frac{\partial V}{\partial Y} = 0, \tag{23}$$

$$\begin{aligned} U\frac{\partial U}{\partial X} + V\frac{\partial U}{\partial Y} = &-\varepsilon^2\frac{\partial P}{\partial X} + \frac{\varepsilon}{\mathrm{Re}}\frac{\mu_{nf}\rho_f}{\mu_{nf}\rho_{nf}}\left(\frac{\partial^2 U}{\partial X^2} + \frac{\partial^2 U}{\partial Y^2}\right) \\ &- \frac{\varepsilon^2}{\mathrm{ReDa}}\frac{\rho_f}{\rho_{nf}}\frac{\mu_{nf}}{\mu_f}U + \frac{F\varepsilon^2}{\sqrt{\mathrm{Da}}}U\sqrt{U^2+V^2}\,, \end{aligned} \tag{24}$$

$$\begin{aligned} U\frac{\partial V}{\partial X} + V\frac{\partial V}{\partial Y} = &-\varepsilon^2\frac{\partial P}{\partial Y} + \frac{\varepsilon}{\mathrm{Re}}\frac{\mu_{nf}\rho_f}{\mu_f\rho_{nf}}\left(\frac{\partial^2 V}{\partial X^2} + \frac{\partial^2 V}{\partial Y^2}\right) \\ &- \frac{\varepsilon^2}{\mathrm{ReDa}}\frac{\rho_f}{\rho_{nf}}\frac{\mu_{nf}}{\mu_f}V + \frac{F\varepsilon^2}{\mathrm{Re}\sqrt{\mathrm{Da}}}V\sqrt{U^2+V^2}\,, \end{aligned} \tag{25}$$

$$U\frac{\partial \theta}{\partial X} + V\frac{\partial \theta}{\partial Y} = \frac{a_{\mathrm{eff}}}{a_f}\frac{1}{\mathrm{Re}\,\mathrm{Pr}}\left(\frac{\partial^2 \theta}{\partial X^2} + \frac{\partial^2 \theta}{\partial Y^2}\right). \tag{26}$$

Dimensionless boundary conditions are expressed as follows:

- at the inlet port:

$$U = 0, \quad V = 1, \quad \theta = 0; \tag{27}$$

- at the outlet port:

$$U = 0, \quad V = 0, \quad \frac{\partial U}{\partial X} = \frac{\partial \theta}{\partial X} = 0; \tag{28}$$

- at the walls:

$$U = 0, \quad V = 0, \quad \frac{\partial \theta}{\partial n} = 0; \tag{29}$$

- at the heated source:

$$U = 0, \quad V = 0, \quad \theta = 1. \tag{30}$$

Taking the same dynamic viscosity ($\mu_p = \mu_{nf}$) in both layers, interface boundary conditions are obtained by equating the tangential and normal velocities, shear and normal stresses, temperatures, and heat flow across the interface. Therefore, interface conditions can be expressed as:

$$\begin{aligned} \theta_p &= \theta_{nf}\,, \quad & \lambda_p \frac{\partial \theta_p}{\partial Y} &= \lambda_{nf} \frac{\partial \theta_{nf}}{\partial Y}\,, \\ U_p &= U_{nf}\,, \quad & \frac{\partial U_p}{\partial Y} &= \frac{\partial U_{nf}}{\partial Y}\,, \\ V_p &= V_{nf}\,, \quad & \frac{\partial V_P}{\partial Y} &= \frac{\partial V_{nf}}{\partial Y}\,. \end{aligned} \tag{31}$$

The local Nusselt number (Nu) along the heat source and the average Nusselt number can be defined as follows:

$$\begin{aligned} \mathrm{Nu} &= -\frac{\varepsilon \lambda_{nf} + (1-\varepsilon)\lambda_s}{\varepsilon \lambda_f + (1-\varepsilon)\lambda_s} \left.\frac{\partial \theta}{\partial y}\right|_{y=0}\,, \\ \overline{\mathrm{Nu}} &= \int_{\frac{h}{2}}^{\frac{3h}{2}} \mathrm{Nu}\, dx. \end{aligned} \tag{32}$$

3 Numerical procedure and code validation

3.1 Numerical scheme

The governing coupled equations, Eqs. (1)–(8), with the boundary conditions, Eqs. (27)–(28), were solved with the finite volume method (FVM). The SIMPLE (semi-implicit method for pressure linked equations) algorithm was adopted for the pressure velocity coupling (Patankar [55]). The second order QUICK (quadratic upstream interpolation for convective kinematics) scheme was used to discretize the continuity, momentum and energy equations. The obtained discretized equations were solved using a Gauss-Seidel iteration technique. A convergence criterion for continuity, momentum and energy equations was defined as such that the residuals become lower than 10^{-6}. In this study, the computations were performed on a personal computer with an Intel Core i3 – 3.6 GHz processor. The typical CPU time is around 100 423 s for a productive run.

3.2 Grid dependency

The grid independence test was performed for the present formulation (see Fig. 1) at $\mathrm{Gr} = 10^4$, $\mathrm{Re} = 10$, $\phi = 0$, $\mathrm{Da} = 10^{-3}$, $\delta = 0.5$ and $\gamma = 0.2$. Six uniform grids were tested. Table 2 shows the effect of mesh resolution on the average Nusselt number along the heated source. Using this result, a uniform finer grid of 140×140 was found to meet the requirements of both the grid independency study and the computational time limits.

Table 2: Grid independence study for $\mathrm{Gr} = 10^4$, $\mathrm{Re} = 10$ and $\mathrm{Da} = 10^{-3}$

Grid size	60×60	80×80	100×100	120×120	140×140	160×160
Average Nusselt number	7.688	7.686	7.683	7.695	7.709	7.713

3.3 Code validation

Validation of this study was done for natural convection flow in a layered porous cavity filled with nanofluid, as investigated by Chamkha and Ismael [39], for $\mathrm{Da} = 10^{-5}$, Rayleigh number (Ra) of 10^5 and $\phi = 0$. Comparisons with streamlines and isotherms are shown in Fig. 2, respectively. Results are in very good agreement with the benchmark solution for the considered range of parameters.

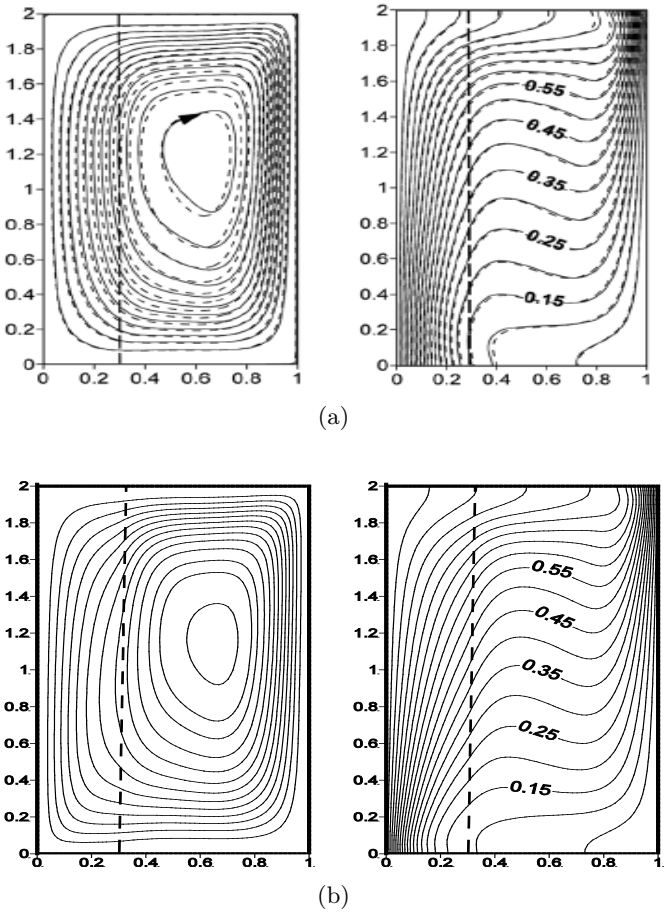

Figure 2: Comparison of streamlines and isotherms at Da = 10^{-5} and Ra = 10^5: a) numerical results of Chamkha and Ismael [39], b) present study.

4 Results and discussion

This section presents numerical results for streamlines, isotherms and the average Nusselt number for various values of the Reynolds number ($1 \leq \mathrm{Re} \leq 1000$), the Grashof number ($10^3 \leq \mathrm{Gr} \leq 10^6$), the Darcy number ($10^{-1} \leq \mathrm{Da} \leq 10^{-5}$), nanoparticles volume fraction ($0 \leq \phi \leq 0.06$), different nanoparticles (Fe_3O_4, Cu, Ag, Al_2O_3), thickness and position of porous layer ($0 \leq \gamma \leq 1$), ($0.1 \leq \delta \leq 0.9$), respectively. The porous layer porosity is fixed at $\varepsilon = 0.9$.

4.1 Effect of Reynolds and Grashof numbers

Figure 3 illustrates the effects of Reynolds and Grashof numbers on the structure of streamlines (top row) and isotherms (bottom row) at $\mathrm{Da} = 10^{-3}$, $\phi = 0$, $\delta = 0.5$ and $\gamma = 0.2$. As can be seen from the figure, in the present study the Reynolds number characterizes the inlet vertical velocity of nanofluid at the inlet zone. Growth of this dimensionless parameter reflects more intensive penetration of nanofluid inside the cavity.

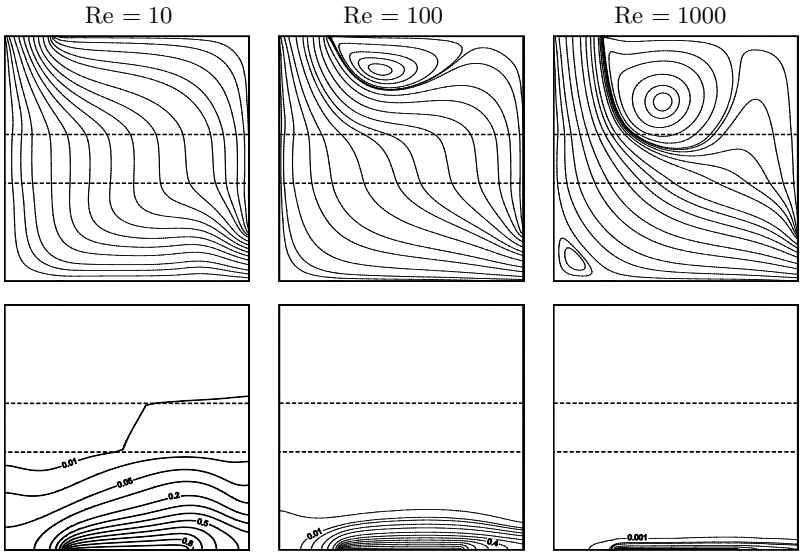

Figure 3: Streamlines (top) and isotherms (bottom) for different Reynolds numbers at $\mathrm{Da} = 10^{-3}$, $\mathrm{Gr} = 10^4$, $\phi = 0$, $\delta = 0.5$ and $\gamma = 0.2$.

At low $\mathrm{Re} = 10$, flow is generally made up of a main (forced) flow, characterized by open streamlines, connecting the inlet and outlet of the cavity. However, near the porous layer, streamlines become vertical. This is due to the hydrodynamic resistance provided by the porous layer. An additional vortex is generated near the inlet port at the upper wall when Re is further increased to $\mathrm{Re} = 100$. As the value of Reynolds number increases further ($\mathrm{Re} = 1000$), the last vortex becomes stronger and a new small vortex appears in the left bottom corner, proving that the convection is more or less dependent on the intensity of the inflow.

On the other hand, isotherm lines for all values of Reynolds number are below the porous layer; cold nanofluid occupies entirely the cavity. For high Reynolds numbers, isotherms are clustered toward the bottom part of the

cavity. Due to inlet flow with high momentum, flow is entirely dominated by inertia forces.

The variation of the average Nusselt number on the heated plate with the Reynolds number for different Grashof numbers at $\phi = 0$, Da $= 10^{-3}$, $\delta = 0.5$ and $\gamma = 0.2$ is shown in Fig. 4. Results indicate that the average Nusselt number enhances significantly with the increasing Reynolds and Grashof numbers, the increase of the latter leads to an improvement in the heat transfer rate. But, it is interesting to note that for Re $= 100$, the average Nusselt number stays nearly the same with the increasing Grashof number.

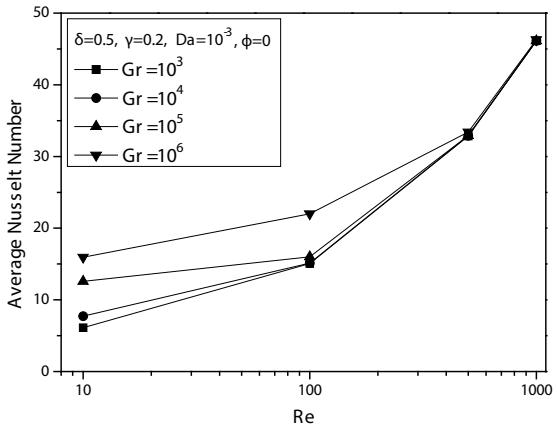

Figure 4: Variation of average Nusselt number with Reynolds number for different values of Grashof number at Da $= 10^{-3}$, $\phi = 0$, $\delta = 0.5$ and $\gamma = 0.2$.

4.2 Effect of Darcy number

Figure 5 illustrates the distributions of streamlines and isotherms for different Darcy numbers (100, 10^{-2} and 10^{-5}) at Gr $= 10^4$, Re $= 100$, $\phi = 0.03$, $\delta = 0.5$, $\gamma = 0.2$ and Fe_3O_4. It can be seen from this figure that for a tiny Darcy number 10^{-5}, i.e., low permeability, flow is similar to the previous case of (Da $= 10^{-3}$) and is characterized by open streamlines and a small vortex in the upper wall. The porous layer hinders fluid flow acting like a solid; streamlines are vertical in this section. Increasing Darcy number (10^{-2} and 100) means increasing the porous layer permeability and therefore, more cold nanofluid is allowed to penetrate the porous layer, considerably increasing the strength of the vortex. However, the Darcy number

variation does not have a significant effect on the distribution of isothermal lines, which are almost completely confined around the heated source, except for a slight rise of isotherms.

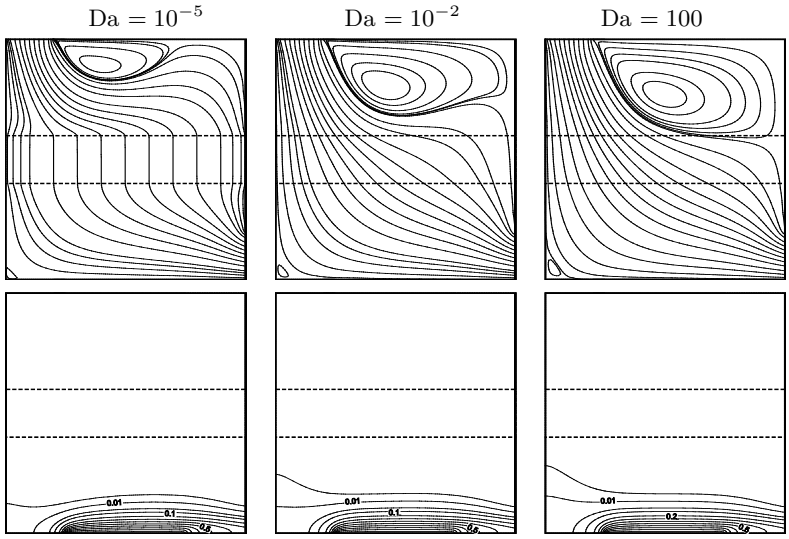

Figure 5: Streamlines (top) and isotherms (bottom) for different Darcy numbers at $\mathrm{Gr} = 10^4$, $\mathrm{Re} = 100$, $\phi = 0.03$, $\delta = 0.5$ and $\gamma = 0.2$ for Fe_3O_4.

Figures 6–7 show the overall heat transfer rate for different values of Darcy number, volume fraction of nanoparticle and Reynolds number with fixed

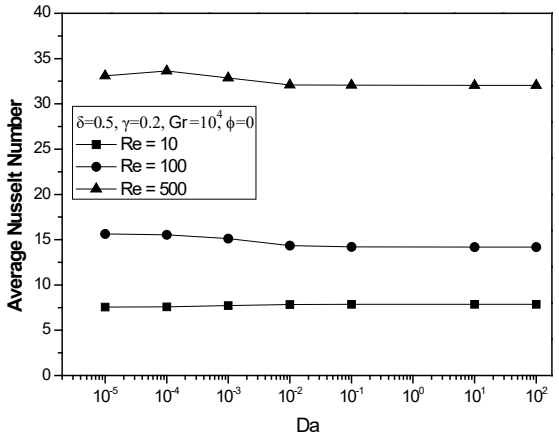

Figure 6: Variation of average Nusselt number with Darcy number for different values of Reynolds number at $\mathrm{Gr} = 10^4$, $\phi = 0$, $\delta = 0.5$ and $\gamma = 0.2$.

values of $Gr = 10^4$, $\delta = 0.5$ and $\gamma = 0.2$ for Fe_3O_4 nanoparticles. Similar to the previous case, an increase in the overall heat transfer rate is observed with the increasing Reynolds number for the fixed value of Darcy number. It can be seen, that for the fixed value of the Reynolds number, the Darcy number has not a significant effect on the average Nusselt number. The Darcy number effect is more clear in Fig. 7, where it demonstrates that the average Nusselt number is optimal at lower values of Darcy number ($Da = 10^{-5}$). On the other hand, the average Nusselt number increases with the increasing nanoparticles volume fraction for different Darcy numbers. In fact, the nanofluid thermal conductivity and heat transfer rate increase with the increasing nanoparticles volume fraction.

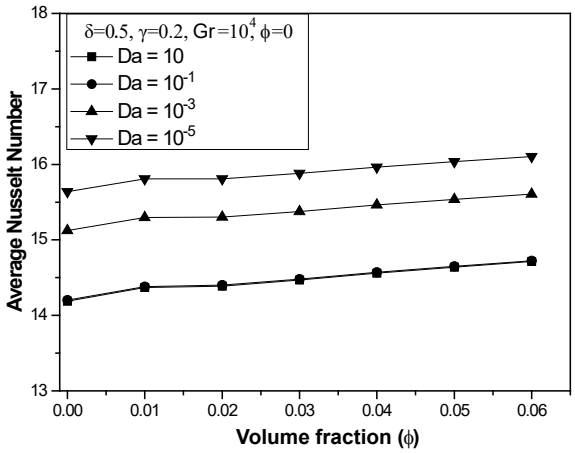

Figure 7: Variation of average Nusselt number with nanoparticles volume fractions for different values of Darcy number at $\gamma = 0.2$, $\delta = 0.5$, $Gr = 10^4$, $Re = 100$ for Fe_3O_4 nanoparticles.

4.3 Effect of nanoparticles type

Figure 8 shows streamline (top row) and isotherm (bottom row) profiles for three types of nanoparticles (Cu, Ag, Al_2O_3) in association with $Gr = 10^4$, $Da = 10^{-5}$, $Re = 10$, $\delta = 0.5$ and $\gamma = 0.2$. Therefore, a concentration of 4% has been chosen as a reference for each type of nanofluid. The flow structure is wired, connecting the inlet and outlet of the cavity and the isotherms are concentrated in the cavity lower part. It is noted that changing the type of nanoparticles has no discernible impact on the flow pattern and temperature distribution.

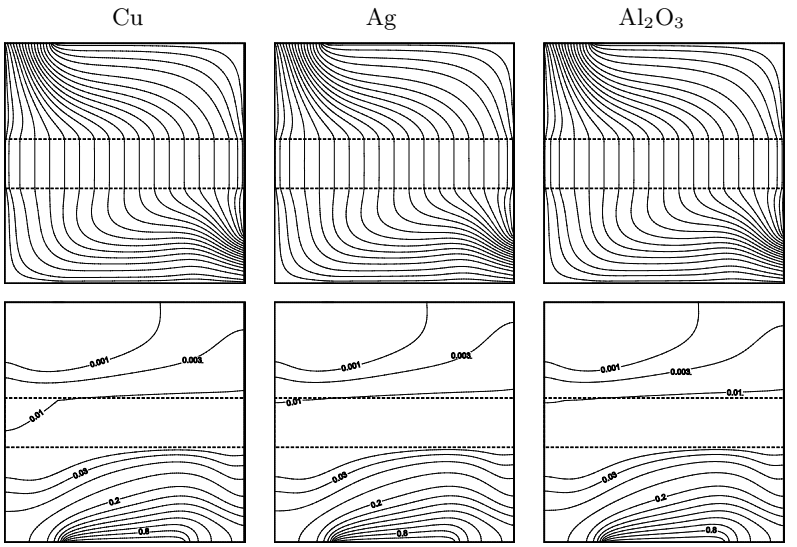

Figure 8: Streamlines (top) and isotherms (bottom) for different types of nanoparticles at $\mathrm{Gr} = 10^4$, $\mathrm{Re} = 10$, $\mathrm{Da} = 10^{-5}$, $\phi = 0.04$, $\delta = 0.5$ and $\gamma = 0.2$.

The comparison of Nusselt number for various working nanofluids with various nanoparticles volume fractions for three different Darcy numbers and $\mathrm{Gr} = 10^4$, $\mathrm{Re} = 100$, $\gamma = 0.2$ and $\delta = 0.5$ is presented in Fig. 9. It is notable that Ag nanoparticles have the uppermost heat transfer rate chased by Cu, Fe_3O_4 and Al_2O_3 nanoparticles. This is due to the fact that Ag nanoparticle has a higher thermal conductivity compared to other nanoparticles. On the other hand, the Nusselt number increases with the

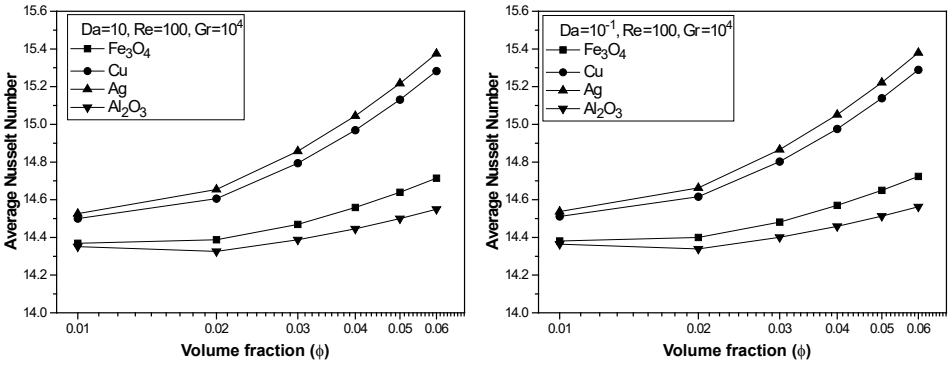

Figure 9: For caption see next page.

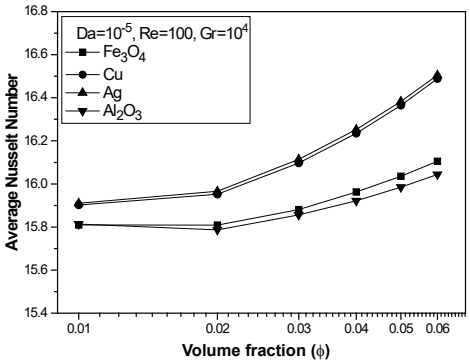

Figure 9: Variation of average Nusselt number with nanoparticles volume fractions for different types of nanoparticles and Darcy number at $\gamma = 0.2$, $\delta = 0.5$, $\mathrm{Gr} = 10^4$ and $\mathrm{Re} = 100$.

increasing volume fraction whatever the Darcy number and nanoparticle type.

4.4 Effect of porous layer thickness

Figure 10 illustrates the effects of porous layer thickness on streamline contour maps and isotherms, when $\mathrm{Da} = 10^{-3}$, $\mathrm{Re} = 100$, $\mathrm{Gr} = 10^4$ and $\phi = 0.04$ for Fe_3O_4 nanoparticles. It is observed that the change of porous layer thickness leads to significant changes in flow patterns. At $\gamma = 0$ (pure nanofluid), two vortices develop, a large one is located at the right top corner and a small vortex is located at the left bottom corner. As the value of γ increases, the size of circulating two cells gradually decreases. It should be noted that flow is directed toward the outlet port as the porous layer thickness increases. Corresponding isotherms are compressed near the heated source at the bottom wall, while all the upper part of the cavity is at a cold jet temperature, due to dominated forced convection. However, for a cavity completely filled by the porous medium ($\gamma = 1$) the through-flow fluid stream occupies the entire cavity and isotherm lines become wider and stratified due to strong effects of conduction larger than those of convection.

The behaviour of the average Nusselt number with γ is presented in Fig. 11. A growth of the porous layer size results in a rise of the heat transfer rate. This behaviour is imputed be to a reason that the effective thermal conductivity of the porous layer (Eq. (11)) is larger than that of the nanofluid layer.

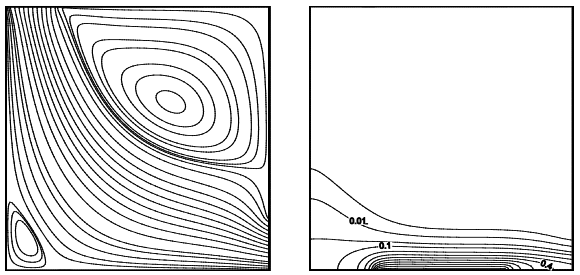

$\gamma = 0$

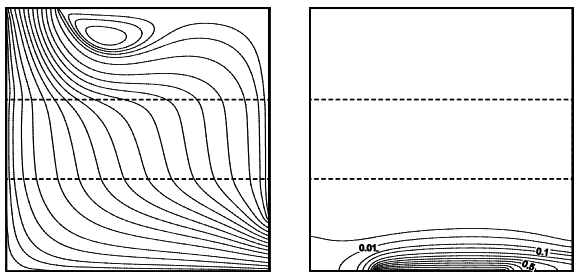

$\gamma = 0.3$

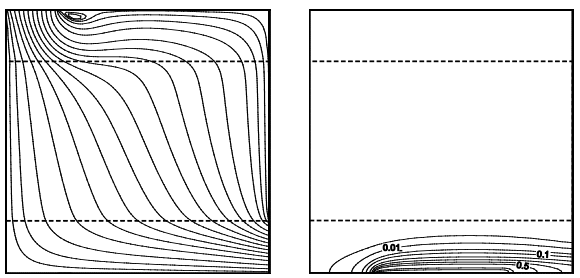

$\gamma = 0.6$

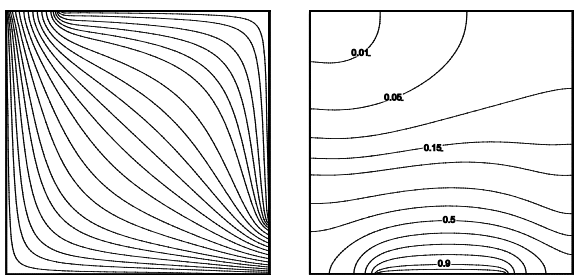

$\gamma = 1$

Figure 10: Streamlines (left) and isotherms (right) for different porous layer thicknesses (γ) at $\mathrm{Gr} = 10^4$, $\mathrm{Re} = 100$, $\mathrm{Da} = 10^{-3}, \phi = 0.04$ for Fe_3O_4 nanoparticles.

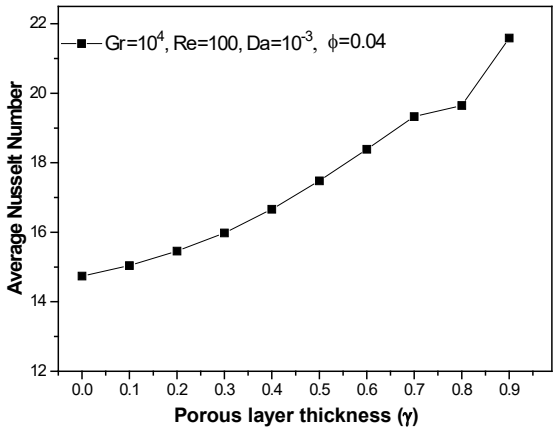

Figure 11: Variation of average Nusselt number with porous layer thickness for at $\mathrm{Gr} = 10^4$, $\mathrm{Re} = 100$, $\mathrm{Da} = 10^{-3}$ and $\phi = 0.04$ for Fe_3O_4 nanoparticles.

4.5 Effect of porous layer position

Figure 12 shows the distribution of streamlines (left row) and isothermal lines (right row) for various porous layer locations ($\delta = 0.1$, 0.3, 0.7 and 0.9) in the cavity for $\gamma = 0.2$, $\mathrm{Da} = 10^{-3}$, $\mathrm{Re} = 100$, $\mathrm{Gr} = 10^4$ and $\phi = 0.04$ for Fe_3O_4 nanoparticles. When the porous layer is located at the top wall ($\delta = 0.9$), two vortices appear in the right top corner and in the left bottom corner. However, for the case $\delta = 0.7$, cells disappear leaving a space for the main flow stream. Gradually as the porous layer approaches the bottom wall, two vortices reappear and become stronger, due to the dominance of convection flow. Isotherms are compressed at the cavity lower part as $\delta \leq 0.9$. It is noticed that when the heater source is surrounded by porous media ($\delta = 0.1$), isotherms ascend slightly, which means that the porous layer acts as a heat diffuser.

Figure 13 illustrates the average Nusselt number for the heated source at different aspect ratios (δ) and Darcy numbers. It is noted from the figure that the Nusselt number increases with the decreasing aspect ratio δ for all values of Darcy number. On the other hand, the Nusselt number is not much affected by a change in the Darcy number for $\delta \geq 0.5$, i.e., when the porous layer is far from the heated source. But usually, the Nusselt number increases with the decreasing Darcy number. In contrast, this tendency changes for the case $\delta = 0.1$, the heat transfer rate increases with the increasing Darcy number,which is due to the increase of effective thermal conductivity of the porous layer.

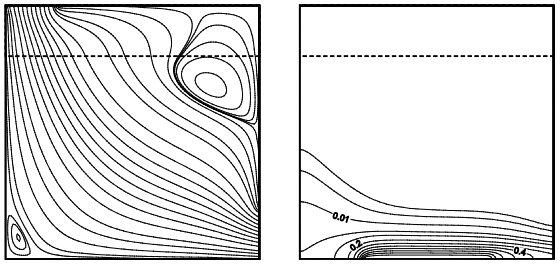

$\delta = 0.9$

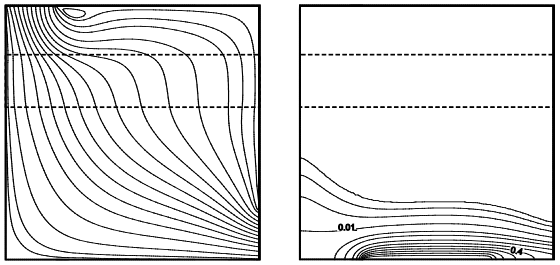

$\delta = 0.7$

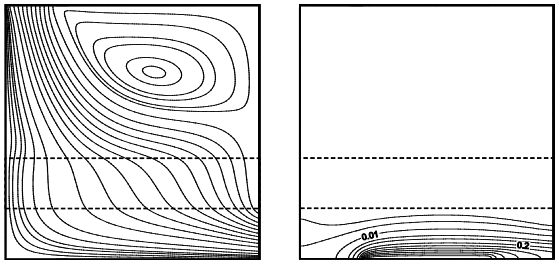

$\delta = 0.3$

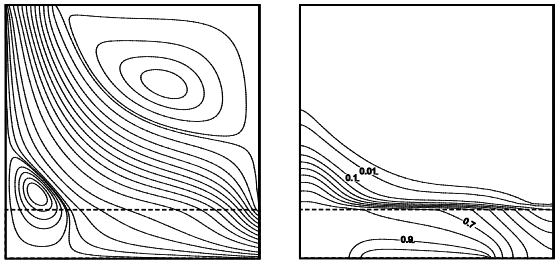

$\delta = 0.1$

Figure 12: Streamlines (left) and isotherms (right) for different porous layer positions (δ) at Gr = 10^4, Re = 100, Da = 10^{-3}, $\gamma = 0.2$ and $\phi = 0.04$ for Fe_3O_4 nanoparticles.

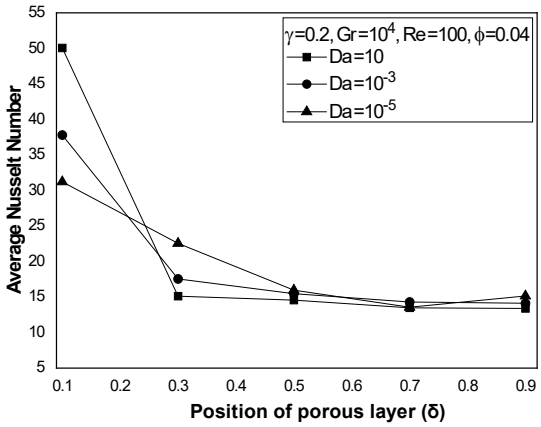

Figure 13: Variation of average Nusselt number with porous layer position at $\mathrm{Gr} = 10^4$, $\mathrm{Re} = 100$, $\mathrm{Da} = 10^{-3}$ and $\phi = 0.04$ for Fe_3O_4 nanoparticles.

5 Conclusions

The purpose of this work was to numerically analyze mixed convection in a vented square cavity filled with different nanofluids having a horizontal porous layer. The effects of governing parameters on flow and thermal fields characteristics were analyzed. A detailed analysis of streamlines distribution, isotherms and the average Nusselt number in the cavity were carried out to investigate the effect of Reynolds, Grashof and Darcy numbers, nanoparticle volume fraction, thickness and positions of porous layer on fluid flow and heat transfer in the mentioned cavity. The numerical results reported lead us to the following conclusions:

1. The average Nusselt number increases with the increasing volume fraction of nanoparticles, Reynolds and Grashof numbers for all studied Darcy numbers.

2. The flow pattern does not change substantially with the volume fraction and nanoparticles type.

3. The average Nusselt number is optimal at lower values of Darcy number.

4. An addition of nanoparticles to basic fluid leads to an increase of the average Nusselt number.

5. Ag nanoparticles seem to produce the highest values of Nusselt number compared to other types of nanoparticles.

6. A growth of the porous layer size increases the heat transfer rate and the position of the porous layer at the bottom wall has an uppermost effect on the heat transfer rate.

These various results should be useful for the design and optimization of several thermal engineering problems associated with heat exchangers. Subsequently, it would be interesting to complete this initiative by continuing the analysis and exploring the impact of discrete source location and three-dimensionality on the flow and heat transfer when the governing parameters are changed.

Received 12 October 2022

References

[1] Selvakumar R.D., Zhonglin D., Wu J.: *Heat transfer intensification by EHD conduction pumping for electronic cooling applications.* Int. J. Heat Fluid Flow **95**(2022), 108972.

[2] Ren F., Du J., Cai Y., Xu Z., Zhang D., Liu Y.: *Numerical simulation study on thermal performance of sub-tropical double-layer energy storage floor combined with ceiling energy storage radiant air conditioning.* Case Stud. Therm. Eng. **28**(2021), 101696.

[3] Niemann P., Schmitz G.: *Air conditioning system with enthalpy recovery for space heating and air humidification: An experimental and numerical investigation.* Energy **213**(2020), 118789.

[4] Dawar A., Wakif A., Thumma T., Shah N.A.: *Towards a new MHD non-homogeneous convective nanofluid flow model for simulating a rotating inclined thin layer of sodium alginate-based iron oxide exposed to incident solar energy.* Int. Commun. Heat Mass Transf. **130**(2022), 105800.

[5] Hongtao L., Zhang S., Ji Y., Sun M., Li X., Sheng Y.: *The influence of catchment scale on comprehensive heat transfer performance about tube fin heat exchanger in numerical calculation.* Energ. Rep. **8**(2022), 147–155.

[6] Raja M.A.Z., Shoaib M., Zubair G., Khan M.I., Gowda R.J.P., Prasannakumara B.C., Guedri K.: *Intelligent neuro-computing for entropy generated Darcy-Forchheimer mixed convective fluid flow.* Math. Comput. Simul. **201**(2022), 193–214.

[7] Awan A.U., Ahammad N.A., Ali B., Tag-ElDin E.M., Guedri K., Gamaoun F.: *Significance of thermal phenomena and mechanisms of heat transfer through the dynamics of second-grade micropolar nanofluids.* Sustainability **14**(2022), 9361.

[8] Mehrizi A.A., Farhadi M., Hassanzade Afroozi H., Sedighi K., Darz A.A.R.: *Mixed convection heat transfer in a ventilated cavity with hot obstacle: Effect of nanofluid and outlet port location.* Int. Commun. Heat Mass Transf. **39**(2012), 1000–1008.

[9] Ismael M.A., Jasim H.F.: *Role of the fluid-structure interaction in mixed convection in a vented cavity.* Int. J. Mech. Sci. **135**(2018), 190–202.

[10] Benzema M., Benkahla Y.Kh., Labsi N., Ouyahia S., El Ganaoui M.: *Second law analysis of MHD mixed convection heat transfer in a vented irregular cavity filled with Ag-MgO/water hybrid nanofluid.* J. Therm. Anal. Calorim. **137**(2019), 1113–1132.

[11] Selimefendigil F., Öztop H.F.: *Magnetohydrodynamics forced convection of nanofluid in multi-layered U-shaped vented cavity with a porous region considering wall corrugation effects.* Int. Commun. Heat Mass Transf. **113**(2020), 104551.

[12] Ataei-Dadavi I., Chakkingal M., Kenjeres S., Kleijn C.R., Tummers M.J.: *Experiments on mixed convection in a vented differentially side-heated cavity filled with a coarse porous medium.* Int. J. Heat Mass Transf. **149**(2020), 119238.

[13] Dhahad H.A., Al-Sumaily G.F., Alawee W.H., Thompson M.C.: *Aiding and opposing re-circulating mixed convection flows in a square vented enclosure.* Therm. Sci. Eng. Progress **19**(2020), 100577.

[14] Moayedi H.: *Investigation of heat transfer enhancement of Cu-water nanofluid by different configurations of double rotating cylinders in a vented cavity with different inlet and outlet ports.* Int. Commun. Heat Mass Transf. **126**(2021), 105432.

[15] Velkennedy R., Nisrin J.J., Kalidasan K., Rajeshkanna P.: *Numerical investigation of convective heat transfer in a rectangular vented cavity with two outlets and cold partitions.* Int. Commun. Heat Mass Transf. **129**(2021), 105659.

[16] Jamshed W., Eid M.R., Hussain S.M., Abderrahmane A., Safdar R., Younis O., Pasha A.A.: *Physical specifications of MHD mixed convective of Ostwald-de Waele nanofluids in a vented-cavity with inner elliptic cylinder.* Int. Commun. Heat Mass Transf. **134**(2022), 106038.

[17] Benos L., Sarris I.E.: *Analytical study of the magnetohydrodynamic natural convection of a nanofluid filled horizontal shallow cavity with internal heat generation.* Int. J. Heat Mass Transf. **130**(2019), 862–873.

[18] Arani A.A.A., Mahmoodi M., Amini M.: *Free convection in a nanofluid filled square cavity with a horizontal heated plate.* Defect Diffus. Forum **312-315**(2011), 433–438.

[19] Selimefendigil F., Öztop H.F.: *Mixed convection of ferrofluids in a lid driven cavity with two rotating cylinders.* Eng. Sci. Techn. Int. J. **18**(2015), 439–451.

[20] Rabbi Kh.Md., Saha S., Mojumder S., Rahman M.M., Saidur R., Ibrahim T.A.: *Numerical investigation of pure mixed convection in a ferrofluid-filled lid-driven cavity for different heater configuration.* Alexandria Eng. J. **55**(2016), 127–139.

[21] Elshehabey H.M., Raizah Z., Öztop H.F., Ahmed S.E.: *MHD natural convective flow of Fe_3O_4-H_2O ferrofluids in an inclined partial open complex-wavy-walls ringed enclosures using non-linear Boussinesq approximation.* Int. J. Mech. Sci. **170**(2020), 105352.

[22] Jakeer S., Reddy P.B.A., Rashad A.M., Nabwey H.A.: *Impact of heated obstacle position on magneto-hybrid nanofluid flow in a lid-driven porous cavity with Cattaneo-Christov heat flux pattern.* Alexandria Eng. J. **60**(2021), 821–835.

[23] Wang A., Xu H.: *Highly accurate wavelet-homotopy solutions for mixed convection hybrid nanofluid flow in an inclined square lid-driven cavity.* Comput. Math. Appl. **108**(2022), 88–108.

[24] Jayaprakash M.C., Alsulami M.D., Shanker B., Kuma R.S.V. *Investigation of Arrhenius activation energy and convective heat transfer efficiency in radiative hybrid nanofluid flow.* Waves Random Complex Media (2022), 1–13.

[25] Dutta S., Bhattacharyya S., Pop I.: *Effect of hybrid nanoparticles on conjugate mixed convection of a viscoplastic fluid in a ventilated enclosure with wall mounted heated block.* Alexandria Eng. J. **62**(2023), 99–111.

[26] Neild D.A., Bejan A.: *Convection in Porous Media.* (3rd Edn.). Springer-Verlag, 2006.

[27] Balla C. S., Kishan N., Gorla R.S.R, Gireesha B.J.: *MHD boundary layer flow and heat transfer in an inclined porous square cavity filled with nanofluids.* Ain Shams Eng. J. **8**(2017), 237–254.

[28] Malik S., Nayak A.K.: *MHD convection and entropy generation of nanofluid in a porous enclosure with sinusoidal heating.* Int. J. Heat Mass Transf. **111**(2017), 329–345.

[29] Sheremet M.A., Roşca N.C., Roşca A.V., Pop I.: *Mixed convection heat transfer in a square porous cavity filled with a nanofluid with suction/injection effect.* Comput. Math. Appl. **76**(2018), 2665–2677.

[30] Abu-Hamdeh N.H., Öztop H.F., Alnefaie K.A.: *A computational study on mixed convection in a porous media filled and partially heated lid-driven cavity with an open side.* Alexandria Eng. J. **59**(2020), 1735–1750.

[31] Mabood F., Yusuf T.A., Sarris I.E.: *Entropy generation and irreversibility analysis on free convective unsteady MHD Casson fluid flow over a stretching sheet with Soret/Dufour in porous media.* Spec. Top. Rev. Porous Media: Int. J. **11**(2020), 6, 595–611.

[32] Kumar R.N., Gowda R.J.P., Gireesha B.J., Prasannakumara B.C.: *Non-Newtonian hybrid nanofluid flow over vertically upward/downward moving rotating disk in a Darcy–Forchheimer porous medium.* Eur. Phys. J. Spec. Top. **230**(2021), 1227–1237.

[33] Kashyap D., Dass A.K.: *Influence of cavity inclination on mixed convection in a double-sided lid-driven cavity with a centrally inserted hot porous block.* Int. J. Therm. Sci. **181**(2022), 107732.

[34] Alsedais N., Aly A.M., Mansour M.A.: *Local thermal non-equilibrium condition on mixed convection of a nanofluid-filled undulating cavity containing obstacle and saturated by porous media.* Ain Shams Eng. J. **13**(2022), 101562.

[35] Choudhary P., Ray R.K.: *MHD natural convective flow in a porous corrugated enclosure: Effects of different key parameters and discrete heat sources.* Int. J. Therm. Sci. **181**(2022), 107730.

[36] Nammi G., Deka D.K., Pati S., Baranyi L.: *Natural convection heat transfer within a square porous enclosure with four heated cylinders*. Case Stud. Therm. Eng. **30**(2022), 101733.

[37] Kumar V., Murthy S.V.S.S.N.V.G.K., Kumar B.V.R.: *Multi-force effect on fluid flow, heat and mass transfer, and entropy generation in a stratified fluid-saturated porous enclosure*. Math. Comput. Simul. **203**(2023), 328–367.

[38] Mercier J-F., Weisman C., Firdaouss M., Le Quéré P.: *Heat transfer associated to natural convection flow in a partly porous cavity*. J. Heat Transf. **124**(2002), 130–143.

[39] Chamkha A.J., Ismael M.A.: *Natural convection in differentially heated partially porous layered cavities filled with a nanofluid*. Numer. Heat Transf. A-Appl. **65**(2014), 1089–1113.

[40] Le Bars M., Worster M.G.: *Interfacial conditions between a pure fluid and a porous medium: implications for binary alloy solidification*. J. Fluid Mech. **550**(2006), 149–173.

[41] Carcadea E., Varlam M., Ismail M., Ingham D.B., Marinoiu A., Raceanu M., Jianu C., Patularu L., Ion-Ebrasu D.: *PEM fuel cell performance improvement through numerical optimization of the parameters of the porous layers*. Int. J. Hydrogen Energ. **45**(2020), 7968–7980.

[42] Aly A.M., Raizah Z.A.S., Ahmed S.E.: *mixed convection in a cavity saturated with wavy layer porous medium: Entropy generation*. J. Thermophys. Heat Transf. **32**(2018), 3, 764–780.

[43] Astanina M.S., Sheremet M.A., Oztop H.F., Abu-Hamdeh N.: *MHD natural convection and entropy generation of ferrofluid in an open trapezoidal cavity partially filled with a porous medium*. Int. J. Mech. Sci. **136**(2018), 493–502.

[44] Selimefendigil F., Öztop H.F.: *Thermal management and modeling of forced convection and entropy generation in a vented cavity by simultaneous use of a curved porous layer and magnetic field*. Entropy **23**(2021), 152.

[45] Gibanov N.S., Sheremet M.A., Öztop H.F., Abu-Hamdeh N.: *Effect of uniform inclined magnetic field on mixed convection in a lid-driven cavity having a horizontal porous layer saturated with a ferrofluid*. Int. J. Heat Mass Transf. **114**(2017), 1086–1097.

[46] Al-Srayyih B.M., Gao S., Hussain S.H.: *Natural convection flow of a hybrid nanofluid in a square enclosure partially filled with a porous medium using a thermal non-equilibrium model*. Phys. Fluids **31**(2019), 043609.

[47] Al-Zamily A.M.J.: *Analysis of natural convection and entropy generation in a cavity filled with multi-layers of porous medium and nanofluid with a heat generation*. Int. J. Heat Mass Transf. **106**(2017), 1218–1231.

[48] Moria H.: *Natural convection in an L-shape cavity equipped with heating blocks and porous layers*. Int. Commun. Heat Mass Transf. **126**(2021), 105375.

[49] Alsabery A.I., Hajjar A., Raizah Z.A.S., Ghalambaz M., Hashim I., Chamkha A.J.: *Impact of finite wavy wall thickness on entropy generation and natural convection of nanofluid in cavity partially filled with non-Darcy porous layer*. Neural Comput. Appl. **32**(2020), 13679–13699.

[50] Chordiya J.S., Sharma R.V.: *Numerical study on the effects of multiple internal diathermal obstructions on natural convection in a fluid-saturated porous enclosure.* Arch. Mech. Eng. **65**(2018), 4, 553–578.

[51] Rana G.C.: *The onset of thermal convection in couple-stress fluid in hydromagnetics saturating a porous medium.* Bull. Pol. Acad. Sci. Tech. Sci. **62**(2014), 2, 357–362.

[52] Saeed F., R., Al-Dulaimi M.A.: *Numerical investigation for convective heat transfer of nanofluid laminar flow inside a circular pipe by applying various models.* Arch. Thermodyn. **42**(2021), 1, 71–95.

[53] Korib K., Ihaddadene N., Bouakkaz R., Khelili Y.: *Numerical simulation of forced convection of nanofluid around a circular cylinder.* Arch. Thermdyn. **40**(2019), 2, 3–16

[54] Brinkman H.C.: *The viscosity of concentrated suspensions and solutions.* J. Chem. Phys. **20**(1952), 571–581.

[55] Patankar S.V.: *Numerical Heat Transfer and Fluid Flow.* Hemisphere, McGraw-Hill, Washington DC 1980.

archives
of thermodynamics
Vol. **44**(2023), No. 2, 115–138
DOI: 10.24425/ather.2023.146561

Numerical study of MHD Williamson-nano fluid flow past a vertical cone in the presence of suction/injection and convective boundary conditions

MANTHRI SATHYANARAYANA[a]
TAMTAM RAMAKRISHNA GOUD[b*]

[a] Osmania University, Department of Mathematics, University College of Science, Hyderabad – 500007, Telangana Sate, India

[b] Osmania University, Department of Mathematics, University College of Science, Saifabad, Hyderabad – 500004, Telangana Sate, India

Abstract The primary objective is to perform a numerical synthesis of a Williamson fluid that has nanoparticles added to it and is directed toward a vertical cone in a uniform transverse magnetic field, under heat and mass transport, suction and injection, and convective boundary conditions. For this particular fluid flow, by utilising similarity transformations, the partial differential equations are transformed into ordinary differential equations. Calculating these kinds of equations with their suitable bounds requires the Runge–Kutta technique in combining a shooting strategy. The functions of a vast number of parameters are graphically represented and assessed on flow field profiles. The results show the local skin friction, local Nusselt number, and local Sherwood number and the changing values of the flow constraints. Finally, the results are compared to those from the previously published works and found to be in good agreement.

Keywords: Williamson fluid; Nanofluid; Vertical cone; Suction/Injection; Convective boundary condition

*Corresponding Author. Email: manthrisathyam926@gmail.com

Nomenclature

a	–	constant
B_o	–	uniform magnetic field, T
Bi	–	Biot number
C	–	fluid nanoparticle volume concentration, mol/m^3
C_w	–	dimensional nanoparticle concentration at the stretching surface
C_∞	–	dimensional ambient volume fraction
C_f	–	skin-friction coefficient, $1/s$
D_B	–	coefficient of Brownian diffusion, m^2/s
D_T	–	coefficient of thermophoresis diffusion, m^2/s
f	–	dimensionless stream function
f'	–	fluid velocity, m/s
Gc	–	Grashof number for mass transfer
Gr	–	Grashof number for heat transfer
g	–	gravitational acceleration, m/s^2
h_1	–	heat transfer coefficient
J_w	–	mass flux coefficient
k^*	–	thermal conductivity of the fluid
L	–	characteristic length, m
M	–	magnetic field parameter
Nb	–	Brownian motion parameter
Nt	–	thermophoresis parameter
Nu	–	Nusselt number
Pr	–	Prandtl number
q_w	–	heat flux coefficient
r	–	radius of the cone, m
r_1	–	wall thermal factor
r_2	–	nanofluid concentration parameter
T	–	fluid temperature, K
T_w	–	surface temperature, K
T_∞	–	temperature of the fluid far from the stretching sheet, K
S	–	suction/injection parameter
Sc	–	Schmidt number
Sh	–	Sherwood number
$u,\ v$	–	x and y directions of velocity components, m/s
$u_w(x)$	–	stretching velocity of the fluid, m/s
v_w	–	suction/injection velocity, m/s
We	–	Williamson fluid parameter
$x,\ y$	–	Cartesian coordinates calculated along the stretching sheet, m

Greek symbols

α	–	half angle of the cone
α^*	–	thermal diffusivity, m^2/s
β_C	–	coefficient of concentration expansion
β_T	–	coefficient of thermal expansion
Γ	–	shear stress, 1/s
η	–	dimensionless similarity variable

θ – non-dimensional temperature
κ – thermal conductivity of the fluid, W/(mK)
μ – dynamic viscosity of the fluid, Pa s
ν – kinematic viscosity, m^2/s
ρ – density, kg/m^3
σ – Stefan–Boltzmann constant, W/m^2K^4
τ – Ratio of nano particles heat capacity to fluid heat capacity
τ_B – wall shear stress, Nm^{-2}
ϕ – non-dimensional nanoparticle concentration

Subscripts

f – fluid
ρ – nanoparticles
w – condition on the sheet,
∞ – ambient conditions

Superscripts

$(\cdot)'$ – differentiation with respect to η

1 Introduction

Nowadays, non-Newtonian fluids have garnered a lot of attention from hydrodynamics specialists all over the world. This interest may be attributable to the significant scientific advancements that have been made in the applications of this field. In terms of viscosity and the rate of shear stress, the Williamson fluid is remarkably similar to polymeric solutions. Because of this, the Williamson fluid is considered. According to the Williamson fluid model, as the shear rate increased, the viscosity would fall [1]. These flows are often used in a wide variety of industrial applications, including the extrusion of polymer sheets from a die, the production of the boundary layer in processes that include the condensation of liquid films, and the emulsion coating of photographic films. Severa; reseachers examined the Williamson model and, as a consequence of covering a variety of flow patterns, presented a number of different tests, covering a wide range of topics. Aldabesh *et al.* [2] investigated the effects of gyrotactic bacteria on the unsteady flow of Williamson nanofluid using a revolving cylinder. The heat radiation and chemical reaction were examined by Krishnamurthy *et al.* [3] using porous media as the delivery medium. Amer [4] examined the results of numerical simulations of heat flow that made use of Williamson nanofluid MHD and thermal radiation. Loganathan and Rajan [5] investigated Joule

heating and Williamson nanofluid flow with negligible nanoparticle mass floodway. Dawar *et al.* [6] conducted research to determine which analysis was the most accurate for three-dimensional flow across a stretched surface in convective conditions. Yahya *et al.* [7] studied heat flux on Williamson sutter through the use of nanofluid transportation generated by a stretched surface. This was done in order to better understand how these two heat fluxes interact with Williamson sutter. Sreedevi and Reddy [8] looked at the spinning cylinder with the Cattaneo-Christov heat flux and the gyrotactic microbe. Shafiq and Sindhu's presentation [9] described a Williamson flow that lacked compressibility and was unstable. A unique notion for entropy amplification and activation energy in the transient axis-symmetric flow of Williamson nanofluid was suggested by Azam *et al.* [10]. Ahmed *et al.* [11] investigated the heat transfer mechanism in a Williamson-type fluid in a magnetohydrodynamic (MHD) mixed convection flow over an exponentially stretched porous curved surface. The transfer of heat and mass in Williamson fluid was studied by Nazir *et al.* [12] using generalised non-Fourier models. Kumaran et al. [13] directed research on the impacts of gooey dispersal and intensity moves in a radiative MHD Williamson liquid stream over the top paraboloid of upheaval. At the point when the liquid stream was influenced by the presence of a temperature-subordinate intensity source, Raju *et al.* [14] assessed the Williamson and Casson liquid streams through an extended sheet while thinking about both intensity and mass exchange. It has been accounted for by Bhatti *et al.* [15] that the MHD Williamson nanofluid stream was influenced by gyrotactic microorganisms as it went through spinning round plates. Shateyi *et al.* [16] conducted a thorough investigation into the behaviour of an incompressible conductive Williamson-nanofluid over an extending penetrable sheet. It was conjectured by Nadeem *et al.* [17] that the Williamson liquid stream would happen across an extended sheet.

Nano-fluids are a whole new category of fluids that were invented by Choi [18]. Researchers from all around the world who specialise in studying fluids have shown a great deal of interest in this particular kind of fluid. It is an essential component in a wide variety of today's technological applications that make people's lives easier and more enjoyable. On the other hand, nanofluids have applications in a diverse variety of industries, including the satellite industry. Nanofluids are also vital in the field of medicine. For example, the use of gold nanoparticles in the treatment of cancerous tumours and the assembly of minuscule bombs that are utilised to wipe out destructive tumours are both examples of how nanofluids are employed

in these fields. Suresh and colleagues [19] produced a hybrid nanofluid by adding nanoparticles to the basic fluids. They claim that this nanofluid surpasses traditional nanofluids in terms of its heat transfer rate. In their study [20], Nadeem and Abbas looked at the behaviour of a micropolar hybrid nanofluid as it moved around a circular cylinder. In addition to this, they emphasised the sliding effects by using a numerical technique. The authors of the study, Devi and Devi [21], conducted their investigation of the hybrid nanofluid at a stretched surface using numerical simulations. Khan *et al.* [22] studied the unsteady flow over a stretched sheet by using a chemical reaction in their research. Lu *et al.* [23] investigated the flow of hybrid nanofluids through a curved surface as part of their research. Khan *et al.* [24] placed a strong focus on the significance of activation energy in relation to chemical processes. Khan *et al.* [25] employed computer simulations to research the flow of a nonlinear radiative fluid that was coupled with a chemical process. Khan *et al.* [26] researched and represented the conditions directing the MHD radiative nanofluid stream with heat age and substance responses toward a wedge. They found that these equations guide the flow of nanofluids under MHD conditions. Motsumi and Makinde [27] explored heat radiation and viscous dissemination in nanofluids as they went through a formerly level subsurface. Rana *et al.* [28] determined how much entropy is created by a nanofluid slip stream when exposed to the impact of the Stefan blowing impact by utilising a changed form of the Buongiorno model. Qing Song and colleagues [29] investigated the flow of a topsy-turvy turning circle. Alsabery *et al.* [30] took a gander at the impact that half-breed nanofluid has on the properties of a blended convection stream in a cover-driven pit. Turkyilmazoglu *et al.* [31] discussed the intensity exchange of nanofluid streams as they passed through an infinitely high-level plate. They did this while considering the effects of radiation caused by two different types of warm boundary conditions. In order to solve the problem of spinning Maxwell liquid in a three-dimensional nano-fluid while it was being hit by an ever-expanding surface, Hayat *et al.* [32] used the homotopy research approach. Sheikholeslami and Shehzad [33] looked into the heat transport of a non-equilibrium nanofluid in the presence of an attractive field and a permeable medium. Their research was published in the journal Nano Letters. The bio-convection of nanofluid through a porous surface that extends vertically was shown by Sarkar *et al.* [34]. Rao *et al.* [37] studied three-dimensional flow of inclined magneto Carreau nanofluid with chemical reactions. Sathyanarayana *et al.* [38] studied the characteristics of MHD nanofluid flow towards a vertical cone under convective cross-diffusion

effects. Archana *et al.* [39] focused on the bidirectionally stretched flow of a Jeffrey liquid with nanoparticles.

This work is persuaded by the past exploration works, and its goal is to research the progression of a two-layered magnetohydrodynamics (MHD) Williamson-nanofluid across an upward cone with heat transfer, mass transfer, pull/infusion, and convective boundary conditions. The review will likely figure out additional details about these parts of the stream. The halfway differential conditions (partial differential equations, PDEs) are controlled by the fundamental Navier-Stokes equation and the Williamson liquid model, and fitting similitude changes are used to transform them into customary differential conditions (ordinary differential equations, ODEs). The conventional differential equations that result are then mathematically addressed using the Runge–Kutta method. The effects of a variety of various physical parameters on the temperature, velocity, and concentration profiles are shown using graphs and tables.

2 Flow governing equations

This research investigates the heat and mass transfer in a continuous flow of Williamson-nanofluid that is viscous and incompressible around a vertical cone when suction/injection and convective boundary conditions are present. The flow is described as being around the cone. The physical coordinates and the geometry of the issue are shown in Fig. 1. The following presumptions have been made with regard to this project:

- The limit calculations are forced by circumstances.
- Brownian movement impacts are likewise thought of.
- The stretching velocity of the surface is taken as $u_w = \dfrac{x\nu}{L^2}$ whereas the suction/injection velocity is denoted as v_w.
- The surface temperature is taken as $T_w = T_\infty + ax^{r_1}$ where $a$is a constant and r_1 is the wall thermal factor.
- The concentration near the surface is expressed as $C_w = C_\infty + ax^{r_2}$ where a is a constant and r_2 is the nanofluid concentration parameter.
- The half place of the cone is given by α, with sweep r of the cone.

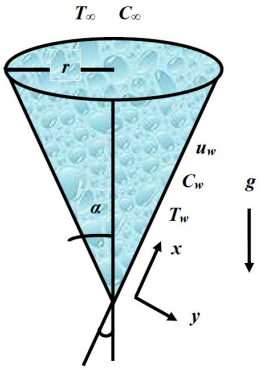

Figure 1: Geometry representation of the fluid flow.

- In light of the above presumptions, the governing equations for consistent, two-layered, electrically directing, incompressible, Williamson-nanoliquid stream are:

Continuity equation:

$$\frac{\partial u}{\partial x} + \frac{\partial v}{\partial y} = 0. \tag{1}$$

Momentum equation:

$$u\frac{\partial u}{\partial x} + v\frac{\partial u}{\partial y} = \nu\frac{\partial^2 u}{\partial y^2} + \sqrt{2}\nu\Gamma\frac{\partial u}{\partial y}\frac{\partial^2 u}{\partial y^2} - \left(\frac{\sigma B_o^2}{\rho_f}\right)u + g\left[\left(1 - C_\infty\right)\rho\beta_T\left(T - T_\infty\right) - \beta_C\left(\rho_p - \rho_f\right)\left(C - C_\infty\right)\right]\cos\alpha. \tag{2}$$

Equation of thermal energy:

$$u\frac{\partial T}{\partial x} + v\frac{\partial T}{\partial y} = \alpha^*\frac{\partial^2 T}{\partial y^2} + \tau_B\left[D_B\frac{\partial C}{\partial y}\frac{\partial T}{\partial y} + \frac{D_T}{T_\infty}\left(\frac{\partial T}{\partial y}\right)^2\right]. \tag{3}$$

Equation of species nanoparticle volume concentration:

$$u\frac{\partial C}{\partial x} + v\frac{\partial C}{\partial y} = D_B\frac{\partial^2 C}{\partial y^2} + \frac{D_T}{T_\infty}\frac{\partial^2 T}{\partial y^2}. \tag{4}$$

The boundary conditions for this flow are:

$$\left.\begin{aligned} u = u_w, \quad v = -v_w(x), \quad -k^*\left(\frac{\partial T}{\partial y}\right) = h_1\left(T_w - T\right), \\ D_B\left(\frac{\partial C}{\partial y}\right) + \frac{D_T}{T_\infty}\left(\frac{\partial T}{\partial y}\right) = 0 \quad \text{at} \quad y = 0, \\ u \to 0, \quad T \to T_\infty, \quad C \to C_\infty \quad \text{as} \quad y \to \infty. \end{aligned}\right\} \tag{5}$$

The following similarity transformations are introduced

$$u = \frac{x\nu}{L^2} f'(\eta), \quad v = -\frac{\nu}{L} f(\eta), \quad \theta = \frac{T - T_\infty}{T_w - T_\infty}, \quad \phi = \frac{C - C_\infty}{C_w - C_\infty}, \quad \eta = \frac{y}{L}. \tag{6}$$

Making help of Eq. (6), the continuity equation is identically fulfilled and Eqs. (2)–(4) get the subsequent forms:

$$f''' + ff'' + \mathrm{We} f''' f'' - \mathrm{We} f' - f'^2 + \mathrm{Gr}\theta \cos\alpha + \mathrm{Gc}\phi \cos\alpha = 0, \tag{7}$$

$$\theta'' + \mathrm{Pr}\, f\theta' - \mathrm{Pr}\, r_1 f'\theta + \mathrm{Pr}\, \mathrm{Nb}\theta'\phi' + \mathrm{Pr}\, \mathrm{Nt}(\theta')^2 = 0, \tag{8}$$

$$\mathrm{Nb}\phi'' + \mathrm{Sc} f\phi' - \mathrm{Sc} r_2 f'\phi + \mathrm{Sc}\mathrm{Nt}\theta'' = 0, \tag{9}$$

and the corresponding boundary conditions (5) become:

$$\begin{gathered} f(0) = \mathrm{S}, \quad f'(0) = 1, \quad \theta'(0) = \mathrm{Bi}\,[\theta(0) - 1], \quad \mathrm{Nb}\phi'(0) + \mathrm{Nt}\theta'(0) = 1, \\ f'(\infty) \to 0, \quad \theta(\infty) \to 0, \quad \phi(\infty) \to 0, \end{gathered} \tag{10}$$

where the involved physical parameters are defined as:

$$\begin{aligned} &\mathrm{We} = \frac{2\sigma B_o^2 L}{\rho_f}, \quad \mathrm{Pr} = \frac{\alpha}{\mu C_p}, \quad \mathrm{Nb} = \frac{\tau D_B\,(C_w - C_\infty)\,h}{\nu}, \\ &\mathrm{Nt} = \frac{\tau D_T\,(T_w - T_\infty)}{\nu T_\infty}, \quad \mathrm{We} = \frac{\sqrt{2}\Gamma}{L} u_w, \\ &\mathrm{Bi} = \frac{Lh_1}{k^*}, \quad \mathrm{Gr} = \frac{gL^2\beta_T\,(T_w - T_\infty)}{\nu u_w}, \\ &\mathrm{Gc} = \frac{gL^2\beta_C\,(C_w - C_\infty)}{\nu u_w}, \quad \mathrm{S} = \frac{v_w L}{\nu}. \end{aligned} \tag{11}$$

Quantities of actual interest, the actual boundaries of the skin-friction coefficient, the nearby Nusselt number and neighbourhood Sherwood number are introduced as follows:

$$C_f = \frac{\tau_w}{\rho u_w^2} = \frac{1}{\rho\left(\frac{x\nu}{L^2}\right)} \mu \left[\frac{\partial u}{\partial y} + \frac{\Gamma}{\sqrt{2}} \left(\frac{\partial u}{\partial y}\right)^2\right]_{y=0}$$

$$\Rightarrow C_f = f''(0) + \frac{\mathrm{We}}{2} \left[f''(0)\right]^2, \tag{12}$$

$$\mathrm{Nu} = \frac{xq_w}{\kappa\,(T_w - T_\infty)} = \frac{\left[-x\frac{\partial T}{\partial y}\right]_{y=0}}{\kappa\,(T_w - T_\infty)} = -\theta'(0), \tag{13}$$

$$\mathrm{Sh} = \frac{xJ_w}{D_B\left(C_w - C_\infty\right)} = \frac{\left[-x\dfrac{\partial C}{\partial y}\right]_{y=0}}{D_B\left(C_w - C_\infty\right)} = -\phi'(0). \tag{14}$$

3 Method of solution

The Runge–Kutta method, along with the shooting approach, can solve non-linear governing equations in terms of partial derivatives. The procedure for this method is shown in Fig. 2. Other numerical approaches provide less precise results than this method. Using similarity transformations, the controlling halfway differential conditions are transformed into common differential conditions. Utilizing extra factors, non-straight conditions are changed over completely to direct conditions. For the conversion of higher

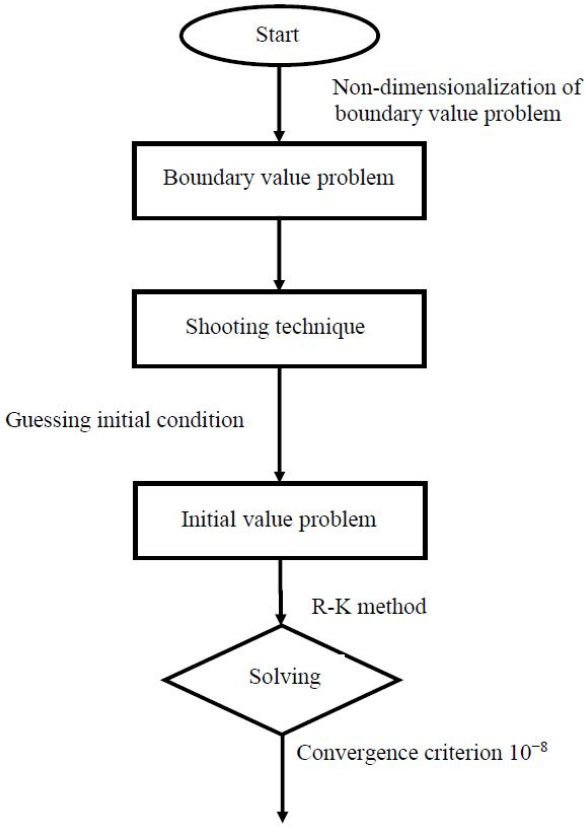

Figure 2: Flow diagram of the numerical procedure.

order to linear differential equations, the following additional variables are introduced:

$$f_1 = f, \quad f_2 = f', \quad f_3 = f'', \quad f_4 = \theta, \quad f_5 = \theta', \quad f_6 = \phi, \quad f_7 = \phi'. \tag{15}$$

Equations (7)–(9) are transformed to the following first order ODEs:

$$\begin{aligned} f_3 &= f_2', \\ f_3' &= -f_1 f_3 - \mathrm{We} f_3' f_3 + \mathrm{We} f_2 + f_2^2 - \mathrm{Gr} f_4 \cos\alpha - \mathrm{Gc} f_6 \cos\alpha, \\ f_5' &= -\mathrm{Pr}\, f_1 f_5 + \mathrm{Pr}\, r_1 f_2 f_4 - \mathrm{Pr}\, \mathrm{Nb} f_5 f_7 - \mathrm{Pr}\, \mathrm{Nt} f_5^2, \\ f_7' &= -\frac{1}{\mathrm{Nb}} \left(-\mathrm{Sc} f_1 f_7 + \mathrm{Sc} r_2 f_2 f_6 - \mathrm{Sc}\, \mathrm{Nt} f_5'\right). \end{aligned} \tag{16}$$

Using Eq. (16), the corresponding boundary conditions (10) are:

$$\begin{aligned} & f_1(0) = \mathrm{S}, \quad f_2(0) = 1, \quad f_5(0) = \mathrm{Bi}\left[f_4(0) - 1\right], \\ & \mathrm{Nb} f_7(0) + \mathrm{Nt} f_5(0) = 1, \\ & f_2(\infty) \to 0, \quad f_4(\infty) \to 0, \quad f_6(\infty) \to 0. \end{aligned} \tag{17}$$

To demonstrate the physical relevance of non-dimensional parameters, the approximate solutions are numerically derived, resulting in a graphical representation using MATLAB bvp4c programming. The iterative approach is repeated until we achieve data that are accurate to a precision of 10^{-6}.

4 Program code validation

For the accuracy and approval of the ongoing model, the current discoveries connected with the skin-friction coefficient and Nusselt number outcomes are contrasted with those of Vajravelu and Nayfeh [35] and Chamkha [36] as shown in Tables 1 and 2.

Table 1: Evaluation of the present skin-friction number results with the previously published skin-friction number results for various r_1.

r_1	Vajravelu and Nayfeh [35]	Chamkha [36]	Present Nusselt number results
–2.1	0.155592	0.155592	0.155488203126587
2.0	0.156001	0.155995	0.155862001723045

Table 2: Evaluation of the present Nusselt number results with the previously published Nusselt number results for various r_1.

r_1	Vajravelu and Nayfeh [35]	Chamkha [36]	Present Nusselt number results
–2.1	2.237475	2.238739	2.228503154257842
2.0	2.232780	2.234070	2.227400532610918

5 Results and discussion

After converting the system of partial differential equations used to study the flow of fluid into a system of ordinary differential equations, it has a set of important parameters that we list in the following order: We, M, Gr and Gc which are the Williamson liquid parameter, magnetic field, thermal Grashof number and solutal Grashof number, while S, Pr, Bi and r_1 represent the suction/injection, Prandtl number, Biot number and thermal wall concentration parameters, respectively; also, r_2, Nb, Nt and Sc are the solutal wall concentration, Brownian motion, thermophoresis and Schmidt number, respectively. The effect of all the previous physical parameters on the velocity, temperature, and concentration distributions has been studied by making graphical figures that clarify this and by showing the physical meanings of each parameter and its importance in this study.

Figure 3 shows the effects of the Williamson fluid parameter on the velocity profile. By increasing the Williamson fluid parameter, there is an increase in the value of velocity. This behaviour is well understood by the physics of the Williamson fluid parameter.

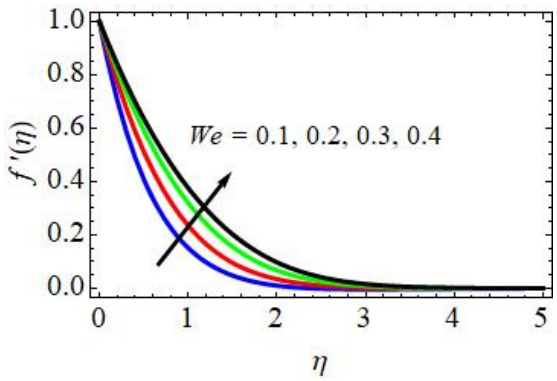

Figure 3: We impact on velocity.

Figures 4 and 5 show the impact of the magnetic field parameter (M) on the flow velocity and temperature, respectively. The fluid velocity was found to decrease and the temperature was found to increase as the magnetic field increased between 0.5, 0.8, 1.0, and 1.2. This is on the grounds that the attractive field gives what is known as a Lorentz force, which is a decelerating body force that acts in the opposite direction to the actual magnetic field. On account of this body force, the progression of the boundary layer as well as the thickness of the energy boundary layer are both decreased. Likewise, it produces heat due to the Lorentz force, which is a fragmentary resistive power that neutralises the velocity of the liquid. In view of this property, the warm boundary layer will be more prominent in thickness when the magnetic field is stronger.

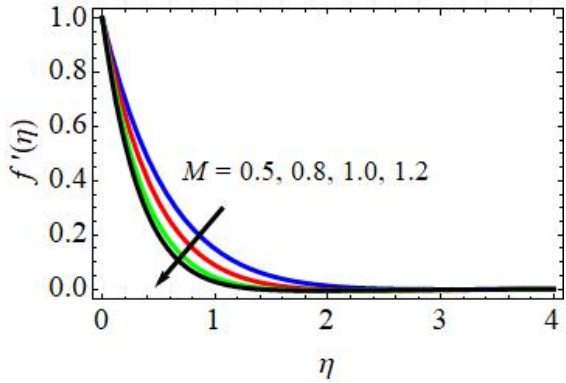

Figure 4: M impact on velocity.

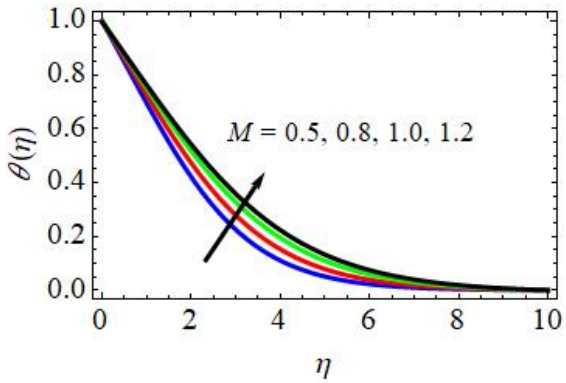

Figure 5: M influence on temperature.

Figure 6 indicates the effect of thermal Grashof number (Gr) on the velocity distribution for a cone. The increased Grashof number enhances the velocity distribution for cones. The increased thermal Grashof number reduces the viscosity of the nanofluid, which decreases the boundary layer thickness. Thus, the reduced viscosity of the nanofluid flow increases the velocity distribution. Figure 7 shows the impact of the solutal Grashof number (Gc) on the velocity distribution. A similar response of the solutal Grashof number to the thermal Grashof number is depicted here. It is noteworthy that the solutal Grashof number has a greater effect for a wedge as compared to a cone. In addition, when Gr = 0 and Gc = 0, the phenomenon has no thermal or solutal buoyancy forces.

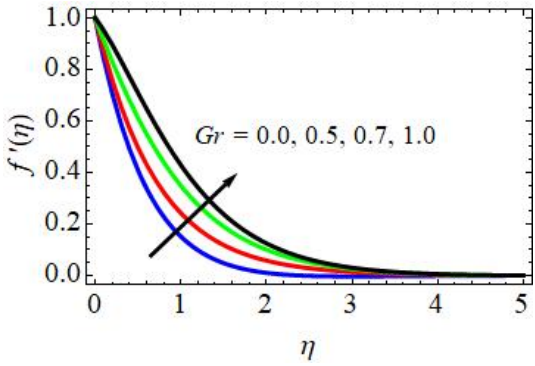

Figure 6: Gr influence on velocity.

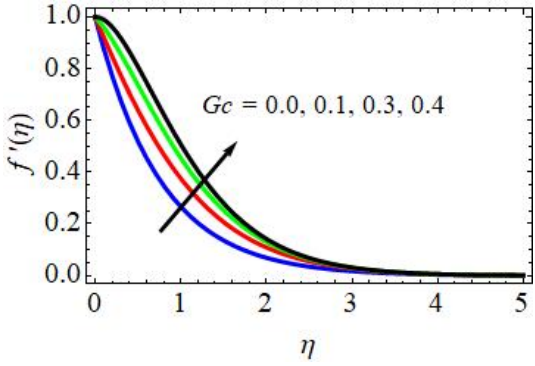

Figure 7: Gc impact on velocity.

Figure 8 illustrate the effect of suction/injection parameter (S) on velocity profiles. The suction/injection parameter controls fluid flow. It is easy to

discern that for greater values of S the velocity profile tends to decrease. For $S < 0$ (injection), the fluid nearest the boundary boosts which increases the flow velocity and the collision between the molecules, which in turn causes an increase in the internal kinetic energy. On the other hand, for $S > 0$ (suction), the fluid near the boundary is sucked, which creates porosity near the boundary, which in turn reduces the velocity profile. Figure 9 shows the impact of the suction/injection parameter (S) on the dimensionless velocity profiles. The curves in Fig. 9 show that the parameter S affects the thickness of the boundary layer. With the rising S, the flow appears to decelerate dramatically. The border layer adheres more tightly to the wall because of suction/injection. As a result, momentum is lost, resulting in a decrease in velocity. As a result of suction/injection, the thickness of the energy boundary layer is decreased.

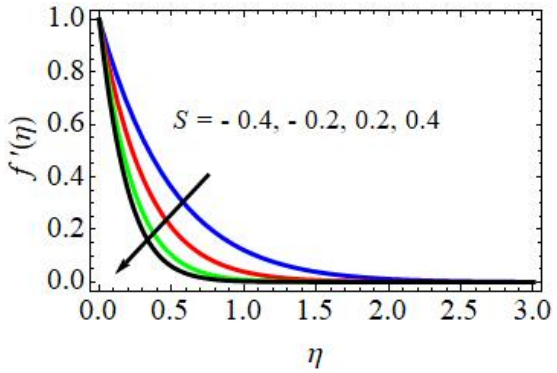

Figure 8: S impact on velocity.

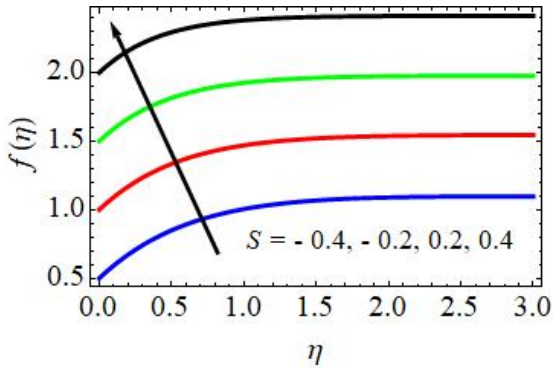

Figure 9: S impact on velocity.

An illustration of the impact of the Prandtl number (Pr) on temperature profiles is presented in Fig. 10 Increased Prandtl numbers over a certain threshold indicate that the temperature is decreased. When the thermal diffusivity and Prandtl number are inverted, a cooling effect is seen. Figure 11 delineates that the warm Biot number has a direct connection with temperature distributions. Figure 11 depicts the upsides of warm increments. The thermal Biot number increase (Bi $>$ 0) means that the heat transfer rate increases, which causes an increase in the temperature profile.

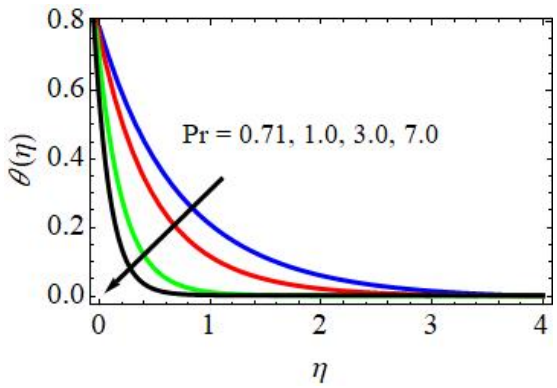

Figure 10: Pr impact on temperature.

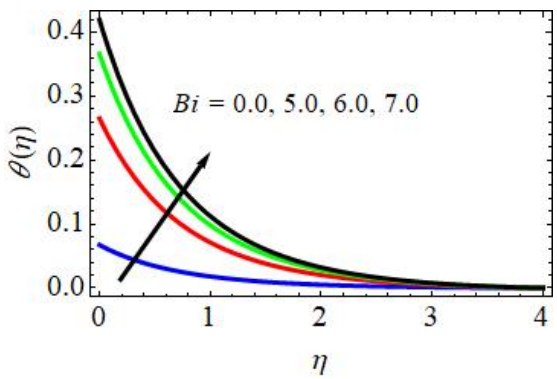

Figure 11: Bi impact on temperature.

Figures 12 and 13 show the impact of the thermal wall factor (r_1) and nanofluid concentration parameter (r_2) on non-dimensional temperature and nanoparticle concentration profiles for a cone. Both the thermal and concentration distributions are reducing functions of wall concentration.

The boundary layer thickness declines with the greater wall concentration. Thus, the reduction in temperature and concentration of the nanofluid flow is depicted.

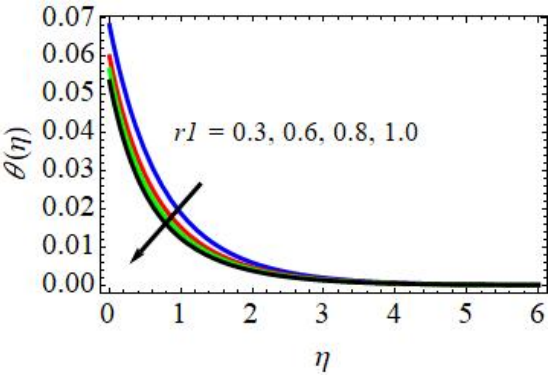

Figure 12: r_1 impact on temperature.

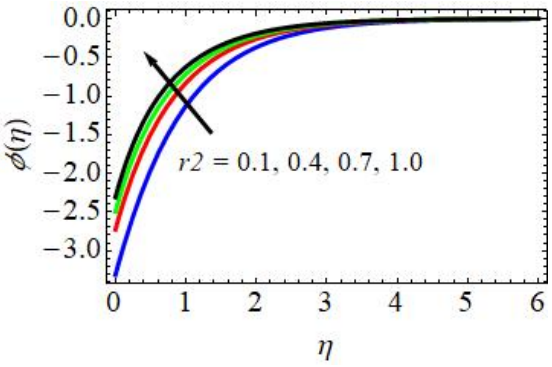

Figure 13: r_2 impact on concentration.

The impact of the Brownian motion parameter (Nb) on temperature and concentration profiles is displayed in Figs. 14 and 15. Figures 14 and 15 show that as the Brownian motion parameter rises, both the temperature and concentration rise.

Figures 16 and 17 uncover the effect of thermophoresis parameter (Nt) on temperature and concentration profiles. Both profiles increase with higher potential gains of Nt. Thermophoresis is the transport force that occurs due to the temperature gradient between layers of the fluid. A higher thermophoresis parameter means that the temperature difference between the

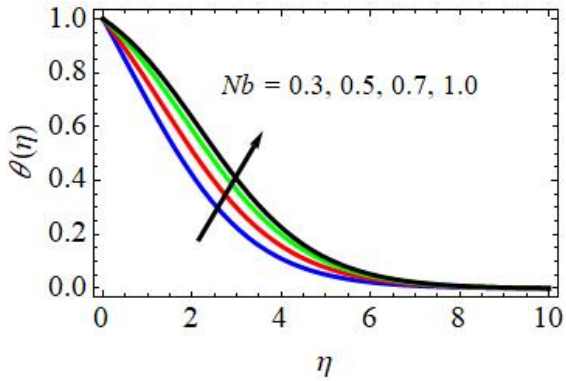

Figure 14: Nb impact on temperature.

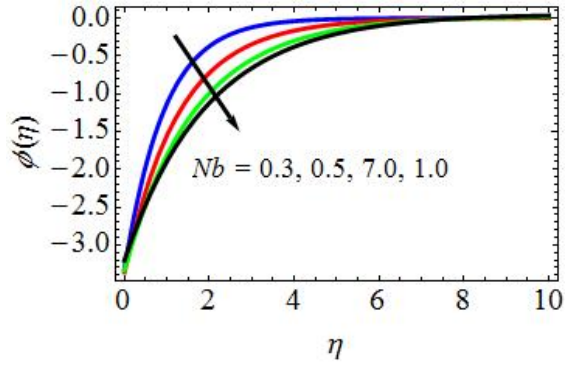

Figure 15: Nb impact on concentration.

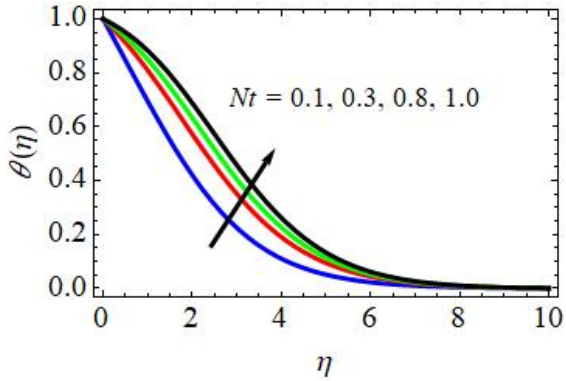

Figure 16: Nt impact on temperature.

layers increases, so the heat transfer rate also increases. By increasing the nanoparticles, the concentration of the fluid increases. With more nanoparticles and more heat transfer between the layers, as Nt increase s, both the temperature and concentration profiles have increased values.

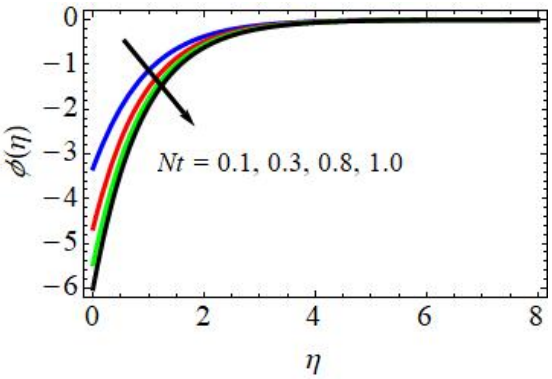

Figure 17: Nt impact on concentration.

Figure 18 depicts the impact of Schmidt number (Sc) on the concentration profile showing that the expanding Sc diminishes the concentration profile since Sc is the proportion of the kinematic viscosity to the molecular diffusion rate.

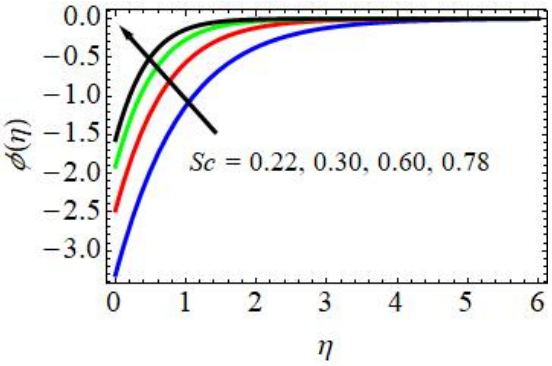

Figure 18: Sc influence on concentration profiles.

Table 3 shows the numerical values of skin-friction coefficient for varying values of the engineering parameters such as We, M, Gr, Gc, Pr, S, Bi, r_1, r_2, Nb, Nt and Sc. From this table, it is observed that the skin-friction coefficient increases with the rising values of Gr, Gc, Bi, Nb, Nt, while it

decreases with the increasing values of We, M, Pr, S, r_1, r_2 and Sc. The numerical values of heat transfer coefficient in terms of the Nusselt number are displayed in Table 4 for different values of Pr, Bi, r_1, Nb and Nt. The heat transfer coefficient gradually rises with the increasing values of Bi, Nb, Nt while the reverse effect is observed for the increasing values of Pr and r_1. The effects of Sc, r_2, Nb and Nt on the mass transfer coefficient in terms of the Sherwood number coefficient are discussed in Table 5. From this table, it is observed that the mass transfer coefficient increases with

Table 3: Skin-friction coefficient (C_f) for various We, M, Gr, Gc, Pr, S, Bi, r_1, r_2, Nb, Nt and Sc.

We	M	Gr	Gc	Pr	S	Bi	r_1	r_2	Nb	Nt	Sc	C_f
0.1	0.5	0.5	0.1	0.71	–0.4	5.0	0.3	0.1	0.3	0.1	0.22	1.263774585842895
0.2												1.227465743637469
0.3												1.176965909390956
	0.8											1.216574017409364
	1.0											1.185683746349504
		0.7										1.302680743987436
		1.0										1.338609348608739
			0.3									1.316758374183899
			0.4									1.346508346984842
				1.0								1.209852676358384
				3.0								1.165787638708037
					–0.2							1.240567896438927
					0.2							1.227678956041874
					0.4							1.205671346648317
						6.0						1.295704360376410
						7.0						1.318578036473463
							0.6					1.236587634806086
							0.8					1.217693960734634
								0.4				1.230738976903837
								0.7				1.214585489259855
									0.5			1.297692365906361
									0.7			1.327651076736500
										0.3		1.307936705163089
										0.8		1.337651756108073
											0.30	1.227693916334563
											0.60	1.216873680746348

the increasing values of Nt and decreases with the increasing values of Sc, r_2 and Nb.

Table 4: Nusselt number for various Pr, Bi, r_1, Nb and Nt.

Pr	Bi	r_1	Nb	Nt	Nu
0.71	5.0	0.3	0.3	0.1	0.349569273975659
1.0					0.303476376573034
3.0					0.286597362937563
	6.0				0.365643377877981
	7.0				0.376982396736472
		0.6			0.317537924073740
		0.8			0.297673969724909
			0.5		0.375676872391038
			0.7		0.398576124087621
				0.3	0.382298459127092
				0.8	0.406976301073374

Table 5: The rate of mass transfer coefficient for different values of Sc, r_2, Nb and Nt.

Sc	r_2	Nb	Nt	Sh
0.22	0.1	0.3	0.1	0.410696923637232
0.30				0.366739692394710
0.60				0.347593477650983
	0.4			0.375657034347986
	0.7			0.354768973991028
		0.5		0.372654701576319
		0.7		0.356767895753858
			0.3	0.436560564563508
			0.8	0.453767901612703

6 Conclusions

In this article, the two-layered, viscous, incompressible, electrically directed attractive progression of the Williamson nanofluid towards an upward cone in the presence of heat and mass transfer was considered. On the other hand, the basic governing partial differential equations were converted into a system of ordinary differential equations using similarity transformations and

the non-dimensional variables under the impacts of the Williamson fluid parameter and magnetic field, Biot number and thermal wall focus, solutal wall fixation, Brownian movement, thermophoresis and Schmidt number on dispersion of velocity, temperature and concentration. The main conclusion drawn from this study are the following:

1. The velocity distribution of the fluid flow is negatively affected by the influence of the magnetic field parameter, the Williamson fluid parameter, and suction or injection, and positively affected by the influence of the thermal Grashof number and the solutal Grashof number.

2. The enhancement in the values of Biot number, thermophoresis number, and Brownian motion resulted in an enhancement of the temperature of the fluid flow, while the opposite occurs with the increasing values of Prandtl number and thermal wall concentration parameters.

3. It was found that the distribution of the concentration of nanoparticles decreased under the influence of Schmidt number, Brownian motion coefficient and solutal wall concentration parameter, while the reverse effect was observed in the presence of the thermophoresis coefficient.

Received 20 November 2022

References

[1] Williamson R.V.: *The flow of pseudoplastic materials.* Ind. Eng. Chem. **21**(1929), 11, 1108–1111.

[2] Aldabesh A., Khan S.U., Habib D., Waqas H., Tlili I., Khan M.I., Khan W.A.: *Unsteady transient slip flow of Williamson nanofluid containing gyrotactic microorganism and activation energy.* Alexandria Eng. J. **59**(2020), 6, 4315–4328.

[3] Krishnamurthy M.R., Prasannakumara B.C., Gireesha B.J., Gorla R.S.R.: *Effect of chemical reaction on MHD boundary layer flow and melting heat transfer of Williamson nanofluid in porous medium.* Eng. Sci. Technol. **19**(2016), 1, 53–61.

[4] M. Amer Q.: *Numerical simulation of heat transfer flow subject to MHD of Williamson nanofluid with thermal radiation.* Symmetry. **13**(2020), 1, 1–10.

[5] Loganathan K., Rajan S.: *An entropy approach of Williamson nanofluid flow with joule heating and zero nanoparticle mass flux.* J. Therm. Anal. Calorim. **141**(2020), 6, 2599–2612.

[6] Dawar A., Shah Z., Islam S., Khan W., Idrees M.: *An optimal analysis for Darcy-Forchheimer three-dimensional Williamson nanofluid flow over a stretching surface with convective conditions*. Adv. Mech. Eng. **11**(2019), 3, 1687814019833510.

[7] Yahya A.U., Salamat N., Habib D., Ali B., Hussain S., Abdal S.: *Implication of bio-convection and Cattaneo-Christov heat flux on Williamson sutter by nanofluid transportation caused by a stretching surface with convective boundary*. Chinese J. Phys.**73**(2021), 706–718.

[8] Sreedevi P., Reddy P.S.: *Williamson hybrid nanofluid flow over swirling cylinder with Cattaneo-Christov heat flux and gyrotactic microorganism*. Wave Random Complex Med. (2021), 1–28. doi: 10.1080/17455030.2021.1968537.

[9] Shafiq A., Sindhu T.N.: *Statistical study of hydromagnetic boundary layer flow of Williamson fluid regarding a radiative surface*. Results Phys. **7**(2017), 3059–3067.

[10] Azam M., Mabood F., Xu T., Waly M., Tlili I.: *Entropy optimized radiative heat transportation in axisymmetric flow of Williamson nanofluid with activation energy*. Results Phys. **19**(2020), 103576.

[11] Ahmed K., Khan W.A., Akbar T., Rasool G., Alharbi S.O., Khan I.: *Numerical investigation of mixed convective Williamson fluid flow over an exponentially stretching permeable curved surface*. Fluids **6**(2021), 7, 260.

[12] Nazir U., Sadiq M.A., Nawaz M.: *Non-Fourier thermal and mass transport in hybridnano-Williamson fluid under chemical reaction in Forchheimer porous medium*. Int. Commun. Heat Mass Transfer. **127**(2021), 105536.

[13] Kumaran G., Sandeep N., Vijayaragavan R.: *Melting heat transfer in magnetohydrodynamic radiative Williamson fluid flow with non-uniform heat source/sink*. IOP Conf. Ser.: Mater. Sci. Eng. **263**(2017), 6, 062022.

[14] Raju C.S., Sandeep N., Ali M.E., Nuhait A.O.: *Heat and mass transfer in 3-D MHD Williamson-casson fluids flow over a stretching surface with non-uniform heat source/sink*. Therm. Sci. **23**(2019), 1, 281–293.

[15] Bhatti M., Arain M., Zeeshan A., Ellahi R., Doranehgard M.: *Swimming of gyrotactic microorganism in MHD Williamson nanofluid flow between rotating circular plates embedded in porous medium: Application of thermal energy storage*. J. Energ. Stor. **45**(2022), 103511.

[16] Shateyi S., Muzara H.: *On the numerical analysis of unsteady MHD boundary layer flow of Williamson fluid over a stretching sheet and heat and mass transfers*. Computation **8**(2020), 2, 30–55.

[17] Nadeem S., Hussain S.T., Lee C.: *Flow of a Williamson fluid over a stretching sheet*. Braz. J. Chem. Eng. **30**(2013), 3, 619–625.

[18] Choi S.U.S., Eastman J.A.: *Enhancing thermal conductivity of fluids with nanoparticles*. In: Proc. ASME Int. Mechanical Engineering Cong. Expo., San Francisco, 12–17 Nov. 1995, 196525.

[19] Suresh S., Venkitaraj K.P., Selvakumar P., Chandrasekar M.: *Effect of Al_2O_3-Cu/water hybrid nanofluid in heat transfer*. Exp. Thermal Fluid Sci. **38**(2012), 54–60.

[20] Nadeem S., Abbas N.: *On both MHD and slip effect in micropolar hybrid nanofluid past a circular cylinder under stagnation point region*. Can. J. Phys. **97**(2018), 4, 392–399.

[21] Devi S.S.U.: *Numerical investigation of three-dimensional hybrid Cu-Al2O3/water nanofluid flow over a stretching sheet with effecting Lorentz force subject to Newtonian heating*. Can. J. Phys. **94**(2016), 5, 490–496.

[22] Khan W.A., Alshomrani A.S., Alzahrani A.K., Khan M., Irfan M.: *Impact of autocatalysis chemical reaction on nonlinear radiative heat transfer of unsteady three-dimensional Eyring-Powell magneto-nanofluid flow*. Pramana **9**1(2018), 5, 1–9.

[23] Lu D., Ramzan M., Ahmad S., Shafee A., Suleman M.: *Impact of nonlinear thermal radiation and entropy optimization coatings with hybrid nanoliquid flow past a curved stretched surface*. Coatings **8**(2018), 12, 414–430.

[24] Khan W. A., Sultan F., Ali M., Shahzad M., Khan M., Irfan M.: *Consequences of activation energy and binary chemical reaction for 3D flow of cross-nanofluid with radiative heat transfer*. J. Braz. Soc. Mech. Sci. Eng. **41**(2019), 1, 1–13.

[25] Khan W.A., Ali M., Sultan F., Shahzad M., Khan M., Irfan M.: *Numerical interpretation of autocatalysis chemical reaction for nonlinear radiative 3D flow of cross magneto-fluid*. Pramana **92**(2019), 2, 1–16.

[26] Khan M.S., Karim I., Islam M. S., Wahiduzzaman M.: *MHD boundary layer radiative, heat generating and chemical reacting flow past a wedge moving in a nanofluid*. Nano Converg. **1**(2014), 1, 1–13.

[27] Motsumi T.G., Makinde O.D.: *Effects of thermal radiation and viscous dissipation on boundary layer flow of nanofluids over a permeable moving flat plate*. Phys. Scr. **86**(2012), 6, 045003.

[28] Rana P., Shukla N., Bég O.A., Bhardwaj A.: *Lie group analysis of nanofluid slip flow with Stefan blowing effect via modified Buongiorno's model: entropy generation analysis*. Differ. Equ. Dyn. Syst. **29**(2021), 193–210.

[29] Song Y.Q., Khan S.A., Imran M., Waqas H., Khan S.U., Khan M.I., Chu Y.M.: *Applications of modified Darcy law and nonlinear thermal radiation in bioconvection flow of micropolar nanofluid over an off centered rotating disk*. Alexandr. Eng. J. **60**(2021), 5, 4607–4618.

[30] Alsabery A. I., Tayebi T., Kadhim H. T., Ghalambaz M., Hashim I., Chamkha A. J.: *Impact of two-phase hybrid nanofluid approach on mixed convection inside wavy lid-driven cavity having localized solid block*. J. Adv. Res. **30**(2021), 63–74.

[31] Turkyilmazoglu M., Pop I.: *Heat and mass transfer of unsteady natural convection flow of some nanofluids past a vertical infinite flat plate with radiation effect*. Int. J. Heat Mass Tran. **59**(2013), 167–171.

[32] Hayat T., Muhammad T., Shehzad S. A., Alsaedi A.: *Three-dimensional boundary layer flow of Maxwell nanofluid: mathematical model*. Appl. Math. Mech. **36**(2015), 6, 747–762.

[33] Sheikholeslami M., Shehzad S. A.: *Simulation of water based nanofluid convective flow inside a porous enclosure via non-equilibrium model*. Int. J. Heat Mass Transf. **120**(2018), 1200–1212.

[34] Sarkar A., Das K., Kundu P.K.: *On the onset of bioconvection in nanofluid containing gyrotactic microorganisms and nanoparticles saturating a non-Darcian porous medium*. J. Mol. Liq. **223**(2016), 725–733.

[35] Vajravelu K., Nayfeh J.: *Hydromagnetic convection at a cone and a wedge*. Int. Commun. Heat Mass Transf. **19**(1992), 701–710.

[36] Chamkha A.J.: *Non-Darcy hydromagnetic free convection from a cone and a wedge in porous media*. Int. Commun. Heat Mass Transf. **23**(1996), 875–887.

[37] Rao BM., Gopal D., Kishan N., Ahmed S., Prasad P.D.: *Heat and mass transfer mechanism on three-dimensional flow of inclined magneto Carreau nanofluid with chemical reaction*. Arch. Thermodyn. **41**(2020), 6, 223–38.

[38] Sathyanarayana M., Ramakrishna Goud T.: *Characteristics of MHD nanofluid flow towards a vertical cone under convective cross-diffusion effects through numerical solutions*. Heat Transfer. **52**(2022), 2, 1734–1753.

[39] Archana M., Gireesha B.J., Rashidi M.M., Prasannakumara B.C., Gorla R.S.: *Bidirectionally stretched flow of Jeffrey liquid with nanoparticles, Rosseland radiation and variable thermal conductivity*. Arch. Thermodyn. **39**(2018), 4, 33–57.

archives
of thermodynamics
Vol. **44**(2023), No. 2, 139–157
DOI: 10.24425/ather.2023.146562

3D simulation of incompressible flow around a rotating turbulator: Effect of rotational and direction speed

ELHADI ZOUBAI[a]
HOUSSEM LAIDOUDI[a*]
ISMAIL TLANBOUT[a]
OLUWOLE DANIEL MAKINDE[b]

[a] University of Science and Technology of Oran Mohamed-Boudiaf, Faculty of Mechanical Engineering, Laboratory of Sciences and Marine Engineering, BP 1505, El-Menaouer, Oran, 31000, Algeria

[b] Stellenbosch University, Faculty of Military Science, Private Bag X2, Saldanha 7395, South Africa

Abstract This paper presents new results for the dynamic behaviour of fluid around a rotating turbulator in a channel. The turbulator has a propeller form which is placed inside a flat channel. The research was carried out using 3D numerical simulation. The rationale of the experiment was as follows: we put a propeller-turbulator inside a flat channel, and then we insert a water flow inside the channel. The turbulator rotates at a constant and uniform speed. The main points studied here are the effect of the presence of turbulator and its rotational direction on the flow behaviour behind the turbulator. The results showed that the behaviour of flow behind the turbulator is mainly related to the direction of turbulator rotating. Also, the studied parameters affect coefficients of drag force and power number. For example, when the turbulator rotates in the positive direction, the drag coefficient decreases in terms of rotational speed of the turbulator, while the drag coefficient increases in terms of rotational speed when the turbulator rotates in the negative direction.

Keywords: Rotating turbulator; Straight tube; Drag coefficient; Power number; Laminar flow

*Corresponding Author. Email: houssem.laidoudi@univ-usto.dz

Nomenclature

A	–	frontal surface, m^2
C_D	–	coefficients of drag force
c	–	thickness of the core, m
D	–	total diameter of the propeller, m
d	–	diameter of the core, m
F_D	–	drag force, N
J	–	advance ratio
H	–	diameter of the channel, m
N_p	–	power number
P	–	dimensionless pressure
p	–	pressure, Pa
Re	–	Reynolds number
T	–	torque, J
U, V, W	–	dimensionless components of velocity
u, v, w	–	components of velocity, m/s
u_{in}	–	inlet velocity, m/s
X, Y, Z	–	dimensionless coordinates
x, y, z	–	Cartesian coordinates, m/s

Greek symbols

μ	–	dynamic viscosity, Pa·s
ρ	–	density, kg/m^3

1 Introduction

Many recent studies aim to induce geometric changes for the purpose of accelerating the flow within the channel. This dynamic behaviour can be exploited to speed up the fluid mixing process [1–3], or increase the process transferring in thermal applications [4–6]. Previous studies showed that the presence of a solid body inside a channel accelerates the movement of the flow as it passes around this body. The shape and the position of the body also play a role in the dynamic behaviour of the flow [7–10]. On the other hand, a group of researchers focused on changing the shape of the outer wall of the channel in order to develop the dynamic behavior of the fluid [11–14].

With regard to the previous work related to the subject, we mention the following: Fang *et al.* [15] studied the flow of a fluid inside a straight channel, and in order to accelerate the flow, an innovative turbulator was added inside the channel. The study included the effect of the turbulator shape. The results showed that the invented forms have a strong effect on accelerating the flow, and therefore there is a stimulation of thermal ac-

tivity.Farshad and Sheikholeslami [16] investigated the development of the stream velocity inside a canal. For this purpose, they added a turbulator whose cross-section is spiral in shape. The body is placed along the channel, and its streamlined form does not hinder the movement of the flow. The study showed that this shape helps to create a circular flow, which in turn enhances the thermal activity between the fluid and the channel. Yan *et al.* [17] studied the effect of a double tube inside a channel in order to determine its effect on the flow velocity. The study also included the impact of thermal properties on the heat transfer. It was estimated that this new design of the system can enhance the mass transfer which has a direct reflection on the heat transfer.Ebrahimpour and Sheikholeslami [18] studied the system of absorbing heat from the sun. This system relies on a straight channel placed above a thermal collector. Inside the channel, fluid passes through and absorbs energy. For the purpose of developing the fluid behaviour, a longitudinal turbulator was placed inside the channel. The study showed that the spiral shape of the tabulator causes the flow to move in a spiral manner, which increases its speed and has an increase in thermal absorption capacity of the fluid from the channel wall. Sheikholeslami *et al.* [19] inserted turbulators into a channel with the aim of strengthening the fluid's dynamic performance. This study was carried out in order to develop the thermal system of the channel, which is used in thermal exchangers related to clean energy. The new shape of these turbulators is that theycontain holes, which allows for reducing the resistance of the turbulators to fluid flow, in return accelerating the flow. The results showed an improvement in the speed of the flow with significant development in thermal activity. In general, there are other works aimed at studying the shape of the inner turbulator and its spiral form on the general system of the stream [20–25].

There is also another type of turbulator, in the form of fixed rings placed in the centre of the channel. When the liquid passes around it, the flow path changes from a parallel shape to a circular shape. Among these works, we mention for example: Shafee *et al.* [26]. The shape of the ring is spiral and circular. This geometry allowed the flow to accelerate in a superior way, which effectively reflected the thermal activity of the fluid. Nakhchi *et al.* [27] and Bellos *et al.* [28] used a cylindrical turbulator that was hollow inside and had holes that allowed the liquid to pass through. That proposed form was found to have a high influence on the behaviour of the fluid.

Other researchers have combined the existence of more than two turbulators placed in parallel [29–31]. Also a positive development of the fluid

was elicited. Furthermore, there are also some works directly related to the subject under study [32–35].

It has already been noted from the previous works that the presence of a turbulator inside the straight channel increases the flow velocity, and this is what makes the thermal activity better for the fluid. Despite this, there are few works on propeller-shaped turbulators rotating at a constant speed. For this reason, this work aims to bridge this gap. In general, this paper aims to present the simulation of flow in a channel with a turbulator in the form of a propeller rotating at a constant speed. The purpose of this study is to understand the influence of both the speed of rotation of the turbulator and its direction of rotation on the dynamic and kinematic activity of the flow. This work can be used in many applications including a primarily thermal solar panel, thermal exchangers and semi-static mixers.

2 Physical problem and mathematical equations

The domain to be studied is described in Fig. 1. The domain is a straight channel with a propeller-turbulator rotating at a constant speed (Fig. 1a). The flow enters the channel uniformly at a constant initial velocity and exits from the other end of the channel. Fig. 1b represents the cross-section of the turbulator with the channel. The propeller-turbulator is composed of four blades and a core of diameter (d). The total diameter of the propeller is given by (D). Also, the diameter of the channel is given by the symbol (H). Furthermore, Fig. 1b shows the positive direction of the propeller. Figure 1c shows the longitudinal section of the turbulator. The thickness of the core is denoted by the symbol (c). The propeller blades are directed at an angle of 45°. All these channel and turbulator geometric proprieties are set in Table 1.

Table 1: Geometrical characteristics of the studied domain

D/H	d/H	c/H
0.65	0.25	0.5

The fluid used in this research is water, which has the following properties: density (ρ) is 998 kg/m^3, dynamic viscosity (μ) is 0.00000232 Pa·s. The flow entering the channel has a constant velocity determined by the Reynolds

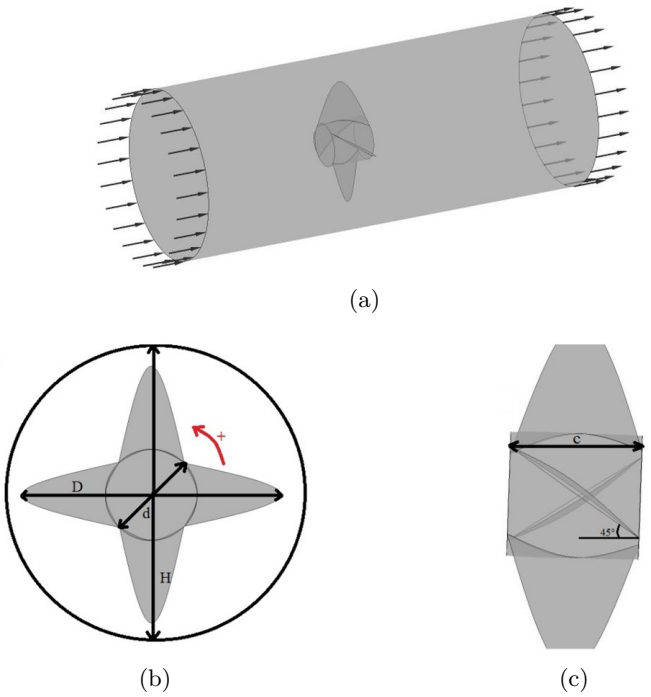

(a) (b) (c)

Figure 1: The studied physical domain: (a) general view of the turbulator with a channel, (b) cross-section of the turbulator, (c) longitudinal section of the turbulator.

number (Re = 100), while the Reynolds number is given by the following expression:

$$\mathrm{Re} = \frac{\rho u_{\mathrm{in}} D}{\mu}\,, \tag{1}$$

where u_{in} denotes the velocity value at the channel entrance.

The differential equations needed to be solved to achieve numerical simulation of the problem areas follows [36–43]:

$$\frac{\partial U}{\partial X} + \frac{\partial V}{\partial Y} + \frac{\partial W}{\partial Z} = 0\,, \tag{2}$$

$$U\frac{\partial U}{\partial X} + V\frac{\partial U}{\partial Y} + W\frac{\partial U}{\partial Z} = -\frac{\partial P}{\partial X} + \frac{1}{\mathrm{Re}}\left(\frac{\partial^2 U}{\partial X^2} + \frac{\partial^2 U}{\partial Y^2} + \frac{\partial^2 U}{\partial Z^2}\right), \tag{3}$$

$$U\frac{\partial V}{\partial X} + V\frac{\partial V}{\partial Y} + W\frac{\partial V}{\partial Z} = -\frac{\partial P}{\partial Y} + \frac{1}{\mathrm{Re}}\left(\frac{\partial^2 V}{\partial X^2} + \frac{\partial^2 V}{\partial Y^2} + \frac{\partial^2 V}{\partial Z^2}\right), \tag{4}$$

$$U\frac{\partial W}{\partial X}+V\frac{\partial W}{\partial Y}+W\frac{\partial W}{\partial Z}=-\frac{\partial P}{\partial Z}+\frac{1}{\mathrm{Re}}\left(\frac{\partial^2 W}{\partial X^2}+\frac{\partial^2 W}{\partial Y^2}+\frac{\partial^2 W}{\partial Z^2}\right), \quad (5)$$

where U, V, and W are the dimensionless component of velocity along X, Y, and Z directions, respectively, P is the dimensionless pressure, and Re is Reynolds number.

These equations are written in non-dimensional form after setting these variables:

$$(X,Y,Z)=\frac{(x,y,z)}{D}, \quad (U,V,W)=\frac{(u,v,w)}{u_{\mathrm{in}}}, \quad P=\frac{p}{\rho u_{\mathrm{in}}^2}, \quad (6)$$

where x, y and z are the directions in Cartesian coordinate system, u, v, and w are the velocity component, p is the pressure, and u_{in} is the flow velocity at the inlet.

The turbulator is characterized by a constant called the advance ratio (J). It relates the velocity of the flow at the channel inlet to the speed of rotation of the turbulator:

$$J=\frac{u_{\mathrm{in}}}{nD}, \quad (7)$$

where n is the rotational speed. $J = 0.2$ to 0.9. When J increases, the rotational speed of the turbulator decreases.

The power number of the turbulator can be calculated as:

$$N_p=\frac{T}{\rho n^2 D^5}, \quad (8)$$

where T is the torque. The drag coefficient of the turbulator is calculated as:

$$C_D=\frac{F_D}{0.5\rho n^2 A}, \quad (9)$$

where F_D is the drag force exerted by the flow on the turbulator, A is the frontal surface of the propeller.

The appropriate boundary conditions for these non-dimensional equations are:

- at the inlet of the channel:

$$U=1, \quad V=0, \quad W=0, \quad (10)$$

- at the channel and turbulator walls – no-slip condition:

$$U=0, \quad V=0, \quad W=0, \quad (11)$$

- at the outlet tube – the Neumann condition:

$$\frac{\partial U}{\partial X} = 0, \quad \frac{\partial V}{\partial X} = 0, \quad \frac{\partial W}{\partial X} = 0. \tag{12}$$

3 Grid independency test and validation test

The propeller-turbulator geometry as well as the mesh were created using Gambit [44]. The number of mesh elements was set after checking its effectiveness and the results of this test are shown in Table 2. This table shows variations of the coefficient N_p in terms of mesh element number for $J = 0.8$ and $\mathrm{Re} = 100$. It is noted that the mesh of the second case of 883113 elements is very suitable for solving the above equations. We mention that the form of the mesh element is triangular. The elements are concentrated around the propeller to determine correctly the calculated results.

Table 2: Results of grid independency test

Case	Elements	Power number	Variation, %
1	441556	1.55984	2.07
2	883113	1.52743	0.23
3	1766226	1.52389	–

The numerical technique used in this research is called multiple reference frames (MRF). This technique is based on dividing the domain of computation into two main parts. The first is rotating and the second is fixed. Figure 2 illustrates this technique in the studied domain. The differential equations were solved using finite volume method (FVM). The high-resolution

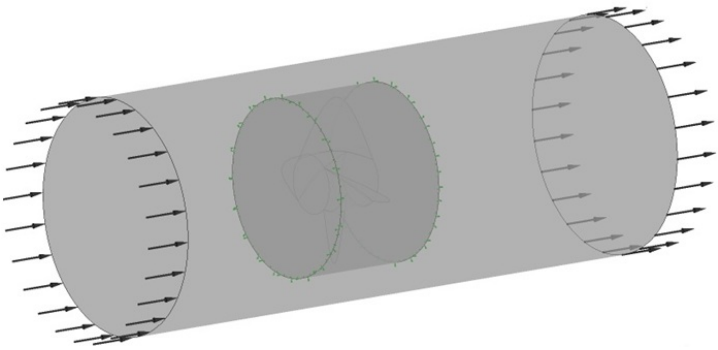

Figure 2: MRF method for the present geometry.

discretisation scheme was used for solving the convective term, whereas the SIMPLEC (semi-implicit method for pressure linked equations-consistent) algorithm was used for coupling pressure and velocity. The relative error of calculations was 10^{-6} for momentum and continuity equations.

In order to validate this technique to reach accurate results, we conducted a test where we compared the results of this technique with previous research. The comparison was made with research done by Ameur and Bouzit [37]. The comparison was made on a two-bladed impeller. The values of the coefficient N_p are presented in Fig. 3 in terms of rotational speed of the mixer (Re). Figure 3 shows that the applied technique (MRF) is very accurate in determining the results.

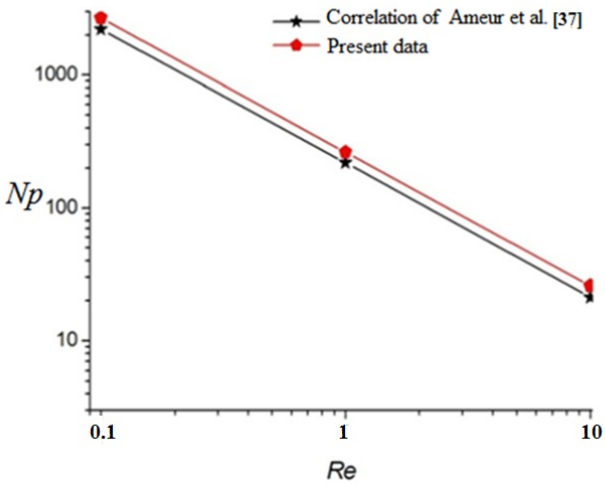

Figure 3: Validation test – comparison with the work of Ameur and Bouzit [37].

4 Results and discussion

Through this work, numerical experience is gathered on the effects of rotating turbulator within a tube channel. The research presents new results about the effect of rotational speed of the turbulator, as well as the direction of its rotation on flow behind the turbulator. To get an accurate understanding, numerical simulation results are presented in the form of streamlines and contours of velocity. In addition to all this, values of the coefficients N_p and C_D are presented in terms of the studied parameters.

Figure 4 shows a 3D representation of the rotating turbulator and the streamlines behind it for a constant value of the factor $J = 0.7$. Figure 4 shows the effect of the direction of rotation of the turbulator on the hydrodynamic behaviour of the fluid in the back. It is clearly noticed that the direction of the rotation greatly affects the performance of the turbulator, that is, the flow motion in the first case (positive direction) is more circular compared to the second case (negative), and this is a result of the shape of the turbulator blades.

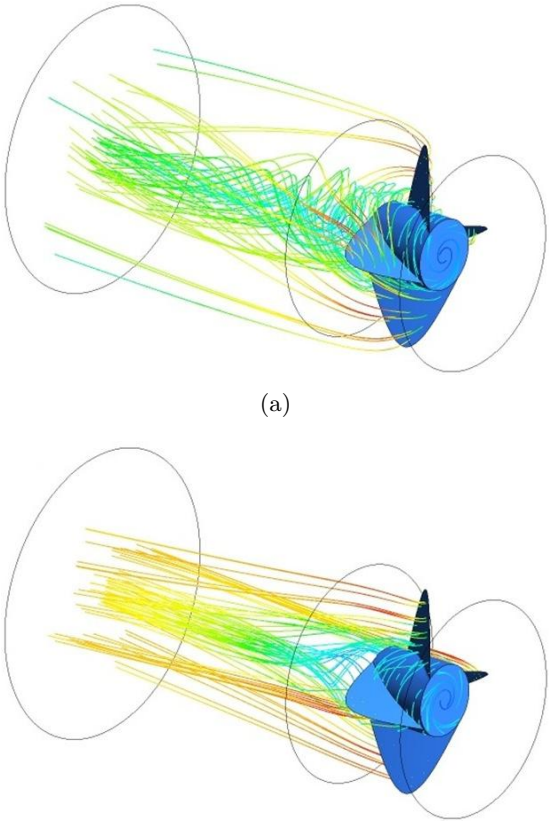

(a)

(b)

Figure 4: Streamlines behind the turbulator for $J = 0.7$: (a) turbulator rotates in the positive direction, (b) the turbulator rotates in the negative direction.

Figures 5 and 6 illustrate the streamlines of several cross-sections of the tube. The first section is before the turbulator; the second is located just behind the turbulator; the third section is after the turbulator. The purpose

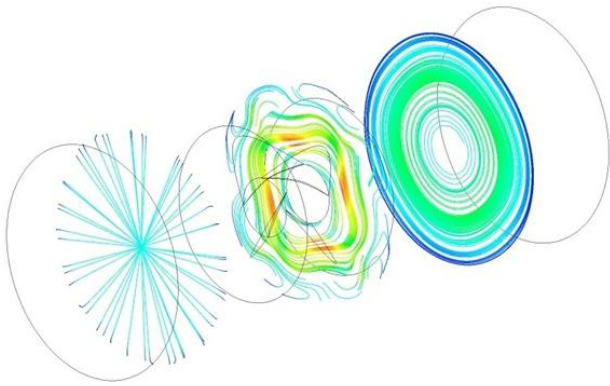

$J = 0.3$

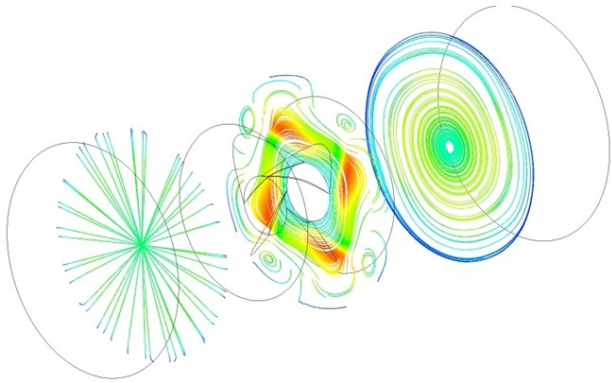

$J = 0.6$

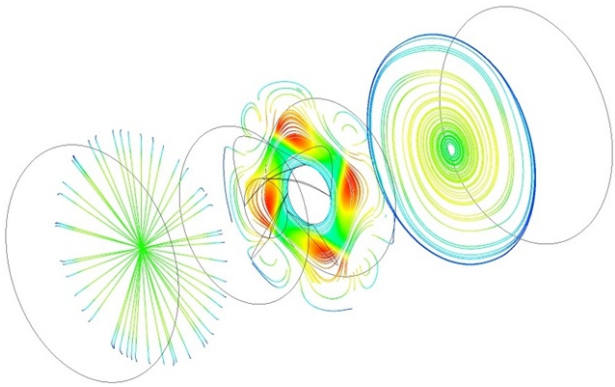

$J = 0.9$

Figure 5: Two-dimensional streamlines for the positive rotational direction of the turbulator for different values of J.

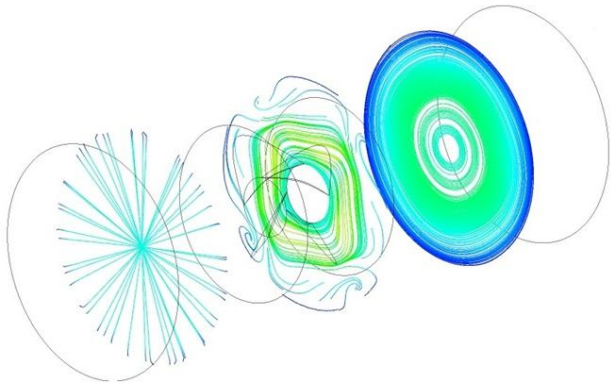

$J = 0.3$

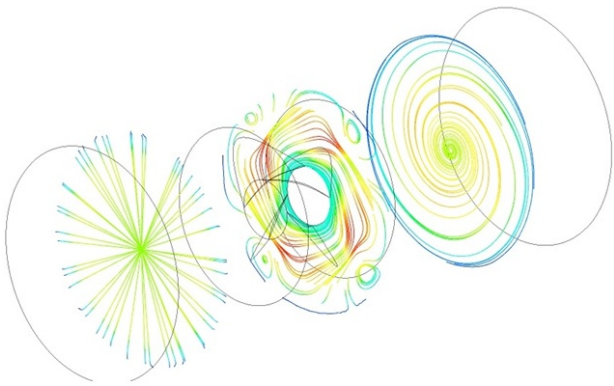

$J = 0.6$

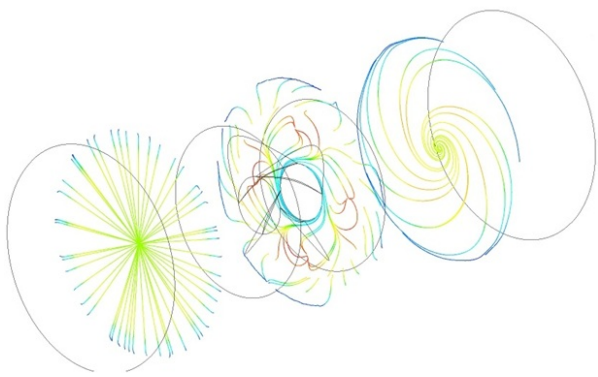

$J = 0.9$

Figure 6: Two-dimensional streamlines for the negative rotational direction of the turbulator for different values of J.

of these figures is to understand exactly the behaviour of the flow along the tube, i.e. before and after the turbulator. Figure 5 is for the positive rotation of the turbulator. Meanwhile, Fig. 6 is for the negative direction. We also mention that the higher the value of factor J, the rotational speed of the turbulator is decreased. The two figures show that the dynamic behaviour of the flow is divided into three main parts. The first part is before the turbulator, and here the flow is stable and regular. The second part is near the turbulator from the back side, and here we notice that the flow changes its regular pattern to a circular pattern due to the circular movement of the turbulator. In this section, we notice a large vortex inside the section with small vortices near the inner wall of the tube. The reason for the formation of small vortices is due to the difference in pressure between the ends of the turbulator blades (four small vortices for four blades). In the third part, the flow becomes purely rotational, having only a main vortex. Moreover, through the third section, we can deduce the direction of the flow motion and the turbulator as well.

Figures 7 and 8 show contours of dimensionless velocity along the channel. The longitudinal view of these figures was taken in the middle of the channel. The figures show the effect of direction of rotation of the turbulator and the effect of rotational speed on the local distribution of flow velocity. It is noticed in all cases that the maximum value of the velocity is located at the turbulator sides. For the first case (Fig. 7), the values of velocity behind the turbulator increase with a gradual increase in the rotational speed of the turbulator. For the second case (Fig. 8), the values of velocity behind the turbulator remain almost constant with the increasing rotational speed of the turbulator. Furthermore, in both cases, the higher the rotational speed of the turbulator, the lower the value of the maximum flow velocity at the turbulator side. In general, it is noted that the flow velocity increases significantly after passing through the turbulator. In addition, the flow velocity values are higher when the turbulator rotates in the positive direction.

Figure 9 represents the variation of the power number (N_p) in terms of the factor J and the direction of rotation of the turbulator. This coefficient indicates the mechanical power required for the turbulator to rotate. It is well shown that in the first case, the rotation of the turbulator creates a thrust for the propeller in the opposite direction to the flow entering the channel, so it is noted that the values of the power number are much larger as compared to the second case. Also, the values of this number increase with the decreasing rotational speed of the turbulator in the first case.

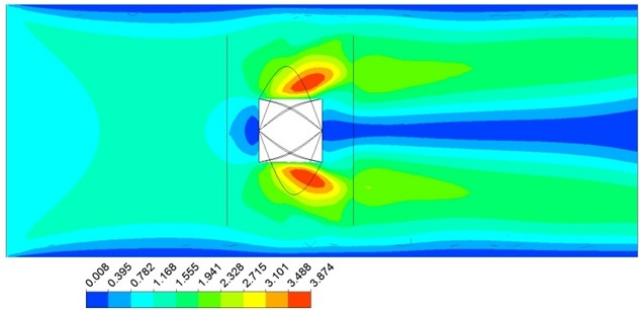

$J = 0.3$

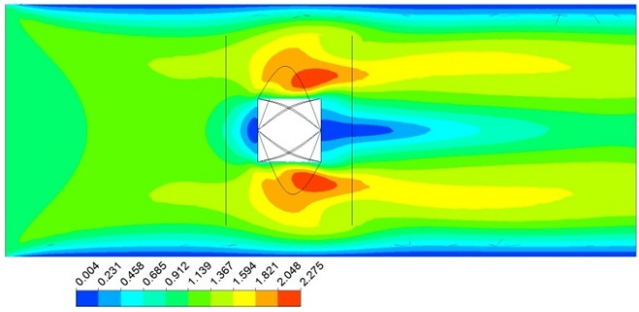

$J = 0.6$

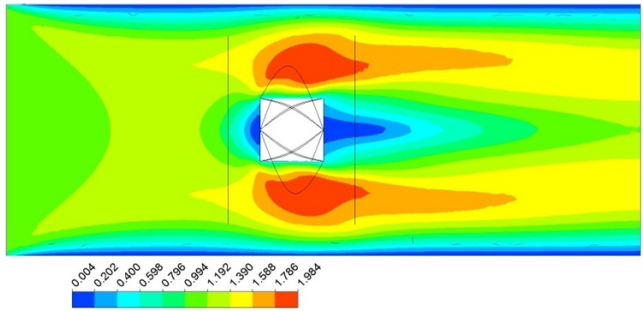

$J = 0.9$

Figure 7: Contours of dimensionless velocity for the positive rotational direction of the turbulator for different values of J.

On the other hand, in the second case, the resulting thrust is in the same direction as the flow, so the values of the power number is lower. Also, there is a different trend in the relationship as compared to the first case. There is a maximum value of N_p when J takes the value of 0.6.

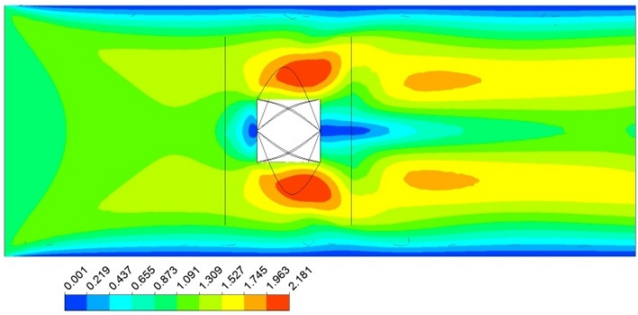

$J = 0.3$

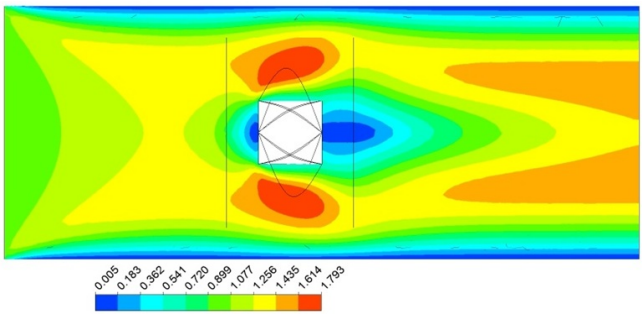

$J = 0.6$

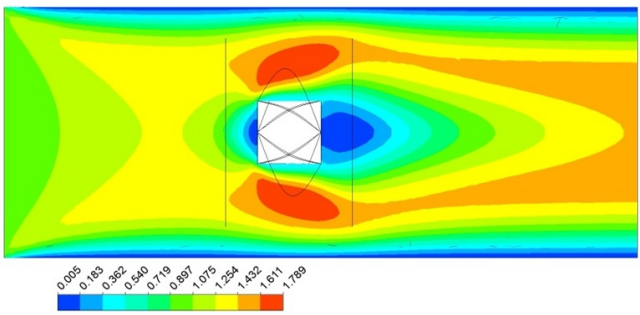

$J = 0.9$

Figure 8: Contours of dimensionless velocity for the negative rotational direction of the turbulator for different values of J.

Figure 10 presents the variation of the drag coefficient in terms of factor J and direction of the turbulator rotation. Obviously, the values of this coefficient in the first case are greater than in the second case. In addition to this, in the first case, the higher the value of factor J, the lower the

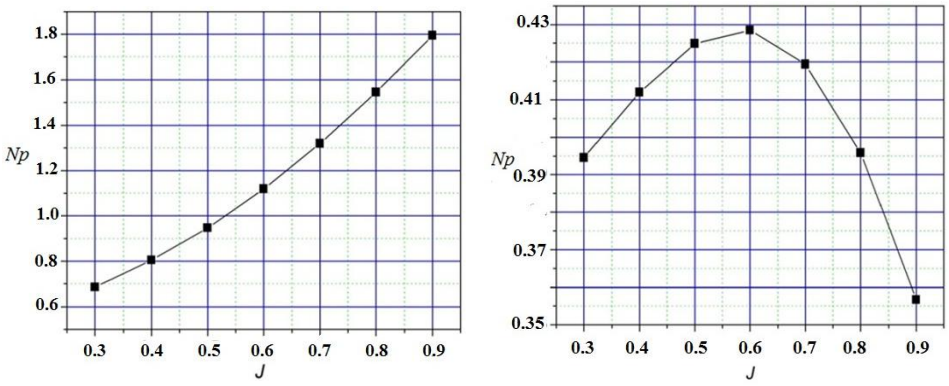

Figure 9: Variation of power number (N_p) of the turbulator *versus* J: (a) for the case of positive direction, (b) for the case of negative direction.

value of drag coefficient, while in the second case, the decrease in the rotational speed of the turbulator increases the value of this coefficient. This shows that in the first case, the thrust force of the turbulator is in the direction opposite to the flow motion, while in the second case, the thrust force of the turbulator is in the same direction as the flow entering the tube.

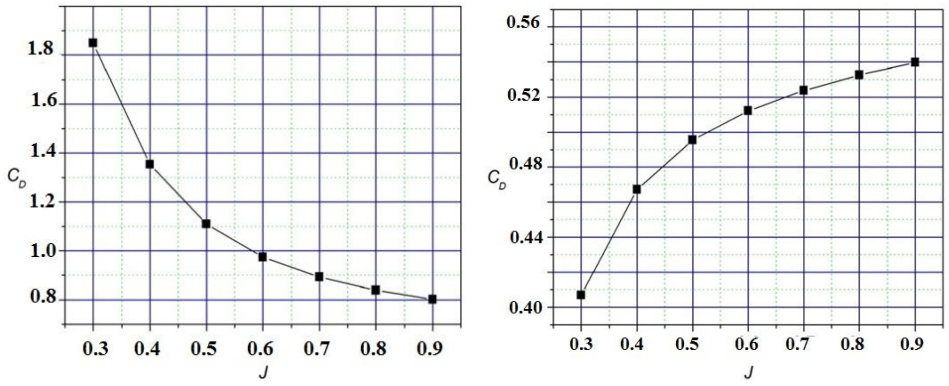

Figure 10: Variation of drag coefficient (C_D) of the turbulator *versus* J: (a) for the case of positive direction, (b) for the case of negative direction.

5 Conclusions

In this work, we performed a numerical simulation of a marine turbulator inside a straight channel. The purpose of this study was to understand the hydrodynamic behaviour of flow in this case. The elements studied here are the speed and direction of rotation of the turbulator, while the velocity of the flow entering the channel is constant and determined in terms of the Reynolds number equal to 100. The main points drawn from this work are:

- The turbulator rotation in the first case (positive rotation) creates an opposite thrust to the directionof flow entering the channel.
- The thrust force of the turbulator in the second case (negative rotation) has the same direction as the flow motion.
- The dynamic behaviour of the water inside the channel is divided into three main parts: the first part extends from the entrance of the canal to the end of the turbulator; the second part is from the back of the turbulator a little backwards, then the third part begins where the flow motion becomes perfectly circular.
- It was concluded that the presence of the rotating turbulator in the canal accelerates the flow and makes the velocity higher near the canal wall.
- With regard to the effect of rotation direction, it was found that when the turbulator rotates in the positive direction, a higher flow is produced near the canal wall compared to the negative direction.

Received 16 February 2023

References

[1] Ameur H.: *Agitation of yield stress fluids in different vessel shapes.* Eng. Sci. Technol. Int. J. **19**(2016), 1, 189–196.

[2] Laidoudi H.: *Hydrodynamic analyses of the flow patterns in stirred vessel of two bladed impeller.* J. Serb. Soc. Comput. Mech. **14**(2020), 2, 117–132.

[3] Mishra V.P., Kumar P., Joshi J.B.: *Flow generated by a disc turbine in aqueous solutions of polyacrylamide.* Chem. Eng. J. **71**(1998), 1, 11–21.

[4] Acharya N.: *Magnetized hybrid nanofluid flow within a cube fitted with circular cylinder and its different thermal boundary conditions.* J. Magn. Magn. Mater. **564**(2022), 2, 170167.

[5] Laidoudi H., Bouzit M.: *The effect of asymmetrically confined circular cylinder and opposing buoyancy on fluid flow and heat transfer.* Defect Diffus. Forum **374**(2017), 18–28

[6] Dawar A., Acharya N.: *Unsteady mixed convective radiative nanofluid flow in the stagnation point region of a revolving sphere considering the influence of nanoparticles diameter and nanolayer.* J. Indian Chem. Soc. **99**(2022), 10, 100716.

[7] Goldanlou A.S., Sepehrirad M., Papi M., Hussein A. K., Afrand M., Rostami S.: *Heat transfer of hybrid nanofluid in a shell and tube heat exchanger equipped with blade-shape turbulators.* J. Therm. Anal. Calorim. **143**(2021), 1689–1700.

[8] Saleh B., Sundar L.S., Aly A. A., Ramana E. V., Sharma K. V., Afzal A., Abdelrhman Y., Sousa A.C.M.: *The Combined effect of Al_2O_3 nanofluid and coiled wire inserts in a flat-plate solar collector on heat transfer, thermal efficiency and environmental CO_2 Characteristics.* Arab. J. Sci. Eng. **47**(2022), 9187–9214.

[9] Rani P., Tripathy P.P.: *Heat transfer augmentation of flat plate solar collector through finite element-based parametric study.* J. Therm. Anal. Calorim. **147**(2022), 639–660.

[10] Laidoudi H., Helmaoui M., Bouzit M., Ghenaim A.: *Natural convection of Newtonian fluids between two concentric cylinders of a special cross-sectional form.* Therm. Sci. **25**(2021), 5, 3701–3714.

[11] Zaboli M., Ajarostaghi S.S.M., Saedodin S., Kiani B.: *Hybrid nanofluid flow and heat transfer in a parabolic trough solar collector with inner helical axial fins as turbulator.* Eur. Phys. J. Plus. **136**(2021), 841.

[12] Oleiwi A., Mohsen A. M., Abdulkadhim A., Abed A.M., Laidoudi H., Abderrahmane A.: *Experimental and numerical study on the heat transfer enhancement over scalene and curved-side triangular ribs.* Heat Transf. **52**(2023), 5, 3433–3452.

[13] Ramla M., Laidoudi H., Bouzit M.: *Behaviour of a non-newtonian fluid in a helical tube under the influence of thermal buoyancy.* Act. Mech. Auto. **16**(2022), 2, 111–118.

[14] Acharya N.: *Spectral quasi linearization simulation of radiative nanofluidic transport over a bended surface considering the effects of multiple convective conditions.* Eur. J. Mech. B-Fluid. **84**(2020), 139–154.

[15] Fang Y., Mansir I.B., Shawabkeh A., Mohamed A., Emami F.: *Heat transfer, pressure drop, and economic analysis of a tube with a constant temperature equipped with semi-circular and teardrop-shaped turbulators.* Case Stud. Therm. Eng. **33**(2022), 101955.

[16] Farshad S.A., Sheikholeslami M.: *FVM modeling of nanofluid forced convection through a solar unit involving MCTT.* Int. J. Mech. Sci. **159**(2019), 126–139.

[17] Yan S.R., Golzar A., Sharifpur M., Meyer J. P., Liu D.H., Afrand M.: *Effect of U-shaped absorber tube on thermal-hydraulic performance and efficiency of two-fluid parabolic solar collector containing two-phase hybrid non-Newtonian nanofluids.* Int. J. Mech. Sci. **185**(2020), 105832.

[18] Ebrahimpour Z., Sheikholeslami M.: *Intensification of nanofluid thermal performance with install of turbulator in a LFR system.* Chem. Eng. Process. Proc. Intensific. **161**(2021), 108322.

[19] Sheikholeslami M., Abohamzeh E., Jafaryar M., Shafee A., Babazadeh H.: *CuO nanomaterial two-phase simulation within a tube with enhanced turbulator*. Powder Technol. **373**(2020), 1–13.

[20] Farshad S.A., Sheikholeslami M.: *Nanofluid flow inside a solar collector utilizing twisted tape considering exergy and entropy analysis*. Renew. Energ. **141**(2019), 246–258.

[21] Sheikholeslami M., Ebrahimpour Z.: *Thermal improvement of linear Fresnel solar system utilizing Al_2O_3-water nanofluid and multi-way twisted tape*. Inter. J. Therm. Sci. 176(2022), 107505.

[22] Khetib Y., Sait H., Habeebullah B., Hussain A.: *Numerical study of the effect of curved turbulators on the exergy efficiency of solar collector containing two-phase hybrid nanofluid*. Sustain. Energ. Technol. Assess. **47**(2021), 101436

[23] Aghaei A., Enayati M., Beigi N., Ahmadi A., Pourmohamadian H., Sadeghi S., Dezfulizadeh A., Golzar A.: *Comparison of the effect of using helical strips and fines on the efficiency and thermal–hydraulic performance of parabolic solar collectors*. Sust. Energ. Technol. Assess. **52**(2022), 102254.

[24] Yang L., Du K.: *Thermo-economic analysis of a novel parabolic trough solar collector equipped with preheating system and canopy*. Energy **211**(2020), 118900.

[25] Farshad S.A., Sheikholeslami M.: *Simulation of nanoparticles second law treatment inside a solar collector considering turbulent flow*. Physica A **525**(2019), 1–12.

[26] Shafee A., Arabkoohsar A., Sheikholeslami M., Jafaryar M., Ayani M., Nguyen-Thoi T., Basha D.B., Tlili I., Li Z.: *Numerical simulation for turbulent flow in a tube with combined swirl flow device considering nanofluid exergy loss*. Physica A **542**(2020), 122161.

[27] Nakhchi M.E., Hatami M., Rahmati M.: *Effects of CuO nano powder on performance improvement and entropy production of double-pipe heat exchanger with innovative perforated Turbulators*. Adv. Powder Technol. **32**(2021), 8, 3063–3074.

[28] Bellos E., Tzivanidis C., Tsimpoukis D.: *Enhancing the performance of parabolic trough collectors using nanofluids and turbulators*. Renew. Sust. Energ. Rev. **91**(2018), 358–375.

[29] Sheikholeslami M., Farshad S.A., Said Z.: *Analyzing entropy and thermal behavior of nanomaterial through solar collector involving new tapes*. Int. Comm. Heat Mass Transf. **123** (2021), 105190.

[30] Sheikholeslami M., Ali Farshad S., Shafee A., Babazadeh H.: *Influence of Al_2O_3 nano powder on performance of solar collector considering turbulent flow*. Adv. Powder Technol. **31**(2020), 9, 3695–3705.

[31] Sheikholeslami M., Farshad S. A.: *Nanoparticles transportation with turbulent regime through a solar collector with helical tapes*. Adv. Powder Technol. **33**(2022), 3, 103510.

[32] Mustafa J., Alqaed S., Sharifpur M.: *Numerical study on performance of double-fluid parabolic trough solar collector occupied with hybrid non-Newtonian nanofluids: Investigation of effects of helical absorber tube using deep learning*. Eng. Anal. Bound. Elem. **140**(2022), 562–580.

[33] Dovom A.R.M., Aghaei A., Joshaghani A.H., Dezfulizadeh A., Kakavandi A.A.: *Numerical analysis of heating aerosol carbon nanofluid flow in a power plant recuperator with considering ash fouling: a deep learning approach*. Eng. Anal. Bound. Elem. **141**(2022), 75–90.

[34] Afshari F., Sozen A., Khanlari A., Tuncer A.D., Sirin C.: *Effect of turbulator modifications on the thermal performance of cost-effective alternative solar air heater*. Renew. Energ. **158**(2020), 297–310.

[35] Abu-Hamdeh N.H., Bantan R.A.R., Khoshvaght-Aliabadi M., Alimoradi A.: *Effects of ribs on thermal performance of curved absorber tube used in cylindrical solar collectors*. Renew. Energ. **161**(2020), 1260–1275.

[36] Mokeddem M., Laidoudi H., Makinde O.D., Bouzit M.: *3D simulation of incompressible Poiseuille flow through 180° curved duct of square cross-section under effect of thermal buoyancy*. Period. Polytech. Mech. Eng. **63**(2019), 4, 257–269.

[37] Ameur H., Bouzit M.: *Power consumption for stirring shear thinning fluids by two-blade impeller*. Energy **50**(2013), 326–332.

[38] Hassouni S., Laidoudi H., Makinde O. D., Bouzit M., Haddou B.: *A qualitative study of mixing a fluid inside a mechanical mixer with the effect of thermal buoyancy*. Arch. Thermodyn. **44**(2023), 1, 105–119.

[39] Seddik-Bouchouicha M., Laidoudi H., Hassouni S., Makinde O.D.: *Study of the effect of geometric shape on the quality of mixing: examining the effect of length of the baffles*. Arch. Thermodyn. **44**(2023), 2, 69–85.

[40] Bulat P.V., Volkov K.N.: *Fluid/solid coupled heat transfer analysis of a free rotating disc*. Arch. Thermodyn. **39**(2018), 3, 169–192.

[41] Szymanski P., Mikielewicz D.: *Challenges in operating and testing loop heat pipes in 500-700 K temperature ranges*. Arch. Thermodyn. **43**(2022), 2, 61–73.

[42] Cyklis P.: *Heat transfer in falling film evaporators during the industrial process of apple juice concentrate production*. Arch. Thermodyn. **39**(2018), 3, 3–13.

[43] Aliouane I., Kaid N., Ameur H., Laidoudi H.: *Investigation of the flow and thermal fields in square enclosures: Rayleigh-Bénard's instabilities of nanofluids*. Therm. Sci. Eng. Prog. **25**(2021), 100959

[44] Gambit. http://www.gambit-project.org/ (acessed 11 Aug. 2022).

archives
of thermodynamics
Vol. **44**(2023), No. 2, 159–175
DOI: 10.24425/ather.2023.146563

Numerical analysis of the heating of a die for the extrusion of aluminium alloy profiles in terms of thermochemical treatment

DAMIAN JOACHIMIAK*
WOJCIECH JUDT
MAGDA JOACHIMIAK

Poznan University of Technology, Institute of Thermal Engineering, Piotrowo 3a, 60-965, Poznan, Poland

Abstract Thermochemical treatment processes are used to produce a surface layer of the workpiece with improved mechanical properties. One of the important parameters during the gas nitriding processes is the temperature of the surface. In thermochemical treatment processes, there is a problem in precisely determining the surface temperature of heat-treated massive components with complex geometries. This paper presents a simulation of the heating process of a die used to extrude aluminium profiles. The maximum temperature differences calculated in the die volume, on the surface and at the most mechanically stressed edge during the extrusion of the aluminum profiles were analysed. The heating of the die was simulated using commercial transient thermal analysis software. The numerical calculations of the die assumed a boundary condition in the form of the heat transfer coefficient obtained from experimental studies in a thermochemical treatment furnace and the solution of the nonstationary and non-linear inverse problem for the heat conduction equation in the cylinder. The die heating analysis was performed for various heating rates and fan settings. Major differences in the surface temperature and in the volume of the heated die were obtained. Possible ways to improve the productivity and control of thermochemical treatment processes were identified. The paper investigates the heating of a die, which is a massive component with complex geometry. This paper indicates a new way to develop methods for the control of thermochemical processing of massive components with complex geometries.

Keywords: Temperature distribution in a solid component; Extrusion die for aluminium profiles; Gas nitriding; Direct and inverse problem for the heat conduction equation

*Corresponding Author. Email: damian.joachimiak@put.poznan.pl

Nomenclature

c	–	specific heat, J/(kgK)
h	–	heat transfer coefficient, W/(m^{2}K)
k	–	thermal conductivity, W/(mK)
P1	–	heating process (heating rate 5 K/min, fan speed 50%)
P2	–	heating process (heating rate 5 K/min, fan speed 100%)
P3	–	heating process (heating rate 10 K/min, fan speed 50%)
T	–	temperature, K
t	–	time, s
ρ	–	density, kg/m^3

Subscripts

A	–	area
b	–	boundary
e	–	edge
g	–	gas
max	–	maximum value
min	–	minimum value
V	–	volume

1 Introduction

Aluminium hot extrusion dies are exposed to thermal and mechanical loads [1]. These profiles are created by extruding aluminium through a die at a temperature of 723 K to 772 K and at a speed of 5 to 100 m/min [1]. The complex character of the extrusion process is the reason for the problems in designing a long-life die [2]. The hard working conditions of the dies cause them to fail very often. Production of dies with a long operational life reduces the cost of the extrusion of aluminium profiles. So far, there has been analysis on tooling impact of the lifetime during hot metal forming on the efficiency and the quality of the process [3]. The damage to the dies was studied in a sample of 616 cases. Analysis of die damage is the basis for reducing the cost intensity of aluminium extrusion processes [3]. In addition to the working conditions, the shape of the die also influences the durability of the die [4], the steel grade of which it is made, and the heat and thermochemical treatment of the die [1, 5].

In the paper [6] a numerical simulation of the heat treatment of the die used in the extrusion processes is presented. In [7] the die hardening procedure for Alvar 14 steel (DIN 56 NiCrMoV7) was analysed for aluminium extrusion in vacuum furnaces. The study of the solid disc-shaped die involved experiment and numerical simulations. The values of the convective

and radiation heat transfer coefficient and Biot number were obtained. The obtained temperature gradients showed that higher heating rates could be used, which reduces the time and cost of the quenching. The simulation of heat flow in a heat treatment or thermochemical furnace has an important impact on the control of the resulting surface layers and their properties [8]. So far, numerical simulations of laser and induction hardening [9] and gas jet hardening have been performed [10]. The paper [8] proposes models based on numerical simulation and analytical methods to determine radiation, convection, and heat conduction in heat treatment processes.

The dies are also treated with gas nitriding. The duration of the nitriding process, and thus the thickness of the nitrided layer, is directly correlated with the cost of the process. A die with a worn-out nitrided layer can be re-nitrided [1]. It is possible to find the optimum diffusion layer thickness for which die wear will generate the lowest operating costs [1]. In order to minimise the cost of "regenerating" the dies, the gas nitriding process needs to be precisely controlled. So far, models have been developed for the growth kinetics of the nitrided layer [11]. A weakness of these models is the lack of knowledge of the surface temperature of thermochemically treated components.

Thermochemical treatment processes are used to produce a surface layer of the processed workpiece with improved mechanical properties [12]. Important parameters during the heat treatment processes are the composition and temperature of the gas in the furnace retort, the temperature of the surface to be processed, and the duration of the treatment [11]. The temperature of the furnace atmosphere can be measured with a high level of accuracy. The composition of the furnace atmosphere is regulated and precisely determined throughout the process. During gas nitriding, the surface temperature of the thermochemical workpieces is between ambient and 550°C. In thermal machines, there is a great challenge to determine the precise surface temperature [13, 14]. In thermochemical treatment processes, there is also the problem of determining the precise surface temperature of heat-treated solid components [15, 16]. The direct measurement of the surface temperature of workpieces in atmospheric furnaces is subject to a high error rate [14–16]. In order to precisely determine the boundary condition in terms of temperature, heat flux, or heat transfer coefficient (HTC), the temperature inside the heated element is measured and the inverse problem for the heat conduction equation is solved [17–21]. Inverse problems are numerically determined incorrectly [22–26]. Controlling the heat treatment processes prevents cracking of the work pieces [27]. In the

study [27] the heat treatment of a turbine disc was analysed. Heat transfer coefficients were calculated using the inverse thermal problem. Solving the inverse problem for heat conduction equation was used for the analysis of an incomplete die hardening for aluminium-based foam parts [28].

The inverse model has been used to control of induction heat treatments so far [29]. The temperature in the cylindrical sample was controlled and the nonlinear electromagnetic-thermal problem was solved. In the heat treatment furnace, an inverse problem was used together with an artificial neural network to estimate the optimal control parameters of the heat source [30]. Artificial neural networks together with inverse heat conduction problem were also used to reconstruct the HTC waveform from temperature signals recorded during actual heat treatment processes [31]. The analysis of the heat flow in industrial furnaces in many cases is still based on the operator's experience [8,32]. Heat flow phenomena in furnaces have not yet been adequately studied. A similar issue arises with regard to heat flow in the components being treated.

This paper presents a simulation of the die heating process based on the heat transfer coefficient. This coefficient was determined from the solution of the inverse problem based on experimental data. So far, temperature distributions in thermo-chemically treated dies have not been studied, and the inverse heat conduction problem has not been used to analyze the heating of such components.

2 Description of die geometry and material properties

The paper presents the problem of heating a die for the extrusion of aluminium alloy profiles (Fig. 1). This is a massive component with a complex shape. The temperature changes in selected areas of the die during three heating processes differing in the rate of heating and the intensity of gas flow in the furnace chamber were analysed. The heating processes start at about 295 K (ambient temperature) and finish at about 823 K. The conducted analysis of die heating was performer for gas nitriding. The process starts at ambient temperature and usually reaches the temperature of 823 K. During the heating process, the temperature must correlate with the atmosphere inside the furnace. The proper adjustment of those parameters ensures the creation of surface and near-surface layers with high mechanical parameters. The author heated a roller for chemical and heat treatment

inside the roller at an earlier stage of research also to the temperature of 823 K [16]. The selection of 823 K as the maximum temperature was discussed with individuals responsible for gas nitriding in industrial conditions as well as based on literature [11]. For the temperature range mentioned above, the variation in the heat transfer coefficient and the specific heat is significant. Therefore, the heat flow analyses were performed taking into account the varying properties of WCLV steel as a function of temperature. WCLV steel is tool alloy steel for hot work.

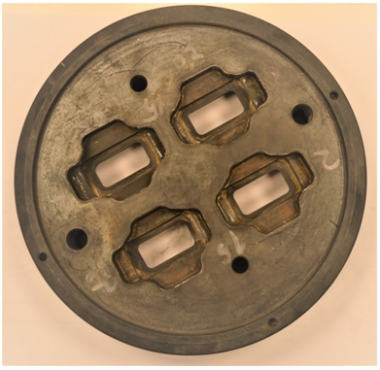

Figure 1: Extrusion die for aluminium alloy profiles [34].

Table 1 presents the chemical composition of the WCLV steel [36]. The temperature dependence of the thermal conductivity and specific heat is shown in Tables 2 and 3 [33]. Linear interpolation was carried out between

Table 1: Chemical composition of the WCLV steel (%) [36]

C	0.35–0.42
Si	0.80–1.20
Mn	0.25–0.50
P	max 0.030
S	max 0.030
Cr	4.80–5.50
Mo	1.20–1.50
W	–
V	0.85–1.15
Co	–
Ni	–

the specified points. Due to the negligible effect of changes in steel density as a function of temperature, the calculation assumes that the steel density does not change and is 7850 kg/m^3 [33].

Table 2: Thermal conductivity coefficient (k) as a function of temperature for WCLV steel

T (K)	k (W/(m K))
293.15	25.5
624.15	27.6
975.15	30.3

Table 3: Specific heat c as a function of temperature for WCLV steel

T (K)	c (J/(kgK))
273.15	460
365.15	521
962.15	620

3 Computational grid

The temperature distribution inside the die was determined using commercial Ansys Transient Thermal software [37]. The calculations were carried out for a three-dimensional model, representing the actual die geometry. Due to the presence of symmetry planes in the die, a quarter of the element was analysed, assuming symmetry conditions in the cross-sectional planes (Fig. 2a, planes marked by green). The mesh constructed from approximately 500 000 tetrahedral elements is shown in Figs. 3 and 4. The impact of the number of mesh elements on the obtained calculation results was analysed. Calculations were also performed for mesh types with higher and lower number of elements than in the case of the selected mesh. Grid elements of three different sizes (G1–G3, Figs. 3 and 4) were used at the main edges of the geometry. The smallest elements of size equal to 5×10^{-4} m (G3, Fig. 4) were used to create a mesh discretization of the edge of the die most mechanically stressed the most during its operation (edge E, Fig. 2b). It is crucial for the correct operation of the die to determine the thermochemical treatment conditions and consequently produce

a layer with high mechanical properties of the mentioned edge. Larger grid elements of 10^{-3} m (G2, Fig. 4) were used to prepare a grid of die sections that do not operate under such harsh conditions as the aforementioned

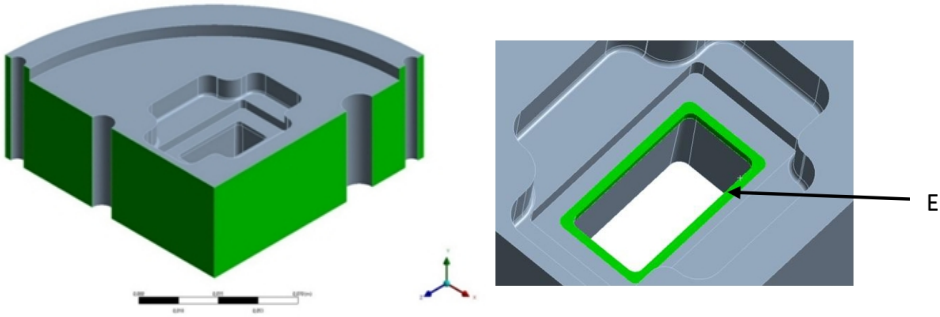

(a) (b)

Figure 2: Fragment of a die with marked: a) planes of symmetry, b) edge E.

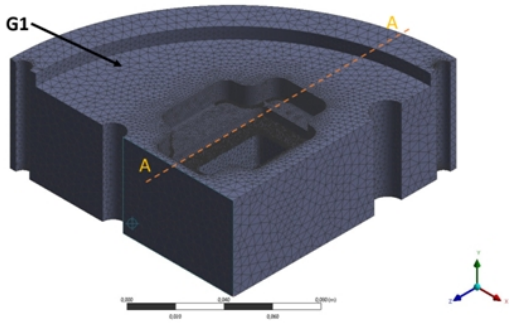

Figure 3: Die fragment mesh with marked G1 type elements.

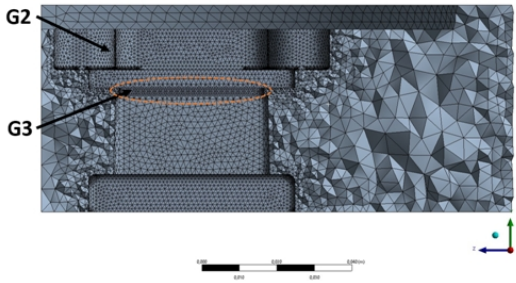

Figure 4: Cross-section $A-A$ of the die grid showing edge E with grid elements G2 and G3 marked.

edge. The grid elements located in other parts of the die were characterised by a grid size of 4×10^{-3} m (G1, Fig. 3). The average orthogonality of the grid elements was 0.75.

4 Initial and boundary conditions

In Ansys Transient Thermal, the heat conduction equation in the die fragment was solved in the following form

$$\rho c(T)\frac{\partial T}{\partial t} = \frac{\partial}{\partial x}\left[k(T)\frac{\partial T}{\partial x}\right] + \frac{\partial}{\partial y}\left[k(T)\frac{\partial T}{\partial y}\right] + \frac{\partial}{\partial z}\left[k(T)\frac{\partial T}{\partial z}\right], \quad (1)$$

where the variability of $k(T)$ is shown in Table 2. The assumed initial die temperature was 295 K. Calculations were carried out using a boundary condition of the form

$$k(T)\frac{\partial T}{\partial n} = h(t)\left[T_g(t) - T_b(t)\right], \quad (2)$$

where $h(t)$ was obtained from solving the inverse problem for the experimental data which are shown in Fig. 6.

Three processes were used to analyse the heating process, differing in the set heating rate and fan speed, which are summarised in Table 4.

Table 4: Heating processes

Process	Heating rate (K/min)	Percentage of maximum fan speed (%)
P1	5	50
P2	5	100
P3	10	50

The heating rate values given in Table 4 are the set values for the furnace control system. Different furnace control modes resulted in different gas temperature waveforms (Fig. 5) and heat transfer coefficient values (Fig. 6) [16, 35]. The boundary conditions in the form of temperature, heat flux and heat transfer coefficient for the cylinder were determined from previous experimental studies in a thermochemical treatment furnace and by solving the inverse problem for the heat conduction equation for the analyzed processes P1–P3 [16]. The inverse heat conduction problem is ill-posed. Even the slightest disturbance in input data can have a significant impact on the calculation results. It was taken into consideration

and self-regulation was done using the time series method described in [16]. The proper selection of a time series significantly reduced the oscillation of the result. A time series of $\Delta t = 30$ s was selected for the analysed processes. So far, on the basis of experimental studies and the stable solution of the inverse heat conduction problem, a slight variation of the heat transfer coefficient at different locations in the furnace working chamber has been shown [15]. Therefore, the boundary condition in the form of the heat transfer coefficient determined earlier in the study was adopted for all the walls of the die model in contact with the furnace atmosphere during the thermochemical treatment. The remaining planes are planes of symmetry (Fig. 2). The boundary conditions obtained from the processes analysed (Table 4) in the form of gas temperature and heat transfer coefficient for the cylinder are shown in Figs. 5 and 6.

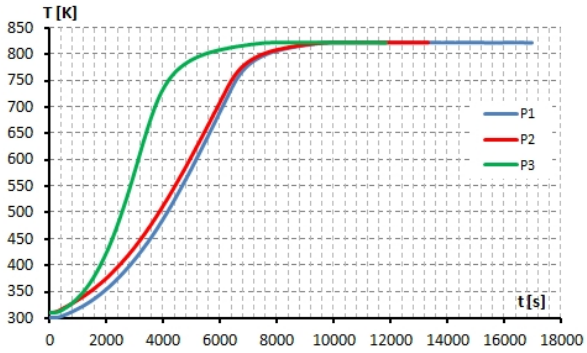

Figure 5: Gas temperature for heating processes P1–P3 in the thermochemical treatment furnace.

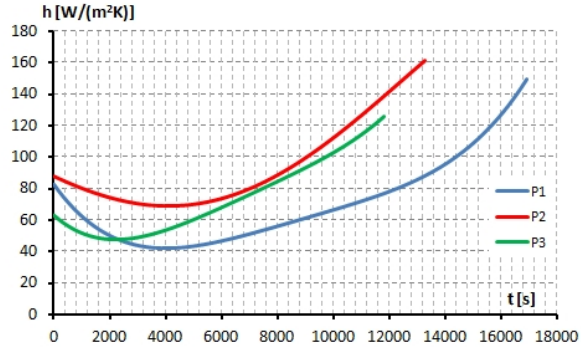

Figure 6: Heat transfer coefficient for heating processes P1–P3 in a thermochemical treatment furnace.

The P1 process had the longest duration and the largest range of heat transfer coefficient values (Fig. 6). At the beginning of the process, the value of h was 84 W/(m^{2}K) after which it decreased to a minimum value equal to 43 W/(m^{2}K) for a time of about 4000 s. Subsequently, the value of the heat transfer coefficient increased and at the end of the process exceeded 140 W/(m^{2}K). The P2 process (Fig. 6) had the same controlled heating rate as the P1 process, but because the fan speed was set to maximum, the gas flow in the furnace chamber was intensified, improving the heat transfer conditions. At the beginning of the process, a higher heat transfer coefficient was obtained than in the P1 process, with a value of 88 W/(m^{2}K). The minimum value for the P2 process is 69 W/(m^{2}K). This occurred for a time of 4100 s. At the end of the process, a heat transfer coefficient value was reached of 160 W/(m^{2}K). The P3 process was characterised by twice the heating rate of the P1 and P2 processes and the fan speed set at 50% of its maximum value. These conditions reduced the process time to 11 820 s. The heat transfer coefficient curves described above were used as boundary conditions in the die heating analysis.

5 Description and analysis of the results for die heating

The effect of the 3D simulation was to obtain the temperature in the entire volume of the die during the heating process. The nature of the gas temperature variation (Fig. 5), the distribution of the heat transfer coefficient (Fig. 6) and the unbalanced distribution of the die mass resulted in uneven heating. The distribution of the difference in the gas temperature and the average die surface temperature for the processes P1–P3 is shown in Fig. 7. This difference reaches 115, 72 and 148 K for processes P1–P3, respectively. Figure 7 shows that the processes examined varied significantly in the values of the temperature difference between the gas and the average temperature of the die surface. The value of the difference is related to the intensity of the heat flow from the gas to the die at the surface. The intensity of heat flow at the surface causes temperature differences in the volume of the die. These, in turn, affect the formation of temperature gradients, thermal stresses and deformations in the die.

Each heating process was characterised by a different distribution of the maximum temperature difference in the volume of the die (Fig. 8). For process P1 and a time of 6540 s, a maximum temperature difference

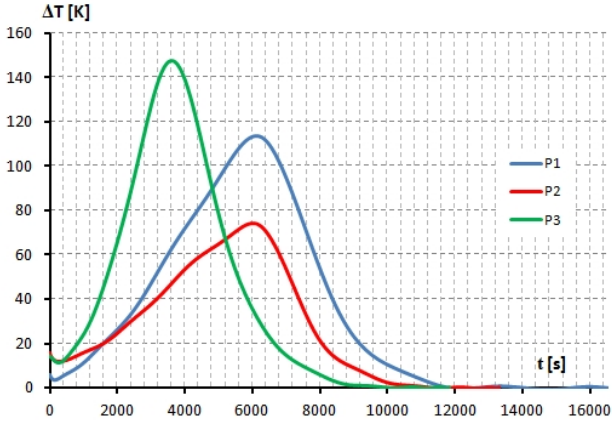

Figure 7: The difference between gas temperature and average die surface temperature during heating for the P1–P3 processes.

in the die volume of 15.2 K was obtained. For the P2 process, a more uniform temperature in the volume of the die was obtained due to the higher value of the heat transfer coefficient. The maximum temperature difference in die volume for the P2 process was 14.2 K. For the P3 process with the highest heating rate, a much larger temperature divergence was obtained in the volume was obtained, which reached a value of 21.2 K for a time of 3780 s. Table 5 summarises the time of occurrence of the maximum temperature divergence values in selected areas: on the heated surface ($T_{\max,A} - T_{\min,A}$), in the volume ($T_{\max,V} - T_{\min,V}$) and on the edge E

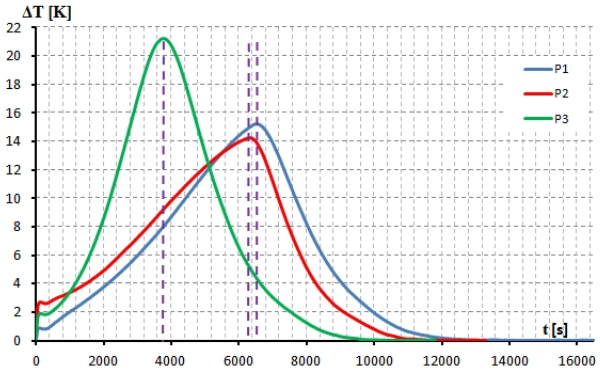

Figure 8: Difference between the maximum and minimum temperatures in the volume of the die.

$(T_{\max,E} - T_{\min,E})$ (Fig. 2b). For each of the analysed heating processes P1–P3, the maximum temperature differences at the edge surface were obtained at the same process time as the maximum differences in die volume.

Table 5: Maximum temperature differences in selected areas of the die and their time of occurrence for each process

Process	t (s)	$T_{\max,A} - T_{\min,A}$ (K)	$T_{\max,V} - T_{\min,V}$ (K)	$T_{\max,E} - T_{\min,E}$ (K)
P1	6540	12.9	15.2	4.2
P2	6390	11.9	14.2	3.9
P3	3780	19.0	21.2	5.9

Figure 9 shows the temperature distribution on the heated die surface according to the boundary condition for the P3 process and the time $t = 3780$ s in which the maximum temperature difference occurred (Table 5). The lowest temperature of about 557 K can be observed in area A with the high mass of the die, while the highest temperature of about 578 K can be observed in area B.

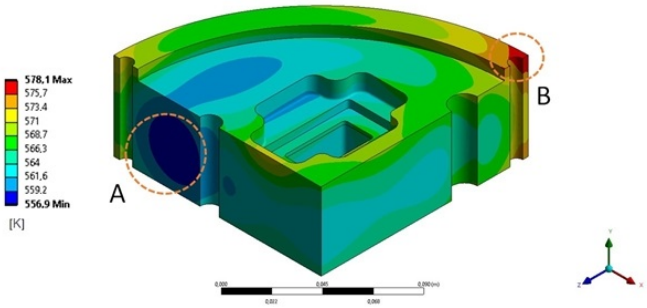

Figure 9: Temperature distribution in the volume of the die in process P3 for time $t = 3780$ s, for which the maximum temperature difference occurred during the entire heating process.

A crucial part of the die geometry is the edge of the die that is mechanically stressed during extrusion of aluminium alloy profiles (the edge E). To give the E-edge the necessary hardness, the die is subjected to gas nitriding. Knowing the exact value of the surface temperature during the process will allow for a precise control of the thermochemical treatment process. For this reason, the temperature distribution on the E edge was subjected to a special analysis. (Figs. 2b, 10, and 11).

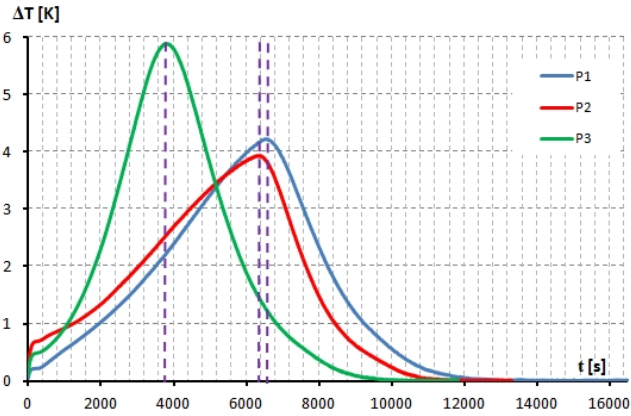

Figure 10: Maximum temperature differences on the surface of the E edge for processes P1–P3.

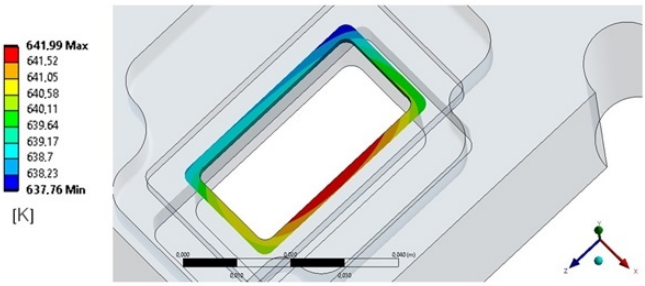

Figure 11: Temperature distribution on edge surface E for process P1 and time $t = 6540$ s.

The maximum temperature difference at the edge surface (Fig. 10) for the analysed processes P1, P2, and P3, respectively, is 4.2, 3.9 and 5.9 K. These are relatively large values considering the precise control of the edge temperature during the nitriding process. Figure 11 shows the temperature field with maximally varying values (for $t = 6540$ s) at the edge surface E for process P1.

For the analysed processes, edge E has the highest temperature on the surface of the long side in the plane of symmetry. For comparison, the lowest temperature occurs at the corner on the side of the high-mass die fragment (area A). The temperature difference then reaches 4.23 K. The temperature distribution at the edge is influenced by the varying mass

of the die geometry. From the analysis of the data obtained for the P1, P2, and P3 process, it can be seen that the position of the maximum and minimum temperature areas does not change for different heating rates and fan settings (gas flow rate in the chamber of the furnace).

6 Conclusions

In the study, the heating of a massive die with complex geometry was analysed. A boundary condition was applied in the form of a heat transfer coefficient obtained for three different heating processes. The variants of boundary conditions considered match the heating rates and fan settings used in thermochemical treatment processes.

The analysis shows that the maximum temperature differences at the edge E occur at the same time as the maximum temperature differences in the volume. The unevenness of the mass distribution of the die is the cause of the temperature variation on the edge E. This variability is significant and reaches 4.2, 3.9, and 5.9 K for P1–P3 processes.

The data show that heating at the maximum fan speed has the positive effect of reducing the process time and achieving a more uniform temperature in the die volume.

In order to achieve a more homogenous temperature in the volume of the component to be worked, and therefore to minimise the occurrence of thermal stresses, it is necessary to intensify: the gas flow in the furnace chamber in order to increase the heat transfer coefficient.

A time-varying heating rate can be used to reduce the temperature differences in the volume of the die. To increase the productivity of the processing, the heating rate can be increased at the beginning and end of each process. However, during the heating stage, when the temperature differences reach a maximum for a constant heating rate, the speed can be reduced. Die heating rate control can be achieved by solving the inverse problem.

Received 9 February 2023

References

[1] Małdziński L., Ostrowska K., Okoniewicz P.: *Controlled ZeroFlow gas nitriding as a method increasing the durability of dies for hot extrusion of aluminum profiles.* Obróbka Plastyczna Metali **25**(2014), 3, 169–183.

[2] Miles N., Evans G., Middleditch A.: *Bearing lengths for extrusion dies: rationale, current practice and requirements for automation.* J. Mater. Process. Tech. 72(1997), 1, 162–176.

[3] Arif A.F. M, Sheikh A.K., Qamar S.Z.: *A study of die failure mechanisms in aluminum extrusion.* J. Mater. Process. Tech. **134**(2003), 3, 318–328.

[4] Fang W., Tang D., Wang H., Li D., Peng Y.: *Optimization of die design for thin-walled flat multi-port tube with the aid of finite element simulation.* J. Mater. Process. Tech. **277**(2020), 116418.

[5] Zinner S., Lenger H., Jesner G., Siller I.: *Analysis of the cooling conditions during heat treatment of die casting dies by use of FEM simulation.* J. Heat Treat. Mater. **67**(2012), 2, 95–99.

[6] Redl C., Friesenbichle, C., Wieser V.: *Numerical simulation of residual stresses during the heat treatment of dies made of hot work tool steel.* Mater. Sci. Forum **524-525**(2006), 433–438. doi: 10.4028/www.scientific.net/MSF.524-525.433

[7] Oliveira M., Duarte A., Coelho P., Marafona J.: *Heat treatment of aluminum extrusion dies and study of their heating by convection/radiation.* Int. J. Adv. Manuf. Technol. **78**(2015), 1–4, 419–430. doi: 10.1007/s00170-014-6618-5

[8] Kang J., Rong Y.: *Modeling and simulation of heat transfer in loaded heat treatment furnaces.* In: Proc. 1st Int. Surface Engineering Cong. – 13th IFHTSE Cong. 7–10 Oct. 2002, 337–343.

[9] Fuhrmann J., Hömberg D.: *Numerical simulation of the surface hardening of steel.* Int. J. Numer. Method. Heat Fluid Fl. **9**(1999), 5–6, 705–724. doi: 10.1108/09615539910286042

[10] Heck U., Fritsching U., Bauckhage K.: *Fluid flow and heat transfer in gas jet quenching of a cylinder.* Int. J. Numer. Method. Heat Fluid Fl. **11**(2001), 1, 36–49. doi: 10.1108/09615530110364079

[11] Małdziński L.: *Thermodynamic, Kinetic and Technological Aspects of Nitrided Layer Production on Iron and Steel in Gas Nitriding Processes.* Wydawnictwo Politechniki Poznańskiej, Poznań 2002 (in Polish).

[12] Dossett J., Totten G.E., Eds.: *ASM Metal Handbook Vol. 4: Steel Heat Treating Fundamentals and Processes.* ASM Int., 1991.

[13] Judt W., Ciupek B., Urbaniak R.: *Numerical study of a heat transfer process in a low power heating boiler equipped with afterburning chamber.* Energy **196**(2020), 117093. doi: 10.1016/j.energy.2020.117093

[14] Taler J.: *Theory and Practice of Identifying Heat Transfer Processes.* Ossolineum, Wrocław – Warszawa – Kraków 1995 (in Polish).

[15] Joachimiak M.: *Analysis of thermodynamic parameter variability in a chamber of a furnace for thermo-chemical treatment.* Energies **14**(2021), 10, 2903. doi: 10.3390/en14102903

[16] Joachimiak M., Joachimiak D., Ciałkowski M., Małdziński L., Okoniewicz P., Ostrowska K.: *Analysis of the heat transfer for processes of the cylinder heating in the heat-treating furnace on the basis of solving the inverse problem.* Int. J. Therm. Sci. **145**(2019), 105985.

[17] Frąckowiak A., Spura D., Gampe U., Ciałkowski M.: *Determination of heat transfer coefficient in a T-shaped cavity by means of solving the inverse heat conduction problem*. Int. J. Numer. Meth. Heat Fluid Fl. **30**(2020), 4, 1725–1742.

[18] Frąckowiak A., Wróblewska A., Ciałkowski M.: *Trefftz numerical functions for solving inverse heat conduction problems*. Int. J. Therm. Sci. **177**(2022), 107566-1-107566-9.

[19] Joachimiak M., Ciałkowski M.: *Optimal choice of integral parameter in a process of solving the inverse problem for heat equation*. Arch. Thermodyn. **35**(2014), 3, 265–280.

[20] Joachimiak M., Ciałkowski M.: *Stable solution to nonstationary inverse heat conduction equation*. Arch. Thermodyn. **39**(2018), 1, 25–37.

[21] Joachimiak M., Joachimiak D., Ciałkowski M.: *Investigation on thermal loads in steady-state conditions with the use of the solution to the inverse problem*. Heat Transfer Eng. **44**(2022), 1–12, 963–969. doi: 10.1080/01457632.2022.2113451

[22] Ciałkowski M., Olejnik A., Joachimiak M., Grysa K., Frąckowiak A.: *Cauchy type nonlinear inverse problem in a two-layer area*. Int. J. Numer. Meth. Heat Fluid Fl. **32**(2022), 1, 313–331.

[23] Joachimiak M.: *Choice of the regularization parameter for the Cauchy problem for the Laplace equation*. Int. J. Numer. Meth. Heat Fluid Fl. **30**(2020), 10, 4475–4492.

[24] Joachimiak M., Ciałkowski M., Frąckowiak A.: *Stable method for solving the Cauchy problem with the use of Chebyshev polynomials*. Int. J. Numer. Meth. Heat Fluid Fl. **30**(2020), 3, 1441–1456.

[25] Joachimiak M., Frąckowiak A., Ciałkowski M.: *Solution of inverse heat conduction equation with the use of Chebyshev polynomials*. Arch. Thermodyn. **37**(2016), 4, 73–88.

[26] Mierzwiczak M., Chen W., Fu Z.-J.: *The singular boundary method for steady-state nonlinear heat conduction problem with temperature-dependent thermal conductivity*. Int. J. Heat Mass Tran. 91(2015), 205–217.

[27] Zhang J., Kang J., Guo Z., Xiong S., Liu B., Zou J., Liu S.: *Study on the heat transfer coefficients during the heat treatment process of a turbine disk*. In: Proc. TMS 2009 138th Ann. Meet. Vol. 2: Materials Characterization, Computation, Modeling, 2009, 27–32.

[28] Lázaro-Nebreda J., Solórzano E., Escudero J., de Saja J.A., Rodríguez-Pérez M.A.: *Applicability of solid solution heat treatments to aluminum foams*. Metals **2**(2012), 4, 508–528. doi: 10.3390/met2040508

[29] Asadzadeh M.Z., Raninger P., Prevedel P., Ecker W., Mücke M.: *Inverse model for the control of induction heat treatments*. Materials (Basel) **12**(2019), 17, 2826. doi: 10.3390/ma12172826

[30] Yadav R., Tripathi S., Asati S., Das M.K.: *A combined neural network and simulated annealing based inverse technique to optimize the heat source control parameters in heat treatment furnaces*. Inverse Probl. Sci. Eng. **28**(2020), 9, 1265–1286. doi: 10.1080/17415977.2020.1719087

[31] Szenasi S., Fried Z., Felde I.: *Training of artificial neural network to solve the inverse heat conduction problem*, In: Proc. 2020 IEEE 18th World Symp. on Applied Machine Intelligence and Informatics (SAMI), Herlany, 2020, 293–298. doi: 10.1109/SAMI48414.2020.9108733

[32] Joachimiak D., Frąckowiak A.: *Experimental and numerical analysis of the gas flow in the axisymmetric radial clearance*. Energies **13**(2020), 21, 5794-1-5794-13. doi: 10.3390/en13215794

[33] Incropera F.P., de Witt D.P.: *Fundamentals of Heat and Mass Transfer*. Wiley, New York 1996.

[34] Photo of a die for the extrusion of aluminium alloy profiles. Poznan University of Technology, Institute of Machines and Motor Vehicles, Poznan 2021.

[35] Joachimiak M., Ciałkowski M.: *Non-linear unsteady inverse boundary problem for heat conduction equation*. Arch. Thermodyn. 38(2017), 2, 81–100.

[36] https://akrostal.pl/stale/wclv-1-2344/?print=pdf (accessed 16 Nov. 2022).

[37] Ansys Transient Thermal Analysis Guide. Ansys 2021R1, Inc.

archives
of thermodynamics
Vol. **44**(2023), No. 2, 177–194
DOI: 10.24425/ather.2023.146564

Analysis of heat and mass transfer in an adsorption bed using CFD methods

SZYMON JANUSZ[a,b*]
MACIEJ SZUDAREK[c]
LESZEK RUDNIAK[d]
MARCIN BORCUCH[b]

[a] Cracow University of Technology, Jana Pawla II 37, 31-864 Kraków, Poland

[b] M.A.S. Sp z o.o., Research and Development Department, Składowa 34, 27-200 Starachowice, Poland

[c] Warsaw University of Technology, Institute of Metrology and Biomedical Engineering, św. Andrzeja Boboli 8, 02-525 Warszawa, Poland

[d] Warsaw University of Technology, Faculty of Chemical and Process Engineering, Waryńskiego 1, 00-645 Warszawa, Poland

Abstract The trend of reducing electricity consumption and environmental protection has contributed to the development of refrigeration technologies based on the thermal effect of adsorption. This article proposes a methodology for conducting numerical simulations of the adsorption and desorption processes. Experimental data available in the literature were used as guidelines for building and verifying the model, and the calculations were carried out using commercial computational fluid dynamics software. The simulation results determined the amount of water vapor absorbed by the adsorbent bed and the heat generated during the adsorption process. Throughout the adsorption process, the inlet water vapor velocity, temperature, and pressure in the adsorbent bed were monitored and recorded. The results obtained were consistent with the theory in the literature and will serve as the basis for further, independent experimental studies. The validated model allowed for the analysis of the effect of cooling water temperature on the sorption capacity of the material and the effect of heating water temperature on bed regeneration. The proposed approach can be useful in

*Corresponding Author. Email: szymon.janusz@doktorant.pk.edu.pl

analyzing adsorption processes in refrigeration applications and designing heat and mass exchangers used in adsorption systems.

Keywords: Heat transfer; Adsorption; CFD; Mass transfer; Refrigeration devices

Nomenclature

a	–	amount of adsorbed water vapor, kg/kg
a_{eq}	–	equilibrium concentration, kg/kg
C	–	coefficient of inertial resistance, 1/m
c_p	–	specific heat capacity, J/kgK
D_e	–	effective diffusion coefficient, m^2/s
D_p	–	diameter of the bed particles, m
D_0	–	kinematic diffusion coefficient, m^2/s
E_a	–	activation energy, J/mol
H	–	heat of adsorption, J/kg
k	–	thermal conductivity of the medium
k_m	–	LDF model coefficient, 1/s
P	–	pressure, Pa
P_s	–	saturation pressure, Pa
P_v	–	absolute pressure, Pa
Q	–	energy source term, W/m^3
R	–	gas constant, J/(molK)
r_a	–	radius of bed particles, m
S_i	–	source term of momentum, N/m^3
S_m	–	source term of mass, kg/(s m^3)
T	–	temperature, K
v	–	velocity, m/s
v_i	–	Cartesian components of velocity in x_i-direction
x_i	–	Cartesian coordinates, m

Greek symbols

α	–	permeability, m^2
ε	–	porosity of the medium
μ	–	dynamic viscosity of the medium, Pa·s
ρ	–	density of the medium, kg/m^3
τ	–	time, s

Subscripts

b	–	adsorption bed
c	–	cooling water
f	–	fluid
h	–	heating water
i, j	–	components
s	–	solid
sc	–	single cycle
v	–	vapor

Abbreviations

ads	–	adsorption/
CFD	–	(computational fluid dynamics
COP	–	coefficient of performance
des	–	desorption

1 Introduction

As a result of the increasing demand for heating, cooling, and air conditioning over the last century, numerous refrigeration technologies have been developed. Compressor cooling systems dominate the market due to their high coefficient of performance (COP). Although these devices perform well in terms of heating and cooling, they have a negative impact on the environment. This is due to the refrigerants (such as freon, propane, and carbon dioxide) used in compressor devices, which have a negative impact on the ozone layer and global warming. The mentioned refrigerants, despite the reduction of the global warming potential parameter, are still more harmful to the environment than, for example, water. Additionally, refrigeration devices account for approximately 20% of worldwide electrical energy used in buildings [1]. Technologies based on sorption processes are free of the drawbacks mentioned above [2]. One of these technologies is adsorption.

Adsorption cooling systems operate on environmentally friendly refrigerants (such as water) and allow to recover waste heat, thus to reduce primary energy consumption [3]. Furthermore, adsorption systems are characterized by low operating and maintenance costs, lack of vibration, and quiet operation [4]. Despite their numerous advantages, adsorption cooling systems also have drawbacks, such as intermittent operation, large equipment size, the need for vacuum maintenance, and, above all, low COP [5]. Therefore, there are ample opportunities for research to improve the efficiency of adsorption systems.

To provide continuous cooling production, adsorption cooling devices must be equipped with at least two beds. When a refrigerant is adsorbed in one bed, the other bed undergoes regeneration or desorption. The cycle starts with the refrigerant vaporizing in the evaporator. As a result of refrigerant vaporization, heat is being drawn from the water flowing through the heat exchanger, and cooling water is produced as a result [6]. The operating conditions of the process are closely related to the required parameters of cooling water.

In the case of using water as a refrigerant, it is necessary to maintain a very low working pressure of the unit, as for water temperature of 280 K (7°C) the saturation pressure is 1000 Pa. This poses additional requirements regarding the construction of adsorption equipment – it must be sufficiently airtight to maintain low pressure. During evaporation, the evaporator is connected to a chamber where an adsorption bed is located. The produced vapor is adsorbed by the bed, which makes it possible to maintain low pressure in the evaporator. The adsorption chamber is not connected to the condenser at this stage. When the adsorption bed becomes saturated, the evaporator chamber is disconnected, and the regeneration process of the bed begins. A working fluid at an elevated temperature is supplied to the adsorption bed to force the desorption of refrigerant molecules from the adsorbent pores. After a certain period called switching time, the connection with the condenser chamber is opened. This stage is called the desorption stage. After condensation, the refrigerant flows to the evaporator, where the next cycle of the device operation begins [7].

Adsorption technology is based on surface sorption phenomena. In the case of refrigeration devices, water is most commonly used as the adsorbate, as it is a chemically stable and environmentally friendly liquid. Porous materials with a developed active surface area (such as silica gels) are used as adsorbents. Adsorbate molecules are trapped in the adsorbent pores by van der Waals forces (weak intermolecular electrostatic bonds). According to the law of conservation of mass, the mass of the adsorbent (porous material) changes, while the adsorbate (refrigerant) only changes its state and condenses on the porous surface of the adsorbent [8]. As a result, energy called adsorption heat is released. This means that adsorption is an exothermic phenomenon, and it is necessary to cool the bed for the process to proceed properly. This is an essential element of the process that affects its efficiency [9]. Similarly, desorption is an endothermic process, so to regenerate a saturated adsorption bed, energy must be supplied from outside. This is one of the reasons why adsorption aggregates have a low COP coefficient, but they are still used in places where waste low-temperature heat can be utilized.

The significant influence of heating and cooling the bed on the efficiency of the adsorption process requires intensive energy exchange between the adsorbent and the heating/cooling source. This is one of the main design challenges for adsorption heat exchangers. Additionally, the temperature distribution in the exchanger should be as uniform as possible, and the pressure drops of the working fluid should be minimized. Numerical simu-

lations using CFD (computational fluid dynamics) are increasingly used to optimize such devices, e.g. improve the geometry of the exchanger [10, 11], determine the optimal cycle time of the device [12], or determine the effect of the adsorbent size on the sorption capacity and heat exchange in the adsorption bed [13].

Modelling the adsorption process using CFD poses several challenges. Fine-grained adsorbent materials generate a significant number of computational elements, making calculations infeasible. Therefore, simplifying the model is necessary by replacing the adsorbent bed with a porous material, which requires determining the substitute characteristics of the porous material. Another challenge is the selection of appropriate equilibrium equations, process kinetics, and their implementation method. Each adsorbent-adsorbate pair has unique features, which means that developed models are not universal.

In this paper, a methodology for simulating mass and heat transfer in an adsorbent bed is presented, which is then validated against available experimental data [14]. The influence of the cooling water temperature on the sorption capacity of silica gel and the dependence of the cooling device's operating cycle on the cooling water temperature are shown.

2 Method and results

The analyzed sample consisted of a heat exchanger with an insulated aluminium housing filled with silica gel (Fig. 1). The geometry was simplified for computational purposes and consisted of only two elements, as shown in Fig. 2: the adsorption bed and the water vapor volume. The heat exchanger was replaced by a convective boundary condition with a heat transfer coefficient of 600 W/m^{2}K and a temperature of 303 K. An adiabatic boundary

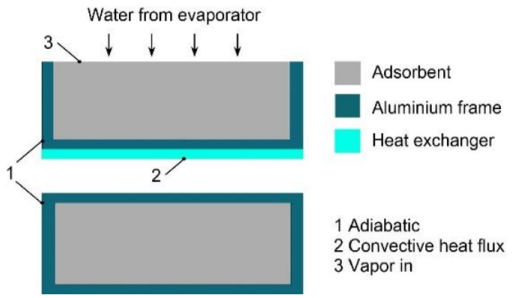

Figure 1: Experimental setup diagram, based on [14].

condition replaced the aluminum frame. The computational mesh which consists of 537 600 hexahedral cells is presented in Fig. 3.

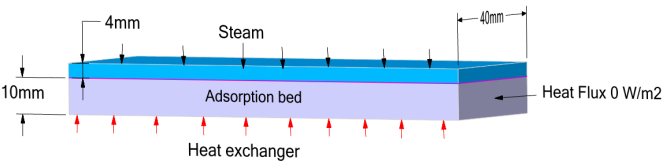

Figure 2: Simplified geometry used in the simulation.

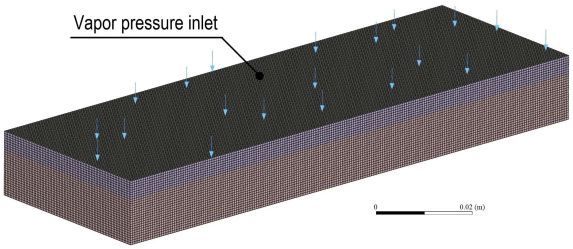

Figure 3: View of the numerical mesh of the studied sample.

The calculations were carried out using commercial computational fluid dynamics software Ansys Fluent [15] in which unsteady Navier-Stokes equations and energy conservation equation were solved using the finite volume method, assuming laminar flow and using superficial velocity formulation. Thermal equilibrium between the adsorption bed (porous medium) and the fluid was assumed:

$$\frac{\partial \rho_f}{\partial \tau} + \frac{\partial (\rho_f v_i)}{\partial x_i} = -S_m \rho_s \frac{1-\varepsilon}{\varepsilon}\,, \tag{1}$$

$$\rho\left(\frac{\partial v_i}{\partial \tau} + v_j \frac{\partial v_i}{\partial x_j}\right) = \frac{\partial P}{\partial x_i} + \mu\left[\left(\frac{\partial v_i}{\partial x_j} + \frac{\partial v_j}{\partial x_i}\right) - \frac{2}{3}\frac{\partial}{\partial x_i}\left(\frac{\partial v_k}{\partial x_k}\right)\right] + S_i\,, \tag{2}$$

$$\left[(\rho c_p)_s (1-\varepsilon) + (\rho c_p)_f \varepsilon\right]\left(\frac{\partial T}{\partial \tau} + v_j \frac{\partial T}{\partial x_j}\right) = \frac{\partial}{\partial x_i}\left[(k_s(1-\varepsilon) + k_f \varepsilon)\frac{\partial T}{\partial x_i}\right] + Q. \tag{3}$$

Due to the small grain size of the adsorbent material, it was necessary to simplify the bed by using a porous medium, i.e., by adding a negative

momentum source term to the standard momentum conservation equation:

$$S_i = -\left(\sum_{j=1}^{3}\frac{1}{\alpha}\mu v_j + \sum_{j=1}^{3} C\frac{1}{2}\rho|v|v_j\right). \tag{4}$$

The source term S_i consists of two parts: viscous losses (classical Darcy's law, the first part of the right-hand side of Eq. (1)) and inertial losses (the second part of the right-hand side of Eq. (1)). The essence of replacing real structures with a porous medium is to determine their equivalent characteristics [16]. In laminar flows through porous media, the pressure drop is usually proportional to the velocity, and the inertial resistance C is equal to 0. The viscous resistance $1/\alpha$ was determined from the transformed Blake-Kozeny equation

$$\alpha = \frac{D_p^2}{150}\frac{\varepsilon^3}{(1-\varepsilon)^2}, \tag{5}$$

assuming a bed particle diameter of $D_p = 35 \times 10^{-5}$ m. The porosity $\varepsilon = 0.37$ was determined as the ratio of free space in the bed to its total volume. In a result, viscous resistance amounted to 9.60×10^9 m^{-2}

Water vapor was used as a fluid and silica gel was used as the solid body material. The adsorption process kinetics were modeled using the linear driving force (LDF) model [17], which takes into account the influence of mesopore and micropore structures. The form of the equation modified by Sun and Chakraborty [18] was used to incorporate the adsorption isotherms and activation energy:

$$S_m = \frac{\partial a}{\partial \tau} = k_m\left(a_{eq} - a\right), \tag{6}$$

where a is the amount of adsorbed water vapor in grams of water vapor per gram of bed and a_{eq} is the equilibrium value for the given conditions. The k_m coefficient depends on the bed parameters and is defined by

$$k_m = \frac{15 D_e}{r_a^2}, \tag{7}$$

where r_a is the radius of the adsorbent particle. The effective diffusion coefficient, D_e, which includes both surface and pore diffusion, is related to the isotherm:

$$D_e = D_0 \exp\left(-\frac{E_a}{RT}\right), \tag{8}$$

where $D_0 = 2.54 \times 10^{-4}$ m^2/s, $E_a = 42$ kJ/mol is the activation energy, R is the gas constant, and T is the temperature. Equation (6) was also used as a source term in the water vapor mass conservation equation (Eq. (1)).

The equilibrium concentration a_{eq} of the adsorbed water vapor was described by the Dubinin-Astakhov adsorption isotherm. This equation is frequently used for silica gel-water vapor systems and was originally developed based on Polanyi's adsorption theory, taking various forms [8, 19]. The model used in this study employed an equation based on the saturation pressure and temperature of the adsorbent:

$$\frac{a}{a_{eq}} = 0.37 \exp\left[-\left(\frac{RT}{E} \ln \frac{P_v}{P_s}\right)^n\right], \tag{9}$$

where P_v is the absolute pressure of water vapor, P_s is the saturation pressure for a given temperature, R is the gas constant, and the isothermal parameters n and E take values of 1.15 and 4280 J/mol, respectively.

Thermal effects were modeled as an energy source term Q, according to Eq. (10)

$$Q = H \frac{\partial a}{\partial \tau}, \tag{10}$$

where H is the heat of adsorption equal to 2415 kJ/kg.

The Green-Gauss node based gradient calculation scheme and the QUICK (quadratic upstream interpolation for convective kinematics) momentum, density, and energy discretization schemes (a high-order scheme for Cartesian grids) were used. The calculations were performed using a pressure-based solver with the PISO (pressure-implicit with splitting of operators) scheme. First order implicit transient formulation was applied.

The water vapor inlet was modeled as a pressure boundary condition with a absolute pressure $P_v = 1230$ Pa and an incoming temperature $T_v = 283.15$ K. The initial conditions were $T = 331.15$ K, $P = 1230$ Pa, and $a = 0.054$ kg/kg.

Iterative calculations were then carried out for 2000 time steps. Each time step lasted 1 s and consisted of a maximum of 30 iterations until the normalized residuals decreased by 4 orders of magnitude. In addition, the average vapor velocity at the inlet, the average temperature in the adsorption bed, and the amount of water vapor adsorbed by the bed were monitored to confirm iterative convergence.

In Figs. 4a and 4b, as well as 5a and 5b, different scales were used to clearly visualize the temperature distribution and saturation within the

adsorption bed. Figures 4a and 4b show the temperature distributions in the adsorption bed at $\tau = 200$ s and 2000 s, respectively. In the initial phase of the adsorption process (Fig. 4a), the highest temperature was found in the middle and upper parts of the bed, reaching approximately 323 K. The lowest temperature was observed in the lower part of the bed, at 305 K. This is because adsorption is an exothermic process and generates a large amount of heat throughout the volume of the bed in the initial stages, while the lower part of the bed was being cooled most intensively by the heat exchanger. At 2000 s (Fig. 4b), the adsorption proceeded with much lower intensity, and the coolest spot (300 K) was in the upper part of the bed, where $T_v = 283.15$ K was introduced due to the pressure difference between the bed and the evaporator. The temperature on the lower surface of the bed was approximately 303 K. The highest temperature, approximately 304 K, was observed in the middle part of the bed, where the adsorption process generated more heat than the cooling effect of the cooling medium.

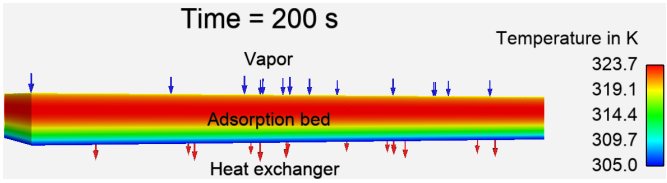

(a)

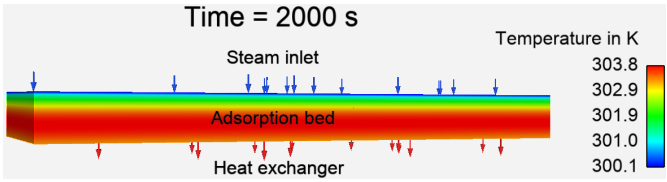

(b)

Figure 4: Graphical distribution of temperature in the adsorption bed at: (a) $\tau = 200$ s, (b) $\tau = 2000$ s.

At time $\tau = 200$ s of simulation, the largest amount of adsorbed vapor was observed in the lower part of the bed (Fig. 5a), as the heat exchanger cooling action locally intensified the adsorption. After 2000 s more uniform distribution of adsorbed water vapor is observed, with maximum in the upper part of the bed (Fig. 4b). This is again due to thermal effects (compare with Fig. 4b), also the top surface is more easily accessible to the water vapor.

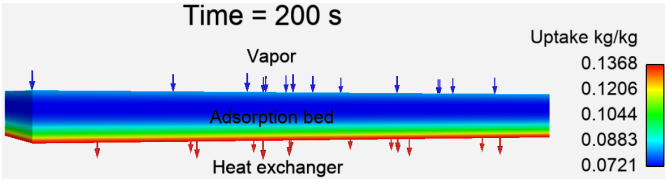

(a)

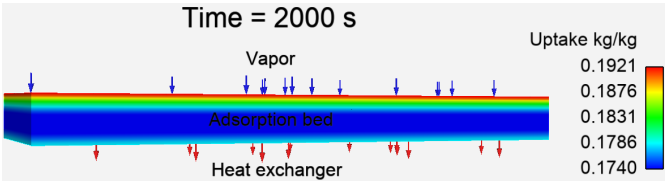

(b)

Figure 5: Graphical distribution of adsorbed vapor at: (a) $\tau = 200$ s, (b) $\tau = 2000$ s.

Model validation is presented in Fig. 6. The amount of water vapor adsorbed by the bed and the average bed temperature was compared between the simulation and experimental data [14].

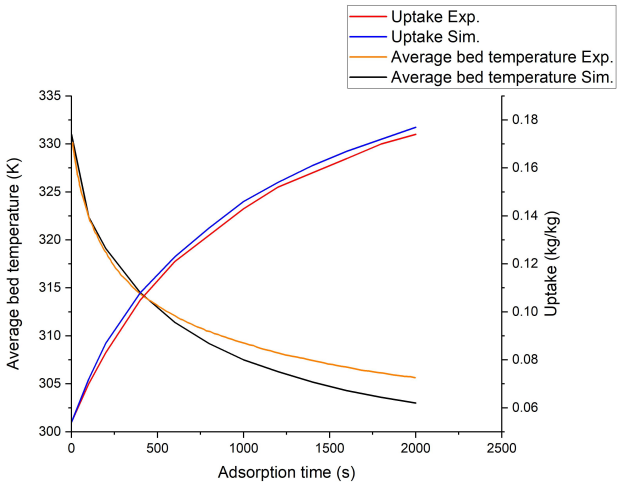

Figure 6: Comparison of experimental and numerical results: average bed temperature and the amount of adsorbed water vapor in the bed.

The maximum relative error between numerical simulation and experimental data for vapor uptake was 3%. For temperature, the maximum relative

error was 1%. Discrepancies may be attributed mostly to the uncertainty of experimental data and modelling assumptions (thermal equilibrium assumption, boundary conditions). The discrepancies were judged as small enough to use the developed model to analyze the influence of various factors on mass and heat transfer in the adsorption bed.

In this work, an analysis was performed on how the temperature of the cooling medium affects the sorption capacity of the bed. Several simulations were conducted at different temperatures of the cooling water (293–313 K), monitoring the change in vapor uptake (Fig. 7).

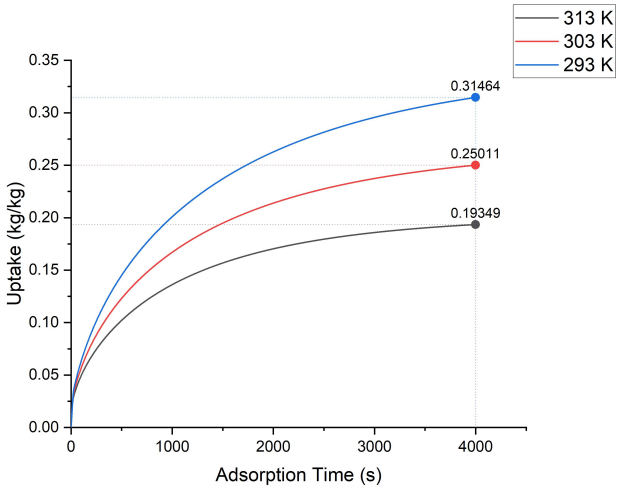

Figure 7: Comparison of the amount of vapor adsorbed by the bed at different cooling water temperatures.

The highest amount of water vapor was adsorbed at the lowest tested temperature (293 K), and the least at the highest tested temperature (313 K), with a difference of 0.121 kg/kg, which is in accordance with adsorption theory and implemented isotherms. This is particularly important considering the availability of cooling medium in different applications and geographic locations. In areas with warm climates where it might not be possible to obtain cooling water for the bed below 303 K using fan-cooling, the device efficiency would already decrease at the design stage due to the lower saturation achievable during each cycle.

In adsorption refrigeration systems, the adsorption and desorption processes occur alternately between two beds, so their time must be equal. The next step was to investigate how the temperature of hot water affects

the desorption process (Figs. 8–10). For this purpose, the bed regeneration process was simulated, starting from saturation condition. The initial degree of sorbent saturation, which largely depends on the temperature of the cooling medium, as shown in Fig. 7, significantly affects the course of the desorption process.

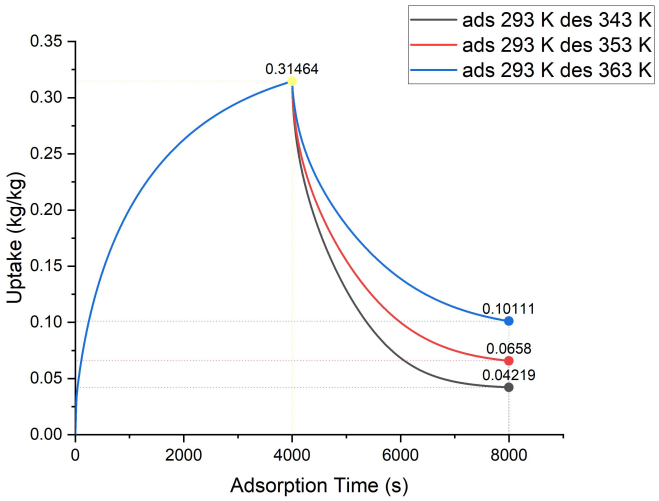

Figure 8: Comparison of the amount of vapor desorbed by the bed at different temperatures of the heating water.

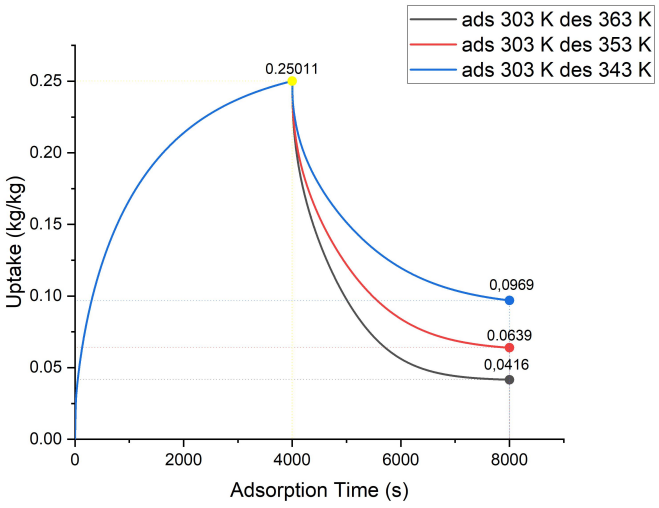

Figure 9: Comparison of the amount of vapor desorbed by the bed at different temperatures of the heating water.

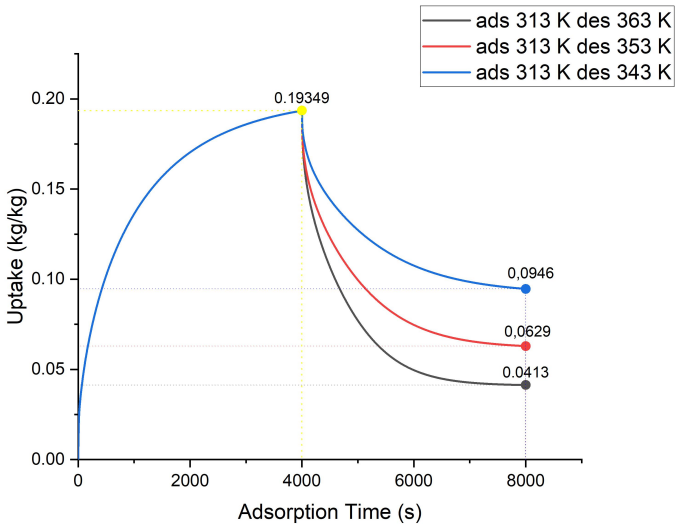

Figure 10: Comparison of the amount of vapor desorbed by the bed at different temperatures of the heating water.

The lowest vapor uptake at the end of the desorption cycle was achieved when the adsorption process was powered by cooling water at $T_c = 313$ K and regenerated with heating water at $T_h = 363$ K, which amounted to 0.0413 kg/kg. The highest amount of adsorbed vapor, 0.1011 kg/kg, remained within the sorbent grains when the bed was cooled with $T_c = 293$ K during the adsorption process and desorption was carried out at a temperature of 343 K.

The relationship between these two processes is significant, as the more vapor remains in the adsorbent material after the regeneration process, the less it can adsorb in the subsequent adsorption process. Also, the adsorption process is more intense the further the bed is from the saturation point. This means that in regions with a warm climate it is possible to achieve higher temperatures of hot water used for bed regeneration. This will result in a lower degree of bed saturation, which will compensate for the higher temperature of the cooling water during the adsorption process. This indicates the possibility of utilizing external conditions during the device design process.

The course of the adsorption/desorption process was analyzed for various single-cycle times of 4000, 6000, and 8000 s and the results are shown in Fig. 11. The analysis was performed for the case where the cooling water

temperature during the adsorption process was 303 K, while the hot water temperature during the desorption process was 353 K.

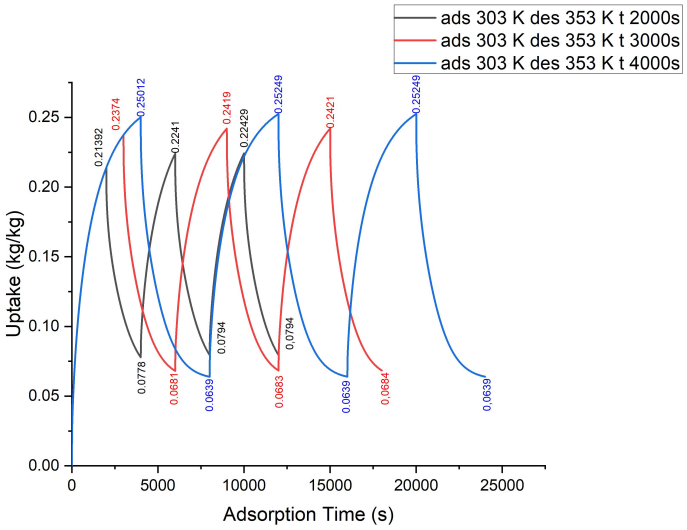

Figure 11: Comparison of the vapor uptake for cooling water temperature of 303 K, heating water temperature of 353 K and for various cycle lengths.

Assuming zero uptake as an initial condition, the degree of saturation at key moments (beginning of adsorption and beginning of desorption) reaches equilibrium after about 3 cycles for cases where the single cycle time was $\tau_{sc} = 4000$ s and 6000 s, respectively. For the case where $\tau_{sc} = 8000$ s, stability was achieved after only 2 cycles. Shortening the single cycle time of the device increases the number of cycles required to stabilize the saturation of the adsorbent bed.

In the case of refrigeration devices, the intensity with which water vapor is adsorbed by the adsorption bed is important, because it affects the device's efficiency. In the case of the third cycle, where adsorption processes reached stability, the amount of absorbed water vapor (the difference in saturation level between the beginning and end of adsorption) in the adsorbent bed was 0.1449 kg/kg for $\tau_{sc} = 4000$ s, 0.1737 kg/kg for $\tau_{sc} = 6000$ s, and 0.1885 kg/kg for $\tau_{sc} = 8000$ s.

Increasing the duration of the adsorption process from 2000 s to 3000 s resulted in an increase of the amount of absorbed water vapor by 0.0228 kg/kg. Increasing the duration of the adsorption process from 3000 s to 4000 s resulted in an increase in the amount of absorbed water vapor

by only 0.0148 kg/kg. The increase in adsorbed water vapor was almost twice as low when extending the time from 3000 s to 4000 s compared to extending the time from 2000 s to 3000 s.

Differences can also be observed on the adsorption and desorption graph where the single cycle duration is 4000 s (Fig. 12). The amount of adsorbed vapor in the third cycle during the first 1000 s of the adsorption process (from 8000 s to 9000 s) is 0.108 kg/kg, while in the subsequent 1000 s (from 9000 s to 10000 s) it decreases to 0.0361 kg/kg. This indicates that the intensity of the adsorption process significantly decreases with the duration of the process.

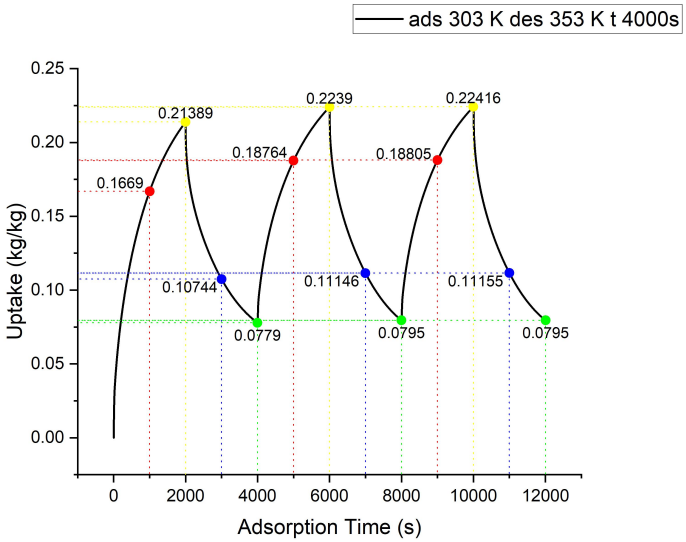

Figure 12: Vapor uptake in function of time for cooling water temperature of 303 K and heating water temperature of 353 K, for cycle lengths of 4000 s.

The effect of the duration of the adsorption process on its course is due to the degree of saturation of the bed. This means that the optimal cycle duration depends on the intensity of the process (cooling water temperature of the bed during the adsorption process), the initial degree of saturation (heating water temperature of the bed during the desorption process), and the type of adsorbent-adsorbate pair. It should be remembered that the main task of the adsorption process in adsorption refrigeration devices is to maintain a low evaporation temperature by extracting the vapor generated in the evaporator. Therefore, the main criterion for selecting the cycle

duration of the adsorption/desorption process is the minimum amount of vapor that can be adsorbed at any given time corresponding to the amount of vapor generated at the same time in the evaporator.

3 Summary

The article presents a method for modeling mass and heat transfer in an adsorption bed using CFD methods. The proposed equation implementation approach is universal for modeling adsorption processes, while the kinetic and equilibrium equations used are specific to the analyzed type of silica gel. The calculations obtained using the model were in agreement with the experimental results available in the literature. The presented approach will be the basis for further experimental research.

Numerous scenarios were tested numerically. The study of the influence of the cooling and heating temperatures on the adsorption/desorption process showed the significance of these parameters and indicated the possibility of utilizing external conditions during the device design process. The impact of cycle length on the intensity of absorbed vapor was also analyzed. Cycles with a duration of 4000 s, 6000 s, and 8000 s were tested. It was demonstrated that the intensity of the adsorption process significantly decreases with the duration of the process. By doubling the cycle length from 4000 s to 8000 s, the amount of adsorbed vapor increased by only 23%.

The developed numerical model allows for the selection of optimal cycle times for adsorption refrigeration devices under specific conditions, which can translate into improving their COP cooling efficiency. This, in turn, can contribute to their competitiveness in the market and environmental protection.

Acknowledgments

The paper was prepared as part of the research and development activities of M.A.S. Sp. z o.o. implementing projects: POIR.01.01.01-00-0628/19 “Development of an innovative, multi-module chiller with increased energy efficiency” and POIR.02.01.00-00-0172/19 “M.A.S. R&D Center of Innovative, Environmentally-Friendly Devices and Systems for Cooling and Energy Storage”.

Received 13 March 2023

References

[1] International Energy Agency (IEA: *The future of cooling opportunities for energy-efficient air conditioning*, 2018. https://iea.blob.core.windows.net/assets/0bb45525-277f-4c9c-8d0c-9c0cb5e7d525/The_Future_of_Cooling.pdf (accessed 18 Aug. 2022).

[2] Fan Y., Luo L.: *Review of solar sorption refrigeration technologies: Development and applications*. Renew. Sust. Energ. Rev. **11**(2007), 8, 1758–1775.

[3] Wang D., Li H., Li D., Xia Y., Zhang J.: *A review on adsorption refrigeration technology and adsorption deterioration in physical adsorption systems*. Renew. Sust. Energ. Rev. **14**(2010), 1, 344–353.

[4] Kuchmacz J., Bieniek A., Mika Ł.: *The use of adsorption chillers for waste heat recovery*. Polityka Energetyczna – Energ. Policy J. **22**(2019), 2, 89–106.

[5] Krzywanski J., Sztekler K., Bugaj M., Kalawa W., Grabowska K., Chaja P., Sosnowski M., Nowak W., Mika Ł., Bykuć S.: *Adsorption chiller in a combined heating and cooling system: simulation and optimization by neural networks*. Bull. Pol. Acad. Sci. Tech. Sci. **69**(2021), 3, e137054.

[6] Li X., Hou X., Zhang X., Yuan Z.: *A review on development of adsorption cooling – Novel beds and advanced cycles*. Energ. Convers. Manage. **94**(2015), 221–232.

[7] Elsheniti M.B., Elsamni O.A., Al-Dadah R.K., Mahmoud S., Elsayed E., Saleh K.: *Adsorption refrigeration technologies*. In: Sustainable Air Conditioning Systems. IntechOpen, 2018.

[8] Wang R., Wang L., Wu J.: *Adsorption Refrigeration Technology – Theory and Application*. Wiley, 2014.

[9] Rani S., Sud D.: *Effect of temperature on adsorption-desorption behaviour of triazophos in Indian soils*. Plant Soil Environ. **61**(2015), 1, 36–42.

[10] Papakokkinos G., Castro J., López J., Oliva A.: *A generalized computational model for the simulation of adsorption packed bed reactors – Parametric study of five reactor geometries for cooling applications*. Appl. Energ. **235**(2019), 409–427.

[11] Petrik M., Szepesi G., Jármai K.: *CFD analysis and heat transfer characteristics of finned tube heat exchangers*. Pollack Period. **14**(2019), 3, 165–176.

[12] Wang X., Chua H., Ng K.: *Simulation of the silica gel-water adsorption chillers*. In: Proc. Int. Refrigeration and Air Conditioning Conf., July 12-15, 2004, 663.

[13] White J.: *A CFD Simulation on how the different sizes of silica gel will affect the adsorption performance of silica gel*. Model. Simul. Eng. **2012**(2012), 65143.

[14] Mohammed H.: *Assesment of numerical models in the evaluation of adsorption cooling system performance*. Int. J. Refrig. **99**(2019), 166–175.

[15] Ansys Fluent Theory Guide, 2023, https://www.ansys.com/

[16] Śmierciew K.: *Numerical and Experimental Aspects of Selected Thermal and Flow Problems of Equipment Used in Refrigeration and Thermal Technology*. Oficyna Wydawnicza Politechniki Białostockiej, Białystok 2018 (in Polish).

[17] Glueckauf E.: *Theory of chromatography. Part 10 – formula for diffusion into spheres and their application to chromatography.* Trans. Faraday Soc. **51**(1955), 1540–1551.

[18] Sun B., Chakraborty A.: *Thermodynamic frameworks of adsorption kinetics modeling: dynamic water uptakes on silica gel for adsorption cooling applications.* Energy **84**(2015), 296–302.

[19] Tran H.: *Mistakes and inconsistencies regarding adsorption of contaminants from aqueous solutions: A critical review.* Water Res. **120**(2017), 88–116.

Notes for Contributors

Archives of Thermodynamics publishes original papers which have not previously appeared in other journals. The journal does not have article processing charges (APCs) nor article submission charges. The language of the papers is English. The paper should not exceed the length of 25 pages. All pages should be numbered. The plan and form of the papers should be as follows:

1. The heading should specify the title (as short as possible), author, his/her complete affiliation, town, zip code, country and e-mail. Please indicate the corresponding author. The heading should be followed by *Abstract* of maximum 15 typewritten lines and *Keywords*.

2. More important symbols used in the paper can be listed in *Nomenclature*, placed below *Abstract* and arranged in a column, e.g.:
   u – velocity, m/s
   v – specific volume, m/kg
   etc.
   The list should begin with Latin symbols in alphabetical order followed by Greek symbols also in alphabetical order and with a separate heading. Subscripts and superscripts should follow Greek symbols and should be identified with separate headings. Physical quantities should be expressed in SI units (*Système International d'Unités*).

3. All abbreviations should be spelled out first time they are introduced in the text.

4. The equations should be each in a separate line. Standard mathematical notation should be used. All symbols used in equations must be clearly defined. The numbers of equations should run consecutively, irrespective of the division of the paper into sections. The numbers should be given in round brackets on the right-hand side of the page.

5. Particular attention should be paid to the differentiation between capital and small letters. If there is a risk of confusion, the symbols should be explained (for example *small c*) in the margins. Indices of more than one level (such as B_{f_a}) should be avoided wherever possible.

6. Computer-generated figures should be produced using **bold lines and characters**. No remarks should be written directly on the figures, except numerals or letter symbols only. Figures should be as small as possible while displaying clearly all the information requires, and with all lettering readable. The relevant explanations can be given in the caption.

7. The figures, including photographs, diagrams, etc., should be numbered with Arabic numerals in the same order in which they appear in the text. Each figure should have its own caption explaining the content without reference to the text.

8. Computer files on an enclosed disc or sent by e-mail to the Editorial Office are welcome. The manuscript should be written as a MS Word file – $*.doc$, $*.docx$ or LaTeX file – $*.tex$. For revised manuscripts after peer review process, figures should be submitted as separate graphic files in either vector formats (PostScript (PS),

Encapsulated PostScript (EPS), preferable, CorelDraw (CDR), etc.) or bitmap formats (Tagged Image File Format (TIFF), Joint Photographic Experts Group (JPEG), etc.), with the resolution not lower than 300 dpi, preferably 600 dpi. These resolutions refer to images sized at dimensions comparable to those of figures in the print journal. Therefore, electronic figures should be sized to fit on single printed page and can have maximum 120 mm x 170 mm. Figures created in MS World, Exel, or PowerPoint will not be accepted. The quality of images downloaded from websites and the Internet are also not acceptable, because of their low resolution (usually only 72 dpi), inadequate for print reproduction.

9. The references for the paper should be numbered in the order in which they are called in the text. Calling the references is by giving the appropriate numbers in square brackets. The references should be listed with the following information provided: the author's surname and the initials of his/her names, the complete title of the work (in English translation) and, in addition:

   (a) for books: the publishing house and the place and year of publication, for example:
   [1] Holman J.P.: *Heat Transfer*. McGraw-Hill, New York 1968.

   (b) for journals: the name of the journal, volume (Arabic numerals in bold), year of publication (in round brackets), number and, if appropriate, numbers of relevant pages, for example:
   [2] Rizzo F.I., Shippy D.I.: *A method of solution for certain problems of transient heat conduction*. AIAA J. **8**(1970), No.11, 2004–2009.

   For works originally published in a language other than English, the language should be indicated in parentheses at the end of the reference.

   Authors are responsible for ensuring that the information in each reference is complete and accurate.

10. As the papers are published in English, the authors who are not native speakers of English are obliged to have the paper thoroughly reviewed language-wise before submitting for publication.

Manuscript submission Manuscripts to be considered for publication should be electronically submitted to the Editorial Office via the online submission and reviewing system, the Editorial System, at http://www.editorialsystem.com/aot. Submission to the journal proceeds totally on line and you will be guided stepwise throughout the process of the creation and uploading of your files. The body of the text, tables and figures, along with captions for figures and tables should be submitted separately. The system automatically converts source files to a single PDF file article, for subsequent approval by the corresponding Author, which is then used in the peer-review process. All correspondence, including notification confirming the submission of the manuscripts to the Editorial Office, notification of the Editors's decision and requests for revision, takes place by e-mails. Authors should designate the corresponding author, whose responsibility is to represent the Authors in contacts with the Editorial Office. Authors are requested not to submit the manuscripts by post or e-mail.

The illustrations may be submitted in color, however they will be printed in black and white in the journal, so the grayscale contributions are preferable. Therefore, the figure

caption and the entire text of the paper should not make any reference to color in the illustration. Moreover the illustration should effectively convey author's intended meaning when it is printed as a halftone. The illustrations will be reproduced in color in the online publication.

Further information All manuscripts will undergo some editorial modification. The paper proofs (as PDF file) will be sent by e-mail to the corresponding author for acceptance, and should be returned within two weeks of receipt. Within the proofs corrections of minor and typographical errors in: author names, affiliations, articles titles, abstracts and keywords, formulas, symbols, grammatical error, details in figures, etc., are only allowed, as well as necessary small additions. The changes within the text will be accepted in case of serious errors, for example with regard to scientific accuracy, or if authors reputation and that of the journal would be affected. Submitted material will not be returned to the author, unless specifically requested.
A PDF file of published paper will be supplied free of charge to the Corresponding Author.

Submission of the manuscript expresses at the same time the authors consent to its publishing in both printed and electronic versions.

Transfer of Copyright Agreement Submission of the manuscript means that the authors automatically agree to assign the copyright to the Publisher. Once a paper has been accepted for publication, as a condition of publication, the authors are asked to send by email a scanned copy of the signed original of the Transfer of Copyright Agreement, signed by the Corresponding Author on behalf of all authors to the Managing Editor of the Journal. The copyright form can be downloaded from the journal's website at http://www.imp.gda.pl/archives-of-thermodynamics/ under Notes for Contributors.

The Editorial Committee